Title
Phases of information encoding in many-body quantum states

Permalink
https://escholarship.org/uc/item/2mx3g7j1

Author
Bao, Yimu

Publication Date
2023

Peer reviewed|Thesis/dissertation

Phases of information encoding in many-body quantum states

by

Yimu Bao

A dissertation submitted in partial satisfaction of the

requirements for the degree of

Doctor of Philosophy

in

Physics

in the

Graduate Division

of the

University of California, Berkeley

Committee in charge:

Professor Ehud Altman, Chair
Professor Norman Yao
Professor Umesh Vazirani

Summer 2023

Phases of information encoding in many-body quantum states

Abstract

Phases of information encoding in many-body quantum states

by

Yimu Bao

Doctor of Philosophy in Physics

University of California, Berkeley

Professor Ehud Altman, Chair

Intermediate-scale quantum devices operate controllably and can maintain quantum entanglement in systems of up to a few hundred qubits. From a many-body perspective, these devices exhibit a novel interplay of entangling unitary evolution, measurements, and decoherence, which is expected to give rise to new emergent phenomena. In this dissertation, we study the collective phenomena associated with information encoding and focus on two broad classes of systems: (i) monitored quantum circuits that consist of unitary evolution and measurements; (ii) topologically ordered states subject to local decoherence.

Monitored random quantum circuits have been shown to undergo a measurement-induced phase transition in the steady state when increasing the measurement rate. In the first part of the dissertation, we develop a theoretical framework that maps the quantum information dynamics in monitored circuits to equilibrium statistical mechanics models. We show that the measurement-induced transition can be formulated as a transition in the capacity of the circuit to encode quantum information and further as symmetry-breaking transitions in statistical-mechanical models. Within this framework, we also identify new phases of information flow in monitored circuits, both when symmetry is imposed on circuit elements and when the circuit is at finite times.

Topologically ordered states in quantum codes can store quantum information in the presence of local decoherence up to a finite threshold. In the second part of this dissertation, we study the effect of decoherence on general quantum ground states with topological order. We develop a theoretical framework based on effective field theory to identify the possible phases induced by decoherence and characterize their capacity to encode quantum information. We further propose information-theoretical quantities to define topological order in the ensuing decoherence-induced mixed states.

To my parents, for your enduring love and support.

Contents

List of Figures

List of Tables

Acknowledgments

My time at Berkeley is stimulating and fruitful. It is emotional at the end of this journey.

I want to start by expressing my gratitude to my advisor Prof. Ehud Altman. Ehud deeply influenced me in many ways both as a physicist and also as a person. He has a high standard and always seeks the simplest understanding of physics problems and the most transparent presentation of ideas. I am always amazed by his unbelievable intuition and his inexhaustible energy and passion. Conversations with him always reward me with refreshing perspectives and a boost in morale. I am grateful to him for his kind guidance and being approachable in my early years and also for encouraging me and giving me the freedom to be an independent researcher toward the end. I am especially indebted to him for his extreme patience in helping me improve my writing skills.

My deep appreciation extends to Soonwon Choi, a mentor and a friend who has guided and encouraged me throughout the past few years. Working with Soonwon in my second year is a huge turning point and starts the research that leads to this dissertation. I owe him many thanks for helping me through the most down-to-earth calculation and also for always sharing his crazy ideas. His knowledge of quantum information theory and atomic physics broadens my horizon and allows us to uncover many connections between concepts in different disciplines.

The visit to Harvard University during the summer of 2021 is an eye-opener for me. I want to thank Prof. Ashvin Vishwanath and Ruihua Fan for their guidance, vision, and collaboration. A significant part of this dissertation would not be possible without many illuminating discussions. Special appreciation also goes to Ruihua for being a sincere friend since college.

I also had the privilege to interact with many other remarkable people. In particular, I am grateful to Prof. Norman Yao for many inspiring discussions. His passion for scientific research always spurs me on, especially after regular working hours. I thank Prof. Xiao-Liang Qi for many helpful discussions over the years. Those discussions are usually brief but packed with information, and I always feel enlightened afterward. I thank Prof. Mike Zaletel for insightful conversations over the years and for his sincere and candid advice. I extend my thanks to Maxwell Block for fruitful collaborations and for showing me his extensive English vocabulary. Also many thanks to Zack Weinstein, Zhehao Dai, Yantao Wu, Zhuo Chen, and Hanyu Xue for numerous illuminating discussions. It is a great pleasure to collaborate on research projects.

My research in grad school would be not possible without the wisdom of the crowd. I extend my thanks to the postdocs and other graduate students in the Berkeley theory community that I interacted with in day-to-day work. Thanks to Erik Aldape, Kamphol Akkaravarawong, Sajant Anand, Alex Avdoshkin, Xiangyu Cao, Shubhayu Chatterjee, Stefan Divic, Sam Garratt, Jaewon Kim, Bryce Kobrin, Chunxiao Liu, Francisco Machado, Dan Parker, Thomas Scaffidi, Tommy Schuster, Karthik Siva, Tomo Soejima, Taige Wang, Tianle Wang, and Bingtian Ye for always being there to answer my questions, encouraging me to overcome all the challenges, and creating a relaxed environment at Berkeley.

Furthermore, I owe deep gratitude to Prof. Felix von Oppen, who advised me when I was merely an enthusiastic novice in the field. I was extremely fortunate that he hosted me as a visiting student in the summer of 2016. Everything I achieved traces back to his encouragement and support. I also extend my thanks to Prof. Yang Peng for teaching me everything from the basics and collaborating on my very first project.

Outside physics, I am fortunate to have many friends and mentors in the field of theoretical computer science. I am grateful to Prof. Dorit Aharonov, Xun Gao, Zeph Landau, Yunchao Liu, and Prof. Umesh Vazirani for many illuminating discussions. Their intuition and knowledge from different background helps me think critically and forces me to examine what I take for granted.

Beyond research, life in the past six years was not short of unforeseeable changes. I owe many thanks to my roommates at APT 218. It has been a memorable experience going through the pandemic together. Besides, I have special thanks to Yuchen Tang for being the special friend and sharing many memorable moments in life.

Finally, I would like to thank my family for everything they have done for me.

Citations to previously published work

Most of the chapters in this dissertation are adapted from previously published work. In order of appearance:

- Chapter 2 is adapted from

  Soonwon Choi*, **Yimu Bao***, Xiao-Liang Qi, Ehud Altman, *Quantum error correction in scrambling dynamics and measurement induced phase transition* Phys. Rev. Lett. 125, 030505 (2020)

- Chapter 3 is adapted from

  Yimu Bao*, Soonwon Choi*, Ehud Altman, *Theory of the phase transition in random unitary circuits with measurements* Phys. Rev. B 101, 104301 (2020)

- Chapter 4 is adapted from

  Yimu Bao, Soonwon Choi, Ehud Altman, *Symmetry enriched phases of quantum circuits* Annals of Physics 435 (2021) 168618

- Chapter 5 is adapted from

  Yimu Bao, Maxwell Block, Ehud Altman, *Finite-time teleportation phase transition in random quantum circuits* arXiv:2110.06963

- Chapter 6 is adapted from

  Yimu Bao, Ruihua Fan, Ashvin Vishwanath, Ehud Altman, *Mixed-state topological order and the errorfield double formulation of decoherence-induced transitions* arXiv:2301.05687

- Chapter 7 is adapted from

  Ruihua Fan*, **Yimu Bao***, Ehud Altman, Ashvin Vishwanath, *Diagnostics of mixed-state topological order and breakdown of quantum memory* arXiv:2301.05689

Chapter 1

Introduction

The complexity of many-body systems underlies a plethora of emergent phenomena. As explained in Anderson's famous essay "More is different" [12], many-body systems can develop macroscopic structures, such as liquids and crystals, which cannot be easily deduced from understanding only the constituent elements. These emergent structures, arising from complexity, are universal features shared among different systems and define the phases of matter.

The complexity of many-body *quantum* system also underlies another type of emergent property — their advantage in performing computational tasks. Pioneering works have demonstrated that *quantum computers*, programmable devices over many coherent quantum degrees of freedom, can outperform their classical counterparts in solving many challenging problems [238, 175, 111, 7]. However, maintaining the coherence of macroscopic quantum systems is a challenging task, which hinders the experimental realization of full-fledged quantum computers.

In recent years, quantum technologies have made significant development toward realizing quantum computers. Several near-term devices based on leading experimental platforms have emerged, including Rydberg atom arrays [29, 48, 80, 234, 34], trapped ion systems [193, 281, 197], superconducting qubit circuits [15, 275, 226, 284, 180, 6]. These devices now operate on up to a few hundred qubits, offer control over individual degrees of freedom, and can perform measurements in underlying quantum states. Despite inevitable decoherence from environmental noise and imperfection in gate operations, they are able to host large-scale quantum entanglement, prepare novel quantum states, and perform quantum simulation tasks [213, 96, 10]. Questions arise regarding the capacity of these devices to process quantum information and whether they can offer advantages in solving certain computational problems that are beyond the capabilities of classical computers within a reasonable timeframe.

The questions above can be addressed in part from a many-body perspective using the tools developed in condensed matter physics. From this perspective, the near-term devices constitute a new class of many-body systems — *quantum circuits*. The interplay among entangling unitary evolution, measurements, and decoherence in quantum circuits is expected to give rise to new emergent phenomena ("phases" of matter) associated with information

encoding in the circuits. At the same time, these emergent phenomena may provide insights into the potential computational advantage that the circuit can offer.

Several key aspects distinguish the emergent phenomena associated with information encoding in quantum circuits from those in traditional condensed matter systems, making them particularly intriguing and novel. The first difference lies in the diagnostics of the phases. Phases in traditional condensed matter physics are characterized by observables in the quantum state. For example, broken symmetry phases are probed by local order parameters [223, 266]. The more exotic topological phases feature either gapless edge modes or deconfined anyon excitations detected by string order parameters [88, 279]. The defining properties of these phases are operator expectation values, i.e. linear functions of the density matrix. On the other hand, information encoding in the system is characterized by information-theoretical quantities, e.g. entanglement entropy, which are non-linear functions of the density matrix. The associated emergent phenomena do not necessarily manifest in the expectation values of local operators and therefore require a new framework to study their properties.

Second, these information-theoretical quantities behave differently than local observables under local operations. Local operations on quantum states are generally described by quantum channels, which can always be formulated as local unitary operations coupling the system to ancillary degrees of freedom [212]. Usual correlation functions, or other observables, cannot exhibit many-body singularities under such local unitaries. The locality of their response is ensured by the Lieb-Robinson bound [167]. In contrast, the change in information theoretical quantities is not subject to this restriction, opening the possibility for new emergent phenomena in quantum information encoding. For example, topological quantum memories can undergo a phase transition under local decoherence [74]. The encoded information becomes irrecoverable when the decoherence strength is above a finite threshold.

Third, quantum circuits can involve measurements, which are inherently non-unitary operations. The measurement-induced collapse can leave a highly non-local effect in the post-measurement state[1]. In particular, measurements can create nonlocal correlations between far-separated degrees of freedom. This allows phenomena that are strictly impossible in a purely unitary system due to the Lieb-Robinson bound, such as quantum teleportation over a long distance [27] and fast preparation of long-range entangled states [47, 216]. Conversely, in traditional solid-state experiments, measurements are performed only in the end to diagnose the quantum states, and the post-measurement states are not considered.

Due to the novel aspects above, our understanding of these emergent phenomena remains limited. In this dissertation, we develop theoretical frameworks to characterize the phases of information encoding in many-body quantum states in two broad classes of systems: (1) monitored quantum circuits that consist of unitary gates and measurements; (2) topologically ordered states subject to local decoherence. In particular, we elucidate the role of symmetry and topology in characterizing information encoding in these systems.

---

[1]The nonlocal effect does not violate causality as we assume instantaneous classical communication of measurement results.

In the rest of this chapter, we first present background materials setting the stage for the subsequent chapters and then provide an overview of the dissertation.

1.1 Quantum measurement and quantum channel

In this section, we introduce the concepts of quantum measurements and quantum channels, which are used throughout the dissertation.

Quantum measurements

In quantum theory, measurement returns a classical outcome and allows one to read out from the underlying quantum state. At the same time, measurement imposes a generally non-unitary operation and allows one to manipulate the quantum state.

According to the axioms of quantum mechanics, measuring an observable, i.e. a hermitian operator, in a quantum state yields a random outcome drawn from the eigenvalues of the operator. The probability p_m for each outcome m in a quantum state is determined by the Born rule

$$p_m = \mathrm{tr}\left(\hat{P}_m \rho\right), \tag{1.1}$$

where $\hat{P}_m = |m\rangle\langle m|$ is the projector onto the eigenspace. After the measurement, the state is projected onto the eigenspace associated with m, i.e.

$$\rho \mapsto \frac{\hat{P}_m \rho \hat{P}_m}{\mathrm{tr}\left(\hat{P}_m \rho\right)}. \tag{1.2}$$

The projectors $\hat{P}_m$ are orthogonal to each other. We call this type of measurement, *projective measurements*.

Measurement in a more realistic setting is generally different from projective measurements and does not necessarily lead to a projection in the system. The generalized measurement involves two steps. First, we couple the system qubit to a measurement apparatus represented by an ancilla qudit (prepared in a given state, e.g. $|0\rangle$). Then, we perform a projective measurement on the ancilla. The unitary coupling correlates the system Q and the ancilla M, allowing the measurement on the ancilla to reveal the information about the system. To understand the post-measurement state of the system, we consider a general unitary coupling acting on the input state, which can be written as

$$U_{QM} : |\Psi\rangle_Q \otimes |0\rangle_M \mapsto \sum_{m=0}^{N-1} \hat{M}_m |\Psi\rangle_Q \otimes |m\rangle_M, \tag{1.3}$$

where $\sum_{m=0}^{N-1} \hat{M}_m^\dagger \hat{M}_m = \mathbb{1}$ required by unitarity. Measuring the ancilla in the computational basis has N outcomes, and each outcome m has a probability $p_m = \mathrm{tr}\left(\hat{M}_m^\dagger \hat{M}_m \rho\right)$. After the measurement, the system is evolved by a generally non-projective operator $\hat{M}_m$

$$\rho \mapsto \frac{\hat{M}_m \rho \hat{M}_m^\dagger}{\mathrm{tr}\left(\hat{M}_m^\dagger \hat{M}_m \rho\right)}. \tag{1.4}$$

We remark that the probability distribution of measurement outcomes only depends on a set of non-negative hermitian operators $\hat{\Pi}_m := \hat{M}_m^\dagger \hat{M}_m$, which is said to form a positive operator-valued measure (POVM).

Quantum channel

Quantum channel describes the most general evolution of a quantum state, which is a linear, trace-preserving, and completely positive (TPCP) map. According to the Choi-Kraus theorem, any linear TPCP map acting on a density matrix ρ can always be expressed through a Kraus decomposition [271]

$$\mathcal{N}[\rho] = \sum_{\alpha=0}^{N-1} K_\alpha \rho K_\alpha^\dagger, \tag{1.5}$$

where K_α is called the *Kraus operator* and satisfies $\sum_{\alpha=0}^{N-1} K_\alpha^\dagger K_\alpha = \mathbb{1}$ [2].

A quantum channel can be equivalently formulated as the unitary evolution acting on an extended system that includes an environment [212]. Specifically, the channel $\mathcal{N}$ can be realized by coupling the system Q to an ancilla qudit E (representing the environment) by a unitary gate U_{QE} and then tracing over the ancilla, i.e.

$$\mathcal{N}[\rho] = \mathrm{tr}_E\left(U_{QE}\left(\rho \otimes |0\rangle\langle 0|_E\right) U_{QE}^\dagger\right), \tag{1.6}$$

where

$$U_{QE} = \sum_{\alpha=0}^{N-1} K_\alpha \otimes \sum_{\beta=0}^{N-1} |\alpha + \beta \mod N\rangle\langle \beta|_E. \tag{1.7}$$

The unitary coupling U_{QE} is similar to the coupling between the system and a measurement apparatus when describing a generalized measurement. In fact, if one discards the measurement outcome, the resulting state of the system is an incoherent superposition of

---

[2]The Choi-Kraus theorem works in general for the map $\mathcal{N}$ from a finite-dimensional Hilbert space $\mathcal{H}_A$ to $\mathcal{H}_B$. The resulting Kraus operator is a map $K_\alpha : \mathcal{H}_A \to \mathcal{H}_B$, and its total number has an upper bound, $N \leq \dim(\mathcal{H}_A)\dim(\mathcal{H}_B)$. We also note that the Kraus decomposition of a quantum channel is not unique, and in fact, there are infinitely many equivalent decompositions.

post-measurement states, which is equivalent to the system evolved by a quantum channel with K_α given by the measurement operator $\hat{M}_\alpha$.

A crucial quantity associated with the quantum channel is the *quantum channel capacity*, which quantifies the maximum amount of quantum information one can send from the input to the output [212, 271]. To define the channel capacity, we first introduce the *coherent information* defined for a quantum channel $\mathcal{N} : \mathcal{H}_Q \mapsto \mathcal{H}_{Q'}$ and an input state ρ of the system Q. Considering the input density matrix ρ as an entangled pure state of the system Q and a reference R, the coherent information is given by

$$\mathcal{I}_c(\mathcal{N}, \rho) := S_{Q'} - S_E = S_{Q'} - S_{Q'R}. \tag{1.8}$$

where Q' is the output of the channel. The environment E together with Q' and R is in a pure state, thus $S_E = S_{Q'R}$. The coherent information $\mathcal{I}_c$ characterizes the amount of entanglement between R and Q (equiv. the amount of information encoded in Q) that can be recovered from R and Q', and $\mathcal{I}_c$ is upper bounded by the entropy of the input state ρ, $\mathcal{I}_c \leq S_Q$ [3].

The channel capacity is given by the maximum coherent information per single channel usage. Specifically, we consider applying n copies of the channel $\mathcal{N}$ simultaneously to an input state $\rho^{(n)}$ in the duplicated Hilbert space. The capacity of $\mathcal{N}$ is defined as

$$\mathcal{Q} := \lim_{n \to \infty} \frac{1}{n} \max_{\rho^{(n)}} \mathcal{I}_c \left(\mathcal{N}^{\otimes n}, \rho^{(n)} \right), \tag{1.9}$$

where $\rho^{(n)}$ is allowed to be entangled between different copies of the input Hilbert space. We note that one needs to consider n copies of the channel because the quantum channel can be "superadditive" and may transmit more information when channels are applied simultaneously.

1.2 Quantum state teleportation

In this section, we review the canonical protocol of quantum state teleportation as a simple example to demonstrate that measurements can have a nonlocal effect on an entangled state [27, 37, 39]. We show that the nonlocal correlations produced by the measurement can be characterized by the coherent information defined above.

The protocol involves two parties: Alice and Bob. They share a Bell pair and use it as a resource to teleport an unknown single-qubit quantum state from Alice to Bob. Specifically, we consider the initial state of Alice and Bob given by

$$|\Psi_0\rangle_{AB} = |\phi\rangle_{A_1} \otimes \frac{1}{\sqrt{2}} \left(|00\rangle + |11\rangle \right)_{A_2 B}. \tag{1.10}$$

To teleport the quantum state $|\phi\rangle$, Alice performs a Bell measurement on two qubits, A_1 and A_2, and sends the outcome to Bob. The Bell measurement has four different outcomes

---

[3]The inequality follows from the subadditivity of von Neumann entropy, $S_Q = S_R \leq S_{RE} - S_E = I_c$.

labeled by two binary variables $m_1, m_2 = 0, 1$ and projects the quantum state onto a Bell basis state

$$|\Psi_{m_1 m_2}\rangle = \frac{1}{\sqrt{2}} X_1^{m_1} Z_1^{m_2} (|00\rangle + |11\rangle)_{A_1 A_2},$$ (1.11)

where X_1 and Z_1 are Pauli operators of the first qubit. After the measurement, Bob's qubit is in a pure state

$$|\varphi_{m_1 m_2}\rangle_B = \langle \Psi_{m_1 m_2}|\Psi_0\rangle = Z^{m_2} X^{m_1} |\phi\rangle.$$ (1.12)

With the information of measurement outcome, Bob can apply a decoding unitary gate $X^{m_1} Z^{m_2}$ to recover the quantum state $|\phi\rangle$ that Alice sent. The successful teleportation demonstrates the nonlocal effect of measurement, namely measurement on Alice can affect the quantum state of Bob nonlocally when the outcome is communicated.

Instead of considering an explicit decoding scheme, the teleportation can be also understood by the information flow in the system. Specifically, the successful teleportation is a result that the encoded information in A_1 is retained in the post-measurement state in B together with classical measurement outcomes. To see this, we quantify the information retained in the density matrix

$$\rho_{A'B} = \sum_{m_1, m_2} p_{m_1 m_2} |\Psi_{m_1 m_2}\rangle\langle \Psi_{m_1 m_2}|_{A'} \otimes \rho_{B, m_1 m_2},$$ (1.13)

which is an incoherent mixture of the post-measurement states held by Alice and Bob. Here, A' denotes Alice's qubits after the measurement. Formally, the state in Eq. (1.13) is obtained by applying a complete dephasing channel in the Bell basis to the input state. The dephasing channel reflects the fact that measurements only reveal partial information in the state, and the coherence between different Bell basis states is lost in the post-measurement ensemble.

The amount of encoded information that is retained in the process is characterized by the coherent information of the quantum channel from A_1 to $A'B$. To compute the coherent information, we formulate the input state in A_1 as an entangled state with a reference R and the dephasing channel as a unitary coupling $U_{A'E}$ with an environment E. The coherent information is then given by

$$\begin{aligned}
\mathcal{I}_c(R\rangle A'B) &= S_{A'B} - S_{A'BR} \\
&= S_{B|A'} - S_{BR|A'} \\
&= \sum_{m_1 m_2} p_{m_1 m_2} (S_{B, m_1 m_2} - S_{BR, m_1 m_2}), \\
&= \sum_{m_1 m_2} p_{m_1 m_2} \mathcal{I}_c(R\rangle B)_{m_1 m_2}
\end{aligned}$$ (1.14)

where $S_{B|A'} = S_{A'B} - S_{A'}$ and $S_{BR|A'} = S_{A'BR} - S_{A'}$ are the conditional entropies, and $\mathcal{I}_c(R\rangle B)_{m_1 m_2} = S_{B, m_1 m_2} - S_{BR, m_1 m_2}$ is coherent information conditioned on the outcome.

The coherent information saturates its maximum value (i.e. one qubit) when the input state is a maximally entangled state between A_1 and R. In this case, $\mathcal{I}_c(R\rangle B)_{m_1 m_2} = S_{B,m_1 m_2} - S_{BR,m_1 m_2} = 1$ for each outcome $m_1 m_2$, and therefore $\mathcal{I}_c(R\rangle A'B) = 1$. This indicates the quantum channel has a full channel capacity allowing Alice to send one qubit to Bob.

It is crucial to note that the encoded information is not present in the quantum state of B alone, but only when taken together with the classical information in the measurement outcomes. Discarding the outcomes leads to a maximally mixed state in B. Hence, the channel from A_1 to B carries no quantum information. Indeed, without the classical information of measurement outcomes, Bob cannot perform the decoding to achieve the teleportation.

In Chapter 2, we show that the monitored quantum circuits in the volume-law phase retains an extensive amount of encoded information and can be regarded as a many-body generalization of the teleportation protocol. The measurement-induced transition in the circuit is characterized by the capacity of the dynamics to retain quantum information, which, as in the teleportation protocol quantifies the ability to reconstruct the input state from the output with knowledge of the measurement outcomes. In Chapter 3, we develop a statistical mechanics description that captures the phase transition in the information flow in the monitored circuit.

In Chapter 6 and 7, we discuss the effect of decoherence on topologically ordered states that encode quantum information. The decoherence-induced transition can be similarly characterized by the coherent information between the input and the output. However, no classical measurement outcomes is needed to determine the capacity of the state.

1.3 Measurement-induced phase transition

Monitored quantum circuits that consist of random unitary evolution interpersed by measurements were shown to undergo a *measurement-induced phase transition* (MIPT) [163, 239]. Specifically, the subsystem entanglement entropy in the steady state sharply changes from a volume- to an area-law scaling when increasing the measurement rate. We here review the phenomenology and basic properties of MIPT.

In pioneering works, Refs. [163, 239] demonstrated the MIPT in the steady state of one-dimensional random unitary circuits interrupted by projective measurements. The circuit consists of unitary gates acting on neighboring qubits and arranged in a brick-layer structure. Each unitary gate is drawn independently from a distribution, e.g. Haar distribution over SU(4) group or uniform distribution over Clifford group. After each layer of unitary gates, a projective measurement is performed in the computational basis on every qubit with a probability p. We consider the circuit which acts on N qubits initialized in a product state $|\Psi_0\rangle = |0\rangle^{\otimes N}$ and operates for T time steps. We are interested in the regime $N, T \gg 1$. A schematic of the circuit is presented in Fig. 1.1(a).

The measurements at different spacetime locations generate an ensemble of wavefunctions, dubbed *quantum trajectories*, labeled by the collection of outcomes $\vec{m}$ [illustrated in Fig. 1.1(b)].
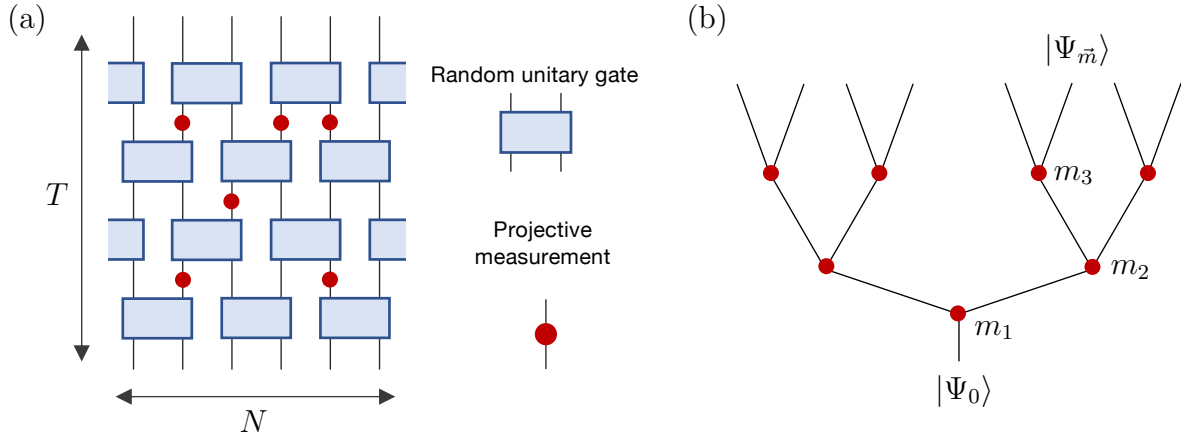
Figure 1.1: Monitor random unitary circuit in one dimension. (a) The circuit operates on N qubits for T time steps. In each time step, random unitary gates (blue boxes) are applied to neighboring qubits. Each gate is independently drawn from the Haar random distribution. After each layer of unitary gates, each qubit is projectively measured in the computational basis with probability p. (b) The measurements (red dots) have random outcomes $\vec{m}$ determined by the Born rule and generate an ensemble of trajectory wave functions $|\Psi_{\vec{m}}\rangle$.

The resulting unnormalized wave function for each trajectory is given by

$$\left|\tilde{\Psi}_{\vec{m}}\right\rangle = \hat{P}_{m_T} U_T \cdots \hat{P}_{m_2} U_2 \hat{P}_{m_1} U_1 \left|\Psi_0\right\rangle, \tag{1.15}$$

where U_t is the unitary evolution during each time step, and $\hat{P}_{m_t}$ denotes the projector associated with measurement outcomes m_t at time step t. The probability for each trajectory is given by the normalization $p_{\vec{m}} = \langle\tilde{\Psi}_{\vec{m}}|\tilde{\Psi}_{\vec{m}}\rangle$, and the normalized trajectory wave function is $|\Psi_{\vec{m}}\rangle = |\tilde{\Psi}_{\vec{m}}\rangle/\sqrt{p_{\vec{m}}}$. The wave functions and their probability together define the *trajectory ensemble*, $\{p_{\vec{m}}, |\Psi_{\vec{m}}\rangle\}$.

By numerical simulation, Ref. [239, 163] showed that a phase transition exists in the subsystem entanglement entropy averaged over quantum trajectories

$$S_A = \sum_{\vec{m}} p_{\vec{m}} S_{A,\vec{m}} = \sum_{\vec{m}} -p_{\vec{m}} \operatorname{tr} \rho_{A,\vec{m}} \log \rho_{A,\vec{m}}, \tag{1.16}$$

where $S_{A,\vec{m}}$ is the von Neumann entropy in the trajectory $\vec{m}$. The subsystem entanglement entropy S_A sharply changes from a volume- to an area-law scaling at a critical measurement

rate p_c, and S_A exhibits a logarithmic scaling at the critical point:

$$S_A = \begin{cases} \mathcal{O}(|A|) & p < p_c \\ \mathcal{O}(\log|A|) & p = p_c \\ \mathcal{O}(1) & p > p_c \end{cases} . \tag{1.17}$$

The finite-size scaling collapse indicates a diverging correlation length at the critical point and thus a second-order phase transition. The scaling analysis determines the critical measurement rate $p_c \approx 0.17$ for monitored Haar random circuits and $p_c \approx 0.15$ for monitored random Clifford circuits [278][4]. Further numerical results suggest that the critical point exhibits conformal invariance [164]. We note that, despite numerical results, an analytical understanding of the critical point of MIPT is still incomplete [130]. However, the universality of MIPT in random Clifford and Haar random circuits is believed to be different [165].

The MIPT can be also formulated as a purification transition in a slightly different setup [104]. Instead of considering qubits initialized in a product state, we prepare the qubits in the maximally mixed state, i.e. a maximally entangled state with reference qubits. Under the monitored random circuit dynamics, the purity of the system qubits increases due to measurements. Ref. [104] showed that the system undergoes a purification transition from a mixed phase to a pure phase simultaneously with the MIPT. In the mixed phase, the system density matrix exhibits a low purity, and the system remains extensively entangled with the reference up to a time scale $T \sim \exp(\mathcal{O}(N))$. In the pure phase, the purity system increases rapidly to an $\mathcal{O}(1)$ value within a time scale $T \sim \mathcal{O}(1)$, and the extensive entanglement between the system and the reference is destroyed by the measurements. The purification transition can be detected by the von Neumann entropy of the entire system averaged over quantum trajectories, $S := \sum_{\vec{m}} S_{\vec{m}}$, which is of a volume- and an area-law scaling in the mixed and pure phase, respectively. The average entropy is closely related to the amount of encoded quantum information retained in the output state and classical measurement outcomes, which we explain in Chapter 2.

Diagnostics of MIPT. — An important distinction between the MIPT and phase transitions in statistical mechanics models lies in their diagnostics. The phase transition in statistical mechanics models can always be detected by an *order parameter*, which is an observable in the state. In contrast, detecting MIPT requires non-linear functions of the quantum state, such as entanglement entropy.

To understand this, we consider the operator expectation value averaged over the entire trajectory ensemble, which is given by that in an average state, i.e.

$$\langle O \rangle = \sum_{\vec{m}} p_{\vec{m}} \operatorname{tr}\left(O \left|\Psi_{\vec{m}}\right\rangle\!\left\langle\Psi_{\vec{m}}\right|\right) = \operatorname{tr}\left(O\rho\right). \tag{1.18}$$

---

[4]The accuracy of finite-size scaling based on half-chain entanglement entropy is limited by the subleading correction in the volume-law phase [239]. To overcome this issue, Ref. [278] divides the system into four regions of equal size (A, B, C, D) and performs the analysis based on the tripartite mutual information $I_3 := S_A + S_B + S_C - S_{AB} - S_{BC} - S_{AC} + S_{ABC}$, in which the subleading correction is largely canceled.

The average state $\rho := \sum_{\vec{m}} p_{\vec{m}} |\Psi_{\vec{m}}\rangle\langle\Psi_{\vec{m}}|$ undergoes unitary evolution interspersed by averaged measurements over all different outcomes, which are described by dephasing channels. Such a dynamics has a steady state being maximally mixed regardless of the measurement rate p. Therefore, $\langle O \rangle$ is a smooth function of p and cannot detect the MIPT[5].

Experimental observation of MIPT.— The fact that MIPT can be only detected by non-linear functions of the state poses challenges for observing such phenomena in experiments. First, measuring an observable in the experiment can be achieved by sampling from a single copy of the quantum state. However, measuring a non-linear function requires either sampling observables from multiple copies of the identical quantum states simultaneously [136] or reconstructing the full density matrix by tomography. Furthermore, measuring quantities in a particular trajectory requires realizing the same trajectory in the experiment for sufficiently many times. However, each trajectory typically occurs with an exponentially small probability, and it takes exponentially many trials to repeat the same trajectory, leading to the so-called *post-selection problem.* The current experiments that observe signatures of measurement-induced phenomena either deal with the exponential difficulty by brutal force [148] or rely on the complementary classical simulation [197, 117].

While probing MIPT might be challenging in experiments, identifying the phases of monitored circuits away from the critical point is a scalable task [105]. Both the volume- and the area-law phase feature a finite correlation length ξ. Hence, it is expected that one can identify the scaling of entanglement in the system of size comparable to ξ, and the required number of sample scales as $e^{\mathrm{Poly}(\xi)}$. The sample complexity diverges, when approaching the critical point, due to the divergence of correlation length ξ. This exponential sample complexity limits the capability to resolve the critical point in experiments.

1.4   Topological quantum memory

Another collective phenomenon of information encoding studied in this dissertation is the *decoding transition in topological quantum memories.* Topological quantum memory encodes quantum information in the degenerate ground states of topologically ordered systems. The encoded information is stored in nonlocal correlations and is robust when local decoherence is weak. It has been shown that topological quantum memory undergoes a decoding transition at a finite decoherence threshold, below which the encoded information can be recovered by quantum error correction algorithms. In this section, we first introduce the Toric code as a paradigmatic example of topological quantum memory and then briefly review the decoding transition in the Toric code.

Toric code.— Toric code is a paradigmatic example of two-dimensional topological order [144]. The model is defined on an $L \times L$ square lattice with periodic boundary conditions and involves $N = 2L^2$ physical qubits on the edges of the lattice. The Toric code

---

[5]The analysis also indicates that the MIPT does not manifest in the entanglement entropy of the averaged state ρ.

Hamiltonian is given by
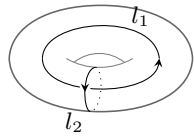
$$H_{\mathrm{TC}} = -\sum_s A_s - \sum_p B_p \,, \tag{1.19}$$

where A_s and B_p are associated with vertices and plaquettes

$$A_s = \prod_{\ell \in \mathrm{star}(s)} X_\ell \,, \quad B_p = \prod_{\ell \in \mathrm{boundary}(p)} Z_\ell \,. \tag{1.20}$$

Here, X_ℓ and Z_ℓ denote the Pauli-X and Z operators on link ℓ, respectively. The operators A_s and B_p are mutually commuting operators called stabilizers. The ground state $|\Psi\rangle$ is a simultaneous eigenstate of the stabilizers satisfying the constraints $A_s |\Psi\rangle = B_p |\Psi\rangle = |\Psi\rangle$. These constraints are redundant, $\prod_s A_s = \prod_p B_p = 1$, and do not uniquely specify the ground state. By simple counting, one can show the ground state is fourfold degenerate.

The topological quantum memory uses the fourfold degenerate ground states to encode two logical qubits. The logical operators are closed-loop operators along two incontractible loops on the torus

$$\bar{Z}_\alpha := \prod_{\ell \in l_\alpha} Z_\ell \,,$$
$$\bar{X}_\alpha := \prod_{\ell \in l_\alpha^*} X_\ell \,, \tag{1.21}$$

where $l = l_\alpha$ and $l^* = l_\alpha^*$ with $\alpha = 1, 2$ are on the original and dual lattice, respectively. Such operators commute with all the stabilizers and thus relate two distinct ground states.

The excited states contain stabilizers A_s (and/or B_p) with -1 eigenvalue, which describe pointlike excitations on the vertices (plaquettes) called e (m) anyon. Anyon e (m) is a self-boson and can only be created in pairs. Anyon e and m are mutual semion; the wavefunction acquires a Berry phase $e^{i\pi}$ under a 2π-braiding of e around m. The bound state of e and m is a fermion labeled by f.

Quantum error correction in Toric code.— The quantum memory that encodes information is inevitably subject to decoherence due to the coupling to the environment. Quantum error correction (QEC) becomes essential to recover the encoded information from a decohered memory. In a pioneering work [74], Dennis et al. showed that QEC algorithms can successfully recover the encoded information in the Toric code as long as the local decoherence rate is below a finite threshold. Here, we review this result and provide a brief introduction to QEC algorithms.

We consider a quantum memory that is subject to local decoherence. The memory is initialized in a Toric code ground state $|\Psi_0\rangle$ that encodes information. For simplicity, we focus on the decoherence that describes single-qubit bit-flip and phase errors

$$\mathcal{N}_{X,i}[\rho] = (1 - p_x)\rho + p_x X_i \rho X_i, \tag{1.22}$$
$$\mathcal{N}_{Z,i}[\rho] = (1 - p_z)\rho + p_z Z_i \rho Z_i, \tag{1.23}$$

where p_x and p_z are the corresponding error rates. The resulting decohered quantum memory is described by a density matrix

$$\rho = \prod_i \mathcal{N}_{X,i} \circ \mathcal{N}_{Z,i}[|\Psi_0\rangle\langle\Psi_0|]. \tag{1.24}$$

The error operator X (Z) creates a pair of m (e) anyon excitations on the adjacent plaquettes (vertices) when acting on the Toric code ground state. These excitations can delocalize and potentially create logical errors when the error rate is large.

Quantum error correction is a process that recovers the encoded state $|\Psi_0\rangle$ from the corrupted state ρ. It begins with measuring the stabilizers A_s and B_p. Due to the phase (bit-flip) errors, certain A_s (B_p) stabilizers are measured in -1 eigenstates indicating the presence of local e (m) excitations. The stabilizer with -1 eigenvalue is called a "syndrome", and we denote the configuration of e (m) syndromes by s_z (s_x).

The e (m) syndromes in the state can be annihilated in pairs by applying a string operator of Pauli Z (X) connecting the two on the original (dual) lattice. The string operator along a path $\mathcal{R}_{x(z)}$ corrects all the syndromes provided that $\partial R_{x(z)} = s_{x(z)}$. However, such a string operator is not unique and can be divided into multiple homological classes; two strings that differ by a contractible loop belong to the same class, and strings in different classes differ by a non-contractible loop. The recovery string operators in the different classes are not equivalent in error correction. If the recovery operator is in the same class as the string operator that creates the syndromes, one recovers the encoded state $|\Psi_0\rangle$. However, applying the recovery string operator in other homological classes will result in a logical error.

To achieve high fidelity in decoding, we first evaluate the probability that the error string belongs to each one of the four classes. We then choose the recovery string from the class with the highest probability to correct the syndromes. This procedure results in a decoding fidelity

$$\mathcal{F} = \sum_s P(s)\frac{\max\{P_{\alpha\beta}(s)|\alpha,\beta=\pm1\}}{\sum_{\alpha,\beta=\pm1} P_{\alpha\beta}(s)} = \sum_s \max\{P_{\alpha\beta}(s)|\alpha,\beta=\pm1\}, \tag{1.25}$$

where $P_{\alpha\beta}(s)$ is the probability of strings in each class, and the total probability $P(s) = \sum_{\alpha,\beta=\pm1} P_{\alpha\beta}(s)$.

Ref. [74] showed that the probability for each class maps to the partition function of the two-dimensional random bond Ising model (RBIM) along the Nishimori line. The RBIM undergoes a ferromagnetic-to-paramagnetic phase transition when tuning the error rate, corresponding to a decoding transition in the Toric code. In the ferromagnetic phase, one homological class has a significantly higher probability, giving rise to a perfect decoding fidelity in the thermodynamic limit, while the probabilities for different classes are roughly the same in the paramagnetic phase.

In the above example, we consider a specific QEC algorithm and focus on information encoding in the Toric code ground states. In Chapter 6 and 7, we show that the decoding transition originates from an intrinsic transition in the corrupted state without relying on

QEC algorithms. Furthermore, such a transition can be generalized to topologically order states perturbed away from the solvable models of topological quantum codes.

1.5   Overview

The rest of the dissertation can be divided into two parts. The first part comprises Chapter 2, 3, 4, and 5 and is devoted to the study of phases and phase transitions in monitored quantum circuits.

- In Chapter 2, we demonstrate that the monitored circuits can be viewed as a self-organized quantum error correction code fueled by scrambling dynamics. We identify a crucial role played by scrambling unitary evolution; the scrambling protects quantum information from being revealed by measurements and therefore can compete with the disentangling effects of measurements giving rise to a phase transition. This allows us to resolve an early debate regarding the stability of volume-law phase. We further formulate the distinct phases in terms of the capacity of the monitored dynamics to retain quantum information. This chapter is adapted from Ref. [65].

- In Chapter 3, we develop a theoretical framework for the MIPT based on a mapping between random quantum circuits and a series of effective classical spin models. Crucially, we identify a $\mathcal{S}_n$ replica permutation symmetry in the n-th spin model, which is spontaneously broken at a critical measurement rate giving rise to distinct phases. The symmetry-breaking transition in the spin model restores the MIPT in an analytic limit $n \to 1$. In this framework, we show the entanglement entropy in the circuit along with a complementary diagnostics based on measurement outcomes, the Fisher information, map to quantities that detect the symmetry-breaking order in the spin model and thus consistently probe the MIPT. Moreover, by exactly solving the spin models, we identify the universality of the MIPT in one-dimensional random circuits with bond percolation on a two-dimensional square lattice in the limit of a large local Hilbert space dimension. Furthermore, we demonstrate that the decoherence in the circuit immediately destabilizes the MIPT as it manifests as a symmetry-breaking field in the spin model. This chapter is adapted from Ref. [18].

- In Chapter 4, we address the question regarding the possible phases of monitored circuits when a physical symmetry is imposed on the circuit elements. Based on the framework we developed, we find that the physical symmetry does not on its own dictate the possible phases, and it is instead extended by dynamical replica symmetries to form an enlarged symmetry. Thus, we predict phases that have no equilibrium counterpart and could not have been supported by the physical circuit symmetry alone. This chapter is adapted from Ref. [17].

- In Chapter 5, we turn to the phases of random circuits at finite times (i.e. constant depths) and showcase a teleportation transition. In concrete examples, we demonstrate

that quantum information can be teleported over an arbitrary distance by performing local measurements in the output state when the circuit depth is above a finite threshold, while the teleportation fidelity decays to zero below the threshold. We provide an analytic understanding of the finite-time transition as replica symmetry breaking in a finite temperature Gibbs state and identify the criteria for circuits to exhibit such a transition. This chapter is adapted from Ref. [16].

The second part comprises Chapter 6, and 7, in which we study the phase transition in topologically ordered states induced by local decoherence.

- In Chapter 6, we develop an effective field theory that characterizes the impact of decoherence on topologically ordered ground states. The decoherence appears as a defect in the topological quantum field theory that describes the topological ground state, and it drives a boundary anyon condensation at a finite critical decoherence rate. We show that the defining features of topologically ordered ground states are generally stable against weak decoherence, allowing one to define topological order in mixed states. We further classify the decoherence-induced phases in terms of possible boundary anyon condensates and address their capability in encoding quantum information. This chapter is adapted from Ref. [19].

- In Chapter 7, we propose three information-theoretical diagnostics of the topological order in mixed states: (1) quantum relative entropy; (2) coherent information; (3) topological entanglement negativity. These quantities generalize the diagnostics of ground-state topological order and are intrinsic to the mixed states. In a concrete example of Toric code with incoherent errors, we show these quantities consistently probe the distinct decoherence-induced phases. The threshold in these intrinsic diagnostics is an upper bound on that achieved in any QEC algorithm and is indeed saturated by that in the optimal decoding algorithm for the Toric code. This chapter is adapted from Ref. [84].

Chapter 2

Information flow in random unitary circuits with measurements

2.1 Introduction

A generic unitary evolution of a quantum many-body system scrambles information. Any local degrees of freedom that are initially in an unentangled state become increasingly more entangled with the rest of the system, making the information encoded in them effectively unrecoverable [75, 241, 219]. The scrambling dynamics [114, 233, 237, 121], evidenced by the growth of the entanglement entropy toward an extensive value [186, 140, 183, 132], underlies the rich complexity of quantum dynamics and the fact that simulating it is beyond the capability of classical computers.

In a realistic system, however, unitary dynamics is often interspersed by occasional measurements of local observables made by external observers either controlled or accidental. This process disentangles the measured degrees of freedom from the rest of the system, which may reduce the entanglement entropy. Thus, it is natural to ask under what conditions the growth of entanglement is tamed to a point allowing efficient classical simulations of the quantum dynamics [4, 259].

This question has been addressed in a number of recent works. In the special case of non-interacting fermions, quantum states with volume scaling entanglement (volume-law phase) are unstable to any small rate of measurements in local occupation basis, leading to steady states in which the entropy only scales with the boundary area of a region (area-law phase) [55]. However, the corresponding behavior in generic interacting systems appears to be much more subtle and has not been fully understood. On the one hand, Ref. [239, 163, 59] suggested that the interplay between the unitary dynamics and measurements can lead to a transition between two distinct phases: for sufficiently small measurement rates, the system remains stable in the volume-law phase, while it undergoes a transition into an area-law phase as the rate exceeds a certain critical value. On the other hand, in its early version, Ref. [59] pointed out that this phase transition cannot be explained by a simple competition
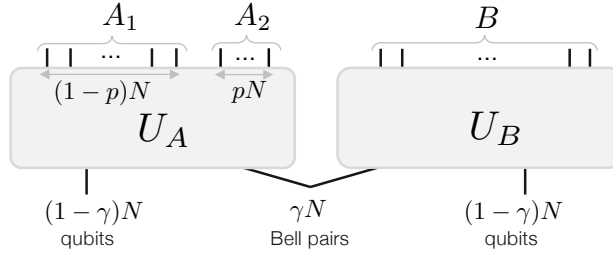
Figure 2.1: Quantum state of $2N$ qubits generated by applying unitaries $U_{A(B)}$ to γN Bell pairs. Measuring p fraction of qubits (A_2) do not reduce the entanglement between $A = A_1 A_2$ and B as long as $1 - 2p > \gamma$ in the limit $N \to \infty$.

between rates of entanglement growth and measurements, as it would always predict the area-law phase for nonzero measurement rates.

In this Chapter, we show that a central ingredient for understanding the entanglement phase transition is the effective quantum error correction enabled by scrambling unitary dynamics. Using simple concepts from quantum information theory, we provide new insight on the mechanism that drives the phase transition. Naïvely, the phase transition seems to hinge on the competition between the rate of entanglement generation by unitary gates and that of disentanglement by measurements. If this perspective were true, the volume-law phase is unstable against an arbitrarily small rate of measurements since the competition is fundamentally not symmetric. Given a bipartition, a local unitary gate may change the entanglement only when it acts nontrivially across the boundary of two subsystems. In contrast, the effect of the measurements could be nonlocal: by disentangling all of the measured qubits inside a subsystem, the rate of entanglement reduction may be extensive. Thus, measurements would always overwhelm the entanglement generation and destabilize the volume-law phase. Here, we argue that this is not the case when information scrambling is taken into account.

Our key observation is that nonlocal effects of sparse measurements are greatly suppressed due to the natural quantum error correction (QEC) property of scrambling dynamics. If quantum information is sufficiently scrambled by unitary evolution, correlations between two subsystems are hidden in highly nonlocal degrees of freedom and cannot be revealed by any local measurements. In such case, sparse local measurements, despite their extensive number, cannot decrease the entanglement entropy significantly. To illustrate this point and quantify the condition under which the entanglement is robustly protected against local measurements, we improve and apply the quantum decoupling theorem to a specially constructed toy model [192, 212], showing the stability of the volume-law phase. We find that the mechanism of the protection is equivalent to that of the QEC scheme [192, 231, 212]. Motivated by this understanding, we introduce a new model and analyze its dynamics both analytically and numerically to obtain the phase diagram. Furthermore, we establish

an exact relation between the steady-state entanglement entropy and the quantum channel
capacity of quantum dynamics.

2.2 Protection against measurement

We now illustrate how entanglement can be protected against measurements using a well-
studied toy example from quantum information theory [76, 120, 3, 212]. Consider a system
of $2N$ qubits ($N \gg 1$) as shown in Fig. 2.1. Initially, the two halves of the system, A and B,
share γN Bell pairs ($0 < \gamma < 1$), which control the amount of the entanglement between the
two. The two subsystems are evolved independently with unitaries U_A and U_B, respectively.
We assume U_A is a random unitary drawn from the Haar distribution (or any unitary 2-
design), and U_B can be arbitrary. Following this evolution, a fraction p of the qubits in
A are measured. The pertinent question is by how much these measurements reduce the
entanglement between A and B. We shall show that under a certain condition the change of
entanglement entropy due to the measurements vanishes in the thermodynamic limit even
though an extensive number of qubits are being disentangled. Note that this result can
be generalized to incorporate measurements performed on both A and B by sequentially
analyzing the effect of measurements.

We first simplify the problem. Since U_B does not affect the entanglement, we may
replace B with its minimal effective degrees of freedom $\tilde{B}$ entangled with A, i.e., the
original γN entangled qubits. Also, we divide A into two parts: subsystem A_1 refers to
the unmeasured qubits and subsystem A_2 contains the measured ones. We now apply the
decoupling theorem [76, 120, 3, 212] to this setup, which will imply that, for a sufficiently small
measurement fraction p, the reduced density matrix of A_2 and $\tilde{B}$ approximately factorizes

$$\mathbb{E}_{U_A}\left[||\rho_{A_2\tilde{B}}(U_A) - \rho_{A_2}^{\max} \otimes \rho_{\tilde{B}}||_1\right] \leq 2^{-(1-2p-\gamma)N/2}. \tag{2.1}$$

Here, the left-hand side denotes the distance, in the L_1 norm, between the exact density
matrix $\rho_{A_2\tilde{B}}$ and a factorized one where $\rho_{A_2}^{\max}$ is the maximally mixed state on the measured
part A_2. $\mathbb{E}_U[\cdot]$ represents averaging over the random unitaries. The inequality implies that
the measured qubits are effectively decoupled from $\tilde{B}$ for $N \gg 1$, provided that the number
of unmeasured qubits A_1 is more than half of the total system $A\tilde{B}$, or equivalently

$$\gamma + p < \frac{1}{2}\left(1 + \gamma\right), \tag{2.2}$$

or simply $\gamma < 1 - 2p$. If this inequality is satisfied, then any observable in A_2 contains no
information about $\tilde{B}$ and vice versa. Therefore, measuring one subsystem does not affect
the other, up to an error exponentially small in N. In particular, any projection (due to
measurements) acting on A_2 does not alter $\rho_{\tilde{B}}$, and the entanglement entropy of subsystem B
is unchanged. In fact, one can show that even the initial γN Bell pairs can be reconstructed
by local operations in A_1 with an exponentially good precision [231].
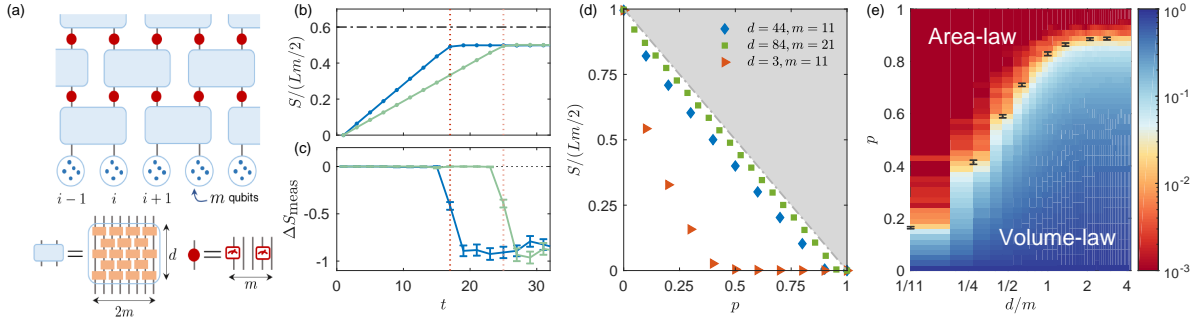
Figure 2.2:   (a) A model with tunable degrees of information scrambling d and measurements p. An array of m-qubit blocks undergoes layers of unitary gates (light blue) and random projective measurements (red). Each unitary acting on neighboring blocks comprises independently random 2-qubit gates (orange). Each measurement projects a randomly chosen p fraction of qubits in each block. (b,c) Entanglement dynamics with $m = 11$, $d = 44$, and $p = 0.4$ for two different system sizes $L = 32$ (blue) and 48 (light green). (b) The growth of entanglement density as a function of time t. The dash-dotted line indicates the upper bound $1 - p$. (c) Change in the entanglement entropy before and after projective measurements at each time step. (d) Steady state entanglement entropy per qubit as a function of p for $(d, m) = (44, 11)$, $(84, 21)$ and $(3, 11)$. (e) Phase diagram for $m = 11$. The color-coded background displays the half-chain entanglement entropies in steady states, normalized by the number of qubits $Lm/2 = 176$. Black markers indicate the phase transition points extracted from finite size scaling analysis up to $L = 64$. The numerical results in (b-e) are averaged over 240 different realizations of random circuits and measurements.

The inequality in Eq. (2.2) is enough to prove the stability of volume-law scaling of the entanglement entropy in the presence of extensive number of measurements. However, it is not tight. This is because in deriving the inequality we assumed that qubits in A_2 are discarded (i.e., qubit loss errors), whereas in our situation they are projectively measured, leaving their measurement outcomes as *accessible classical information*. In Appendix A, we develop an improved decoupling equality, in which the measurement outcomes from A_2 are treated as accessible information. This leads to a tight bound

$$\gamma < 1 - p \tag{2.3}$$

in the limit $N \to \infty$. This inequality can be saturated by typical Haar random unitaries. An intuitive way to understand this new result is to realize that the measurement processes of pN qubits involves entangling those qubits with an equal number of auxiliary qubits representing the environment (or classical measurement devices). These additional degrees of freedom effectively add to the right hand side of Eq. (2.2), i.e., $\gamma + p < (1 + \gamma + p)/2$, leading to the tight bound.

So far, we have considered an ideal situation where the Bell pairs are hidden over the
entire Hilbert space via a nonlocal unitary. However, we emphasize that such information
scrambling is a generic property of quantum dynamics even in local systems [40, 186, 140,
183, 132]. In such cases, we expect that the amount of entanglement reduction is governed by
the competition between the rate of effective information scrambling and that of projective
measurements.

2.3   Model and phase diagram

Having understood the mechanism to protect the entanglement against measurements through
scrambling, we turn to study a local 1D model in which the rates of effective information
scrambling and measurements can be tuned independently.

Our model consists of a chain of L blocks, each containing a fixed number, $m \gg 1$, of
qubits, as illustrated in Fig. 2.2(a). In each time step t, the system is evolved by a network of
random unitaries $U_d(i, t)$ acting on pairs of neighboring blocks at i and $i + 1$, supplemented
by projective measurements. Crucially, the unitaries $U_d(i, t)$ are constructed from an internal
network consisting of d layers of independent random 2-qubit gates (drawn from any unitary
2-design). Thus, the parameter d controls the degree of information scrambling within a
single $U_d(i, t)$, which becomes maximally scrambling in the limit $d/m \gg 1$. In this limit the
distribution of $U_d(i, t)$ approaches a unitary 2-design over $U(2^{2m})$ [40]. After applications of
the $U_d(i, t)$ on pairs of blocks, a fraction p of the qubits in each block are randomly chosen to
be measured in the computational basis [1]. We note that the special case of our model, $d = 1$,
is closely related to the previously studied ones [163, 239, 59].

Before obtaining a quantitative phase diagram from numerical simulations [Fig. 2.2(e)],
one can already predict the stability of volume-law phase in the limit $m \gg 1$ and $d/m \gg 1$.
Consider the unitary evolution $U_d(i, t)$ for a pair of blocks. If we identify the pair of blocks as
subsystem A and the rest of the system as B, we can use the decoupling inequality as discussed
above. As long as the average entropy per qubit γ satisfies the criteria in Eq. (2.3), the
measured qubits contain almost no information about the rest of the system (up to corrections
exponentially small in m). Here, the entanglement reduction is suppressed by information
scrambling within the blocks. Over multiple time steps, quantum information becomes
scrambled over a larger region, further protecting the entanglement from measurements. Thus
we expect a stable volume-law phase in this regime.

We can also make a definitive statement about the other extreme of small d and high
measurement rate. For example, consider $d = 1$, $m \gg 1$ and $p = 1 - 1/m$. In this case there is
no room for scrambling, thus the probability that a single qubit becomes entangled to other
qubits at distance x away (in units of qubit blocks) is exponentially suppressed as $\sim (1/m)^{mx}$
because the information encoded in the qubit needs to propagate without being projected

---

[1]For noninteger pm, the number of measured qubits is determined from a binomial distribution between
$\lfloor pm \rfloor$ and $\lceil pm \rceil$ with mean pm.

at least $\sim mx$ time steps. This implies area-law entanglement [55]. Therefore, we expect a phase transition between the two extreme cases.

We now complement the theoretical arguments with, a numerical simulation of the half-chain entanglement entropy $S(t)$ starting from the initial state $|\Psi_0\rangle = |0\rangle^{\otimes mL}$. We construct the unitary operators $U_d(i,t)$ from random 2-qubit Clifford gates drawn from a uniform distribution instead of taking Haar random unitaries. Such $U_d(i,t)$ still approaches a unitary 2-design as d increases (see Appendix A), hence this simplification does not affect our predictions, while allowing scalable numerical simulation [100, 1, 109, 108]. Furthermore, the wavefunction evolved under Clifford gates always exhibits a flat entanglement spectrum with respect to any bipartition. Thus, different measures of entanglement entropy, e.g. von Neumann versus Rényi entropies, yield the same value. In the following, we focus on $m = 11$.

We first consider a strongly scrambling regime, $d/(2m) \gtrsim 1$, where the unitary network within a single block effectively acts as a random $2^{2m} \times 2^{2m}$ unitary [40] (see Appendix A). We test if the scrambling property of individual blocks leads to the robust volume-law entanglement of the entire system. Figures 2.2(b,c) show the detailed dynamics of the entanglement entropy for two different system sizes. Clearly, the entropy rescaled by the subsystem size exhibits a strict linear growth until it saturates to a constant value. The convergence of these values confirms the volume-law scaling of the entropy (see Appendix A). Moreover, we can directly compute how much the entanglement entropy changes, $\Delta S_{\mathrm{meas}}(t)$, following projective measurements in each time step. Figure 2.2(c) confirms our prediction that in the strongly scrambling regime $d/(2m) \gtrsim 1$ and $m \gg 1$, the entanglement is unchanged by measurements until it reaches a saturation value set by the maximal entanglement that can be protected by the scrambling dynamics [2]. Once saturated, the entanglement added by the unitary gates pushes the entropy above the threshold of the decoupling theorem and it is reduced back to the saturation value by the subsequent measurements. Thus, upon reaching the saturation value we see a jump of ΔS_{meas} from near zero to a negative value. We further note that the saturation value approaches its maximum, $1 - p$, as m is increased in this regime [Fig. 2.2(d)]. This is natural since our tight bound in Eq. (2.3) becomes exact when $m \to \infty$, and it predicts that each qubit on average contributes $\gamma = 1 - p$ to the global entanglement. We note that this analysis does not hold in the weakly scrambling regime $d/(2m) \lesssim 1$, e.g., $d = 3$, $m = 11$ [Fig. 2.2(d)].

We now turn to the phase transition that occurs when d is decreased or p is increased. From numerical simulations, we compute the half-chain entanglement per qubit and tripartite mutual information in the steady state for various L and p for a fixed d (see Appendix A). We perform a finite size scaling analysis in order to extract the critical measurement fraction p_c as well as the correlation length critical exponent ν [239, 104]. By repeating the analysis for various values of d, we obtain a two-dimensional phase diagram shown in Fig. 2.2(e). We find that the fitted critical exponent ν has a universal value around 1.2 independent of

---

[2]We note that, for this purpose, we have only considered odd time steps since in even time steps projective measurements destroy local entanglement within the qubit blocks that are generated by immediately preceding $U_d(i,t)$.

d and m, suggesting the universality of the transition (see Appendix A). When $d = 1$ the extracted critical value $p_c \approx 0.16$ is consistent with previously reported results [163, 162]. More importantly, we find that the volume-law entangled phase extends to a higher measurement fraction, as d increases to $\sim m$, and then saturates for $d/(2m) \gtrsim 1$.

2.4 Discussion

The existence of the stable volume-law phase has a direct interpretation in terms of QEC for quantum communications [192], where the primary goal is to devise an encoding scheme to transfer the maximum amount of quantum information over a noisy or lossy channel. The maximum amount of coherent quantum information that can be transmitted through such a channel is called the quantum channel capacity $\mathcal{Q}$ [212, 271]. Previously, one of the most important applications of the decoupling theorem, had been to show that by using a random unitary encoding it is possible to asymptotically transfer $1 - 2p$ logical qubits per physical qubit over a lossy channel, in which a fraction p of the physical qubits are lost [212]. In our settings, the projective measurements are distinguished from qubit loss errors since their measurement outcomes are available as classical information. This allows achieving a higher quantum channel capacity $1 - p$ which we prove using a new decoupling inequality (see Appendix A).

   The connection between the quantum channel capacity and the volume-law phase can be made more precise in two different settings. In the specific setting of our 1D model, we considered the capacity within a pair of neighboring qubit blocks. Here, the quantum information we wish to protect is quantified by the entanglement entropy between the qubit blocks and the rest of the system. The random unitary circuit is equivalent to repeated encoding of the information without explicit decoding. Since this encoding scheme can protect $\sim (1 - p)2m$ logical qubits in each pair of m-qubit blocks (see Appendix A), we expect that our system should exhibit a stable volume-law scaling of entanglement supported by those logical qubits.

   In a more general setting, we consider the entire system dynamics as a quantum channel and investigate its quantum channel capacity $\mathcal{Q}$. To this end, we take the input state to be entangled with an auxiliary reference such that its reduced density matrix is ρ_{in}. Then, we ask how much entanglement with the reference can be recovered from the combination of the output system density matrix ρ_{out} and a set of classical measurement outcomes after a long time evolution. This can be quantified by the *coherent information* $\mathcal{I}_c(\mathcal{N}, \rho_{\text{in}})$ [77]. For a quantum channel $\mathcal{N}$ consisting of unitary evolution interspersed with measurements (in any positive-operator valued measures), we show that

$$\mathcal{Q} = \max_{\rho_{\text{in}}} \mathcal{I}_c\left(\mathcal{N}, \rho_{\text{in}}\right) = \max_{\rho_{\text{in}}} \langle S(\rho_{\text{out}}) \rangle \tag{2.4}$$

where $\langle S(\rho_{\text{out}}) \rangle$ is the von Neumann entropy of ρ_{out}, averaged over all possible measurement outcomes during the time evolution (see Appendix A). We note that the first equality in

Eq. (2.4) is not generically valid, but it holds for a class of so-called *degradable* quantum channels that include our cases [77, 212, 271]. Using the second equality, we establish an exact connection between quantum channel capacity and the average entropy of a system undergoing any unitary evolution interspersed by measurements. A similar connection was first suggested in a recent paper by Gullans and Huse [104].

In Ref. [104], $\langle S(\rho_{\text{out}}) \rangle$ for the maximally mixed initial state was shown to undergo a phase transition, which coincides with the entanglement phase transition for pure initial states. Specifically, in the volume-law phase, $\langle S(\rho_{\text{out}}) \rangle$ remains extensive at late time, while in the area-law phase, it rapidly approaches a value of order one. This transition was dubbed the purification phase transition [104]. The equivalence between the purification and entanglement phase transitions has later been established analytically for local Haar random unitary circuits with measurements [18]. Therefore, Eq. (2.4) also builds a quantitative connection between the quantum channel capacity and the entanglement phase transition. We note that, in random circuit models studied in Refs. [239, 163, 104, 18, 130], the channel $\mathcal{N}$ itself is random, whose average $\mathcal{I}_c$ is maximized for the maximally mixed input, furthering the connection (see Appendix A).

Chapter 3

Statistical mechanical models for random unitary circuits with measurements

3.1 Introduction

Quantum states with high degree of entanglement cannot be efficiently emulated by classical computers and may serve as a resource for quantum science [192]. A natural way to generate such states is to evolve a quantum system under generic unitary dynamics, which gives rise to extensive entanglement entropy for any subsystems [186, 140, 183, 141, 215]. However, in realistic situations, the dynamics is also subject to nonunitary evolution owing to local measurements of system degrees of freedom (qudits), performed either by an observer or spuriously by environment. Local measurements generally destroy entanglement within a quantum system as they project the measured qudits onto a definite state, disentangled from the rest. This naturally raises a question: how robust is entanglement generation by unitary evolution against measurements?

Recent works presented numerical results as well as general arguments suggesting that volume-law entanglement in steady states may persist if the rate of measurements is sufficiently small, while frequent enough measurements above a critical rate drive a transition to steady states with area-law entanglement entropy [163, 239, 162, 65, 59, 245, 104]. Despite this progress, an analytic framework to describe the phase transition is still lacking. Such a framework is needed in order to understand universal properties of the two distinct dynamical phases and the nature of the transition between them. Does the phase transition belong to a known universality class? How does the transition affects physical properties that are more accessible and relevant to experiments than entanglement entropy such as probability distributions of certain measurement outcomes? These questions are particularly important in the context of current experimental efforts to demonstrate computational advantages of quantum devices over classical computers. In such efforts, quantum systems are interrogated

both by a controlled measurement device and by an uncontrolled environment, and the entanglement transition may imply a change in the complexity of the quantum dynamics they attempt to simulate.

In this Chapter, we address the above questions by developing a theoretical framework, in which an ensemble of quantum circuits with measurements are exactly mapped to a series of classical statistical mechanics models. Our construction generalizes previous works on emergent classical spin models in random tensor networks and random unitary circuits (RUCs) [115, 214, 253, 183, 283, 124]. In particular, mapping to a statistical mechanics model has allowed to analyze entanglement phase transitions in random-tensor networks, which as we will see, are similar to the measurement-induced entanglement transition in quantum circuits [253]. In the framework of random unitary circuits, such mappings allowed understanding the universal features of entanglement growth and operator spreading in a generic unitary time evolution [186, 183, 140, 141, 215]. The essential difficulties in generalizing the existing approach to include measurements are related to the nonlinearity of the process; one needs to normalize a many-body wavefunction after each projective measurement. Furthermore, it is challenging to consider a typical behavior averaged over different measurement outcomes, since their probabilities are not independent of each other and depend on the state history.

In order to address these challenges, we find that it is conceptually simpler to consider quantum circuits in which every qudit is subject to weak measurement at every time step, instead of ones with a set of randomly distributed strong projective measurements. The weak measurements are implemented by coupling the system qudits to a set of ancilla qudits that are subsequently measured by strong projective measurements as illustrated in Fig. 3.1. The strength of measurement is tuned by the strength of the coupling between the system and the ancilla qudits. Later, we show that the case of random projective measurements can be implemented as a special case of this circuit. Hence, our results pertain to random projective measurements studied in Refs. [163, 239, 59, 162, 65], while they also generalize to the case of constant weak measurement. Our main results are insensitive to this detail.

3.2   Overview

Before proceeding, we provide a brief overview of the main ideas and results of this Chapter. First, we present a simple expression of the subsystem entanglement entropy averaged over different measurement outcomes, which is the quantity considered in previous works [239, 163, 59, 162, 65]. We show how this quantity can be mapped to the excess free energy originating from a domain wall in a classical spin model, generalizing the analytic approaches introduced in Refs. [115, 214, 183, 253, 283, 124], and explain the new insights and results obtained from this mapping.

Next, we identify another signature, or an "order parameter," of the same transition, that is more relevant for experiments. The new quantity offers an alternative interpretation of the
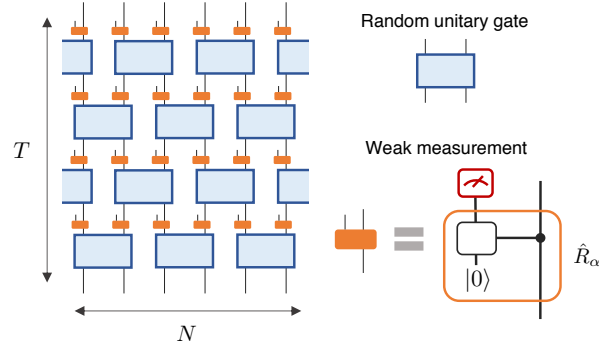
Figure 3.1: Random unitary circuit with weak measurements. After each layer of unitary gates (blue boxes), a weak measurement (orange box) is performed on every system qudit. The red box indicates a strong projective measurement of an ancilla qudit performed after an entangling unitary $\hat{R}_\alpha$.
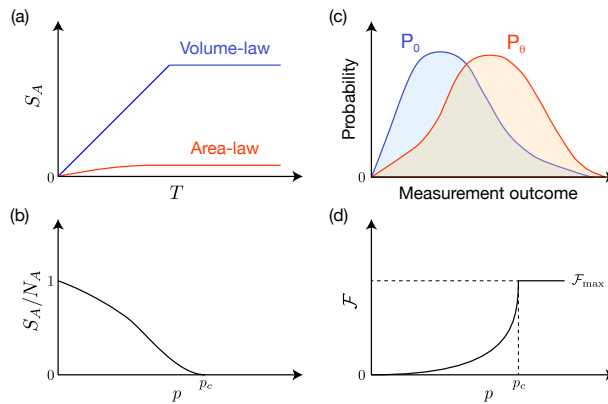
Figure 3.2: Signatures of the phase transition. (a) Growth and saturation of entanglement entropy S_A of a subsystem A (of size N_A). (b) Phase transition in the saturation value of S_A from volume- to area-law scaling. (c) Probability distributions P_0 and P_θ of measurement outcomes arising from two distinct initial states. (d) The phase transition is also seen in the Fisher information, quantifying the amount of information that the measurements carry about the initial state of the system.

phase transition: a sharp change in the amount of information that can be extracted by the measurements about the initial state of the system (see Fig. 3.2).

Replica method: conditional entropy

One of the main quantities considered in previous works is the entanglement entropy of a subsystem A, averaged over measurement outcomes and realizations of the RUC:

$$\overline{\langle\langle S_A(\mathcal{U})\rangle\rangle} \equiv \overline{\sum_{\boldsymbol{i}_M} p_{\boldsymbol{i}_M}(\mathcal{U}) S\left[\rho_A(\mathcal{U}, \boldsymbol{i}_M)\right]}. \tag{3.1}$$

Here, the index $\boldsymbol{i}_M$ runs over all possible measurement outcomes, $p_{\boldsymbol{i}_M}(\mathcal{U})$ is the probability for the measurement outcome $\boldsymbol{i}_M$, $S\left[\rho_A(\mathcal{U}, \boldsymbol{i}_M)\right]$ is von Neumann entanglement entropy of A for a given measurement outcome $\boldsymbol{i}_M$ in a particular realization $\mathcal{U}$ of RUCs, and the overline denotes averaging over the RUC $\mathcal{U}$. By using weak measurement formalism, we can rewrite this quantity in a simpler form by extending the Hilbert space to include the subspace M for ancilla qudits. That is, it exactly equals the conditional entropy:

$$\overline{\langle\langle S_A(\mathcal{U})\rangle\rangle} = \overline{\tilde{S}(A|M)} \equiv \overline{S[\tilde{\rho}_{AM}]} - \overline{S[\tilde{\rho}_M]}, \tag{3.2}$$

where $\tilde{\rho}_X$ denotes the reduced density matrix of subsystem X after ancilla qudits are projected onto their diagonal elements, i.e., measured in their computational basis $|\boldsymbol{i}_M\rangle$: $\tilde{\rho} = \sum_{\boldsymbol{i}} |\boldsymbol{i}_M\rangle \langle \boldsymbol{i}_M| \rho |\boldsymbol{i}_M\rangle \langle \boldsymbol{i}_M|$.

We employ a replica method in order to map the conditional entropy in Eq. (3.2) to a classical spin model. Let us define a series of objects enumerated by an integer n,

$$\tilde{S}^{(n)}(A|M) \equiv \frac{\log\left(\overline{\operatorname{tr}\tilde{\rho}_{AM}^n}\right) - \log\left(\overline{\operatorname{tr}\tilde{\rho}_M^n}\right)}{1 - n}, \tag{3.3}$$

from which the von Neumann conditional entropy $\overline{\tilde{S}(A|M)}$ is recovered in the limit $n \to 1$. It is important to note that $\tilde{S}^{(n)}(A|M)$ is not itself an average conditional (Rényi) entropy, but it recovers its meaning only in the replica limit. Note also that the n-th moments of the replicated density matrices are averaged over $\mathcal{U}$ now inside the logarithms. We will show $\tilde{S}^{(n)}(A|M)$ can be interpreted in terms of free energies of classical spin models in two dimension. The two dimensions arise from the time, which in our convention flows from bottom to top, and the space dimension on the original qudit chain. Each classical "spin" degree of freedom arises from a random unitary gate and may take as its value any one of the $n!$ elements of the permutation group $\mathcal{S}_n$. For example, the case $n = 2$ corresponds to Ising spins, where an up/down spin maps to a trivial/swap element. Increasing the measurement strength weakens the couplings between the spins, leading to a transition from a ferromagnetic to a paramagnetic phase at a critical measurement strength.

The generalized entropy $\tilde{S}^{(n)}(A|M)$ corresponds to the difference between free energies that result from different top boundary conditions. These boundary conditions are arranged

such that $\tilde{S}^{(n)}(A|M)$ describes the excess free energy associated with a domain wall that runs in the bulk and connects the two edges of the subsystem A at the top boundary. The domain wall free energy scales with the length of A in the ferromagnetic phase, which is therefore identified with the volume-law phase, whereas the free energy is of order one in the paramagnetic phase, identified with the area-law phase. We note that entanglement phase transitions in random tensor networks were similarly interpreted in Ref. [253] as a change of domain wall free energies in an emergent statistical mechanics model.

The classical spin model description allows infering crucial information about the transition. First, we obtain an analytic approximation for the critical measurement strength (or the measurement probability in the case of random projective measurements). The spin model description greatly simplifies in the limit of a large local Hilbert space dimension q for a qudit, where our model maps to the $n!$-state standard Potts model on the square lattice. On this lattice, we can obtain the critical coupling strength analytically as a function of n and q using the Kramers-Wannier duality. Taking the replica limit $n \to 1$, we find a critical measurement probability $p_c = 1/2$ in the large-q limit. For a small local Hilbert space dimension $q = 2$, we perform exact numerical simulations for up to $N = 30$ qubits and obtain $p_c = 0.26 \pm 0.02$.

Furthermore, the mapping to an $n!$-state Potts model allows one to infer the universality class of the entanglement transition in the limit $q \to \infty$. Specifically, the partition function of the Q-state standard Potts model approaches that of bond percolation in the physical limit $Q \to 1$. This is similar to the prediction made in Ref. [239] that the special Rényi-0 entropy undergoes a percolation transition. However, in our case, note that the bond percolation transition in the von Neumann entanglement entropy is limited to the case of infinite q.

Alternative signature of the transition

It is important to find the signatures of the phase transition that are more accessible and relevant for experiments than the conditional entanglement entropy. In particular, measuring the conditional entanglement entropy is extremely challenging, as it requires postselecting a particular combination of measurement outcomes with occurrence probability exponentially small in system sizes (in both space and time). Furthermore, for each measurement outcome, estimating entanglement entropy for the quantum state necessitates additional exponentially many repetitions of an experiment [202, 161]. Consequently, the operational meaning of the conditional entanglement entropy is *a priori* not clear from an experimental point of view. A quantity with transparent physical meaning is therefore needed.

The quantum circuit we consider involves measurements. Hence, it is natural to seek the signatures of the transition in the probability distribution (or histogram) of measurement outcomes. Indeed, we show that there is a sharp transition in the amount of information these measurements contain on the initial state of the system, quantified by the Fisher information. The Fisher information can be derived from a closely related quantity, the Kullback-Leibler (KL) divergence (also known as the relative entropy). Given the two distributions $P_0(x)$ and $P_\theta(x)$ of measurement outcomes obtained for two close initial states of the system, the KL

divergence averaged over the RUC is

$$D_{\mathrm{KL}}(P_0||P_\theta) = \overline{\sum_x P_0(x) \log\left(\frac{P_0(x)}{P_\theta(x)}\right)}. \tag{3.4}$$

Here, θ parameterizes the distance between two initial states. The variable x runs over all possible ancilla measurement outcomes. The Fisher information is given by the second order derivative:

$$\mathcal{F} := \partial_\theta^2 D_{\mathrm{KL}}(P_0||P_\theta)\big|_{\theta=0}. \tag{3.5}$$

Note that the first order derivative vanishes due to the positivity of the KL divergence and the fact that it vanishes for $\theta = 0$.

Using the replica method, we recover the KL divergence and the Fisher information in the limit $n \to 1$ from a series of auxilliary functions:

$$D^{(n)}(P_0||P_\theta) := \frac{\log \overline{\mathrm{tr}\left[\tilde{\rho}_{M,0}\,\tilde{\rho}_{M,\theta}^{n-1}\right]} - \log \overline{\mathrm{tr}\left[\tilde{\rho}_{M,0}^n\right]}}{1-n}, \tag{3.6}$$

$$\mathcal{F}^{(n)} := \partial_\theta^2 D^{(n)}(P_0||P_\theta)\big|_{\theta=0}. \tag{3.7}$$

Note that $\tilde{\rho}_{M,\theta}$ denotes the diagonal density matrix of ancilla qudits composed of the probability distribution $P_\theta(x)$. We show that $D^{(n)}$ maps to the excess free energy associated with applying a field on the bottom boundary in the same classical spin model derived for $\tilde{S}^{(n)}$. $\mathcal{F}^{(n)}$ is proportional to the probability of finding a certain subset of spin values (out of the $n!$ possibilities) on the bottom boundary sites. Hence, the Fisher information undergoes the same transition as the entanglement entropy. Above the critical measurement rate, $\mathcal{F}$ reaches a maximal value, reflecting the fact that the measurement device can obtain, over a long enough measurement time, maximal classical information on the initial state. Below p_c, the value of $\mathcal{F}$ starts to deviate from its maximum, reflecting incomplete information on the initial state [see Fig. 3.2(d)].

The transition in information flow can be understood in terms of the natural quantum error correction implemented by the unitary components of the quantum circuit (see Chapter 2). In the volume-law phase, information scrambling by the unitary evolution hides information in nonlocal degrees of freedom, thus protecting it from being revealed by local measurements. The error correction becomes ineffective if the measurement rate exceeds a threshold, or if the measurements are capable of decoding nonlocal correlations, as we show in this work.

The rest of this Chapter is organized in the following order. In Sec. 3.3, we introduce our RUC model with weak measurements and elaborate on the generalized quantities $\tilde{S}^{(n)}$ and $\mathcal{F}^{(n)}$ as well as their relations to the von Neumann entropy and the Fisher information. In Sec. 3.4, we derive the mapping between a RUC with weak measurements and a series of classical statistical mechanics models with various boundary conditions. Section 3.5 is dedicated to discuss the nature of the phase transition for different n. We analytically compute the critical/threshold measurement strength in the large q limit and identify the

universality class of the phase transition. Then, in Sec. 3.6, we slightly digress from our main topic and discuss the absence of the phase transition in the presence of measurements on ancilla qudits in an arbitrary nonlocal basis. Finally, we conclude with discussions and outlook in Sec. 3.7.

3.3 Random unitary circuits with weak measurements

We consider an 1D array of N qudits undergoing random unitary circuit evolution and weak measurements. The unitary circuit consists of independent Haar random $q^2 \times q^2$ unitary gates acting on the nearest neighboring qudits, each with local Hilbert space dimension q. While not very important for our results, we assume a periodic boundary condition for concreteness. The depth of the circuit T corresponds to the discrete time of our model. We are generally interested in the regime $N, T \gg 1$. The layout of the unitary gates is illustrated in Fig. 3.1.

After each layer of unitary gates, every qudit is weakly measured. For each weak measurement, an ancilla qudit with local Hilbert space dimension q' is newly introduced and coupled to the system qudit via an entangling unitary gate $\hat{R}_\alpha$. While a specific choice of q' or $\hat{R}_\alpha$ is not very important for most of our results, we focus on a particular example, where an ancilla has $q' = q + 1$ internal states (enumerated by $|i\rangle_m$ with $i \in \{0, 1, \ldots, q\}$), and the coupling $\hat{R}_\alpha$ takes the form of a controlled rotation:

$$\hat{R}_\alpha = \sum_{i=1}^{q} \hat{P}_i \otimes e^{-i\alpha \hat{X}_i}. \tag{3.8}$$

Here, $\hat{P}_i = |i\rangle_s \langle i|_s$ is the projector onto one of the system qudit states $|i\rangle_s$ (enumerated with $i \in \{1, 2, \ldots, q\}$), $\alpha \in [0, \pi/2]$ is a tunable parameter that controls the strength of the weak measurement, and $\hat{X}_i = |i\rangle_m \langle 0|_m + |0\rangle_m \langle i|_m$ is a generalized Pauli matrix that rotates the quantum state of an ancilla between $|0\rangle_m$ and $|i\rangle_m$. We assume that every ancilla qudit is initially prepared in $|0\rangle_m$. Figure 3.1 shows diagrammatic representations of weak measurements.

The entangling gate $\hat{R}_\alpha$ correlates the quantum state of a system qudit with that of an ancilla qudit. For example, after applying $\hat{R}_\alpha$ with $\alpha = \pi/2$, the ancilla qudit state becomes $|i\rangle_m$ if and only if the system qudit is in $|i\rangle_s$. Therefore, any strong, projective measurements of the ancilla qudit in the computational basis $|i\rangle_m$ reveals the quantum state of the system qudit. When $\alpha < \pi/2$, the correlation between the system and ancilla qudit becomes weaker, thereby a projective measurement of the ancilla constitutes a weak measurement of the system qudit.

The weak measurement strictly generalizes projective measurements. In fact, it can be easily shown that the weak measurement with our choice of $\hat{R}_\alpha$ (followed by a projection in the computational basis) is equivalent to a probabilistic, projective measurement. While the measurement of $|i\rangle_m$ with $i \neq 0$ necessarily implies the system qudit in $|i\rangle_s$, the ancilla in $|0\rangle_m$ for any $\alpha < \pi/2$ reveals no information about the system qudit. Therefore, the measurement

of $|0\rangle_m$ state corresponds to not performing a projective measurement. This relation between weak and projective measurements can be made precise by explicitly computing the density matrix of a system-ancilla qudit pair after applying $\hat{R}_\alpha$ followed by projective measurements of the ancilla in the computational basis:

$$\mathcal{N}_\phi \left[\hat{R}_\alpha \left(\rho_{\text{in}} \otimes |0\rangle_m \langle 0|_m \right) \hat{R}_\alpha^\dagger \right] =$$
$$(1 - p)\rho_{\text{in}} \otimes |0\rangle_m \langle 0|_m + p \sum_i \hat{P}_i \rho_{\text{in}} \hat{P}_i \otimes |i\rangle_m \langle i|_m , \qquad (3.9)$$

where $\mathcal{N}_\phi[\rho] = \sum_i |i\rangle_m \langle i|_m \rho |i\rangle_m \langle i|_m$ is the dephasing channel acting on ancilla that corresponds to the measurement in the computational basis, ρ_{in} is the density matrix of the system qudit before the weak measurement, and $p = \sin^2 \alpha$. We find that the resultant quantum channel is equivalent to that of performing a projective measurement with the probability p. Furthermore, by tracing over system degrees of freedom, one can obtain the probability distribution of different measurement outcomes (including whether or not the measurement has been performed) from the diagonal components of the ancilla density matrix.

When more than one system/ancilla qudits are considered, one can in principle apply a (potentially nonlocal) unitary among the ancilla qudits before performing projective measurements. Such a procedure amounts to probabilistically measuring multi-qudit correlations of physical degrees of freedom. In our work, we first focus on the simple local measurements in computational basis in Secs. 3.4 and 3.5, until we lift this condition later in Sec. 3.6.

Entanglement entropy within the system

One of the central quantities of interest is entanglement entropy within the system. More specifically, we are interested in the entanglement between two complementary subsystems A and B, averaged over all possible measurement outcomes from the collection of ancilla qudit M. Given a particular set of unitary gates $\mathcal{U}$, and measurement outcomes $\boldsymbol{i}_M$, the system remains in a pure state after time evolution, and the von Neumann entropy $S[\rho] \equiv -\text{tr}\{[\rho \log \rho]\}$ of a subsystem characterizes the amount of entanglement. Here, we consider its average behavior:

$$\overline{\langle\langle S_A \rangle\rangle} = \overline{\sum_{\boldsymbol{i}_M} p_{\boldsymbol{i}_M}(\mathcal{U}) S[\rho_A(\mathcal{U}, \boldsymbol{i}_M)]}, \qquad (3.10)$$

where $\overline{}$ and $\langle\langle \cdot \rangle\rangle$ denote the averaging over $\mathcal{U}$ and over measurements $\boldsymbol{i}_M$, respectively; $\rho_X(\mathcal{U}, \boldsymbol{i}_M)$ is the normalized reduced density matrix of the subsystem X for a given pair of $\mathcal{U}$ and $\boldsymbol{i}_M$; and $p_{\boldsymbol{i}_M}(\mathcal{U})$ is the probability associated with a particular outcome $\boldsymbol{i}_M$ for a given $\mathcal{U}$. For a system of N qudits with RUC of depth T, the measurement outcome $\boldsymbol{i}_M$ from a set of ancilla qudits is enumerated by a string of q' outcomes of length NT, i.e., $\boldsymbol{i}_M \in (\mathbb{Z}_{q'})^{\otimes NT}$, which encodes both different positioning of projective measurements and their outcomes. Here and below, we simplify our notations by omitting the explicit dependence of ρ_A and $p_{\boldsymbol{i}_M}$ on $\mathcal{U}$ whenever unambiguous, using S_X to denote $S[\rho_X]$ for any subsystem X, and adapting

a bold symbol for any indices running over exponentially many possibilities, e.g. basis states $|\boldsymbol{i}_M\rangle$, $|\boldsymbol{j}_A\rangle$ or $|\boldsymbol{k}_B\rangle$ for subsystems M, A, or B, respectively.

One of the nice properties of the weak measurement formalism is that it allows us to rewrite the average over measurements $\langle\!\langle S_A \rangle\!\rangle$ in a simple form that depends only on the global density matrix of the system-environment combined without any averaging. Consider the global density matrix $\tilde{\rho}_{ABM}$ in an extended Hilbert space that results from the RUC with given $\mathcal{U}$ and a set of couplings $\hat{R}_\alpha$ followed by the dephasing $\mathcal{N}_\phi$ *without* projecting onto any particular outcome,

$$\tilde{\rho}_{ABM} = \sum_{\boldsymbol{i}_M} p_{\boldsymbol{i}_M} |\Psi(\mathcal{U}, \boldsymbol{i}_M)\rangle \langle\Psi(\mathcal{U}, \boldsymbol{i}_M)| \otimes |\boldsymbol{i}_M\rangle \langle\boldsymbol{i}_M| ,$$

where $|\Psi(\mathcal{U}, \boldsymbol{i}_M)\rangle$ is a normalized pure state of the system for a given pair $\mathcal{U}$ and $\boldsymbol{i}_M$. Then, $\langle\!\langle S_A \rangle\!\rangle$ is exactly the conditional entropy of A on M:

$$\langle\!\langle S_A \rangle\!\rangle = \tilde{S}(A|M) \equiv \tilde{S}_{AM} - \tilde{S}_M, \tag{3.11}$$

where $\tilde{S}_X$ indicates that the corresponding entropy is computed from a reduced density matrix $\tilde{\rho}_X$ in the extended Hilbert space, i.e., $\tilde{S}_X \equiv S[\tilde{\rho}_X]$. We note that $\tilde{\rho}_X$ is diagonal in the measurement basis of the ancilla qudits. This relation is valid for any $\mathcal{U}$ (before averaging) and can be easily derived from explicit expressions:

$$\tilde{S}_{AM} = -\sum_{\boldsymbol{i}_M} \text{tr}\left(p_{\boldsymbol{i}_M}\rho_{A,\boldsymbol{i}_M} \log p_{\boldsymbol{i}_M}\rho_{A,\boldsymbol{i}_M}\right), \tag{3.12}$$

$$\tilde{S}_M = -\sum_{\boldsymbol{i}_M} p_{\boldsymbol{i}_M} \log p_{\boldsymbol{i}_M}, \tag{3.13}$$

where we use $\rho_{A,\boldsymbol{i}_M}$ to denote $\rho_A(\mathcal{U}, \boldsymbol{i}_M)$. We note that Eq. (3.11) holds only when von Neumann (or Shannon) entropy is used as the entropy measure, and the reduced density matrix $\tilde{\rho}_{AM}$ is block-diagonal in the basis $|\boldsymbol{i}_M\rangle$. In our case, the latter is satisfied owing to the dephasing channel $\mathcal{N}_\phi$, which enforces the measurement in the computational basis.

Equation (3.11) greatly simplifies our problem since the conditional entropy $\tilde{S}(A|M)$ can be evaluated without explicitly computing entanglement entropies for different measurement outcomes. However, exact computation of $\tilde{S}(A|M)$ for any given $\mathcal{U}$ is still a formidable task. For this reason, we introduce a series of closely related quantities, the n-th conditional entropies, that are more accessible for analytic calculation and recover $\tilde{S}(A|M)$ averaged over $\mathcal{U}$ in the limit $n \to 1$. For any $n \geq 1$, these objects are defined as

$$\tilde{S}^{(n)}(A|M) \equiv \tilde{S}_{AM}^{(n)} - \tilde{S}_M^{(n)}, \tag{3.14}$$

with

$$\tilde{S}_X^{(n)} \equiv \frac{\log \overline{\text{tr}\,\tilde{\rho}_X^n}}{1-n}. \tag{3.15}$$

While $\tilde{S}^{(n)}(A|M)$ quantifies the amount of the entanglement between subsystems A and B, it does not correspond to the Rényi conditional entropy. Instead, this object measures the n-th moment of the entanglement spectrum, weighted by the n-th power of the measurement outcome probability:

$$\tilde{S}^{(n)}(A|M) = \frac{1}{1-n} \log \left(\frac{\overline{\sum_{\boldsymbol{i}_M} p_{\boldsymbol{i}_M}^n \operatorname{tr} \rho_{A,\boldsymbol{i}_M}^n}}{\overline{\sum_{\boldsymbol{i}_M} p_{\boldsymbol{i}_M}^n}} \right). \tag{3.16}$$

For a larger n, the averaging is more strongly weighted by relatively more likely measurement outcomes. A sharp change in the behavior of $\tilde{S}^{(n)}(A|M)$ signifies a qualitative change in the entanglement spectrum in its n-th moment. It is also worth noting that analytically evaluating $\tilde{S}^{(n)}(A|M)$ is much easier than $\overline{\tilde{S}(A|M)}$ as the average over $\mathcal{U}$ is taken inside the logarithm and $\tilde{S}^{(n)}(A|M)$ depends only on the n-th moment of the system-ancilla density matrix.

Crucially, the average von Neumann conditional entropy is recovered in the limit $n \to 1$

$$\overline{\tilde{S}(A|M)} = \lim_{n \to 1} \tilde{S}^{(n)}(A|M). \tag{3.17}$$

This follows from the analytic relation $\overline{\operatorname{tr}[\rho \log \rho]} = \lim_{n \to 1}(n-1)^{-1} \log \overline{\operatorname{tr} \rho^n}$. In Sec. 3.4, we show that both $\tilde{S}_{AM}^{(n)}$ and $\tilde{S}_M^{(n)}$ (with $n \geq 2$) exactly map to the free energies of classical spin models with $n!$ internal states with different boundary conditions (up to a constant factor $n-1$), which reduce to the $n!$-state standard Potts models in the limit $q \to \infty$. We investigate their behaviors in various parameter regimes and show their implications to the average conditional entropy $\overline{\tilde{S}(A|M)}$ in the interesting physical limit $n \to 1$.

Kullback-Leibler divergence and Fisher information from measurement outcomes

We now introduce another signature of the phase transition in the quantum circuit, which is motivated by the interpretation given in Chapter 2. There, it was argued that the entanglement phase transition can be understood from the perspective of quantum error correction: in the volume-law phase, the scrambling of information by the unitary gates protects quantum correlations from sparse local measurements, thereby providing a natural error correction mechanism. At higher rate of measurement, this mechanism fails, and information encoded in the circuit is no longer protected from measurements. Thus, we expect that there is a sharp difference across the phase transition in the amount of information that can be gained from local measurements about the state of the system.

Here, we utilize the Fisher information [252] as a measure of how much information about a system flows into the ancilla degrees of freedom. Fisher information characterizes how much information a set of observables carry about an unknown parameter, and it can be derived from the closely related Kullback-Leibler (KL) divergence. For example, consider an

observable X drawn from a probability distribution $P(x; \theta)$ that depends on an unknown parameter θ. If θ is perturbed away from its original value θ_0 (without loss of generality, we set $\theta_0 = 0$), the probability distribution for X also changes. Then, one can quantify the amount of the information about θ carried in X by measuring how distinct the new distribution $P_\theta = P(x; \theta)$ is from its original $P_0 = P(x; 0)$, using the KL divergence

$$D_{\mathrm{KL}}(P_0||P_\theta) \equiv \sum_x P_0(x) \log \left(\frac{P_0(x)}{P_\theta(x)} \right). \qquad (3.18)$$

The Fisher information is defined as the second order derivative

$$\mathcal{F} = \partial_\theta^2 D_{\mathrm{KL}}(P_0||P_\theta)\big|_{\theta=0}. \qquad (3.19)$$

The KL divergence cannot be negative and vanishes if and only if $P_0 = P_\theta$, which implies that the first order derivative generally vanishes at $\theta = 0$.

In our model, we are interested in the Fisher information carried by a set of measurement outcomes $\boldsymbol{i}_M$ about the initial quantum state of the system. For simplicity, we assume that the system is initialized in either one of two nearby product states, $|\Psi_0\rangle = |\psi_0\rangle^{\otimes N}$ and $|\Psi_\theta\rangle = \delta U(\theta) |\psi_0\rangle^{\otimes N}$ with local perturbation $\delta U(\theta)$. The parameter θ characterizes the strength of the perturbation. For concreteness (and without loss of generality), we consider the perturbation $\delta U(\theta) = e^{-i\hat{X}_1\theta}$ with $\theta \ll 1$ applied to a qudit at position x_0, where $\hat{X}_1$ is the generalized Pauli matrix in Eq. (3.8).

Consider two systems with initial states $|\Psi_0\rangle$ and $|\Psi_\theta\rangle$ that evolve with identical circuits. We examine the KL divergence averaged over $\mathcal{U}$:

$$D_{\mathrm{KL}}(P_0||P_\theta) \equiv \overline{\sum_{\boldsymbol{i}_M} p_{0,\boldsymbol{i}_M}(T) \log \left(\frac{p_{0,\boldsymbol{i}_M}(T)}{p_{\theta,\boldsymbol{i}_M}(T)} \right)} \qquad (3.20)$$

$$= \overline{\mathrm{tr}\left[\tilde{\rho}_{M,0} \left(\log \tilde{\rho}_{M,0} - \log \tilde{\rho}_{M,\theta} \right) \right]}, \qquad (3.21)$$

where $\tilde{\rho}_{M,\theta}$ is the reduced density matrix of ancilla qudits for a given $\mathcal{U}$ and the initial state $|\Psi_\theta\rangle$. Note that $\tilde{\rho}_{M,\theta}$ is a diagonal matrix, whose elements denote the probabilities for different outcomes $p_{\theta,\boldsymbol{i}_M}$.

A few remarks are in order. First, $D_{\mathrm{KL}}(P_0||P_\theta)$ is only a function of the local perturbation strength θ and time T due to the averaging over random unitary gates. Hence, we simplify our notation by using $D_{\mathrm{KL}}(\theta, T)$ below. Second, when $\theta = 0$, the two initial states coincide, so $D_{\mathrm{KL}}(0, T) = 0$ at all time. However, for any $\theta \neq 0$, one expects that $D_{\mathrm{KL}}(\theta, T)$ would generally grow over time as two initial states should be better distinguished by more accumulated measurement outcomes. Indeed, it can be shown that $D_{\mathrm{KL}}(\theta, T)$ is a nondecreasing function in time, using the monotonicity of relative entropy [14, 169, 251]. Interestingly, we will show in Sec. 3.4 that in our model $D_{\mathrm{KL}}(\theta, T)$ cannot grow indefinitely, but rather approaches a finite saturation value; a nonanalytic change in the saturation value at long time signifies the phase transition. Finally, we note that the Fisher information can be directly extracted by computing the second order derivative in θ.

Similar to the case of the average von Neumann entropy, direct calculations of $D_{\mathrm{KL}}(\theta, T)$ is a formidable task. Once again, we use the replica method and introduce closely related quantities, the n-th divergence and the n-th Fisher information, based on the n-th moment of $\tilde{\rho}_{M,\theta}$:

$$D^{(n)}(\theta, T) \equiv \frac{\log \overline{\mathrm{tr}\left[\tilde{\rho}_{M,0}\tilde{\rho}_{M,\theta}^{n-1}\right]} - \log \overline{\mathrm{tr}\left[\tilde{\rho}_{M,0}^{n}\right]}}{1 - n} \tag{3.22}$$

$$\mathcal{F}^{(n)}(T) \equiv \partial_{\theta}^{2} D^{(n)}(\theta, T)\big|_{\theta=0}. \tag{3.23}$$

The KL divergence and the Fisher information can be obtained via the analytic relations:

$$D_{\mathrm{KL}}(\theta, T) = \lim_{n \to 1} D^{(n)}(\theta, T), \quad \mathcal{F}(T) = \lim_{n \to 1} \mathcal{F}^{(n)}(T). \tag{3.24}$$

We will show that $D^{(n)}$ also maps to the difference of free energies of the same classical spin models as those for $S^{(n)}$ with two different bottom boundary conditions, and $\mathcal{F}^{(n)}$ is proportional to the density of spins coupled to a boundary field (closely related to boundary magnetization) at the bottom boundary.

3.4 Mapping to spin models

In this section, we develop a mapping between the RUC with weak measurements and a series of classical spin models. Within this mapping, the generalized quantities $\tilde{S}^{(n)}$ and $D^{(n)}$ for integer $n \geq 2$ are related to free energies of 2D classical spin models. The distinction between the two is only in the boundary conditions imposed on the top and bottom, while the bulk spin model remains the same. This implies that the two quantities detect the same phase transition.

Our mapping builds on earlier works in which the n-th moment of a density matrix evolved by a random unitary circuit is mapped to the partition function of a classical spin model with $n!$ states [186, 283, 124]. Similar emergent classical spin models have been also studied in random tensor networks [115, 214, 253]. Our mapping generalizes these works by incorporating projective measurements of ancilla qudits.

An essential building block for calculating both the generalized entropies $\tilde{S}^{(n)}$ in Eq. (3.14) and the generalized KL divergences $D^{(n)}$ in Eq. (3.22) is the n-th moment of a density matrix:

$$\mu_{AM}^{(n)} = \mathrm{tr}\left[\tilde{\rho}_{AM,1}\tilde{\rho}_{AM,2}\cdots\tilde{\rho}_{AM,n}\right]. \tag{3.25}$$

Here, $\tilde{\rho}_{AM,i}$ is the reduced density matrix of the ancilla qudits M together with a subsystem A obtained from the evolution of an initial state $|\Psi_i\rangle$ of the system. The form of the quantity in Eq. (3.25) is sufficiently general to cover the calculation of both $\tilde{S}^{(n)}$ and $D^{(n)}$. In the former, we take all $|\Psi_i\rangle$ to be identical. In the latter, we take the subsystem A to be an empty set, while the $\tilde{\rho}_{AM,i}$ are evolved from the initial state $|\Psi_0\rangle$ or $|\Psi_\theta\rangle$ as dictated by Eq. (3.22).

Random unitary circuits	Classical spin models
$\overline{\operatorname{tr} \rho_{AM}^n}$	$\mathcal{Z}_{AM}^{(n)}$
$-\log \overline{\operatorname{tr} \rho_{AM}^n}$	$F_{AM}^{(n)}$
$\tilde{S}^{(n)}(A\|M)$	$(F_{AM}^{(n)} - F_M^{(n)})/(n-1)$
$D^{(n)}(P_0\|\|P_\theta)$	$(F_{M,\theta}^{(n)} - F_M^{(n)})/(n-1)$
$\mathcal{F}^{(n)}$	$2\langle m_1^\downarrow \rangle/(n-1)$

Table 3.1: Dictionary of the mapping between the RUC with weak measurements and classical spin models. On the left column, $\tilde{S}^{(n)}$, $D^{(n)}$, and $\mathcal{F}^{(n)}$ are generalized entropy, the divergence of probability distributions, and Fisher information that identify the phase transition, respectively. On the right column, $\mathcal{Z}^{(n)}$ and $F^{(n)}$ denote the partition function and the free energy of a classical spin model under a certain boundary condition specified by their subscripts. $\langle m_1^\downarrow \rangle$ denotes the probability that a spin at position $\boldsymbol{r} = (x_0, 1)$ belongs to the down-type (see the main text).

The essence of our mapping is the identification of the n-th moment with a classical partition function

$$\overline{\mu_{AM}^{(n)}} = \mathcal{Z}_{AM}^{(n)}, \tag{3.26}$$

where $\mathcal{Z}_{AM}^{(n)}$ is the partition function of a classical spin model with $n!$ internal states:

$$\mathcal{Z}_{AM}^{(n)} = \sum_{\{\sigma_{\boldsymbol{r}}\}} W(\{\sigma_{\boldsymbol{r}}\}). \tag{3.27}$$

Here, $\sigma_{\boldsymbol{r}}$ is a classical variable at $\boldsymbol{r} = (x, t)$ that may take $n!$ different values, $W(\{\sigma_{\boldsymbol{r}}\})$ is the Boltzmann weight given the spin configuration $\{\sigma_{\boldsymbol{r}}\}$. Depending on the choice of the n-th moment $\mu_{AM}^{(n)}$, the partition function $\mathcal{Z}_{AM}^{(n)}$ is evaluated with different boundary conditions. The top boundary condition of the spin model is determined by the choice of subsystem A. The bottom boundary condition depends on initial states of the density matrices. For example, when $\tilde{\rho}_{AM,i}$ have the same initial states, i.e., $|\Psi_i\rangle = |\Psi_j\rangle$ for any i, j, the spin model has an open boundary condition at the bottom. When $\tilde{\rho}_{AM,i}$ have the distinct initial states, the spin model exhibits a boundary "magnetic" field at the bottom boundary. Using this mapping, $\tilde{S}^{(n)}$ and $D^{(n)}$ are mapped to the free energy cost of exciting a domain wall at the top boundary and applying a magnetic field at the bottom boundary, respectively. A dictionary of the mapping is provided in Table 3.1.

Before we present any technical details, we provide the outline of the mapping. Our mapping consists of two steps. In the first step, we consider the n-th moment that involves n copies of density matrix $\tilde{\rho}_{AM,i}$. We note that the n copies of the density matrix is an n-th order monomial of random unitary gate U and its conjugate $U^\dagger$. By averaging over the unitary gates, we rewrite $\overline{\mu_{AM}^{(n)}}$ as a sum of terms labeled by two emergent spin variables σ

and τ, each living on one of the two honeycomb sublattices:

$$\overline{\mu_{AM}^{(n)}} = \sum_{\{\sigma_{\boldsymbol{r}}, \tau_{\boldsymbol{r}'}\}} W(\{\sigma_{\boldsymbol{r}}, \tau_{\boldsymbol{r}'}\}), \tag{3.28}$$

where $W(\{\sigma_{\boldsymbol{r}}, \tau_{\boldsymbol{r}'}\})$ is the weight associated with a given spin configuration $\{\sigma_{\boldsymbol{r}}, \tau_{\boldsymbol{r}'}\}$. We perform this calculation by utilizing a tensor network representation of $\overline{\mu_{AM}^{(n)}}$ and present an explicit expression for W. At this point, the weight $W(\{\sigma_{\boldsymbol{r}}, \tau_{\boldsymbol{r}'}\})$ is not always positive, and the r.h.s. of Eq. (3.28) cannot be interpreted as the partition function of a spin model. In the second step of the mapping, we resolve the negative weight in two different cases. In the case of $n = 2$, the negative weight $W(\{\sigma_{\boldsymbol{r}}, \tau_{\boldsymbol{r}'}\})$ can be removed by integrating out τ variables (or alternatively σ variables). The resultant expression can be interpreted as the partition function of a 2D classical Ising model on a triangular lattice. In the case of $n \geq 3$, integrating out τ variables is not sufficient, and we further consider the limit of large Hilbert space dimension q. For a sufficiently large but finite q, the weights in Eq. (3.28) become positive, and $\overline{\mu_{AM}^{(n)}}$ can be interpreted as the partition function of a spin model with $n!$ internal states on a 2D triangular lattice. In the limit $q \to \infty$, this model further reduces to the $n!$-state standard Potts model on a square lattice.

In what follows, we provide the details of the above procedure, starting from the simplest example $\tilde{S}^{(n)}$ with $n = 2$. Its modification for $D^{(n)}$ and the generalization for $n \geq 3$ are straightforward and will be discussed in detail later in this section.

Mapping between purity and partition function of classical Ising model

Here, we explicitly show that the average purity $\overline{\mu_{AM}^{(2)}} = \overline{\mathrm{tr}\, \tilde{\rho}_{AM}^2}$ for a subsystem AM maps to the partition of a 2D classical Ising model under a certain boundary condition. We will pay close attention to how the partition function of the classical Ising model depends on various parameters of the original model such as the local Hilbert space dimension q of the system qudits and the measurement strength $\alpha \in [0, \pi/2]$. We first discuss the mapping of $\tilde{S}^{(2)}$ and elaborate how the boundary conditions for the spin model depend on the choice of the subsystem A. Once the relationship between the purity and the partition function is established, we will discuss how the boundary conditions are modified for the calculation of $D^{(2)}$. Recall that we choose A to be the empty set when computing $D^{(2)}$. Generalization of the mapping to $\tilde{S}^{(n)}$ and $D^{(n)}$ for $n \geq 2$ is deferred to Secs. 3.4 and 3.4.

The first step of our derivation is to rewrite the second moment (purity) using the swap technique:

$$\mu_{AM}^{(2)} = \mathrm{Tr}\left[\left(\mathcal{C}_A^{(2)} \otimes \mathcal{I}_B^{(2)} \otimes \mathcal{C}_M^{(2)} \right) \left(\tilde{\rho}_{ABM} \otimes \tilde{\rho}_{ABM} \right) \right], \tag{3.29}$$

where Tr represents tracing over a twofold replicated Hilbert space for ABM, $\mathcal{C}_X^{(2)} = \sum_{\boldsymbol{i}_X, \boldsymbol{i}_X'} |\boldsymbol{i}_X\rangle \otimes |\boldsymbol{i}_X'\rangle \langle \boldsymbol{i}_X'| \otimes \langle \boldsymbol{i}_X|$ is an operator that swaps the quantum states of the sub-
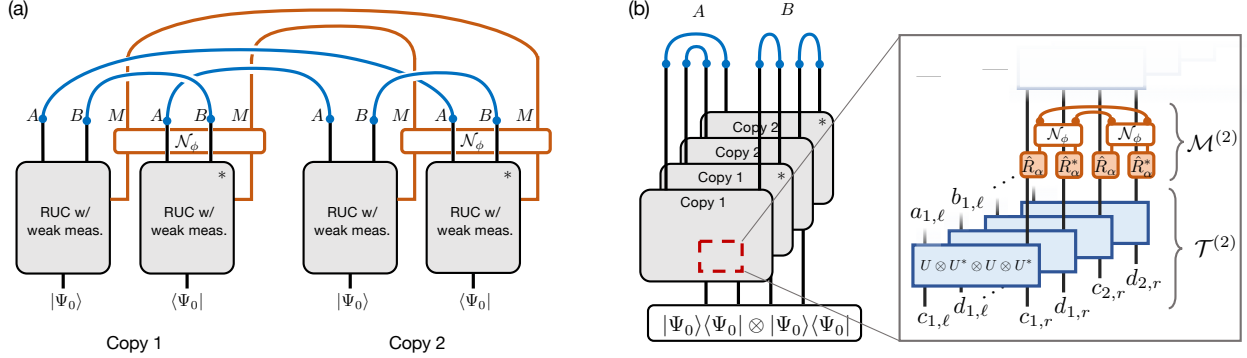
Figure 3.3: Tensor network representation of the purity $\mathrm{tr}\{[\tilde{\rho}_{AM}^2]\}$. (a) Two copies of the initial states $|\Psi_0\rangle\langle\Psi_0|$ are evolved under a RUC with weak measurements, before jointly contracted (or traced out). The asterisk (*) indicates the complex conjugate for the corresponding tensor. Notice the different connectivities for contracting the subsystems A, B, and M (blue and orange lines). (b) The network can be rearranged in such a way that the top boundary contractions are simplified and that the identical unitary tensors are brought together. Inset: Four copies of a random unitary gate $U \otimes U^* \otimes U \otimes U^*$ form a tensor $\mathcal{T}^{(2)}$. The combination of the coupling unitary $\hat{R}_\alpha$, dephasing gates $\mathcal{N}_\phi$, and the contraction of the ancilla qudits is denoted by $\mathcal{M}^{(2)}$.

space X between two copies, and $\mathcal{I}^{(2)}$ is the identity operator. Each copy of the quantum state $\tilde{\rho}_{ABM}$ is generated from an initial product state $|\Psi_0\rangle = |\psi_0\rangle^{\otimes N}$ by evolving it under an identical RUC and weak measurements (i.e., applying the coupling unitaries $\hat{R}_\alpha$ followed by dephasing of every ancilla qudit). Equation (3.29) rewrites a nonlinear function of the density matrix (on the left-hand side) as a linear expectation value of an operator in an extended Hilbert space (on the right-hand side). In turn, this allows the tensor network (TN) representation of $\mu_{AM}^{(2)}$ [see Fig. 3.3(a)]. Notice that the tensors are contracted across the two different copies for the subsystems A and M, reflecting the swap operators, while they are connected within each copy for the subsystem B. For reasons that will become clear below, we call the operators $\mathcal{O}_{\mathrm{top}}^{(2)} = \mathcal{C}_A^{(2)} \otimes \mathcal{I}_B^{(2)} \otimes \mathcal{C}_M^{(2)}$ the top boundary operator.

Our next step is to perform averaging over random unitary gates. Owing to their statistical independence, we can average unitary gates separately. In our diagrammatic representation, a tensor corresponding to each gate U appears exactly four times: U and $U^\dagger$ applied to the bra and ket vectors of the system in two copies. We rearrange the TN such that four identical tensors are placed together [see Figs. 3.3(b) and 3.4(a)] and consider their joint tensor $\mathcal{T}^{(2)}$ defined as

$$\mathcal{T}_{\mathbf{ab};\mathbf{cd}}^{(2)} \equiv U_{a_1 c_1} \otimes U_{b_1 d_1}^* \otimes U_{a_2 c_2} \otimes U_{b_2 d_2}^*, \tag{3.30}$$

where each index on the right-hand side represents a pair of input or output qudits and therefore runs over $d = q^2$ possible quantum states. Specifically, $\mathbf{a} \equiv (a_1, a_2) \equiv (a_{1,\ell}, a_{1,r}, a_{2,\ell}, a_{2,r})$.

Figure 3.3(b) inset shows the diagrammatic representation of Eq. (3.30).

For Haar random unitary gates, the average of $\mathcal{T}^{(2)}$ can be exactly computed using a property of unitary 2-design:

$$\overline{\mathcal{T}^{(2)}_{\mathbf{ab;cd}}} = \sum_{\sigma,\tau=\pm 1} w_g^{(2)}(\sigma,\tau)\hat{\tau}_{\mathbf{ab}}\hat{\sigma}_{\mathbf{cd}}, \tag{3.31}$$

where $\sigma, \tau \in \{\pm 1\}$ are classical Ising variables,

$$w_g^{(2)}(\sigma,\tau) = \frac{\delta_{\sigma,\tau}}{d^2 - 1} - \frac{1 - \delta_{\sigma,\tau}}{d(d^2 - 1)} \tag{3.32}$$

is a coefficient called the Weingarten function [67], and $\hat{\sigma}$ and $\hat{\tau}$ are tensors associated with the variables σ and τ defined as

$$\hat{\xi}_{\mathbf{ab}} = \begin{cases} \delta_{a_1 b_1}\delta_{a_2 b_2} & \text{if } \xi = +1 \\ \delta_{a_1 b_2}\delta_{a_2 b_1} & \text{if } \xi = -1 \end{cases}. \tag{3.33}$$

The diagrammatic representations of Eqs. (3.31) and (3.33) are given in Figs. 3.4(d) and 3.4(e). Equation (3.31) plays the central role in our mapping; practically, it implies that, after averaging, each unitary gate in our TN can be replaced by a sum of simpler tensors labeled by the Ising variables $\sigma, \tau \in \{\pm 1\}$. The corresponding tensors $\hat{\sigma}, \hat{\tau}$ with $\sigma, \tau \in \{\pm 1\}$ in Eq. (3.33) describe different ways to pair up indices associated with bra/ket vectors.

Now, it remains to contract these tensors on the entire network [Fig. 3.4(b)]. In particular, we need to incorporate the effects of weak measurements by contracting tensors associated with ancilla qudits $\mathcal{M}^{(2)}$ [Fig. 3.3(b) inset] with a pair of diagonally neighboring $\hat{\sigma}$ and $\hat{\tau}$ tensors [Fig. 3.4(f)]. As shown in Appendix B.1, these contractions lead to the weight

$$w_d^{(2)}(\sigma,\tau) = \begin{cases} q^2 \cos^4\alpha + q\sin^4\alpha & \text{if } \sigma = \tau \\ q\cos^4\alpha + q\sin^4\alpha & \text{if } \sigma \neq \tau \end{cases}, \tag{3.34}$$

where we recall that q and α denote the local Hilbert space dimension and the measurement strength, respectively. The dependence of $w_d^{(2)}(\sigma,\tau)$ on α distinguishes our spin model from the previous result described in Refs. [186, 283, 124], which is recovered when $\alpha = 0$.

By applying Eq. (3.31) to every gate and Eq. (3.34) to the contraction of the diagonally neighboring tensors, we obtain an expression for the purity

$$\overline{\mu_{AM}^{(2)}} = \sum_{\{\sigma_r,\tau_r\}} W_{\text{top}}W_{\text{bottom}} \prod_{\langle \mathbf{r},\mathbf{r}'\rangle} w^{(2)}(\sigma_{\mathbf{r}}, \tau_{\mathbf{r}'}) \tag{3.35}$$

that indeed looks like the partition function of an Ising spin model. The sum is on all the configurations of the pairs $(\sigma_{\mathbf{r}}, \tau_{\mathbf{r}})$ of Ising variables arising from the unitary gates at $\mathbf{r} = (x,t)$ in two dimension. The weights $w^{(2)}(\sigma_{\mathbf{r}}, \tau_{\mathbf{r}'})$ are functions of nearest neighbor spin variables at $\langle \mathbf{r},\mathbf{r}'\rangle$ in the network given by $w^{(2)} = w_d^{(2)}$ or $w_g^{(2)}$ depending on the orientation of the
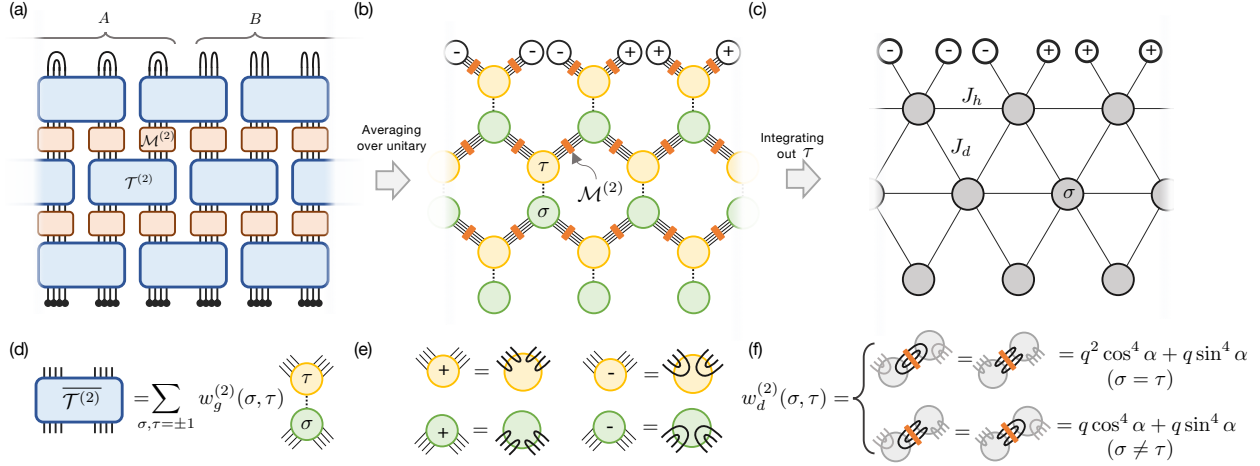
Figure 3.4: Mapping between a RUC with weak measurements and classical Ising model. (a) Tensor network representation of the RUC with weak measurements after the rearrangement [see also Fig. 3.3(b)]. Each $\mathcal{T}^{(2)}$ represents four identical unitary tensors, and $\mathcal{M}^{(2)}$ represents a weak coupling $\hat{R}_\alpha$ followed by the contraction of ancilla qudits [Fig. 3.3(b) inset]. (b) After averaging over unitary, the TN reduces to a network on a honeycomb lattice. Each site of the lattice hosts a classical Ising variable σ or τ. (c) Integrating out τ variables leads to the 2D classical Ising model on a triangular lattice with nearest-neighbor interactions J_h and J_d. (d) Averaging $\mathcal{T}^{(2)}$ over Haar random unitary allows one to replace the tensor as a sum of simple diagrams labeled by a pair of classical variables $\sigma, \tau \in \{\pm 1\}$. (e) Diagrammatic representations of the tensors $\hat{\tau}$ and $\hat{\sigma}$. (f) Contracting a pair of diagonally neighboring $\hat{\sigma}$ and $\hat{\tau}$ tensors leads to a closed loop diagram, whose value depends only on the relative sign between σ and τ.

bond, i.e., the Weingarten function $w_g^{(2)}(\sigma, \tau)$ is treated as the weight for a vertical bond. The weights W_{top} and W_{bottom} are the contributions from boundary conditions.

At the top boundary, closed diagrams arise from contracting $\hat{\tau}$ tensors according to their appropriate boundary conditions: qudit indices are connected across two copies in the subsystem A and within each copy in the subsystem B. According to Eq. (3.33), these contractions are equivalent to introducing of a set of additional $\hat{\sigma}$ tensors at $t = T + 1$ with fixed values $\sigma_{x,T+1} = -1$ for $x \in A$ and $+1$ for $x \in B$ [Fig. 3.3(b)], leading to the top boundary contribution [1]

$$W_{\text{top}} = \prod_{x \in A} w_d^{(2)}(-1, \tau_{x,T}) \prod_{x \in B} w_d^{(2)}(+1, \tau_{x,T}). \tag{3.36}$$

---

[1]When the position x is at the interface between A and B, one needs to first decompose the index $|\mathbf{a}\rangle = |a_{1,\ell}, a_{2,\ell}\rangle \otimes |a_{1,r}, a_{2,r}\rangle$ and use a different boundary condition for each qudit degree of freedom.

In fact, this equivalence is natural since a contraction with $\hat{\sigma}$ represents evaluating the expectation value of an identity $\mathcal{I}^{(2)}$ ($\sigma = 1$) or swap $\mathcal{C}^{(2)}$ ($\sigma = -1$) operator for any state in a two-fold replicated Hilbert space:

$$\hat{\sigma}_{\mathbf{ab}} = \begin{cases} \text{tr}\left(\mathcal{I}^{(2)} |\mathbf{a}\rangle \langle \mathbf{b}|\right) & \text{if } \sigma = +1 \\ \text{tr}\left(\mathcal{C}^{(2)} |\mathbf{a}\rangle \langle \mathbf{b}|\right) & \text{if } \sigma = -1 \end{cases}, \tag{3.37}$$

and similarly for $\hat{\tau}$.

At the bottom boundary, $\hat{\sigma}$ variables are contracted with tensors representing the initial state of the system. Here, both copies are initialized in the same product state $|\Psi_0\rangle = |\psi_0\rangle^{\otimes N}$. In such a case, tensor contractions lead to unity, independent of the Ising variable since $\text{tr}\{(\mathcal{I}^{(2)} |\psi_0\rangle \langle \psi_0| \otimes |\psi_0\rangle \langle \psi_0|)\} = \text{tr}\{(\mathcal{C}^{(2)} |\psi_0\rangle \langle \psi_0| \otimes |\psi_0\rangle \langle \psi_0|)\} = 1$ from Eq. (3.33). As a result, $W_{\text{bottom}} = 1$.

Combining these results, we obtain an intermediate expression

$$\overline{\mu_{AM}^{(2)}} = \sum_{\{\sigma_{\mathbf{r}}, \tau_{\mathbf{r}}\}} \prod_{\langle \mathbf{r}, \mathbf{r}' \rangle}' w^{(2)}(\sigma_{\mathbf{r}}, \tau_{\mathbf{r}'}), \tag{3.38}$$

where the summation runs over all possible assignment of bulk Ising variables while the product with prime runs over every neighboring pairs on a honeycomb lattice including the extra boundary spins at $t = T + 1$ with fixed $\sigma_{x,T+1}$ values. We emphasize that the boundary conditions are implicit and depend on the the choice of the subsystem A [Fig. 3.4(b)]. While the above expression already resembles the partition function of a classical Ising model on a honeycomb lattice, there is still a problem that the Weingarten function contributes negative weights. This sign problem can be fixed by explicitly integrating out all τ variables, which leads to a model defined on a triangular lattice

$$\overline{\mu_{AM}^{(2)}} = \mathcal{Z}_{AM}^{(2)} = \sum_{\{\sigma\}} \prod_{\langle \sigma_1, \sigma_2, \sigma_3 \rangle}' \bar{w}^{(2)}(\sigma_1, \sigma_2, \sigma_3), \tag{3.39}$$

where $\langle \sigma_1, \sigma_2, \sigma_3 \rangle$ denotes a lower-facing triangle with three neighboring vertices $\sigma_1, \sigma_2, \sigma_3$ (in clockwise order starting from top left), and $\bar{w}^{(2)}$ is a three-body weight that is nonnegative for arbitrary choice of q and α. The explicit expression of $\bar{w}^{(2)}$ is given in Appendix B.1. Apparently, the right-hand side of Eq. (3.39) is a partition function of a classical Ising spin model on the 2D triangular lattice [Fig. 3.4(c)].

Crucially, except for boundary contributions, the model given by Eq. (3.39) preserves the Ising $\mathbb{Z}_2$ symmetry associated with the global transformation $\sigma \mapsto -\sigma$ since both $w_g^{(2)}(\sigma, \tau)$ and $w_d^{(2)}(\sigma, \tau)$ only depend on the relative sign of two arguments. Consequently, the bulk three-body weight decomposes into pairwise contributions $\bar{w}^{(2)}(\sigma_1, \sigma_2, \sigma_3) \propto e^{-J_h \sigma_1 \sigma_2 - J_d \sigma_1 \sigma_3 - J_d \sigma_2 \sigma_3}$. The couplings, tuned by the measurement strength, are ferromagnetic $J_d \leq 0$ along diagonal bonds and antiferromagnetic $J_h \geq 0$ along horizontal bonds (Appendix B.1). It is interesting to note that this classical Ising model with anisotropic pairwise interaction on the triangular

lattice is exactly solvable [82, 246]. In our case, $J_h + J_d \leq 0$, hence there is a ferromagnetic-paramagnetic phase transition at a critical value of those parameters tuned by the measurement strength. A large value of $q \gg 1$ and weak measurement $\alpha \ll 1$ correspond to the low-temperature limit of the spin model resulting in the ferromagnetic phase. In the limit of vanishing measurement strength $\alpha = 0$, the model reduces to the previous result discussed in Ref. [186]. On the other hand, the limit of strong measurement $\alpha \to \pi/2$ maps to high temperature, giving rise to the paramagnetic phase. We will elaborate on this phase transition in Sec. 3.5.

Having established the mapping in Eq. (3.39), the second conditional entropy in Eq. (3.16) can be expressed as $\tilde{S}^{(2)} = F_{AM}^{(2)} - F_M^{(2)}$, where $F_X^{(2)} \equiv -\log \mathcal{Z}_X^{(2)}$ with $X = AM$, M is the free energy of the spin model. In the case of $\mathcal{Z}_{AM}^{(2)}$, the Ising symmetry is explicitly broken on the top boundary; the spin variables on the top boundary $(t = T+1)$ are pinned to $\sigma = -1$ and $+1$ in subsystem A and B, respectively. $\mathcal{Z}_M^{(2)}$ corresponds to the special case when the subsystem A is an empty set. Therefore, the second conditional entropy is given by the excess free energy of an Ising domain wall terminating on the edges of region A on the top boundary.

Finally, we discuss the important modification of our mapping that allows analyzing the second KL divergence $D^{(2)}$. Calculation of this object involves comparing two probability distributions (diagonal density matrices) $\tilde{\rho}_{M,0}$ and $\tilde{\rho}_{M,\theta}$ obtained from the evolution of two distinct initial states with the same quantum circuit. This requires the computation of

$$\mu_{M,\theta}^{(2)} := \text{tr}\{[\tilde{\rho}_{M,0}\tilde{\rho}_{M,\theta}]\} = \text{Tr}\left\{\left[\left(\mathcal{I}_{AB}^{(2)} \otimes \mathcal{C}_M^{(2)}\right)\tilde{\rho}_{ABM,0} \otimes \tilde{\rho}_{ABM,\theta}\right]\right\}. \tag{3.40}$$

This equation is related to Eq. (3.29) when the subsystem A is an empty set. The average of $\mu_{M,\theta}^{(2)}$ maps to the same Ising model as Eq. (3.39) in the bulk. A nontrivial modification arises only in the bottom boundary condition, where density matrices for two initial states are contracted with the $\hat{\sigma}$ tensors in the bottom layer. For product states $|\Psi_0\rangle = |\psi_0\rangle^{\otimes N}$ and $|\Psi_\theta\rangle = \delta U(\theta)|\psi_0\rangle^{\otimes N}$, this leads to nontrivial additional weights on the bottom boundary

$$W_{\text{bottom}} = |\langle\psi_0|\, \delta U(\theta)\, |\psi_0\rangle|^{(1-\sigma_{x_0,1})}. \tag{3.41}$$

In terms of the Ising spin model description, the extra weight appears as a "magnetic field" term on the pertubed site

$$\mathcal{Z}_{M,\theta}^{(2)} = \sum_{\{\sigma\}} e^{-h(1-\sigma_{x_0,1})} {\prod_{\langle\sigma_1,\sigma_2,\sigma_3\rangle}}' \bar{w}^{(2)}(\sigma_1, \sigma_2, \sigma_3). \tag{3.42}$$

Here, $h = -\log\cos\theta$ with $\cos\theta \equiv |\langle\psi_0|\, \delta U(\theta)\, |\psi_0\rangle|$. We also note that the top boundary boundary condition is $\sigma_{x,T+1} = +1$ everywhere owing to the trivial choice of A. The generalization of this result for any pair of inhomogeneous product states, e.g. $|\Psi\rangle = \otimes_k |\psi_k\rangle$ is straightforward.

In the Ising model, the second KL divergence $D^{(2)} = F_{M,\theta}^{(2)} - F_M^{(2)}$ with $F_{M,\theta}^{(2)} = -\log \mathcal{Z}_{M,\theta}^{(2)}$ is identified as the free energy cost of applying a boundary magnetic field on the perturbed

site. The corresponding second Fisher information is given by

$$\mathcal{F}^{(2)} = 1 - \langle \sigma_{x_0,1} \rangle, \tag{3.43}$$

where $\langle \sigma_{x_0,1} \rangle$ is the magnetization at $\boldsymbol{r} = (x_0, 1)$.

The boundary magnetization $\langle \sigma_{x_0,1} \rangle$ exhibits distinct behaviors in the two phases of the Ising model. In the ferromagnetic phase (weak or sparse measurements), the top boundary condition ($\sigma = +1$) induces a nonvanishing magnetization on the bottom boundary so that $\langle \sigma_{x_0,1} \rangle > 0$ and $\mathcal{F}^{(2)} < 1$. In the paramagnetic phase (relatively strong or frequent measurements), the bottom boundary magnetization vanishes in the thermodynamic limit $T \to \infty$. We conclude that the second Fisher information $\mathcal{F}^{(2)}$ is less than unity in the volume-law phase, increases continuously with measurement strength, and saturates, in a nonanalytic way, to $\mathcal{F}^{(2)} = 1$ at and beyond the critical point.

Generalization to the n-th moment

We now generalize the mapping discussed in the previous section to arbitrary $n \geq 2$. To this end, consider a generic n-th moment $\mu_{AM}^{(n)}$ that involves n copies of density matrices:

$$\mu_{AM}^{(n)} = \operatorname{tr} \left[\tilde{\rho}_{AM,1} \tilde{\rho}_{AM,2} \cdots \tilde{\rho}_{AM,n} \right]. \tag{3.44}$$

All density matrices $\tilde{\rho}_{AM,i}$ are obtained from the same RUC with weak measurements, but starting from a potentially different initial state of the system $|\Psi_i\rangle$. Similar to the swap trick in Sec. 3.4, $\mu_{AM}^{(n)}$ can be written as

$$\mu_{AM}^{(n)} = \operatorname{Tr} \Big[\Big(\mathcal{C}_A^{(n)} \otimes \mathcal{I}_B^{(n)} \otimes \mathcal{C}_M^{(n)} \Big) \\ \Big(\tilde{\rho}_{ABM,1} \otimes \tilde{\rho}_{ABM,2} \otimes \cdots \otimes \tilde{\rho}_{ABM,n} \Big) \Big], \tag{3.45}$$

where $\mathcal{I}_B^{(n)}$ is the identity operator and $\mathcal{C}_X^{(n)}$ is a cyclic permutation of n copies of the Hilbert space of subsystem X:

$$\mathcal{C}_X^{(n)} = \sum_{\{i_k\}} |i_n, i_1, i_2, \cdots, i_{n-1}\rangle \langle i_1, i_2, \cdots, i_n|, \tag{3.46}$$

where $\boldsymbol{i_k}$ $(\boldsymbol{k = 1, 2, \cdots, n})$ enumerates quantum states of X in the k-th copy. Below we omit the subscript and simply use $\mathcal{I}^{(n)}$ and $\mathcal{C}^{(n)}$ to denote the identity and cyclic permutation operators acting on n copies of an appropriate subsystem. The cyclic permutation $\mathcal{C}^{(n)}$ generalizes the swap operation $\mathcal{C}^{(2)}$ between two copies. The TN representations of the boundary contractions with $\mathcal{C}^{(n)}$ and $\mathcal{I}^{(n)}$ are shown in Figs. 3.5(a) and 3.5(b), respectively.

We now average $\mu_{AM}^{(n)}$ over individual random unitary gate U. Since $\mu_{AM}^{(n)}$ is an n-th order monomial of U and $U^\dagger$, the joint tensor $\mathcal{T}^{(n)}$ takes the form

$$\mathcal{T}_{\mathbf{ab;cd}}^{(n)} \equiv U_{a_1 c_1} \otimes U_{b_1 d_1}^* \otimes \cdots \otimes U_{a_n c_n} \otimes U_{b_n d_n}^*, \tag{3.47}$$
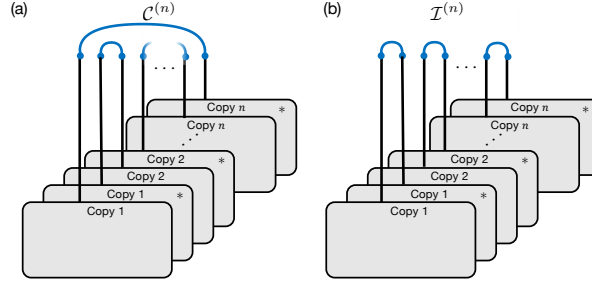
Figure 3.5: TN representations of the top boundary contractions for an n-th moment. (a) For subsystem A and M, n pairs of indices are cyclically shifted before being contracted. (b) For subsystem B, indices are contracted within each copy.

where we used the composite indices, e.g. $\mathbf{a} \equiv (a_1, a_2, \cdots, a_n)$, for multiple copies. For unitary gates drawn from the Haar measure, the average $\mathcal{T}^{(n)}$ can be written as

$$\overline{\mathcal{T}^{(n)}_{\mathbf{ab;cd}}} = \sum_{\sigma,\tau \in \mathcal{S}_n} w_g^{(n)}(\sigma, \tau) \hat{\tau}_{\mathbf{ab}} \hat{\sigma}_{\mathbf{cd}}, \tag{3.48}$$

where the emergent spin degrees of freedom σ and τ can be any of the $n!$ members of the permutation group defined over n elements, $\mathcal{S}_n$. The tensor $\hat{\sigma}$ describes different ways (permutations) to contract indices

$$\hat{\sigma}_{\mathbf{ab}} = \prod_{k=1}^{n} \delta_{a_k, b_{\sigma(k)}}. \tag{3.49}$$

The coefficient $w_g^{(n)}(\sigma, \tau)$ is the Weingarten function for unitary group $U(q^2)$ that depends only on $\sigma\tau^{-1}$. An exact expression for $w_g^{(n)}$ is known [67, 68, 285, 199, 178, 198], and in the limit of a large q [67], it reduces to

$$w_g^{(n)}(\sigma, \tau) = \begin{cases} 1/q^{2n} & \text{if } \sigma = \tau \\ o(1/q^{2n+1}) & \text{if } \sigma \neq \tau \end{cases}. \tag{3.50}$$

Analogous to the case of $n = 2$, the application of Eq. (3.48) to every gate in the RUC leads to an intermediate "spin model" defined on a honeycomb lattice:

$$\overline{\mu_{AM}^{(n)}} = \sum_{\{\sigma_{\mathbf{r}}, \tau_{\mathbf{r}}\}} W(\{\sigma_{\mathbf{r}}, \tau_{\mathbf{r}}\}), \tag{3.51}$$

where the weight $W(\{\sigma_{\mathbf{r}}, \tau_{\mathbf{r}}\})$ can be evaluated by decomposing the tensor network into smaller diagrams. In the bulk, closed diagrams associated with diagonally neighboring spin

pairs take the value (see Appendix B.1)

$$w_d^{(n)}(\sigma, \tau) = q^{\#\mathrm{cycle}(\sigma\tau^{-1})} \cos^{2n}\alpha + q\sin^{2n}\alpha, \tag{3.52}$$

where $\#\mathrm{cycle}(\xi)$ denotes the number of cycles in the cyclic representation of a permutation $\xi \in \mathcal{S}_n$ [2]. The top boundary contractions are equivalent to introducing an additional layer of tensors $\hat{\sigma}$ at time $T+1$. The values of the variables $\sigma_{x,T+1}$ are fixed according to the top boundary operator. For example, $\mu_{AM}^{(n)}$ requires $\hat{\sigma}_{x,T+1}$ to be the cyclic permutation and identity operators in the subsystem A and B, respectively. At the bottom boundary, extra weights arise from the overlap between different initial states $\prod_{k=1}^{n}\langle\psi_{\sigma(k),x}|\psi_{k,x}\rangle$ at each site x.

Integrating out τ variables leads to a spin model on a triangular lattice:

$$\overline{\mu_{AM}^{(n)}} = \mathcal{Z}_{AM}^{(n)} = \sum_{\{\sigma\}} \prod_{\langle\sigma_1,\sigma_2,\sigma_3\rangle}' \bar{w}^{(n)}(\sigma_1,\sigma_2,\sigma_3). \tag{3.53}$$

Unlike the case of $n = 2$, the three-body weight $\bar{w}^{(n)}$ may still be negative for a certain q and α. Nevertheless, we find that for any given n, there exists a finite range of (q,α) for which the weight is nonnegative. More specifically, we introduce $\kappa = q^{n-1}\cot^{2n}(\alpha)$ and show that the weights are all positive provided $q^2 > n$ and

$$\frac{1}{n!}\left(\frac{1}{1+\kappa}\right)^2 > \left(\frac{q^2+n}{q^2-n}\right)^n - 1. \tag{3.54}$$

The proof is given in Appendix B.1. For a given n, the inequality is generally satisfied when fixing κ and considering a large q regime, where the right-hand side can be arbitrarily small.

Our spin model exhibits the $\mathcal{S}_n \times \mathcal{S}_n$ symmetry — the system is invariant under the transformation $\sigma \mapsto \xi_1 \circ \sigma \circ \xi_2$ for any pair $(\xi_1, \xi_2) \in \mathcal{S}_n \times \mathcal{S}_n$. This can be already seen from $w_g^{(n)}$ and $w_d^{(n)}$, which depends only on the conjugacy class of $\sigma\tau^{-1}$. At a sufficiently high temperature, e.g. $\pi/2 - \alpha \ll 1$, the model is in the disordered (paramagnetic) phase. As the effective temperature is lowered by varying q and α, the system may spontaneously breaks the symmetry and undergoes a transition into a ferromagnetic phase. In the limit $q \to \infty$, the ordering transition can be quantitatively investigated as the symmetry of the spin model extends to the Potts symmetry $\mathcal{S}_{n!}$ for $n \geq 3$, for which the ordering transition has been well studied. Crucially, the phase transition point lies within the validity regime of our mapping in Eq. (3.54).

$\tilde{S}^{(n)}$ and $D^{(n)}$ in spin model descriptions

We now present the explicit spin model description of our generalized quantities, $\tilde{S}^{(n)}$ and $D^{(n)}$ (see Table 3.1 for a summary of results). We also discuss their qualitative behaviors in the two different phases.

---

[2]For example, when $\sigma = \tau$, $\sigma\tau^{-1} = (1)(2)\cdots(n)$ in the cyclic representation, hence $\#\mathrm{cycle}(\sigma\tau^{-1}) = n$.

The n-th generalized conditional entropy

The n-th generalized conditional entropy $\tilde{S}^{(n)}$ in Eq. (3.14) can be rewritten in a more suggestive form:

$$\tilde{S}^{(n)}(A|M) = \frac{1}{n-1}\left(F_{AM}^{(n)} - F_M^{(n)}\right), \qquad (3.55)$$

where $F_X^{(n)} \equiv -\log \mathcal{Z}_X^{(n)}$ is the free energy of the classical spin model with the appropriate boundary condition for subsystem X. Specifically, in the first term $F_{AM}^{(n)}$, the top boundary variables are fixed to one of the two distinct elements of $\mathcal{S}_n$ – a cyclic permutation for spins positioned inside subsystem A and an identity element for those in B. In the second term, all variables on the top boundary are uniformly set to the identity element. Therefore, $\tilde{S}^{(n)}$ corresponds to the excess free energy associated with a domain wall terminating on the top boundary at the interfaces between regions A and B (up to a constant factor, $n-1$).

The free energy cost for having a domain wall is qualitatively different in the two phases of the spin model. In the ferromagnetic phase, the excitation of a domain wall requires an energy proportional to its length. Pinning inhomogeneous boundary conditions results in two ordered domains of spin variables, whose interface scales with the linear size of a subsystem. In this phase, $\tilde{S}^{(n)}$ thus also grows linearly with the subsystem size, corresponding to the volume-law entangling phase. In contrast, domain wall excitations are condensed in the paramagnetic phase and do not cost extensive free energies. Hence, in-homogeneous boundary conditions lead to a free energy change of at most order one, leading to the area-law scaling of $\tilde{S}^{(n)}$.

It is interesting to note the close relation between the statistical mechanics interpretation of the entanglement entropy of the time-evolving state in the circuit to holographic entanglement entropy encoded in a random tensor network. In Ref. [253], the latter was similarly mapped to the free energy of a domain wall in a classical spin model. The entanglement phase transition in both cases corresponds to a ferromagnetic transition affecting a change in the scaling of the domain wall free energy.

The n-th generalized KL divergence and Fisher information

The n-th generalized KL divergence $D^{(n)}$ can be rewritten as

$$D^{(n)}(P_0||P_\theta) = \frac{1}{n-1}\left(F_{M,\theta}^{(n)} - F_M^{(n)}\right), \qquad (3.56)$$

where $F_{M,\theta}^{(n)} = -\log \mathcal{Z}_{M,\theta}^{(n)}$ with $\mathcal{Z}_{M,\theta}^{(n)} = \overline{\operatorname{tr} \tilde{\rho}_{M,0}\tilde{\rho}_{M,\theta}^{n-1}}$. Similar to the case of $\tilde{S}^{(n)}$, $D^{(n)}$ also corresponds to the free energy difference in spin models with two distinct boundary conditions. In this case, however, the boundary conditions are identical at the top and distinguished only at the bottom, originating from the different initial states of the n density matrices. More specifically, in order to compute $F_{M,\theta}^{(n)}$, we consider the system initialized in $|\Psi_0\rangle$ for the first copy (or equivalently any one of the n copies) and in $|\Psi_\theta\rangle$ for the rest. Following

our derivation in the preceding section, this leads to nontrivial weights W_{bottom} associated with the contractions of $\hat{\sigma}$ at the site being perturbed: for any $\sigma \in \mathcal{S}_n$ that permutes the first copy to itself, the weight is trivial unity, and otherwise it contributes a factor $|\langle \psi_0 | \delta U(\theta) | \psi_0 \rangle|^2 = \cos^2 \theta$ to W_{bottom}. Among total $n!$ permutations of $\mathcal{S}_n$, $(n-1)!$ elements belong to the former case (up-type) and the remaining $n! - (n-1)!$ elements constitute the latter case (down-type). Hence, the bottom boundary weights can be interpreted as an effect of a boundary "magnetic field" that distinguishes the down-type spin variables from the up-type ones at site x_0. $D^{(n)}$ corresponds to the free energy cost of applying the boundary field at site x_0 up to a constant prefactor.

The qualitative behaviors of $D^{(n)}$ in two different phases of the spin model can be intuitively understood by the n-th Fisher information:

$$\mathcal{F}^{(n)} = \frac{2}{n-1} \left\langle m_{x_0,1}^{\downarrow} \right\rangle, \tag{3.57}$$

where $\langle m_{x_0,1}^{\downarrow} \rangle$ is the probability that the spin at $(x_0, 1)$ belongs to a down-type in the spin model with open bottom boundary conditions.[3] Owing to the translation symmetry of our model (after averaging over $\mathcal{U}$) and top boundary conditions, $\langle m_{x_0,1}^{\downarrow} \rangle$ is independent of x_0, hence we use a simpler notation $\langle m_1^{\downarrow} \rangle$ in the rest of the Chapter.

For a relatively short evolution time T (i.e., the temporal dimension of the spin system is short), the density of down-type spins, $\langle m_1^{\downarrow} \rangle$, is smaller than its naïve statistical average:

$$\langle m_1^{\downarrow} \rangle < \frac{n! - (n-1)!}{n!} = 1 - 1/n \tag{3.58}$$

due to the effect of the symmetry-breaking top boundary conditions at $t = T + 1$ (see Monte Carlo results in Appendix B.5). This memory of the top boundary conditions persists in the ferromagnetic phase even in the long-time limit, so $\lim_{T \to \infty} \langle m_1^{\downarrow} \rangle < 1 - 1/n$ due to the long-range order. On the other hand, in the paramagnetic phase. the state of the bottom boundary becomes uncorrelated with the top boundary; the number of down-type spins saturates to its simple statistical average $1 - 1/n$. Therefore, through Eq. (3.57), the bulk phase transition of the spin model manifests as a nonanalytic change in the long-time limit of the n-th Fisher information at the critical point, which reaches its fully saturated value $\mathcal{F}^{(n)} = 2/n$ only in the paramagnetic phase. In the replica limit $n \to 1$, we get the saturation value $\mathcal{F} = 2$ (see Fig. 3.2).

The saturation of the Fisher information to its maximal value in the paramagnetic phase (or equivalently area-law phase) indicates that the measurement device (ancilla qudits) obtains *all* the information about the initial state, accessible from a set of local measurements. In contrast, the saturation to a value less than its maximum in the volume-law phase implies that *some* information cannot be extracted even after infinitely many measurements, owing to the effective quantum error correcting properties of scrambling dynamics. We note that in the special limit $n \to 1$, the nondecreasing nature of $D^{(1)}$ as a function of T can be independently derived from the monotonicity of the relative entropy [14, 169, 251].

---

[3]We consider the open boundary condition since $\mathcal{F}^{(n)}$ is obtained in the limit $\theta \to 0$.

3.5 Phase transitions

In this section, we provide detailed analysis on the nature of the phase transitions in our models. The phase transition points in our spin models are analytically solvable in two cases: (1) $n = 2$ with an arbitrary choice q, and (2) $n \geq 2$ in the limit $q \to \infty$. The former case is discussed in Sec. 3.5, where we utilize that the emergent 2D Ising model on a triangular lattice is exactly solvable [82, 246]. The phase transition is described by conformal field theory (CFT) with known critical exponents. The latter case is elaborated in Sec. 3.5, where we show that our spin model further reduces to the $n!$-state standard Potts model on a square lattice in the large q limit. The phase transition of such models can be exactly computed using the Kramers-Wannier duality [211, 142] and belongs the first order phase transition for $n \geq 3$. Then, we perform the analytic continuation in order to identify the universality class and extrapolate the phase transition point for the $n = 1$ case in Sec. 3.5. In this limit, our model reduces to a bond percolation problem; the phase transition is described by CFT with well-known critical exponents. In order to study the phase transition for small local Hilbert space dimensions, we perform exact numerical simulations up to $N = 30$ qubits ($q = 2$) and extract the critical point. We also present simulation results for the entanglement phase transition in Rényi-k entropies in Sec. 3.5, which suggests that the phase transition point may not depend on the Rényi order k.

Classical Ising model ($n = 2$ with an arbitrary q)

When $n = 2$, the average purity is mapped to the partition function of 2D classical Ising model on a triangular lattice with appropriate boundary conditions. The bulk Hamiltonian of such system in the unit of the effective temperature is

$$\beta \mathcal{H}_{\text{Ising}} = \sum_{\langle \boldsymbol{r}, \boldsymbol{r'} \rangle_d} J_d \sigma_{\boldsymbol{r}} \sigma_{\boldsymbol{r'}} + \sum_{\langle \boldsymbol{r}, \boldsymbol{r'} \rangle_h} J_h \sigma_{\boldsymbol{r}} \sigma_{\boldsymbol{r'}}, \tag{3.59}$$

where $\langle \boldsymbol{r}, \boldsymbol{r'} \rangle_{d/h}$ represents a pair of diagonally/horizontally neighboring sites, and J_d (J_h) is the corresponding Ising coupling strength that depends on q and α. Exact expressions for J_d and J_h are provided in Appendix B.1. In our model, it can be shown that $J_d \leq 0$ is ferromagnetic, $J_h \geq 0$ is antiferromagnetic, and they satisfy $J_d + J_h \leq 0$ for arbitrary q and α. This model is exactly solvable and exhibits a paramagnetic-to-ferromagnetic phase transition when J_d and J_h satisfy [82, 246]:

$$2e^{2J_h} = e^{-2J_d} - e^{2J_d}. \tag{3.60}$$

From this condition, the critical measurement strength $\alpha_c^{(2)}$ can be computed for an arbitrary q

$$\tan^4 \left(\alpha_c^{(2)} \right) = \frac{(q-1)(q^2+1)}{\sqrt{2 + 2q^4} - 2} - 1. \tag{3.61}$$
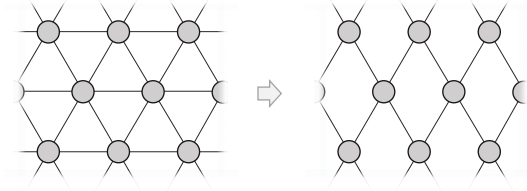
Figure 3.6: Our spin models reduce to the standard Potts models on a square lattice in the limit $q \to \infty$, $\alpha \to \pi/2$ while keeping $\kappa = q^{n-1} \cot^{2n}(\alpha)$ fixed (see the main text). The phase transition occurs at $\kappa_c^{(n)} = \sqrt{n!}$.

The universality of this phase transition is described by the Ising CFT with the critical exponents $\nu = 1$ and $\beta = 1/8$.

Standard Potts model ($n \geq 2$ with $q \to \infty$)

In the case $n \geq 3$, our interpretation of different n-th moments as partition functions of classical spin models is valid only for a finite range of (q, α). A sufficient condition for the validity is provided in Eq. (3.54), which can be satisfied by a finite q for any given n. In this section, we consider a limiting case $1/q \to 0$, where our spin model description becomes valid for every n and is further simplified, allowing extracting exact phase transition points. We believe this analysis should provide insights to the phase transitions even when $1/q \neq 0$, where we expect small modifications to the critical measurement probability arising from corrections in powers of $1/q$.

We begin our analysis by pointing out that, in the limit $q \to \infty$, the phase transition in the spin model occurs close to $\alpha_c^{(n)} \sim \pi/2$ (or $p_c^{(n)} \sim 1$), i.e., the measurement strength is near its maximum. This can be easily checked by estimating the couplings in the spin model as a function of q and α (see Appendix B.1 for an example of $n = 2$). Therefore, we consider the limit $q \to \infty$ together with $\alpha \to \pi/2$ while keeping $\kappa = q^{n-1} \cot^{2n}(\alpha)$ fixed. We will see that our model exhibits the phase transition point at $\kappa_c^{(n)} = \sqrt{n!}$, which is consistent with our limit as well as the validity criterion in Eq. (3.54).

An important consequence of the limit $1/q \to 0$ with a fixed κ is the emergence of the Potts symmetry $\mathcal{S}_{n!}$. More specifically, both weights $w_d^{(n)}$ and $w_g^{(n)}$ become dramatically simplified from Eqs. (3.50) and (3.52):

$$w_d^{(n)}(\sigma, \tau) \approx q\left(1 + \kappa \delta_{\sigma\tau}\right), \tag{3.62}$$

$$w_g^{(n)}(\sigma, \tau) \approx q^{-2n} \delta_{\sigma, \tau}, \tag{3.63}$$

which is invariant under any permutations of $n!$ elements in $\mathcal{S}_n$, hence the symmetry group is $\mathcal{S}_{n!}$. By integrating out τ variables, we obtain the three-body weight and its corresponding

effective Hamiltonian for spin variables on a triangular lattice:

$$\beta\mathcal{H}_{\text{Potts}} \approx \sum_{\langle \boldsymbol{r}, \boldsymbol{r'}\rangle_d} J\delta_{\sigma_{\boldsymbol{r}}\sigma_{\boldsymbol{r'}}}, \tag{3.64}$$

where $J = -\ln(\kappa+1) < 0$ is a ferromagnetic coupling between diagonally neighboring sites, and the couplings between horizontally neighboring sites vanish. Thus, our model simplifies to the standard Potts model defined on a square lattice (Fig. 3.6), for which the phase transition point as a function of J (in units of effective temperature) has been well studied [211, 142].

The transition point of the standard Potts model is exactly solvable using the Kramers-Wannier duality [211, 142], which gives $J_c = -\log\left(1+\sqrt{n!}\right)$, or equivalently $\kappa_c^{(n)} = \sqrt{n!}$. For completeness, we review the duality in Appendix B.4. This transition point corresponds to the strength $\alpha_c^{(n)}$ and the probability $p_c^{(n)}$:

$$\alpha_c^{(n)} = \arctan\left(\left(\frac{q^{n-1}}{\sqrt{n!}}\right)^{1/2n}\right), \tag{3.65}$$

$$p_c^{(n)} = 1/\left(1 + \left(\frac{\sqrt{n!}}{q^{n-1}}\right)^{1/n}\right) \tag{3.66}$$

for weak and projective measurements formalisms, respectively. In the case $n = 2$, this critical point agrees with the exact solution in Eq. (3.61) in the large q limit. It is well known that the $n!$-state Potts model exhibits a first-order phase transition for $n \geq 3$ [22, 23]. A summary of $p_c^{(n)}$ as a function of q for various n is presented in Fig. 3.7.

Bond Percolation ($n \to 1$ and $q \to \infty$)

Our exact results when $q \to \infty$ in the preceding section allow one to perform the analytic continuation to study an important limiting case $n \to 1$, where our generalized quantities $\tilde{S}^{(n)}$ and $\mathcal{F}^{(n)}$ approach the averaged von Neumann entanglement entropy and the Fisher information in measurement outcomes, respectively. Here, we compute the critical point and identify the universality of class of the phase transition.

In the limit $q \to \infty$, we have seen that our model reduces to the $n!$-state standard Potts model on a 2D square lattice with the coupling $J = -\ln(\kappa+1)$. Taking another limit $n \to 1$, the standard Potts model becomes equivalent to a bond percolation problem [134, 274, 56], where each bond of a square lattice is "activated" with the probability

$$f = \frac{\kappa}{1+\kappa} = p. \tag{3.67}$$
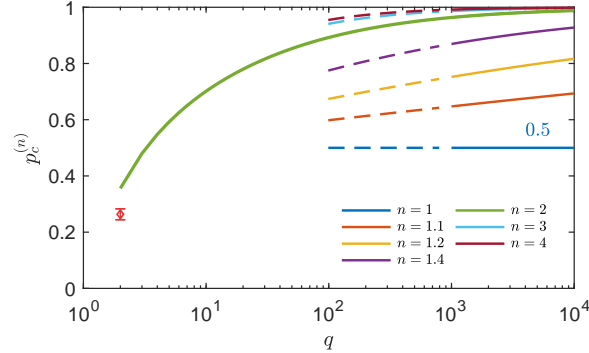
Figure 3.7: Phase transition points $p_c^{(n)}$ as a function of q. Different curves represent various replica index n. For $n = 2$, the critical point is given by the exact solution in Eq. (3.61). For integer $n \geq 3$, $p_c^{(n)}$ is estimated from Eq. (3.66), which is valid for $q \gg 1$. For noninteger n and $n = 1$, the transition points are extracted from the analytic continuation of Eq. (3.66). Solid lines represent the exact value ($n = 2$) or the results in the large q regime ($n \geq 3$ and noninteger n) while dashed lines indicate that our approximation needs not be valid as q decreases. The red diamond indicates numerically extracted critical point $p_c = 0.26 \pm 0.02$ with $q = 2$ for von Neumann entanglement entropy.

The set of activated bonds percolates the network of the 2D square lattice when f exceeds the critical point $f_c = 1/2$. In our model, this criterion leads to $\lim_{n \to 1} \kappa_c^{(n)} = 1$, corresponding to

$$\lim_{n \to 1} \alpha_c^{(n)} = \pi/4, \tag{3.68}$$

$$\lim_{n \to 1} p_c^{(n)} = 1/2. \tag{3.69}$$

Thus, the universality class of the phase transition for $q \to \infty$ belongs to that of a bond percolation transition in the 2D square lattice. At the critical point, the 2D model can be described by CFT with critical exponents $\nu = 4/3$ and $\beta = 5/36$ [138, 139, 102].

A few remarks are in order. First, while the percolation model has been discussed in Ref. [239], we emphasize that the origin of the model in the present work is different. In Ref. [239], the model has been adapted primarily to explain the phase transition in the Rényi-0 entropy, relying on simple geometric properties of tensor network representations of many-body wave functions. In particular, the probability of projective measurement in RUCs has been directly identified with the activation probability in the percolation problem. In this Chapter, however, the percolation problem arises from the analytic continuation of emergent effective spin models that we obtain only after averaging over unitary gates and weak measurements. More importantly, we predict a percolation transition in the von Neumann entanglement entropy *only* in the limit $q \to \infty$ (i.e., large local dimension). As discussed in Ref. [253], the $1/q$ corrections give rise to a reduction of the Potts symmetry ($\mathcal{S}_{n!} \to \mathcal{S}_n \times \mathcal{S}_n$) and constitute relevant perturbations at the percolation fixed point. It is an
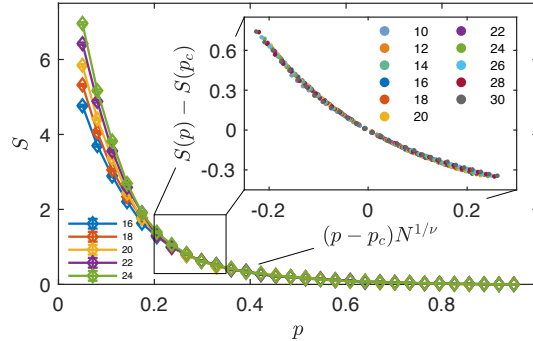
Figure 3.8: Exact numerical simulations for the entanglement phase transition in a RUC
with probabilistic projective measurements. The horizontal and vertical axes represent the
measurement probability p and the half-chain von Neumann entanglement entropy S for $q = 2$
and various system sizes up to $N = 24$. The inset shows the collapse of data from finite-size
scaling analysis based on the scaling formula $S(p, N) - S(p_c, N) = g((p - p_c)N^{1/\nu})$ [239] with
a specific choice $p_c = 0.27$ and $\nu = 2.9$. For the scaling analysis, we use the results from
system sizes up to $N = 30$ with $q = 2$ and a smaller window of $p \in [0.2, 0.35]$.

interesting direction for future research to characterize the critical point in a system of qudits
with a finite number of internal states and in particular qubits with $q = 2$. Second, in the
previous studies [163, 162, 65], the critical point and critical exponents of the entanglement
phase transition in the Clifford circuit are also obtained from numerics. However, the critical
point and the universality extracted from analytic continuation here may not be applied to
the Clifford circuit owing to the fact that the Clifford group does not form a unitary t-design
for $t \geq 4$ [264]. Thus, Eq. (3.66) is not valid for the phase transition in the Clifford circuit
when $n \geq 4$. Finally, we note that, in a strict sense, our analytic continuation is valid only
when $q \to \infty$ since our analytic expressions for $\alpha_c^{(n)}$ (or $p_c^{(n)}$) are exact only in this limit.
Surprisingly, we find that the resultant critical point does not depend on q in its leading
order. A careful quantitative study of potential $1/q$ corrections may be an interesting future
direction.

Exact Numerical Simulations

In order to see the behavior of the phase transition with a small value of q, we perform exact
numerical simulations of a RUC with projective measurements for $q = 2$ (qubits). We are able
to obtain exact results for up to $N = 30$ spins by using a customized algorithm that leverages
tensor representations of many-body wave functions, (see Appendix B.6 for details). Based
on finite size scaling analysis for $10 \leq N \leq 30$, we extract $p_c = 0.26 \pm 0.02$ for von Neumann
entropy, consistent with previous numerical results up to $N = 24$ qubits [239] (Fig. 3.8). The
extracted critical point seems to deviate from our analytic prediction for $q \to \infty$ limit in
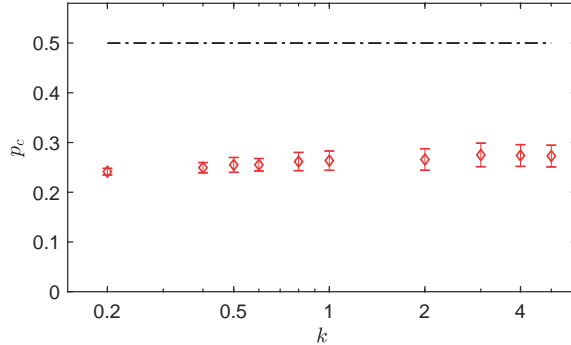
Figure 3.9: Critical measurement probabilities p_c for different orders k of Rényi entropy
fitted from exact numerical simulations. The von Neumann entropy corresponds to $k = 1$.
Red diamonds represent p_c extracted from finite-size scaling analysis using the results from
exact numerical simulation for $q = 2$ up to $N = 30$ and $p \in [0.2, 0.35]$. Error bars are
estimated from statistical fluctuations of our scaling analysis based on the bootstrapping
method and may not represent the accuracy to their true value (see Appendix B.6). The
dash-dotted line shows the analytic prediction $p_c = 1/2$ in the large q limit as well as the
critical point for Rényi-0 entropy based on the percolation in the unitary network [239].

Eq. (3.68), which indicates that a significant $1/q$ correction is present.

  We note that the replica limit introduced in the preceding sections is tailored for von Neu-
mann entropy. For many practical applications, it is also important to understand the
behaviors of Rényi entropies of order $k \neq 1$. In particular, it is well known that quantum
states in 1D with area-law Rényi-k entanglement entropy with $k < 1$ can be efficiently simu-
lated by using matrix product state representations [256, 228]. Therefore, the entanglement
phase transition in Rényi-k entropy with $k < 1$ is directly related to the classical simulability
of quantum dynamics.

  With this motivation in mind, we numerically study the phase transitions in Rényi-k
entropy for various k ranging from 0.2 to 5 and extract critical measurement probabilities.
The results are summarized in Fig. 3.9. Interestingly, p_c does not exhibit a strong dependence
on the order k. This suggests that phase transitions for different Rényi entropies ($k > 0$)
occur simultaneously and that the dynamics in the area-law phase for von Neumann entropy
already implies its simulability using a classical algorithm.

3.6   Absence of phase transition for unrestricted measurements

In previous sections, we focused on the RUC with *simple* weak measurements, in which the
ancilla qudits are measured only in their local computational basis. In this section, we lift

this constraint, allowing measurements of any complete set of observables (positive-operator valued measure), which could be arbitrarily nonlocal. Thus, we must now consider the full quantum density matrix of the ancilla qudits ρ_M without applying the dephasing channel, i.e., without projecting to its diagonal elements in the computational basis. With the full density matrix in hand, we can in principle apply, for example, an arbitrary unitary V to the entire set of NT ancilla qudits before projecting them in the computational basis. By appropriately choosing V, this setup allows one to extract more information about the system including nonlocal correlations (in both space and time) hidden among multiple system qudits. We show that there is no phase transition in the presence of such unrestricted (fully quantum) measurements.

The absence of phase transition under these conditions can be understood from two complementary perspectives. The first perspective is based on the insights of Chapter 2, namely that the volume-law phase remains stable against sufficiently sparse measurements owing to the natural error correction achieved by the information scrambling of unitary gates. The scrambling transforms information into a highly nonlocal form, protecting the information from local measurements. However, if the measurements are also arbitrarily nonlocal, then information is no longer protected. The scrambling becomes meaningless, and the volume-law phase immediately destabilizes.

Another perspective on the problem is afforded by considering the entanglement entropy between the system and ancilla qudits. Through the coupling gates $\hat{R}_\alpha$, the entanglement entropy generally grows linearly in time as $S[\rho_S] \sim pNT \log q$ and is expected to saturate to its maximal possible value $N \log q$, after a time $T^* \sim 1/p$. In this situation, as we show in Sec. 3.6 below, the system qudits reach a steady state (at time $T \gg T^*$), which retains no information about their initial state. Therefore, given the unitarity of the combined system, all the information must have gone into the ancilla qudits [231]. For this reason, we expect no phase transition: the ancilla qudits will eventually attain the full information about the initial state of the system, regardless of the measurement strength.

It is interesting to see how the presence of unrestricted measurements modifies the mapping to the classical spin models. Below, we show that removing the constraint imposed by the dephasing channel results in classical spin models that do not respect the permutation symmetry nor the Potts symmetry when $q \to \infty$, and consequently do not exhibit an ordering phase transition.

Dynamics of quantum relative entropy of ancilla qudits

To characterize the amount of information stored in the full density matrix of the measurement device (ancilla qudits), we generalize the classical KL divergence to the quantum relative entropy

$$D_{\mathcal{Q}}(\theta, T) \equiv \overline{\operatorname{tr} \rho_{M,0} \left(\log \rho_{M,0} - \log \rho_{M,\theta} \right)}. \tag{3.70}$$

Here, there is no dephasing of the ancilla qubits. From the quantum relative entropy, one can readily compute the Kubo-Mori-Bogoliubov (KMB) quantum Fisher information defined as

$$\mathcal{F}_{\mathrm{KMB}} \equiv \partial_\theta^2 D_\mathcal{Q}(\theta, T)\Big|_{\theta=0}, \tag{3.71}$$

which is an attainable upper bound to the (conventional) Fisher information, optimized over all possible choices of positive-operator valued measure [251, 116, 203, 113, 181] (see Appendix B.7 for a review). Thus, $D_\mathcal{Q}$ is an appropriate quantum generalization of D_{KL}.

In order to analyze these quantities in the classical spin model description, we again use the replica method. To this end, we introduce the n-th quantum relative entropy and the corresponding n-th KMB Fisher information:

$$D_\mathcal{Q}^{(n)}(\theta, T) \equiv \frac{1}{1-n} \log \left(\frac{\overline{\mathrm{tr}\, \rho_{M,0}\rho_{M,\theta}^{n-1}}}{\overline{\mathrm{tr}\, \rho_{M,0}^n}} \right), \tag{3.72}$$

$$\mathcal{F}_{\mathrm{KMB}}^{(n)} \equiv \partial_\theta^2 D_\mathcal{Q}^{(n)}(\theta, T)\Big|_{\theta=0}, \tag{3.73}$$

which reduce to $D_\mathcal{Q}$ and $\mathcal{F}_{\mathrm{KMB}}$, respectively, in the limit $n \to 1$.

The mapping to classical spin models described in Sec. 3.4 generalizes to this case in a straightforward way. The n-th moment $\nu_M^{(n)} = \mathrm{tr}[\rho_{M,1}\rho_{M,2}\cdots\rho_{M,n}]$ is mapped to the partition function of a modified classical spin model after averaging over unitaries. As before, in the limit $\theta^2 \ll 1$, the leading order contribution to $D_\mathcal{Q}^{(n)}$ can be interpreted as the density of down-type spins in the bottom layer $\langle m_1^\downarrow \rangle$ up to a constant prefactor. The only modification to our spin model originates from the absence of the dephasing channels $\mathcal{N}_\phi$, which modifies the two-body Boltzmann weight $w_d^{(n)}(\sigma, \tau)$. Crucially, this modification breaks the permutation symmetry (see Appendix B.2). For this reason, the ferromagnetic to paramagnetic phase transition cannot exist.

In order to further develop the intuition, we focus on the second quantum relative entropy $D_\mathcal{Q}^{(2)}$ as a specific example, and explicitly demonstrate the absence of the phase transition verified with numerical simulations. Similar to the discussion in Sec. 3.4, the second moment $\nu_M^{(2)}$ is mapped to the partition function of classical Ising model on a triangular lattice (see Appendix B.2 for detailed derivations). In this case, the down-type spin is identified with a spin with $\sigma = -1$, hence $\langle m_1^\downarrow \rangle = \langle m_1^- \rangle$.

Crucially, the Ising symmetry is explicitly broken: the three-body weights $\bar{v}^{(2)}(\sigma_1, \sigma_2, \sigma_3)$ are larger when the majority of spins are $\sigma = -1$ (rather than $\sigma = +1$), i.e., $\bar{v}^{(2)}(+, -, -) = \bar{v}^{(2)}(-, +, -) > \bar{v}^{(2)}(+, -, +) = \bar{v}^{(2)}(-, +, +)$ and $\bar{v}^{(2)}(-, -, -) > \bar{v}^{(2)}(+, +, +)$ for an arbitrary $\alpha > 0$. These imbalances in weights prefer spin variables $\sigma = -1$ over $\sigma = +1$. Furthermore, $\bar{v}^{(2)}(-, -, +) = 0$ independent of α while $\bar{v}^{(2)}(+, +, -) > 0$. This implies that if $\sigma = -1$ at every position at a certain time t^*, then all the spins at $t < t^*$ must also be in the state $\sigma = -1$. This constraint originates from the unitarity of the dynamics of system and ancilla qudits [183] (see also Appendix B.3). Therefore, we expect $\langle m_1^- \rangle$ to saturate to unity in the limit $T \to \infty$. Numerics provided in Fig. 3.10 verifies this statement.
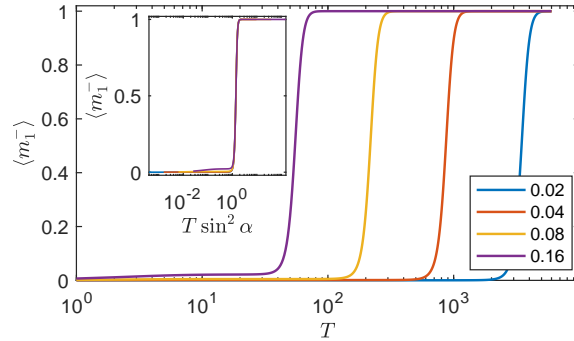
Figure 3.10:   The density of spins with $\sigma = -1$ in bottom layer, $\langle m_1^- \rangle$, as a function of time T when the full density matrix of ancilla qudits is retained, i.e., without projection to diagonal elements. Different curves represent various measurement strengths α from 0.02 to 0.16 given in the legend. The data collapse shown in the inset clearly demonstrates the absence of phase transition. The time dependence of $\langle m_1^- \rangle$ for all measurement strengths collapses onto a single curve when plotted as a function of $T \sin^2 \alpha$. The results are obtained from exact numerical simulation using the transfer matrix method with $N = 20$.

Figure 3.10 presents the exact simulation of $\langle m_1^- \rangle$ as a function of time T using the transfer matrix method for various measurement strengths α from 0.02 to 0.16. $\langle m_1^- \rangle$ remains small for a long time and rapidly increases to unity. In the inset, we obtain a collapse of curves for various measurement strengths when $\langle m_1^- \rangle$ is plotted as a function of rescaled time $T \sin^2 \alpha$. The scaling suggests that $\langle m_1^- \rangle$ approaches close to the saturation value at a timescale T^*, when every system qudit is measured once on average, i.e., $T^* \sin^2 \alpha = T^* p = \mathrm{O}(1)$. Note that this timescale T^* coincides with the timescale at which the system qudits achieve maximal entanglement with the ancilla qudits as estimated earlier in this section.

The dynamics of $\langle m_1^- \rangle$ is reminiscent of the information dynamics in the Hayden-Preskill protocol in black holes [114]. The initial state of system qudits (namely, a newly born black hole) encodes Alice's diary, and the ancilla qudits act as the Hawking radiation collected by an external observer, Bob. Bob cannot decode Alice's diary until the black hole emits sufficiently large amount of Hawking radiations such that the remaining black hole is maximally entangled with the early Hawking radiation, at which point Bob suddenly becomes able to decode the diary by collecting a few more bits of radiation.

Dynamics of the system qudits

In the preceding section, we have shown the absence of a phase transition based on the amount of information accessible to ancilla qudits when the measurement basis is unrestricted and potentially nonlocal. Here, we explore the complementary perspective by considering the reduced density matrix of the system qudits. We will see that the system density matrix

evolves to a maximally mixed steady state independent of its initial state for any $\alpha > 0$ [163, 239]. This observation, together with results in preceding sections, provides a clear intuitive understanding regarding the flow of quantum information: all information about the initial state of the system is transferred to ancilla qudits at a sufficiently long time for $\alpha > 0$. Furthermore, we point out that the presence or the absence of the phase transition cannot be unambiguously answered by the reduced density matrix of the system alone because it does not depend on the choice of measurement basis for ancilla qudits. One of the most important implications of our results in this section is that the phase transition is inherent to the data collected on *individual quantum trajectories* of the system, and it goes away when the quantum state of the system is averaged over those trajectories.

We consider the quantum relative entropy $\bar{D}_{\mathcal{Q}} \equiv \overline{\operatorname{tr} \rho_{S,0}(\log \rho_{S,0} - \log \rho_{S,\theta})}$ between the reduced density matrices of the system originating from two close initial states $|\Psi_0\rangle$ and $|\Psi_\theta\rangle$. $\bar{D}_{\mathcal{Q}}$ can be similarly analyzed using the spin model description, and we show this quantity always decays to zero in the limit $T \to \infty$. As before, we define the replicated objects $\bar{D}_{\mathcal{Q}}^{(n)} \equiv (\log \overline{\operatorname{tr} \rho_{S,0}\rho_{S,\theta}^{n-1}} - \log \overline{\operatorname{tr} \rho_{S,0}^n})/(1-n)$, which is proportional to the number of down-type spins in the bottom layer. An important modification arises from the top boundary conditions: the additional spin degrees of freedom for the system take the value $\mathcal{C}^{(n)}$ (i.e., $\sigma_{x,T+1} = \mathcal{C}^{(n)}$) everywhere, while n copies of ancilla qudits are contracted by the identity operator $\mathcal{I}^{(n)}$ (in contrast to $\mathcal{C}^{(n)}$ for $D_{\mathcal{Q}}^{(n)}$). This leads to modified Boltzmann weights. Here, we focus on the case of $n = 2$. Instead of favoring $\mathcal{C}^{(2)}$, the spin model now favors $\mathcal{I}^{(2)}$ in the bulk for an arbitrary $\alpha > 0$. Consequently, all the spins at the bottom boundary are polarized to $\mathcal{I}^{(2)}$, leading to a vanishing density of down-type spins as $T \to \infty$.

The vanishing $\bar{D}_{\mathcal{Q}}^{(2)}$ implies that the density matrix of system qudits evolves to an identical steady state regardless of its initial state. The steady state is indeed maximally mixed, which can be shown by considering one of the initial states being the maximally mixed state: the bottom boundary condition is modified in a nonperturbative way, but our argument above still holds. Therefore, $\bar{D}_{\mathcal{Q}}^{(n)}$ ($n \geq 2$) and $\bar{D}_{\mathcal{Q}}$ decay to zero as $T \to \infty$. From the information theoretical perspective, the system loses the quantum information of its initial state. Since the system and ancilla qudits combined undergo a closed unitary time evolution, one can conclude that the full quantum information about the initial state is recoverable from the ancilla qudits [231]. Finally, we note that the spin model descriptions of $D_{\mathcal{Q}}$ and $\bar{D}_{\mathcal{Q}}$ are identical up to the exchange of $\mathcal{C}^{(n)}$ and $\mathcal{I}^{(n)}$ in boundary conditions. As a result, the saturation of $D_{\mathcal{Q}}$ and the decay of $\bar{D}_{\mathcal{Q}}$ occur exactly on the same timescale T^*.

3.7 Discussion and outlook

Relation to purification phase transition

Recently, Ref. [104] has pointed out that the entanglement phase transition occurs concurrently with the change in the purification dynamics of an initially mixed state. More specifically, Ref. [104] considers the entropy of an initially maximally mixed state undergoing a RUC with
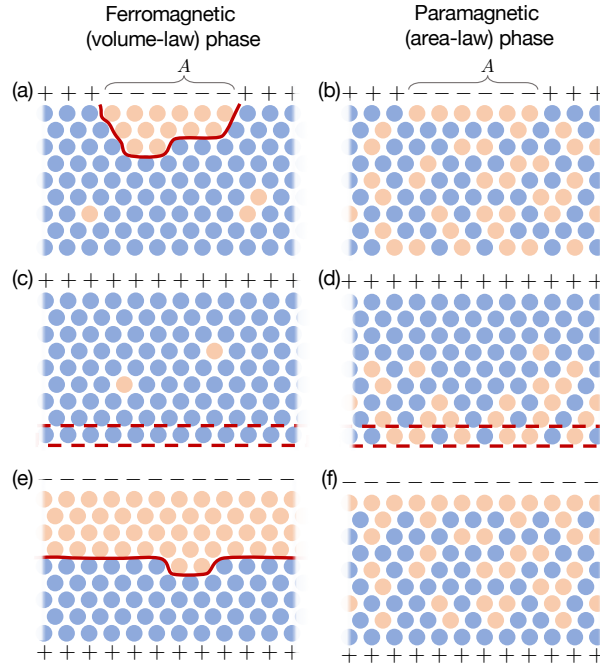
Figure 3.11: The different signatures of the entanglement phase transition as they manifest in the classical spin model descriptions. For simplicity, we present the descriptions in terms of the Ising spin model with $n = 2$. Left and right columns correspond to the ferromagnetic (volume-law) and paramagnetic (area-law) phases. (a) and (b) Average entanglement entropy of a subsystem A is related to the excess free energy of a domain wall (red solid line) terminating at the edges of A on the top boundary. (c) and (d) Fisher information is related to the average magnetization density at the bottom (red dotted box), via Eq. (3.57), when the top boundary is fixed at $\sigma_{x,T+1} = +1$. (e) and (f) Purification of a mixed state evolution (or equivalently the average entropy of the system in steady states) is related to the excess free energy of a domain wall running across the entire system (red solid line).

projective measurements: when $p > p_c$ the quantum trajectories of the system density matrix rapidly approach pure states, while for $p < p_c$ the system remains in a mixed state with a finite entropy density for an exponentially long time in its system size. Based on numerical simulations of 1D qubit chains evolved under Clifford gates and projective measurements, it has been observed that the critical measurement probability of the purification phase transition equals that of the entanglement phase transition with high accuracy [104].

Using our mapping to a series of spin models, we can show that the purification phase transition is indeed identical to the entanglement phase transition for Haar random unitary circuits with projective or weak measurements. As a measure of the purity, we consider the von Neuman entropy of the full system. To this end, we consider the series of generalized

conditional entropies $\tilde{S}_{\mathrm{mix}}^{(n)}(A|M)$, with A now identified with the *entire system* and the
subscript 'mix' indicates that the initial state is maximally mixed. As before, the special
features of $\tilde{S}_{\mathrm{mix}}^{(n)}(A|M)$ are enacted through bottom and top boundary conditions. For the spins
in the bottom layer, contraction with the maximally mixed initial state $\rho_{\mathrm{max}}^{\otimes n} = (\frac{1}{q^n}\mathcal{I}^{(n)})^{\otimes N}$ can
be accounted by introducing additional spins at $t = 0$ with fixed value $\sigma_{x,0} = \mathcal{I}^{(n)}$ (identity
permutation). In this case, since the subsystem A covers the entire system (we are calculating
the entropy of the whole system), the top boundary conditions are also homogenous. Similar
to the discussion in Sec. 3.4, the conditional entropy now corresponds to the difference between
a configuration with all top spins fixed to $\mathcal{C}^{(n)}$ (cyclic permutation) and one with all of them
in the $\mathcal{I}^{(n)}$ (identity permutation), while the bottom boundary condition is uniformly $\mathcal{I}^{(n)}$.
In the paramagnetic (area-law) phase, such free energy cost is of order unity independent
of the system size. This implies a purified phase. In the ferromagnetic (volume-law) phase,
the excess free energy of a domain wall traversing the the entire system scales as $\sim N$. This
corresponds to the mixed phase with total entropy proportional to volume. The spin model
descriptions of the subsystem entanglement entropy, the Fisher information, and the steady
state entropy for a mixed initial state are summarized in Fig. 3.11 for $n = 2$.

Experimental considerations

There are several potential experimental platforms to investigate the phase transition, includ-
ing superconducting quantum circuits, trapped ions and neutral atoms, and ultracold atomic
systems [29, 281, 191, 110, 51, 174]. For theoretical convenience, we have focused on the
entanglement phase transition in a circuit of random unitary gates. However, we expect that
this is not crucial and a system undergoing a chaotic hamiltonian evolution with measurements
would also exhibit a similar phase transition. In experiments, the projective measurements
can be directly implemented when quantum nondemolition (QND) measurements are possible.
Alternatively, one can introduce a set of ancilla qudits coupled to a system, postponing all
measurements to the end of each experimental run of quantum dynamics.

For experimental observations of the phase transition, the biggest challenge in our view
lies in identifying realistic observables that detect the phase transition. As we discussed in the
introduction, the direct measurement of the (conditional) entanglement entropy is extremely
challenging, as it requires a large number of experimental repetitions that scales exponentially
with the value of the entropy. This exponential overhead is fundamental, limited by the
complexity of estimating an entropy [202, 161]. Furthermore, for quantum dynamics with
projective measurements, there are additional multiplicative overhead scaling exponentially
with $\sim pNT$, associated with the postselection of different measurement outcomes. This
is because the entanglement entropy needs to be evaluated for individual trajectory of an
open system dynamics, and, in order to accumulate sufficient statistics for a single trajectory,
experiments need to be repeated over at least $\sim q^{pNT}$ times.[4]

---

[4]For this conservative estimate, we assumed that different measurement outcomes are not correlated as
expected in RUCs.

The transition in the KL divergence introduced in Sec. 3.3 can partially alleviate the exponential overhead since its detection only requires a number of samples sufficient to discriminate two probability distributions without any postselections and/or entanglement measurements. While precisely computing the KL divergence in general still requires exponentially many samples, we note that one can utilize other empirical methods such as Kolmogorov-Smirnov test [73] or evaluating an estimator for cross entropy [35]. It remains open if our phase transition can be faithfully identified by any local observables, or by interferometric methods.

Another important consideration is the effect of imperfections in experiments. Common sources of the imperfections include imprecise implementations of unitary evolutions, and dephasing or depolarization induced by uncontrolled noise. In general, these types of errors can be formulated as a quantum channel. Following the discussion in Sec. 3.6 and Appendix B.2, it is straightforward to see that an uncontrolled quantum channel generally leads to an explicit breaking of the permutation symmetry in the spin model description and hinders the observation of a sharp phase transition. More specifically, for a system of N qudits evolved for T time steps, the effects of explicit symmetry-breaking perturbations (experimental imperfections) become significant when $\eta NT \gtrsim \mathrm{O}(N)$, where η is the effective strength of perturbations for a single qudit per time step obtained in the spin model description. Under this condition, the strength of symmetry-breaking perturbations arising from experimental imperfections exceeds that of boundary conditions discussed in Sec. 3.4.

Finally, we note that the effects of experimental imperfections can be relatively more significant near the phase transition point. In particular, the susceptibility to symmetry-breaking perturbations is significantly enhanced near the phase transition in our spin model descriptions with $n = 2$ or $n \to 1$. This feature suggests a novel approach to characterize the amount of experimental imperfections by studying the phase transition or the lack thereof in quantum systems of finite sizes.

Implications to the simulability of open system dynamics

Quantum dynamics with area-law scaling entanglement entropy can be often simulated using classical computers. In particular, many-body wave functions of 1D systems can be efficiently represented by MPS. Therefore, the entanglement phase transition described in this work may be also interpreted as a phase transition in the simulability of an open system dynamics. Such interpretation, however, requires additional considerations. For simulations of quantum dynamics, it is necessary that expectation values of observables can be approximated within a given accuracy using an MPS with the bond dimension that scales polynomially in the system size. While this is guaranteed from area-law scaling Rényi-k entropies with $k < 1$ [256, 228], it is not necessarily the case for quantum states with area-law scaling von Neumann or Rényi entropies with $k \geq 1$. This is because, under certain circumstances (see Ref. [228] for examples), small Schmidt coefficients in the tail of an entanglement spectrum contribute significantly to evaluating an observable. In many physical quantum states, however, the entanglement spectra often follow well-known distributions, such as the Boltzmann distribution [75, 241, 219, 136, 188, 2], and an area-law scaling

von Neumann or Rényi-k entropy with $k > 1$ already provides pragmatic criteria for classical simulability. Our numerical simulation results in Sec. 3.5 suggest that the phase transition in von Neumann entropy is indeed accompanied by transitions in Rényi-k entropies with $k > 0$. More quantitative analysis of the entanglement spectra of quantum states resulting from chaotic dynamics and projective measurements would be an interesting future direction.

We emphasize that while the area-law scaling entanglement is a sufficient condition for efficient simulations, it is not necessary. In particular, we have seen in Sec. 3.6 that the phase transition (or its existence) sensitively depends on the type of information extracted by the measurements. By choosing a different measurement basis (nonlocal or quasilocal), it may be possible to modify the effective phase transition point such that quantum states in typical trajectories exhibit area-law scaling of entanglement even for p less than its critical value based on naïve local projections. Thus, our result does not rule out the possibility that the volume-law phase can also be efficiently simulated by appropriately sampling different trajectories.

Outlook

Our work opens several new directions. We proposed the KL divergence as a new measure to detect the entanglement phase transition. One intriguing future direction is to find local observables that faithfully and efficiently detect the phase transition. In case such observables do not exist, designing an interferometric method to detect the phase transition or providing a fundamental complexity bound on the hardness of observing the transition would be interesting.

Another intriguing direction is to establish quantitative connections between quantum chaos and the entanglement phase transition. The analyses in Sec. 3.6 and Chapter 2 indicate that the stability of the volume-law entangling phase is intimately related to the effective quantum error corrections arising from information scrambling, which is a generic feature of chaotic many-body dynamics. Quantifying the rate of information scrambling, for instance, by the critical probability or the rate of quasilocal projective measurements may provide new insight to quantum chaos from the perspective of information theory. Indeed, it was previously demonstrated that noninteracting particles or nonscrambling dynamics of Bell pairs cannot exhibit stable volume-law entangled phases, i.e., $p_c = 0$ [55, 59]. It remains open whether or not the phase transition can occur in nontrivial integrable systems such as Bethe ansatz solvable models or strongly disordered systems in many-body localized phases [244, 188, 2]. Alternatively, one may characterize quantum chaos from the Kolmogorov-Sinai entropy [9, 69] of measurement outcomes, which has been widely used as a diagnostic of chaotic dynamics in classical settings.

Finally, our mapping technique in Sec. 3.4 may provide a promising framework to analyze recently proposed quantum supremacy test protocols [35, 38]. We expect that, using classical spin model descriptions, one can efficiently evaluate the average discrepancy between sampling distributions from an ideal RUC and from its experimental realization as a function of the degree of various imperfections. Such analysis would provide an estimate to

the maximum amount of imperfections that are tolerable to demonstrate quantum supremacy under reasonable conditions [38], or allow characterizing near-term quantum devices [29, 281, 191, 110, 51].

Chapter 4

Symmetry enriched phases of quantum circuits

4.1 Introduction

Experiments with quantum circuits designed as platforms for quantum information processing have recently shown remarkable advances and present a new class of many body systems [153, 15, 282]. Generic quantum circuits consist of two distinct components: unitary evolution that generates entanglement and scrambles information and measurements or couplings to a noisy environment that irreversibly reveal or destroy the encoded information. The interplay of these components can lead to novel types of emergent phenomena, which bear on the circuit's capacity to offer a computational advantage over classical devices [15, 282].

A case in point is the newly discovered phase transition in the dynamics of unitary circuits subject to local measurements. As the rate of measurements exceeds a certain threshold, the steady state of the circuit changes from a highly entangled volume-law state to an area-law state [239, 163, 59]. The establishment of a low entanglement state at high measurement rates can be viewed in terms of the standard picture of quantum collapse of the wave function due to the repeated local measurements. On the other hand, the essential mechanism that protects the wave function from collapse at low measurement rates is understood from the viewpoint of quantum error correction: generic unitary gates scramble quantum information and encode it in nonlocal degrees of freedom, thereby affording partial protection of information from the deleterious effects of measurements. Increasing the measurement rate degrades this encoding and reduces the capacity of the dynamics to keep information, the so-called *quantum channel capacity*, until it vanishes at the phase transition point [65, 104, 85, 127].

In his famous essay "More is Different", Anderson remarked that "it is only slightly overstating the case to say that physics is the study of symmetry" [12]. So, it may not be too surprising that the measurement-induced phase transition (MIPT) in the entanglement entropy has an appealing theoretical description in terms of spontaneously broken symmetry [18, 130, 185]. What is somewhat unconventional, however, is that the symmetry in question is not a

physical symmetry of the circuit elements, but is rather a consequence of the ensemble of quantum states that the circuit generates at its output.

Each member state in this circuit ensemble corresponds to a particular sequence, or history, of measurement outcomes and appears with probability assigned by the Born rules. The symmetry arises because distinct features of the ensemble states can be seen only in nonlinear moments of the density matrix, like the entanglement entropy or fluctuations of observables between the different histories, while simple averages over observables give a trivial result. The time dependence of these moments can be expressed through the evolution of $n > 1$ identical copies of the density matrix. Such dynamics, generated by unitary gates and measurements, has a $\mathcal{S}_n$ symmetry to permutation among n forward and, separately, n backward propagating branches (i.e. both ket and bra wave functions). This is the symmetry, which is spontaneously broken in the MIPT. We note that the independent left and right replica symmetries arise from the need to describe a quantum state using a density matrix rather than a probability distribution. This is a crucial distinction from the replica symmetry breaking in classical spin glasses. We make further remarks on this point in the discussion section.

A systematic description of the MIPT has been obtained by mapping the circuit with Haar random unitary gates and measurements to a statistical mechanics model with $(\mathcal{S}_n \times \mathcal{S}_n) \rtimes \mathbb{Z}_2$ symmetry [115, 183, 253, 283, 18, 130, 185]. The extra $\mathbb{Z}_2$ symmetry is inherited from a symmetry of the time evolution to hermitian conjugation of all copies of the density matrix. In these studies, the random unitary gates were assumed to be uniformly distributed over the Haar measure. With the purpose of understanding more structured circuits, it is natural to ask what other phases may arise if physical symmetries or other constraints are imposed on it.

In this Chapter we elucidate how physical symmetries of the circuit elements combine with the intrinsic dynamical symmetries discussed above to determine the classification of the steady state phases. In the time evolution of n copies of the density matrix the physical circuit symmetry G is replicated to the n forward and n backward propagating branches. Conjugating a group element acting in one copy by a permutation in $\mathcal{S}_n$ transforms it to the corresponding group element in another copy. Thus, the dynamics of n copies has the enlarged symmetry $\mathcal{G}^{(n)} = [(G^{\otimes n} \rtimes \mathcal{S}_n) \times (G^{\otimes n} \rtimes \mathcal{S}_n)] \rtimes \mathbb{Z}_2^{\mathbb{H}}$. Here $\mathbb{Z}_2^{\mathbb{H}}$ acts like an anti-unitary time-reversal symmetry. We shall see that for broad classes of circuit architecture the actual effective symmetry that determines the phase structure can be simplified. To substantiate the classification of phases, we develop an exact map of the dynamics of replicated density matrices in a broad class of quantum circuits to the imaginary time evolution under an effective quantum Hamiltonian that inherits the symmetry $\mathcal{G}^{(n)}$ (see Section 4.2). The possible steady states of the circuit ensemble correspond to the ground state phases of this effective Hamiltonian, which thus transcend a naive classification by the physical circuit symmetries. Note that having a volume-law state in the circuit does not imply that the corresponding effective Hamiltonian has a ground state with volume-law entanglement. Rather the volume-law entanglement of the circuit state translates to a certain boundary operator, which roughly speaking measures the free energy of a spacetime domain wall.

We offer an information theoretic interpretation of the phases of the circuit ensemble as distinct patterns of information encoding in the circuit, which remains well-defined in the replica limit $n \to 1$. Nonetheless, we argue and provide numerical evidence that for certain purposes a model with $n = 2$ replicas represents the true effective symmetries of the system and thus gives qualitatively correct predictions.

We demonstrate and explore these ideas on two examples representing different classes of circuits. The first is a circuit with $\mathbb{Z}_2$ symmetry operating on a chain of qubits. The second example is a Gaussian fermionic circuit, which conserves only the $\mathbb{Z}_2$ fermion parity. For the rest of this introduction, we provide a brief overview of the main results and insights obtained from studying the two examples and then lay out the general organization of the Chapter.

Overview: quantum circuits with $\mathbb{Z}_2$ symmetry

In Section 4.3, we investigate the phases of quantum circuits invariant under a global $\mathbb{Z}_2$ symmetry generated by the parity operator $\hat{\pi} = \prod_j Z_j$. Thus, the single-qubit measurements of Z_i or two-qubit measurements of $X_i X_{i+1}$, which commute with $\hat{\pi}$ are allowed, while single-qubit measurements of X_i are not. Similarly, all unitary gates must also commute with $\hat{\pi}$.

It was previously demonstrated, based on a specific one-dimensional model [224], that circuits with $\mathbb{Z}_2$ symmetry can exhibit at least two distinct area-law entangled phases in which the $\mathbb{Z}_2$ symmetry is either preserved or spontaneously broken. The former is stabilized by on-site measurements of Z_i, while the latter is driven by measurements of $X_i X_{i+1}$. The existence of a broken symmetry state in this system agrees with the intuition that area-law entangled states are akin to quantum ground states, which may spontaneously break a physical $\mathbb{Z}_2$ symmetry in one dimension.

One of our main results, however, is that circuits with $\mathbb{Z}_2$ symmetry generally admit a much richer phase structure derived from the enlarged dynamical symmetry. This includes multiple area-law and volume-law phases, characterized by distinct broken symmetry order parameters, which could not have been established in presence of the circuit symmetry alone. Especially unique to this far-from-equilibrium setting is the establishment of states with volume-law entanglement entropy, which nonetheless exhibit spontaneously broken circuit symmetries in a one-dimensional system. In the same vein, we point out the possibility of establishing a new type of symmetry protected topological (SPT) phase [208, 62] as a steady state of the quantum circuit evolution, where the protecting symmetry is the enlarged dynamical symmetry rather than the physical circuit symmetry. In our case, the $\mathbb{Z}_2$ circuit symmetry alone would not be sufficient to support an SPT phase as a ground state. However, such a state could be protected by a $\mathbb{Z}_2 \times \mathbb{Z}_2$ subgroup of the enlarged dynamical symmetry. Here the second $\mathbb{Z}_2$ symmetry originates from the permutation symmetry of forward branches.

We consider a number of physical probes that can distinguish between the symmetry enriched phases of the circuit. A useful probe of broken symmetry in such a system, which

was also used in Ref. [224], is the long distance Edwards-Anderson (EA) correlation function

$$\chi_{EA}(i,j) = \overline{\sum_m p_m \langle X_i X_j \rangle^2}. \tag{4.1}$$

Here the sum is over the quantum trajectories of the circuit wave function, corresponding to different sequences m of measurement outcomes obtained with probabilities p_m. The overline represents averaging over different unitary gates from an ensemble of quantum circuits. In the conclusions, we will discuss the intriguing connection between this problem and the theory of spin glasses pioneered by Edwards and Anderson, who also introduced this order parameter in the 1970s [81].

Another useful diagnostic of symmetry is the subsystem parity variance

$$\Pi(A) = \overline{\sum_m p_m \langle \prod_{j \in A} Z_j \rangle^2}, \tag{4.2}$$

expected to be nondecaying in the limit of a large subsystem size when the state of typical trajectories has a well-defined parity. At a superficial level, this probe appears to be a "disorder parameter" dual to the EA correlations. However, we shall see that this duality does not hold in the enlarged symmetry space, thus allowing phases with coexisting long-range EA correlations and nondecaying parity variance.

Complementary to these physical observables, we also consider information theoretic quantities, such as Fisher information obtained by measurement outcomes about specific perturbations to the initial state. Such information theoretic probes allow to characterize the phases in terms of the flow of information in the circuit rather than steady state equal time properties such as χ_{EA} or $\Pi(A)$.

A crucial point is that all of these diagnostics must be defined as second (or even higher) moments in the ensemble of trajectories. For example, a simple average of order parameter correlation functions, i.e. $\overline{\langle X_i X_j \rangle}$ vanishes because the broken symmetry state is characterized by random X orientations in a given trajectory due to random measurement outcomes. Evaluating second moments necessarily involves the dynamics of two replica copies, which should therefore be viewed as fundamental to the physics of these systems and not merely an averaging trick. Thus, we devote much of our attention to classifying phases in a model with two replicas ($n = 2$).

We note, however, that to ensure proper averaging over the ensemble one needs to invoke auxiliary replicas and ultimately take the the replica limit $n \to 1$. While we do not explicitly construct models for $n > 2$ to facilitate such an extrapolation, we show that, apart from the coexistence phases that feature both nonvanishing χ_{EA} and $\Pi(A)$, the phases predicted for $n = 2$ have natural extensions to higher replicas. Furthermore, when two phases can be distinguished by physical diagnostics in the two-replica model, this distinction holds for $n \geq 2$ and is thus expected to extrapolate to the replica limit.

In Section 4.3, we provide numerical evidence for the phase structure predicted by the two-replica effective theory. The model we consider consists of two chains where chain 1 is

unrestricted by symmetry, while operations on chain 2 obey a global $\mathbb{Z}_2$ symmetry. In other words, only qubits of chain 2 carry a global $\mathbb{Z}_2$ charge. We show that the volume-law phase in this system can host more than two distinct broken symmetry phases, confirming that the symmetry dictating the phase structure is larger than the $\mathbb{Z}_2$ circuit symmetry. The coexistence of long-range quantum orders with volume-law entanglement presents a sharp contrast with thermal states, which exclude such order in one-dimensional systems.

The fact that the volume-law phase can exhibit long-range order naturally raises the question if topological states and the ensuing edge modes can also remain protected in volume-law entangled steady states of quantum circuits. The results of the two-chain model suggest an affirmative answer. We could replace the qubits in chain 2 with Majorana fermions conserving the $\mathbb{Z}_2$ fermion parity (still coupled to the qubits in chain 1). Under a Jordan-Wigner transformation this model maps to the one we computed numerically. The broken symmetry phase of the qubit circuit translates to a topological phase with edge zero modes and volume-law entanglement in the fermionic model.

Overview: Gaussian fermionic circuits

In Section 4.4 we investigate Gaussian fermionic circuits with unitary gates and measurements that only conserve the $\mathbb{Z}_2$ fermion parity, but not fermion number. The elements in these Gaussian circuits preserve the gaussianity of the wave function [248]. In particular, we consider unitary gates generated by a (time-dependent) Hamiltonian that is quadratic in fermion operators and measurements of quadratic observables associated with rank one projectors, such as measuring the local parity. These systems provide a second example of the role played by the enlarged dynamical symmetry in dictating the phase structure.

The effect of local Gaussian measurements on free fermions was first discussed by Cao et al. [55], who argued that these systems cannot sustain a volume-law state for any nonvanishing measurement rate (see also [87]). This can be understood as resulting from the absence of scrambling in Gaussian circuits, which therefore cannot protect quantum information (or equivalently entanglement) from measurements through nonlocal encoding [65, 104]. Recent numerical results on monitored free fermion dynamics indicated, however, a possible measurement-induced phase transition from a critical phase, with entanglement entropy scaling logarithmically in system sizes, to a strict area-law phase [8]. Such a transition is also found in a specific fermion model via a mapping to classical loop models [225]. We note that critical states of nonunitary fermion models (though not measurement circuits) were studied in Refs. [61, 170, 129] as well as in measurement-only models [182].

The framework developed in this Chapter naturally captures the instability of the volume-law state and the emergence of a critical phase. Both properties stem from the effective symmetry associated with the dynamics of two copies of the system, which is enlarged with respect to the physical symmetry of the circuit.

We consider circuits with a $\mathbb{Z}_2$ fermion parity symmetry, described using two Majorana operators on each physical site j, γ_{2j-1} and γ_{2j}. The local observables measured in the circuit are the fermion parities on sites $\hat{\pi}_{s,j} = -\mathrm{i}\gamma_{2j-1}\gamma_{2j}$ and the fermion parity on bonds connecting

two nearest neighbor sites $\hat{\pi}_{b,j} = -\mathrm{i}\gamma_{2j}\gamma_{2j+1}$. These operators are also the generators of all the unitary gates.

Due to the Gaussian constraint and fermion commutation relations, the enlarged dynamical symmetry of this model is different from that of qubit circuits. In the absence of measurements, the unitary evolution of n replica copies of a density matrix exhibits a global $O(2n) \rtimes \mathbb{Z}_2^{\mathbb{T}}$ corresponding to Bogoliubov rotations of Majorana operators between the $2n$ branches. $\mathbb{Z}_2^{\mathbb{T}}$ is a time-reversal like symmetry that squares to -1. This is the same symmetry that emerges in the symplectic class of fermion systems in a random potential [222, 93]. There are two important differences, however. First, the replica limit in this dynamical problem is $n \to 1$, while it is $n \to 0$ in the Anderson localization problem. Second, the measurements break the symmetry down to $[O(n) \times O(n)] \rtimes \mathbb{Z}_2^{\mathbb{T}}$.

As in the qubit circuits, we focus on the dynamics of the minimal model with two replica copies, which is mapped to imaginary time evolution generated by a quantum Hamiltonian. In absence of measurements, averaging over a *purely unitary* circuit of Gaussian fermion gates gives rise to an effective ferromagnetic spin-1 Hamiltonian with $O(3)$ symmetry. The quantum ferromagnet allows establishment of long-range order, which translates to volume-law entanglement, even in a one dimensional system.

With non-vanishing rate of measurements the symmetry of the effective model is reduced to $U(1) \rtimes (\mathbb{Z}_2 \times \mathbb{Z}_2^{\mathbb{T}})$, which cannot support a broken symmetry state. For moderate measurement rate this leads to the establishment of a critical ground state of H_{eff}. The sub-system purity $\exp\left(-S_A^{(2)}\right)$ of the circuit state translates to a boundary correlation function, which decays as a power law in the critical phase of H_{eff} with a decay exponent that decreases continuously with increasing measurement rate. Accordingly, the entanglement entropy scales as $\log|A|$ with a continuously varying pre-factor.

The two-replica theory predicts that the critical phase ends with a Kosterlitz-Thouless transition that takes the system into one of two area-law phases. The circuits diagnostics that allow to distinguish between the two area-law phases are the subsystem site and bond parity variances:

$$\Pi_{a,A} \equiv \overline{\sum_m p_m \langle \prod_{j \in A} \hat{\pi}_{a,j} \rangle_m^2}. \tag{4.3}$$

Here the subscript $a = s, b$ stands for site or bond.

In the area-law phase with dominant site measurements, the subsystem site parity variance is non-decaying, whereas the bond parity variance decays exponentially. If the bond measurements dominate, then the bond parity variance is non-decaying. In terms of the effective ground state description, these two states correspond to a trivial and a Haldane SPT phase, respectively. The transition between the two area-law phases with the same characteristics has been discussed in the context of measurement-only dynamics of a Majorana chain [182, 154].

The fact that all phases can be diagnosed by quantities that are second moments over the ensemble of quantum trajectories hints at that a model of two replica copies captures the correct emergent symmetries in the problem. Nonetheless, appropriate averaging of $\Pi_{a,A}$

requires introducing auxiliary replicas followed by extrapolation to the physical replica limit $n \to 1$. This may alter the critical behavior.

In Section 4.4, we compare the predictions of the effective two-replica theory to exact numerical simulations of the dynamics in the Gaussian fermionic circuits, which can be done on relatively large systems. We find good agreements with the expected properties of the critical phase, the two area-law phases and even the Kosterlitz-Thouless transition. In particular, the correlation length we extract from the numerical simulations shows a divergence that matches well with the hallmark exponential form of the Kosterlitz-Thouless transition $\xi \sim \exp(A/\sqrt{p - p_c})$. On the other hand the two replica model does not capture the observed critical behavior associated with the direct transition between the two area-law phases.

Organization of the chapter

The rest of the chapter is organized as follows. In Section 4.2, we explain the basic formalism and introduce a broad class of circuits that allows a mapping of the replicated dynamics to effective quantum ground state problems. We discuss the basic structure and symmetry of the model and lay out the dictionary for translating between the quantities measured in the physical circuit and the corresponding operators in the effective ground state problem. In Section 4.3, we apply the framework to classify the phases of a random circuit model with $\mathbb{Z}_2$ symmetry. We then demonstrate numerically that some of the new phases are found in the phase diagram of a concrete stabilizer circuit model. In Section 4.4, we consider Gaussian fermionic circuits as outlined above. Section 4.5 presents a broader discussion and summary of the results. In particular, we remark on connections between the quantum circuit ensemble discussed in this Chapter and the theory of spin glasses pioneered by Edwards and Anderson [81]. Close analogies exist both at the level of emergent symmetries and in aspects of information theory. We shall also comment on fundamental differences between the problems associated with the quantum and dynamical nature of the circuit.

4.2 Framework

In this section, we introduce a framework for mapping the time evolution of an ensemble of quantum trajectories to an effective ground state problem. We identify the symmetry of this problem as an extension of the physical circuit symmetry by intrinsic dynamical symmetries.

States and operators in duplicated Hilbert spaces

We consider the dynamics of quantum systems undergoing unitary evolution interspersed by projective measurements. The outcome of each projective measurement is probabilistic, determined by the usual Born rules. This leads to stochastic dynamics of the unnormalized density matrix of the system, which for a particular sequence of measurement outcomes is

given by

$$\tilde{\rho}_m(t) = U_k \dots U_2 P_{m_1} U_1 \rho_0 U_1^\dagger P_{m_1} U_2^\dagger \dots U_k^\dagger. \tag{4.4}$$

Here ρ_0 is the initial state, U_j are the set of unitary evolution, and P_{m_j} are projection operators associated with measurement outcome m_j. Given U_j, the sequence of measurement outcomes $m = (m_1, m_2, \cdots)$ defines the trajectory of the wave function, which occurs with the probability $p_m = \operatorname{tr}\tilde{\rho}_m$. The set of normalized quantum states $\rho_m \equiv \tilde{\rho}_m/p_m$ and their assigned probabilities p_m form the measurement ensemble of the circuit. We are interested in certain steady-state properties of this ensemble.

Recent works have shown that the steady states of quantum circuits with unitary gates and measurements can exhibit measurement-induced phase transitions, characterized by non-analyticities in various information theoretic quantities such as entanglement entropy, the global purity, and the Fisher information [163, 239, 162, 65, 104, 18, 130]. These phase transitions have no signature in the averaged density matrix over quantum trajectories $\rho = \sum_m p_m \rho_m = \sum_m \tilde{\rho}_m$. In fact, it can be shown that ρ approaches the maximally mixed state in the models considered in the literature [163, 239, 18].

To characterize phase transitions in the measurement ensemble, one needs to consider the statistics of the ensemble, which is encoded in the time evolution of multiple copies of the trajectory density matrix, that is $\tilde{\rho}_m^{\otimes n}$. In what follows, it will be convenient to view these objects as state vectors in a duplicated Hilbert space $\mathcal{H}^{(n)} = (\mathcal{H} \otimes \mathcal{H}^*)^{\otimes n}$. Thus, for example, the replicated un-normalized trajectory density matrix is denoted by

$$|\tilde{\rho}_m^{(n)}\rangle\rangle \equiv \tilde{\rho}_m^{\otimes n}. \tag{4.5}$$

This state vector is evolved linearly by unitary and projection operators

$$\mathcal{U}_i^{(n)} \equiv (U_i \otimes U_i^*)^{\otimes n}, \quad \mathcal{M}_{m_i}^{(n)} \equiv (P_{m_i} \otimes P_{m_i})^{\otimes n}, \tag{4.6}$$

defined through their action on the replicated density matrix

$$\mathcal{U}_i^{(n)}|\tilde{\rho}_m^{(n)}\rangle\rangle \equiv \left(U_i \tilde{\rho}_m U_i^\dagger\right)^{\otimes n}, \tag{4.7}$$

$$\mathcal{M}_{m_i}^{(n)}|\tilde{\rho}_m^{(n)}\rangle\rangle \equiv (P_{m_i} \tilde{\rho}_m P_{m_i})^{\otimes n}. \tag{4.8}$$

If the state in the duplicated Hilbert space is not factorizable, we use the linearity of the operators to define the actions of unitary gates and projections.

We will show that pertinent properties of the circuit ensemble are encoded in ensemble states defined as a sum over the replicated trajectory-states

$$|\tilde{\rho}^{(n)}\rangle\rangle \equiv \sum_m |\tilde{\rho}_m^{(n)}\rangle\rangle. \tag{4.9}$$

This un-normalized ensemble state is very convenient because it undergoes a linear time evolution

$$
\begin{aligned}
|\tilde{\rho}^{(n)}(t)\rangle\rangle &= \mathcal{V}^{(n)}(t)|\tilde{\rho}_0^{(n)}\rangle\rangle \\
&\equiv \sum_m \mathcal{U}_t^{(n)} \cdots \mathcal{M}_{m_2}^{(n)} \mathcal{U}_2^{(n)} \mathcal{M}_{m_1}^{(n)} \mathcal{U}_1^{(n)} |\tilde{\rho}_0^{(n)}\rangle\rangle.
\end{aligned}
\tag{4.10}
$$

Later in this section, we present a class of models, in which this time evolution is exactly mapped to an imaginary time evolution generated by an effective quantum Hamiltonian, so that

$$
|\tilde{\rho}^{(n)}(t)\rangle\rangle = e^{-tH_{\mathrm{eff}}^{(n)}}|\rho_0^{(n)}\rangle\rangle.
\tag{4.11}
$$

In these models, the properties of the ensemble state $|\tilde{\rho}^{(n)}(t)\rangle\rangle$ in late times are faithfully encoded in the ground state of $H_{\mathrm{eff}}^{(n)}$.

A key step in mapping of moments in the trajectory ensemble of the circuit to properties of the effective ground state is to translate the trace operation in the replicated Hilbert space to the state-vector formalism. For example, we will need the trace $(\mathrm{tr}\,\tilde{\rho}_m)^n$ in order to normalize the trajectory states. In the state-vector notation, these traces can be expressed as an inner product with a reference state

$$
\langle\langle\mathcal{I}| = \mathbb{1}^{\otimes n} = \sum_{\{\tau_\ell\}} \langle\langle\tau_1\tau_1, \tau_2\tau_2, \ldots, \tau_n\tau_n|,
\tag{4.12}
$$

where each pair of τ_ℓ labels the ket and bra state of copy ℓ. Now, with the inner product between states in the replicated Hilbert space defined as $\langle\langle\chi|\sigma\rangle\rangle \equiv \mathrm{tr}(\chi^\dagger\sigma)$ we can write the trace $(\mathrm{tr}\,\tilde{\rho}_m)^n = \mathrm{tr}(\tilde{\rho}_m^{\otimes n}) = \langle\langle\mathcal{I}|\tilde{\rho}_m^{(n)}\rangle\rangle$.

The simplest quantities that involve higher moments of the density matrix are the average k-th moments of an observable $\hat{O}$ over the measurement ensemble and circuit realizations

$$
O_k = \sum_m p_m \overline{\left[\frac{\mathrm{tr}(\hat{O}\tilde{\rho}_m)}{\mathrm{tr}\tilde{\rho}_m}\right]^k}.
\tag{4.13}
$$

For example, when dealing with circuits with a global $\mathbb{Z}_2$ symmetry (see Section 4.3) it is natural to consider the fluctuations of a local order parameter $\hat{O} = X_i$, which is odd under the symmetry. In this case the object $O_2 = \sum_m p_m \langle X_i\rangle_m^2$ is an Edwards-Anderson type order parameter that can detect the broken symmetry in individual trajectories [81]. More precisely, we'll be interested in the operator $\hat{O} = X_iX_j$ that gives rise to the EA correlations $O_2 = \sum_m p_m \langle X_iX_j\rangle_m^2$. Another example of an operator of interest is the $\mathbb{Z}_2$ parity on subsystem A, $\hat{O} = \prod_{j \in A} Z_j$. In this case, $O_2 = \sum_m p_m \langle \prod_{j \in A} Z_j\rangle_m^2$ measures the parity variance on A.

The quantities given in Eq. (4.13) can be obtained from a replica limit. To formally eliminate the denominator in Eq. (4.13), we introduce a replica index n to write $p_m^{1-k} =$

$\lim_{n\to 1} p_m^{n-k}$. Substituting into (4.13), we can express the k-th moment as a limit $n \to 1$ of the sequence of replica quantities

$$O_k^{(n)} = \frac{\text{tr}\left(\mathcal{O}^{(k)} \tilde{\rho}^{\otimes n}\right)}{\text{tr} \tilde{\rho}^{\otimes n}} = \frac{\langle\!\langle \mathcal{I} | \mathcal{O}^{(k)} | \tilde{\rho}^{(n)} \rangle\!\rangle}{\langle\!\langle \mathcal{I} | \tilde{\rho}^{(n)} \rangle\!\rangle},\tag{4.14}$$

where we defined

$$\mathcal{O}_k^{(n)} \equiv \left[\bigotimes_{i=1}^{k} (\hat{O} \otimes \mathbb{1})\right] \otimes (\mathbb{1} \otimes \mathbb{1})^{\otimes n-k}.\tag{4.15}$$

The denominator in Eq. (4.14) is added to ensure that the quantities $O_k^{(n)}$ correspond to normalized boundary correlations in the effective model. It is exactly equal to unity in the replica limit $n \to 1$.

Subsystem purities can also be expressed in the same framework. The average k-th purity of a subsystem A is given by

$$\mu_{k,A} = \overline{\sum_m p_m \frac{\text{tr}(\tilde{\rho}_{A,m}^k)}{(\text{tr} \tilde{\rho}_m)^k}}.\tag{4.16}$$

We can express it in the form (4.14) by choosing the operator $\mathcal{O}^{(k)}$ to be the subsystem cyclic permutation operator (of kets)

$$\mathcal{C}_{\ell,A}^{(k)} = \sum_{\{\alpha_i\}} \bigotimes_{i=1}^{k} \left(|\alpha_{i+1}\rangle \langle \alpha_i| \otimes \mathbb{1}\right),\tag{4.17}$$

where $\alpha_{k+1} \equiv \alpha_1$ is assumed and the subscript ℓ implies acting on the left of the density matrices (i.e. permutation of kets). $|\alpha_i\rangle$ runs over all basis states of subsystem A, while $\mathcal{C}_{\ell,A}^{(k)}$ acts as the identity outside of subsystem A. That is, we have

$$\mu_{k,A}^{(n)} = \frac{\langle\!\langle \mathcal{I} | \mathcal{C}_{\ell,A}^{(k)} | \tilde{\rho}^{(n)} \rangle\!\rangle}{\langle\!\langle \mathcal{I} | \tilde{\rho}^{(n)} \rangle\!\rangle},\tag{4.18}$$

and $\mu_{k,A} = \lim_{n\to 1} \mu_{k,A}^{(n)}$.

In much of this Chapter we study the behavior of second moments in a two replica model (i.e. $k = 2, n = 2$). It is therefore worth writing the moments explicitly in this special case

$$O_2^{(2)} = \frac{\langle\!\langle \mathcal{I} | \mathcal{O}^{(2)} | \tilde{\rho}^{(2)} \rangle\!\rangle}{\langle\!\langle \mathcal{I} | \tilde{\rho}^{(2)} \rangle\!\rangle} = \frac{\sum_m p_m^2 \langle \hat{O} \rangle_m^2}{\sum_m p_m^2},\tag{4.19}$$

and similarly

$$\mu_{2,A}^{(2)} = \frac{\sum_m p_m^2 \, \text{tr}\left(\rho_{A,m}^2\right)}{\sum_m p_m^2}.\tag{4.20}$$

We see that in the two replica model the trajectories are weighted by a distorted probability distribution $p_m^{(2)} = p_m^2/(\sum_{m'} p_{m'}^2)$.

Finally, for completeness, we discuss the computation of the von Neumann entanglement entropy within the state-vector formalism. For this purpose it is useful to treat the classical measurement device M as a part of the extended system, as we have shown in Ref. [18]. In this picture, the randomness of the measurement outcomes are encoded in the correlation between the system and measurement device.

The average von Neumann entanglement entropy of subsystem A over the possible measurement outcomes is

$$S_A = \sum_m p_m S_{A,m} = \sum_m -p_m \operatorname{tr}(\rho_{A,m} \log \rho_{A,m}). \tag{4.21}$$

In the extended system, we can express this average as the conditional entropy

$$S_A = S(A|M) \equiv S_{MA} - S_M, \tag{4.22}$$

where the measurement device is characterized by a diagonal density matrix $\rho_M = \delta_{mm'} p_m$. In this formulation, we can further include an average over the random unitary gates and express the average conditional von Neumann entropy $\overline{S_A}$ as a limit of "conditional Rényi entropies" [18],

$$\begin{aligned}
S_A^{(n)} &= \frac{1}{1-n} \log\left(\overline{\operatorname{tr}\rho_{MA}^n}\right) - \frac{1}{1-n} \log\left(\overline{\operatorname{tr}\rho_M^n}\right) \\
&= \frac{1}{1-n} \log\left(\frac{\overline{\sum_m p_m^n \operatorname{tr}(\rho_{A,m}^n)}}{\overline{\sum_m p_m^n}}\right).
\end{aligned} \tag{4.23}$$

The properly averaged von Neumann entropy is restored in the replica limit: $\overline{S_A} = \lim_{n \to 1} S_A^{(n)}$. The conditional Rényi entropies have a simple expression within our formalism as the logarithm of a boundary matrix element. As in the case of purity, the relevant operator is the permutation $\mathcal{C}_{\ell,A}^{(n)}$ of forward propagating trajectories (kets) within subsystem A:

$$S_A^{(n)} = \frac{1}{1-n} \log \frac{\langle\langle \mathcal{I} | \mathcal{C}_{\ell,A}^{(n)} | \tilde{\rho}^{(n)} \rangle\rangle}{\langle\langle \mathcal{I} | \tilde{\rho}^{(n)} \rangle\rangle}. \tag{4.24}$$

Note that Eq. (4.23) implies that each of the conditional Rényi entropies involves weighting of the subsystem purities by the outcome probabilities to the n-th power. Thus, they are not identical to the Rényi entropies averaged over the measurement ensemble. However, as noted above, the von Neumann entropy obtained in the replica limit, is correctly weighted by the outcome probabilities. In this Chapter, we mainly focus on $n = 2$ model, the conditional Rényi entropy and purity are related by $e^{-S_A^{(2)}} = \mu_{2,A}^{(2)}$.

Enlarged dynamical symmetry

The dynamics $\mathcal{V}(t)$ of the quantum state in the duplicated Hilbert space exhibits an enlarged symmetry, which is an extension of the physical symmetry of the circuit by the dynamical symmetries inherent to the time evolution of identical copies of the density matrix. In general, the dynamical symmetry does not commute with the physical circuit symmetry, and the combination of the two produces the enlarged symmetry of $\mathcal{V}(t)$. We shall see that this enlarged symmetry dictates the possible steady states of the circuit.

We say that the circuit has a physical symmetry G if all the unitary gates U_i and the projectors P_{m_i} implementing the measurements commute with the symmetry generators $g \in G$. In this Chapter, for simplicity, we assume the symmetry group G has a unitary representation and do not consider the anti-unitary circuit symmetries. Note that the circuit symmetry is important for characterizing the steady state, however, unlike in purely unitary dynamics it does not give rise to a conserved quantity enforced at the level of individual trajectories. Given an initial state with indefinite quantum numbers associated with the symmetry, projective measurements may lead to the collapse of wave functions, such that quantum amplitudes or probabilities in each symmetry sector changes. Once the system has a definite set of quantum numbers, then the measurements cannot change them.

In the dynamics of n replica copies, the physical circuit symmetry G is duplicated to each of the forward and backward evolving branches, leading to a symmetry group $G^{\otimes n} \times G^{\otimes n}$. We call the first and second $G^{\otimes n}$ the *left* and *right* circuit symmetry. In addition, the time evolution $\mathcal{V}(t)$ of n copies of the density matrix is invariant to permutation among the different copies of the identical circuit elements (U_i and P_{m_i}) operating on the density matrix from the left and, independently, to permutation of the circuits elements acting from the right. The operators representing the left and right permutation symmetry are given respectively by

$$\mathcal{C}_{\ell,\xi} = \sum_{\{\alpha_a\}} \bigotimes_a \left(|\alpha_{\xi(a)}\rangle \langle \alpha_a| \otimes \mathbb{1} \right),$$

$$\mathcal{C}_{r,\xi} = \sum_{\{\alpha_a\}} \bigotimes_a \left(\mathbb{1} \otimes |\alpha_a\rangle \langle \alpha_{\xi(a)}| \right), \tag{4.25}$$

where $\xi \in \mathcal{S}_n$ is a member of the permutation group of n elements. Here, we omit the superindex for n replica copies for the simplicity of notation. The left cyclic permutation $\mathcal{C}_\ell$, which is a special case of $\mathcal{C}_{\ell,\xi}$, was already introduced in Eq. (4.17). The left and right permutation symmetries are independent from one another since $[\mathcal{C}_{\ell,\xi}, \mathcal{C}_{r,\eta}] = 0$ for any $\xi, \eta \in \mathcal{S}_n$. These permutation symmetries transform the replicated $G^{\otimes n}$ circuit symmetries into each other giving rise to $G^{\otimes n} \rtimes \mathcal{S}_n$ invariance, independently for the forward and backward branches. The group extension $G^{\otimes n} \rtimes \mathcal{S}_n$ is also known as the wreath product $G \wr \mathcal{S}_n$.

Finally, there is one more dynamical symmetry associated with hermiticity of the density matrix, which the time evolution induced by $\mathcal{V}(t)$ must preserve. The operator representing this symmetry is the hermitian conjugation

$$\mathbb{H} : c_{\alpha\beta\gamma\delta} |\alpha\rangle \langle \beta| \otimes |\gamma\rangle \langle \delta| \mapsto c^*_{\alpha\beta\gamma\delta} |\beta\rangle \langle \alpha| \otimes |\delta\rangle \langle \gamma|, \tag{4.26}$$

which is anti-linear (anti-unitary) and of order 2, such that $\mathbb{H}^2 = \mathbb{1}$. We denote this symmetry by $\mathbb{Z}_2^{\mathbb{H}}$. The physical circuit symmetries combine with the left and right permutation symmetries and hermiticity to give the complete dynamical symmetry

$$\mathcal{G}^{(n)} = \left[\left(G^{\otimes n} \rtimes \mathcal{S}_n \right) \times \left(G^{\otimes n} \rtimes \mathcal{S}_n \right) \right] \rtimes \mathbb{Z}_2^{\mathbb{H}}. \tag{4.27}$$

Equivalently, $\mathcal{G}^{(n)}$ can be written in terms of the wreath product $\mathcal{G}^{(n)} = G \wr \mathcal{S}_n \wr \mathbb{Z}_2^{\mathbb{H}}$.

We make a few remarks. While Eq. (4.27) is generically valid, the symmetry of $\mathcal{V}(t)$ can be even larger in the presence of additional constraints. For example, in Section 4.4, we consider a fermionic circuit that preserves the Gaussianity of the fermionic wave function, which leads to a continuous symmetry. In addition, while $\mathcal{G}^{(n)}$ itself is very large, the physically relevant symmetry can be a smaller subgroup of $\mathcal{G}^{(n)}$, depending on the details of the model. For instance, if $\mathcal{V}$ is averaged over a specific random circuit ensemble, the averaging process can constrain the state to be in faithful representations only of a subgroup of $\mathcal{G}^{(n)}$ thus reducing the available options for symmetry breaking.

We also note that our analysis only concerns the symmetry of $\mathcal{V}(t)$ and does not address additional physical constraints such as the complete positivity of quantum channels.

Effective quantum Hamiltonian

In this section, we introduce an exact mapping of the dynamics $\mathcal{V}(t)$ in a broad class of qubit circuits to imaginary time evolution generated by an effective Hamiltonian H_{eff}, which inherits the enlarged dynamical symmetry. Thus, the long-time steady states of the quantum circuits can be characterized by ground states of H_{eff}.

The structure of the quantum circuits we consider is shown in Fig. 4.1(a). Each "time step" δt is subdivided into layers. The first layer in each time step is made of single-site random unitary phase rotations (i.e. rotation about the Z-axis). This is not a necessary step in our scheme, but we shall see that averaging over the random phases simplifies the effective model by projecting onto a reduced Hilbert space. The next layer consists of near identity unitary gates, such as $U_{ij} = \exp\left(-\mathrm{i}\theta_{ij}^{\alpha\beta} \tau_i^\alpha \tau_j^\beta \right)$, where τ_j^α with $\alpha = 0, \ldots, 3$ represent the identity and Pauli operators on the qubit. The random couplings $\theta_{ij}^{\alpha\beta}$ are drawn from a symmetric Gaussian distribution with variance $\mathrm{var}(\theta_{ij}^{\alpha\beta}) \equiv J_{\alpha\beta}\delta t$. This layer also contains projective measurements of Pauli string operators M_α, applied with probability $p_\alpha = \Gamma_\alpha \delta t$.

The replicated density matrix $|\tilde{\rho}^{(n)}\rangle\!\rangle$ is evolved by the operator $\mathcal{V}(t)$, consisting of the replicated circuit elements. We obtain a transfer matrix by averaging the evolution by one time step over the "circuit ensemble", namely the distribution of unitary gates and the probabilities p_α of applying measurement operators. The latter are also replicated on the n forward and n backward branches [e.g. the case of $n = 2$ is depicted in Fig. 4.1(b)].

For an infinitesimal time step, $\delta t \to 0$, the transfer matrix takes the form $\mathcal{T} = \mathcal{V}(\delta t) = \exp(-\delta t H_{\text{eff}})$. Hermiticity of $\mathcal{T}$ (and thus also of H_{eff}) is ensured if the distribution of the coupling constants in the unitary gates is symmetric about zero. In the long-time evolution, the steady state $|\tilde{\rho}^{(n)}\rangle\!\rangle = \lim_{t\to\infty} e^{-tH_{\text{eff}}}|\rho_0\rangle\!\rangle$ is given by the ground state of H_{eff}.
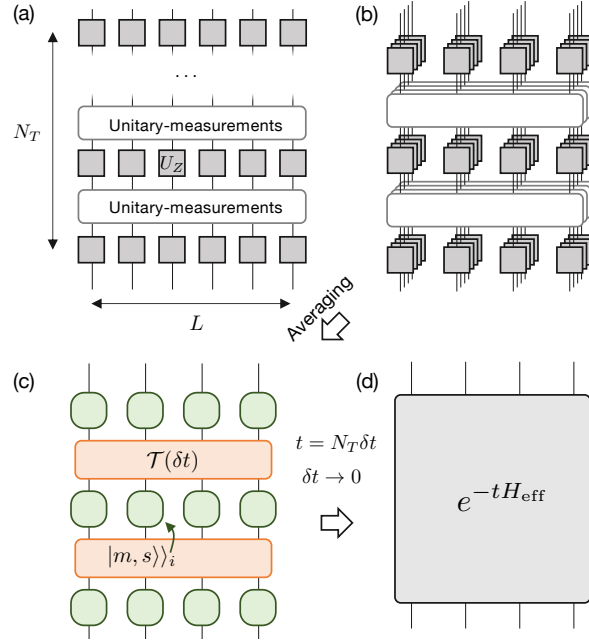
Figure 4.1: Mapping the dynamics of random quantum circuits to the imaginary time evolution with an effective Hamiltonian. (a) A quantum circuit with layers of random on-site Z-rotations $U_Z = e^{-i\theta_i Z_i}$. The inter-layer elements include measurements and unitary gates satisfying conditions needed for a hermitian effective Hamiltonian (see text). (b) The effective time evolution of a doubled density matrix is effected by four copies of the quantum circuit, two corresponding to forward propagation and two backward. (c,d) Averaging over the random Z rotations projects on the reduced site Hilbert space $|m, s\rangle\!\rangle_i$, which can be interpreted as quantum spin states. The states at successive time steps are connected by the transfer matrix $\mathcal{T}(\delta t)$, which is generated by an effective Hamiltonian H_{eff} in the limit $\delta t \to 0$.

For the circuits considered in this section, the effective Hamiltonian H_{eff} has a set of mutually commuting local integrals of motion. These are the local parity operators $\mathcal{X}_j = \prod_{a=1}^{n}(X_a X_{\bar{a}})_j$, $\mathcal{Y}_j = \prod_{a=1}^{n}(Y_a Y_{\bar{a}})_j$, and $\mathcal{Z}_j = \prod_{a=1}^{n}(Z_a Z_{\bar{a}})_j$ (see appendix C.1). The subscript a and $\bar{a}$ denote the Pauli operators acting on the a-th forward and backward branch, respectively. The eigenstates of H_{eff} are labeled by the eigenvalues of the $\mathcal{X}_j$, $\mathcal{Y}_j$, and $\mathcal{Z}_j$ on all sites.

We will only need to characterize the ground state of H_{eff} in the even sector of the local parities in order to compute the physical diagnostics in Eq. (4.13) and (4.23). The reason is that the reference state $\langle\!\langle\mathcal{I}|$ has definite local parities on all sites, $\mathcal{X}_j = \mathcal{Z}_j = +1$ and $\mathcal{Y}_j = (-1)^n$. Meanwhile, all the duplicated operators associated with diagnostics considered in this Chapter, e.g. $\mathcal{O}_2^{(2)} = (X \otimes \mathbb{1})^{\otimes 2}$, preserve the local parities. Therefore, only the

ground state in the same local parity sector as the reference state $|\mathcal{I}\rangle\rangle$ has a nonvanishing contribution to the matrix element in Eq. (4.14) and (4.24).

We now turn to construct the effective Hamiltonian explicitly for the case of $n = 2$ replicas. Generalizing to higher replicas $n \geq 3$ is straightforward. Consider first the single-site phase rotation at the entry to each time step. Averaged over the random phase, the two copy evolution through this layer takes the form

$$\overline{e^{-i\theta_j Z_j} \otimes e^{i\theta_j Z_j} \otimes e^{-i\theta_j Z_j} \otimes e^{i\theta_j Z_j}} = \frac{1}{2\pi} \int_0^{2\pi} d\theta_j e^{-i\theta_j \left(Z_{j1} - Z_{j\bar{1}} + Z_{j2} - Z_{j\bar{2}} \right)} = \sum_{k=1}^{6} |\varphi_k\rangle\rangle \langle\langle\varphi_k|. \quad (4.28)$$

The averaging over the identical rotation angle of the four branches yields a delta function that implements a projection onto the six-dimensional subspace defined by vanishing of $Z_{j1} + Z_{j2} - Z_{j\bar{1}} - Z_{j\bar{2}}$. A convenient basis for this subspace, labeled by $|m, s\rangle\rangle$, is given explicitly by

$$|1, \pm\rangle\rangle = \frac{1}{\sqrt{2}} \left(|1\rangle \langle 1| \otimes |0\rangle \langle 0| \pm |0\rangle \langle 0| \otimes |1\rangle \langle 1| \right),$$

$$|0, \pm\rangle\rangle = \frac{1}{\sqrt{2}} \left(|1\rangle \langle 1| \otimes |1\rangle \langle 1| \pm |0\rangle \langle 0| \otimes |0\rangle \langle 0| \right),$$

$$|-1, \pm\rangle\rangle = \frac{1}{\sqrt{2}} \left(|0\rangle \langle 1| \otimes |1\rangle \langle 0| \pm |1\rangle \langle 0| \otimes |0\rangle \langle 1| \right). \quad (4.29)$$

The quantum numbers $s_i = \pm 1$ on site i happen to be the eigenvalues of the local integrals of motion $\mathcal{X}_i$ (and of $\mathcal{Y}_i$). As discussed above, for $n = 2$, the reference state $|\mathcal{I}\rangle\rangle$ is in the even sector of local parities. Hence, we need to consider only the even sector $s_i = +1$. This leaves us with three states on every site $m = -1, 0, 1$, which can be represented by a spin-1 degree of freedom.

The left permutation (swap) symmetry $\mathcal{S}_2$ has a simple action on the basis (4.29)

$$\mathcal{C}_\ell : |m, s\rangle\rangle \leftrightarrow |-m, s\rangle\rangle. \quad (4.30)$$

Thus, spontaneous breaking of the $\mathcal{S}_2$ permutation symmetry will appear as onset of a spontaneous z-magnetization of the spin-1 degrees of freedom.

We now turn to construct the transfer matrix operating between the states of the reduced Hilbert space

$$\langle\langle\{m, s\}|\mathcal{T}|\{m', s'\}\rangle\rangle = \langle\langle\{m, s\}| \prod_\nu \mathcal{M}_\nu \prod_\mu \mathcal{U}_\mu |\{m', s'\}\rangle\rangle. \quad (4.31)$$

Here, $\mathcal{U}_\mu$ and $\mathcal{M}_\nu$ represent the averaged unitary gates and measurements acting on the duplicated state. The averaging is over both the random couplings in the unitary gates and the probabilistic application of the measurements. The indices μ, ν run over all different unitary gates and measurements in the layers of the circuit that are part of a single time step

δt. All of these operators are designed to be close to unity. The deviation from unity after averaging is of order δt.

The averaged measurement operators take the form

$$\mathcal{M}_\nu = (1 - \Gamma_\nu \delta t)\mathbb{1}^{\otimes 4} + \Gamma_\nu \delta t \sum_{m_\nu = \pm} P_{m_\nu}^{\otimes 4}, \tag{4.32}$$

where Γ_ν may be viewed as the rate at which a measurement of type ν is performed, and $P_\pm = (1 \pm M_\nu)/2$ is the projection onto the $\pm$ eigenstate of the Pauli string operator M_ν.

The unitary gates operating on qubits are of the general form: $U_j = \exp\left(-i\theta_j^{\alpha\beta} \tau_j^\alpha \tau_{j+1}^\beta\right)$, where τ_j^α denote local Pauli operators, including the identity. That is $\tau_i^0 \equiv \mathbb{1}_j$, $\tau_j^1 \equiv X_j$ etc. Averaging over the Gaussian distribution of $\theta_j^{\alpha\beta}$ with variance $J_{\alpha\beta}\,\delta t$ gives:

$$\mathcal{U}_j = \overline{U_j \otimes U_j^* \otimes U_j \otimes U_j^*} \tag{4.33}$$
$$= e^{-\frac{\delta t J_{\alpha\beta}}{2}\left(\tau_{j,1}^\alpha \tau_{j+1,1}^\beta - \tau_{j,\bar{1}}^\alpha \tau_{j+1,\bar{1}}^\beta + \tau_{j,2}^\alpha \tau_{j+1,2}^\beta - \tau_{j,\bar{2}}^\alpha \tau_{j+1,\bar{2}}^\beta\right)^2}.$$

For an infinitesimal δt, the transfer matrix (4.31) takes the form $\mathcal{T} = 1 - H_\mathcal{M}\delta t - H_\mathcal{U}\delta t + O(\delta t^2)$. The effective Hamiltonian $H_{\text{eff}} = H_\mathcal{M} + H_\mathcal{U}$ can be read from Eqs. (4.32) and (4.33) projected to the reduced Hilbert space of three states per site.

In Appendix C.2 we exemplify a detailed construction of an effective Hamiltonian for the two replica dynamics of a simple circuit with $\mathbb{Z}_2$ symmetry. The result is a spin-1 model with $D_4 \times \mathbb{Z}_2^\mathbb{H}$ symmetry. In the next section, we discuss the possible steady-state phases of circuits with $\mathbb{Z}_2$ symmetry more generally. We present direct simulation of a concrete quantum circuit, which exhibits a subset of the possible steady-state phases.

4.3 Qubit circuit with $\mathbb{Z}_2$ symmetry

We now discuss how the phase structure of a quantum circuit with measurements is enriched by imposing a physical $\mathbb{Z}_2$ symmetry on the circuit elements. To derive general results, we go beyond the circuit models discussed in Section 4.2. In particular, we do not enforce a projection to a reduced six-dimensional local Hilbert space.

In Section 4.3 below, we present the general symmetry analysis of the problem to identify the allowed phases and determine what are their sharp signatures in the physical probes of the circuit state. In Section 4.3, we present the results of numerical simulations of a concrete circuit model with $\mathbb{Z}_2$ symmetry. The results demonstrate the establishment of at least two of the possible area-law phases and three of the distinct volume-law phases in the steady state phase diagram of this circuit model.

Phases protected by enlarged symmetry

The circuits we consider in this section operate on a one-dimensional array of qubits. Unitary gates in the circuit are generated by Pauli operators with random couplings drawn from

symmetric distributions as considered in Section 4.2. All circuit operations, unitary gates and measurements, commute with a global $\mathbb{Z}_2$ parity operator defined on a single chain

$$\hat{\pi} = \prod_{j=1}^{L} Z_j. \tag{4.34}$$

To make the model more general, we allow additional chains of qubits, which are not transformed by the above parity operator. Thus, operations applied to qubits on the additional chains are not restricted by symmetry.

We first focus on the phases that arise in the simplest case of two replica copies (i.e. $n = 2$). A model of two copies gives a natural framework to address fluctuations that are second moments of observables over the trajectory ensemble. This is not an exact approach because without extrapolating to the replica limit $n \to 1$ the weighting of trajectories is distorted. To validate key aspects of the phase structure predicted by the two-replica model we use direct simulations of a quantum circuit model. In particular we confirm the existence of new phases enabled by the enlarged symmetry.

According to the analysis presented in Section 4.2, the enlarged symmetry of the two-replica model should be $\mathcal{G}^{(2)} = (D_4 \times D_4) \rtimes \mathbb{Z}_2^{\mathbb{H}}$. The left (right) D_4 group consist of the $\mathbb{Z}_2$ symmetries of the two copies on the forward (backward) branch, compounded with the $\mathcal{S}_2$ permutation symmetry between the two copies, i.e. $D_4 = (\mathbb{Z}_2 \times \mathbb{Z}_2) \rtimes \mathcal{S}_2$. The $\mathbb{Z}_2$ symmetries of a single copy and branch are generated by product operators which we denote as $\prod_j(ZIII)_j$ (copy 1 forward branch), $\prod_j(IZII)_j$ (copy 1 backward), $\prod_j(IIZI)_j$ (copy 2 forward) and $\prod_j(IIIZ)_j$ (copy 2 backward).

The effective symmetry that determines the phase structure can be reduced and simplified by accounting for additional constraints. Specifically, in our case, the effective Hamiltonian conserves a set of local parities $\mathcal{X}_j = (XXXX)_j$, $\mathcal{Y}_j = (YYYY)_j$ and $\mathcal{Z}_j = (ZZZZ)_j$ (see Appendix C.1). This leads to reduction of the effective symmetry $G^{(2)}$ as follows. First, the fact that the operators $\mathcal{X}_j$ have non-vanishing expectation values on every site implies breaking of all four single-branch $\mathbb{Z}_2$ symmetries already at the outset because the $\mathcal{X}_j$ anti-commutes with these symmetries. Second, as noted before, we seek the ground state in the even sector of $\mathcal{X}_j$, $\mathcal{Y}_j$ and $\mathcal{Z}_j$ on every site. The exchange symmetry $\mathcal{S}_2^X$, generated by the product of left and right permutation $\mathcal{C}_\ell \mathcal{C}_r$, acts trivially in this sector (see Appendix C.3). Therefore it cannot be broken and we can quotient it out. Third, we can also quotient out the symmetry $\prod_j \mathcal{Z}_j$ because it is a product of the local parities, which cannot be broken.

The above considerations leave us with an effective global symmetry $\mathcal{G}_{\text{eff}}^{(2)} = D_4 \times \mathbb{Z}_2^{\mathbb{H}}$, where $D_4 = (\mathbb{Z}_2^{\Pi_L} \times \mathbb{Z}_2^{\Pi_1}) \rtimes \mathcal{S}_2$. Here, $\mathbb{Z}_2^{\Pi_L}$ and $\mathbb{Z}_2^{\Pi_1}$ are generated by $\hat{\Pi}_L = \prod_j(ZIZI)_j$ and $\hat{\Pi}_1 = \prod_j(ZZII)_j$, respectively. In Appendix C.2, we explicitly derive the effective Hamiltonian for a concrete model, demonstrating the $D_4 \times \mathbb{Z}_2^{\mathbb{H}}$ symmetry.

The Hermitian conjugate $\mathbb{H}$ in the even parity sector is given by the complex conjugate $\mathcal{K}$ as shown in Appendix C.3 and commutes with the rest symmetry generators in $\mathcal{G}_{\text{eff}}^{(2)}$. Hence, $\mathbb{H}$ can be broken independently. Moreover, the reference state $\langle\!\langle \mathcal{I}|$ and $\langle\!\langle \mathcal{I}| \mathcal{O}_2$ associated

Entropy	Name	Residual symmetry	$\Pi^{(2)}(A)$	$\chi_{EA}^{(2)}(i,j)$	$\Phi^{(2)}$
Area law	Symmetric phase (trivial/SPT)	$(\mathbb{Z}_2^{\Pi_L} \times \mathbb{Z}_2^{\Pi_1}) \rtimes \mathcal{S}_2$	const.	$\to 0$	0
	Coexistence phase (trivial/SPT)	$\mathbb{Z}_2^{\Pi_L} \times \mathcal{S}_2$	const.	const.	0
	Broken symmetry phase	$\mathcal{S}_2$	$\to 0$	const.	const.
	Composite phase	$\mathbb{Z}_4^{\mathcal{C}_\ell \Pi_1}$	const.	const.	0
Vol. law	Symmetric phase	$\mathbb{Z}_2^{\Pi_L} \times \mathbb{Z}_2^{\Pi_1}$	const.	$\to 0$	0
	Featureless phase	$\mathbb{Z}_2^{\Pi_1}$	$\to 0$	$\to 0$	const.
	Coexistence phase I	$\mathbb{Z}_2^{\Pi_1 \Pi_L}$	const.	const.	0
	Coexistence phase II	$\mathbb{Z}_2^{\Pi_L}$	const.	const.	0
	Broken symmetry phase	$\emptyset$	$\to 0$	const.	const.
	Composite phase	$\mathbb{Z}_2^{\mathcal{C}_\ell \Pi_L}$	$\to 0$	const.	0

Table 4.1: Possible phases of a qubit circuit with $\mathbb{Z}_2$ symmetry and their diagnostics. Four area-law and six volume-law phases are characterized by distinct residual symmetries given in the second column. The generators of the respective $\mathbb{Z}_2$ subgroups are specified in superscript. $\hat{\Pi}_L = \prod_j (ZIZI)_j$ is the parity in the two forward branches. $\hat{\Pi}_1 = \prod_j (ZZII)_j$ is the parity in the first copy. For each phase we give the long distance limit of the parity variance $\Pi^{(2)}(A)$ and EA correlation $\chi_{EA}^{(2)}(i,j)$ as well as the value of the Fisher information "order parameter" $\Phi^{(2)} = 1 - \frac{1}{2}F^{(2)}$ in the bulk. The phases we observe numerically in the model studied in Section 4.3 are shaded gray.

with the physical diagnostics are symmetric under Hermitian conjugate, making them blind to its breaking. Therefore, in this Chapter, we do not distinguish phases by the hermiticity breaking and consider the phases allowed by the D_4 symmetry.

We are now in a position to classify the possible steady states for the case of $n = 2$ through their correspondence to ground states of an effective Hamiltonian with D_4 symmetry. This includes broken symmetry states, characterized by the residual subgroups of D_4, as well as SPT phases protected by the D_4 effective symmetry. The results of this analysis are summarized in Table 4.1. We shall also discuss the physical diagnostics in quantum circuits that can distinguish different phases. In Appendix C.4 we comment on the extension to higher replicas.

"Conventional" area-law phases

We start from a working definition of the area-law regime as ground states of the effective Hamiltonian that preserve the $\mathcal{S}_2$ permutation symmetry generated by $\mathcal{C}_\ell$.[1] Indeed in these states domain walls of the $\mathcal{S}_2$ symmetry are condensed. Therefore the sub-system swap operator that inserts such domain walls on either side of the sub-system is non-decaying implying non-decaying purity or $O(1)$ entanglement entropy. However, we shall see that the working definition needs to be modified slightly to account for one possible area-law state with broken $\mathcal{S}_2$ symmetry.

Under the working definition the different area-law states are characterized by distinct residual subgroups of D_4 that contain $\mathcal{S}_2$. Let us start from the most symmetric state, which retains the full D_4 symmetry. We first ask what are the "charges" (order parameters) that can condense and are invariant under the $\mathcal{S}_2$ permutation symmetry.

The first option is to condense the local charge $\mathcal{Q}_{1,j} \equiv (XXII)_j$ together with $(IXXI)_j$, which is related to $\mathcal{Q}_{1,j}$ by the $\mathcal{S}_2$ symmetry. If these two charges condense, then the charges $(IIXX)_j$ and $(XIIX)_j$ must also condense because of the definite local parities $\mathcal{X}_j$ in the ground state. Condensing these charges breaks the $\hat{\Pi}_L$ and $\hat{\Pi}_1$ symmetry, leaving a residual global symmetry $\mathcal{S}_2$ in addition to the local symmetries $\mathcal{X}_j, \mathcal{Y}_j, \mathcal{Z}_j$. We call this phase the broken symmetry area-law phase.

The second route for symmetry breaking, starting from the symmetric phase, is to condense the charges $(XIXI)_j$ and $(IXIX)_j$. This condensate breaks the symmetry $\hat{\Pi}_1$, but leaves intact the symmetry $\hat{\Pi}_L$, which commutes with the order parameter. We shall refer to this phase as the "coexistence phase" for reasons that will become clear below. From the coexistence phase, the system can further break the residual symmetry by condensing $\mathcal{Q}_{1,j}$ and its symmetry related charges defined above. This leads to the broken symmetry area-law phase discussed above. We note that charges containing an odd number of Pauli-X matrices, such as $XIII$ and $XXXI$, cannot condense because they anti-commute with the local parities $\mathcal{Y}_j$ and $\mathcal{Z}_j$, which cannot be broken.

Let us discuss the physical interpretation of the area-law phases outlined above and how they can be distinguished by diagnostics of the circuit. We consider properties of the output state, such as the subsystem entanglement entropy, the Edwards-Anderson correlation function $\chi_{EA} \equiv \sum_m p_m \langle X_i X_j \rangle_m^2$ and the subsystem parity variance $\Pi(A) \equiv \sum_m p_m \langle \hat{\pi}(A) \rangle_m^2 = \sum_m p_m \langle \prod_{j \in A} Z_j \rangle_m^2$. As discussed in Section 4.2, these diagnostics map to different normalized matrix elements between the ground state and a reference state.

Our measure of the purity and entanglement entropy is obtained from the overlap

$$e^{-S^{(2)}(A)} = \frac{\langle\!\langle \mathcal{I}| \prod_{j \in A} \mathcal{C}_{\ell,j} |\psi_{gs}\rangle\!\rangle}{\langle\!\langle \mathcal{I}|\psi_{gs}\rangle\!\rangle}. \tag{4.35}$$

Here the operator acting on $|\psi_{gs}\rangle\!\rangle$ creates a pair of domain walls of the left permutation (swap) symmetry at the two edges of the region A. If the ground state is symmetric under

---

[1]The left and right permutation $\mathcal{C}_\ell$ and $\mathcal{C}_r$ are identified because the exchange operation $\mathcal{C}_\ell \mathcal{C}_r$ acts as an identity matrix in the symmetric sector of the local symmetries.

swap, then these domain walls are condensed, implying $\prod_{j \in A} \mathcal{C}_{\ell,j} |\psi_{gs}\rangle\rangle \approx \lambda |\psi_{gs}\rangle\rangle$ for a long region A, leading to a length independent (area-law) entanglement entropy.

The parity variance in region A is similarly obtained by the matrix element of a nonlocal operator that creates domain walls of the $\mathbb{Z}_2$ symmetry generated by $\hat{\Pi}_L$, $\Pi^{(2)}(A) = \langle\langle \mathcal{I} | \prod_{j \in A} (ZIZI)_j |\psi_{gs}\rangle\rangle / \langle\langle \mathcal{I} |\psi_{gs}\rangle\rangle$. Finally, the Edwards-Anderson order parameter in the circuit maps to the following matrix element in the effective model $\Psi_{EA}^{(2)}(i) = \langle\langle \mathcal{I} | (XIXI)_i |\psi_{gs}\rangle\rangle / \langle\langle \mathcal{I} |\psi_{gs}\rangle\rangle$. Strictly speaking, we need to consider the long-range EA correlation $\chi_{EA}^{(2)}(i,j) = \langle\langle \mathcal{I} | (XIXI)_i (XIXI)_j |\psi_{gs}\rangle\rangle / \langle\langle \mathcal{I} |\psi_{gs}\rangle\rangle$ to detect the spontaneous symmetry breaking because the initial state time evolution and reference state are all symmetric with respect to $\hat{\Pi}_1$. To simplify the explanations below, however, we will assume the presence of an infinitesimal symmetry-breaking field and thus refer to the establishment of an EA order parameter.

To understand the behavior of these objects in the different phases, we need to determine, besides the symmetry of the ground state, also that of the reference state $\langle\langle \mathcal{I} |$ in Eq. (4.12). It is easy to check that $\langle\langle \mathcal{I} |$ is invariant under the $\mathbb{Z}_2^{\Pi_1}$ symmetry generated by $\hat{\Pi}_1 = \prod_j (ZZII)_j$, the $\mathcal{S}_2^X$ exchange symmetry, and the $\mathcal{Z}_2^{\mathbb{H}}$ hermiticity symmetry, while breaking all other global symmetries. In particular, the reference state $\langle\langle \mathcal{I} |$ is a condensate of the charges $(XXII)_j$, $(IIXX)_j$, $(YYII)_j$ and $(IIYY)_j$. For example, we have $\langle\langle \mathcal{I} | (XXII)_j = \langle\langle \mathcal{I} |$.

Consider first the signatures of the symmetric phase, which retains the full D_4 symmetry. Invariance with respect to $\hat{\Pi}_L$ means that the domain wall associated with this symmetry is condensed in the ground state, $\prod_{j \in A} (ZIZI)_j |\psi_{gs}\rangle\rangle \approx c |\psi_{gs}\rangle\rangle$. Thus, the subsystem parity variance $\Pi^{(2)}(A)$ remains constant independent of the size of A. The EA order parameter, on the other hand, vanishes because both the ground state and the reference state are even under $\hat{\Pi}_1$, whereas $XIXI$ is an odd operator with respect to this symmetry (anti-commutes with $ZZII$).

Next, consider the broken symmetry phase, obtained by condensing $\mathcal{Q}_{1,j} = (XXII)_j$ and its symmetry related charges. When calculating the EA order parameter $\Psi_{EA}^{(2)}(i)$ we can replace $(XIXI)_i$ by $(IXXI)_i = (XXII)_i (XIXI)_i$ because the reference state is an eigenstate of $(XXII)_i$ with eigenvalue 1. Hence, we expect a nonzero value of $\Psi_{EA}^{(2)}(i)$ owing to the condensation of $(IXXI)_i$ in the ground state $|\psi_{gs}\rangle\rangle$. At the same time, the parity variance $\Pi^{(2)}(A)$ is expected to decay exponentially. The subsystem parity $\prod_{j \in A} (ZIZI)_j$ acts nontrivially on the broken symmetry ground state $|\psi_{gs}\rangle\rangle$, creating a domain of a symmetry related ground state within region A. Since $\langle\langle \mathcal{I} |$ is a uniform broken symmetry state, its normalized overlap with the transformed region is exponentially decaying, $\Pi^{(2)}(A) \sim e^{-L_A/\xi}$ for $\xi \ll L_A \ll L$.[2]

The symmetric and broken symmetry phases outlined above are the same as those discussed in Ref. [224] and observed there in simulations of a concrete model. The physical intuition for the establishment of these phases is clear. In the broken symmetry phase, dominant

---

[2]The broken symmetry state is strictly speaking a cat-like superposition of the two distinct broken symmetry states, leading to $\Pi^{(2)}(A) \sim e^{-L_A/\xi} + e^{-(L-L_A)/\xi}$ under periodic boundary condition.

nearest neighbor XX measurements collapse the individual trajectories to a near product state with qubits polarized in random directions along X. As in a glassy phase, such random X orientations are detected by averaging the square of individual trajectory expectation values $\Psi_{EA} = \sum_m p_m \langle X_i \rangle_m^2$. At the same time, the parity of a long region A has a vanishing expectation value $\langle \hat{\pi}(A) \rangle_m = \langle \prod_{j \in A} Z_j \rangle_m \to 0$ in every trajectory. In the symmetric phase, dominant single-qubit Z measurements collapse individual trajectories to near product states with definite, yet random parity on each qubit. This is detected by taking the variance over trajectories of the parity in region A: $\sum_m p_m \langle \hat{\pi}(A) \rangle_m^2 \to$ const. At the same time, the EA order parameter vanishes in the symmetric phase because $\langle X_i \rangle_m = 0$ in every trajectory.

Besides these two phases, we have alluded to the possible existence of another, more peculiar phase, in which the symmetry is partially broken by condensing just the charges $XIXI$ and $IXIX$. Such a condensate implies the nonvanishing EA order parameter $\Psi_{EA}^{(2)}(i) \to$ const. At the same time, the parity symmetry generated by $\hat{\Pi}_L$ remains intact, implying nonvanishing parity variance on a long subsystem $\Pi^{(2)}(A) \to$ const.

The coexistence of a nonvanishing EA order parameter with a non-decaying parity variance, allowed within the effective model, may seem paradoxical at first sight when considering the wave functions of individual trajectories. The EA order parameter must originate from trajectories m that exhibit nonvanishing $\langle X_i \rangle_m \neq 0$. The parity expectation value $\langle \hat{\pi}(A) \rangle_m$ must vanish in these symmetry breaking trajectories. Nonetheless, because we have an ensemble of trajectories, the EA order parameter and non-vanishing parity variance can coexist in separate trajectories. In theory, such a phase is established if symmetry breaking and symmetric trajectories both appear with nonvanishing probability in the ensemble. It is left as an open question if there are physical obstructions towards realizing such a coexistence phase.

Having considered area-law states which preserve the $\mathcal{S}_2$ symmetry, we now show that this is not a necessary condition for getting a phase with area-law entanglement. Specifically, consider breaking the D_4 symmetry while preserving a $\mathbb{Z}_4$ subgroup generated by the composite operator $\hat{\Pi}_1 \mathcal{C}_\ell$. This state, which we term th "composite area-law phase", can be obtained from the symmetric phase by condensing the operator $(YZXI)_j$, symmetrized over the residual $\mathbb{Z}_4$ subgroup. The key to calculate the entanglement entropy in this state is to note that the reference state is an eigenstate of $\hat{\Pi}_{1,j} = (ZZII)_j$ with eigenvalue 1. This allows to make the replacement $\langle\!\langle \mathcal{I} | \mathcal{C}_{\ell,j} = \langle\!\langle \mathcal{I} | \hat{\Pi}_{1,j} \mathcal{C}_{\ell,j}$ when calculating the subsystem purity to obtain

$$e^{-S^{(2)}(A)} = \frac{\langle\!\langle \mathcal{I} | \prod_{j \in A} \left(\hat{\Pi}_{1,j} \mathcal{C}_{\ell,j} \right) | \psi_{gs} \rangle\!\rangle}{\langle\!\langle \mathcal{I} | \psi_{gs} \rangle\!\rangle} \to \text{const.} \tag{4.36}$$

The subsystem purity tends to a constant for large L_A because the operator appearing in the matrix element creates domain walls of the unbroken $\mathbb{Z}_4$ symmetry at the two boundaries of A.

Besides area-law entanglement, the "composite phase" is also characterized by non-decaying EA correlations and subsystem parity variance. To see the former we use the fact that $\langle\!\langle \mathcal{I} |$ is an eigenstate of $(ZZII)_j$ to replace the operator $(XIXI)_j$ with $\mathrm{i}(YZXI)_j =$

$(ZZII)_j(XIXI)_j$ in the EA correlation

$$\chi_{EA}^{(2)}(i,j) = \frac{\langle\!\langle\mathcal{I}|\mathrm{i}(YZXI)_i\mathrm{i}(YZXI)_j|\psi_{gs}\rangle\!\rangle}{\langle\!\langle\mathcal{I}|\psi_{gs}\rangle\!\rangle} \to \text{const.} \tag{4.37}$$

This is non-decaying because the operator $(YZXI)_j$ overlaps with the order parameter of the state as discussed above. The parity variance is non-decaying because the symmetry $\hat{\Pi}_L = (\hat{\Pi}_1\mathcal{C}_\ell)^2$ is preserved.

We note that the residual $\mathbb{Z}_4$ symmetry enforces an exact relation between different EA correlations, which distinguishes the composite area-law phase from the coexistence phase. To see this we consider a distinct EA correlation $\chi'_{EA}(i,j) \equiv \sum_m p_m \langle X_i Y_j\rangle_m^2$. The corresponding quantity in the two-replica model can be written as $\chi_{EA}^{\prime(2)}(i,j) = \langle\!\langle\mathcal{I}|\mathrm{i}(YZXI)_i(-\mathrm{i})(XZYI)_j|\psi_{gs}\rangle\!\rangle/\langle\!\langle\mathcal{I}|\psi_{gs}\rangle\!\rangle$. Here, we replace $(YIYI)_j$ with $(-\mathrm{i})(XZYI)_j = (ZZII)_j(YIYI)_j$. In the composite phase, we have an exact relation $\chi_{EA}^{(2)} = \chi_{EA}^{\prime(2)}$ because charges $\mathrm{i}(YZXI)$ and $(-\mathrm{i})(XZYI)$ related by the conjugation of $\hat{\Pi}_1\mathcal{C}_\ell$ are condensed in the ground state with the same amplitude. However, in the coexistence phase, $\chi_{EA}^{\prime(2)}(i,j)$ and $\chi_{EA}^{(2)}(i,j)$ are both nonvanishing but generally of different values. Further reducing the $\mathbb{Z}_4^{\mathcal{C}_\ell\Pi_1}$ symmetry will give rise to volume-law phases discussed in the subsection 4.3.

SPT area-law phases

In this section, we point to the possibility of establishing *symmetry protected topological* (SPT) area-law phases protected by the effective D_4 symmetry. To identify and characterize such phases, we employ the decorated domain wall picture of Ref. [63]. Starting from the broken symmetry area-law phase, symmetry can be restored by condensing the domain walls of the symmetry $\hat{\Pi}_L$. For the ensuing phase to be distinct from the trivial symmetric phase the domain walls must condense only while bound to charges of an independent symmetry. In this case the only option is the $\mathcal{S}_2$ permutation symmetry. Note that condensing the $\mathcal{S}_2$ charges bound to a domain wall, does not lead to breaking of the $\mathcal{S}_2$ symmetry in this case because the condensed object is nonlocal. Indeed, a dual description of the same phase is a condensate of the $\mathcal{S}_2$ domain walls bound to the charges of the symmetry $\hat{\Pi}_L$. The state established in this way is a fully symmetric SPT phase, protected by the $\mathbb{Z}_2^{\Pi_L} \times \mathcal{S}_2$ symmetry. Starting from this SPT phase we can obtain another one by condensing the charges $XIXI$ and $IXIX$, which commute with the protecting symmetry. This gives the "coexistence" SPT phase.

We emphasize that the enlarged dynamical symmetry is essential for establishing these topological phases as the $\mathbb{Z}_2$ symmetry of the physical circuit does not, on its own, allow an SPT phase in a one-dimensional system. This is different from the SPT state obtained in a measurement-only model in Ref. [156], which is protected by the physical $\mathbb{Z}_2 \times \mathbb{Z}_2$ symmetry of the measurement operators.

Let us confirm that these are indeed area-law phases, by considering the boundary overlap of the operator that creates a pair of $\mathcal{S}_2$ domain walls, $\mathcal{D}_{i_\ell}$ and $\mathcal{D}_{i_r}$, at the ends of the region A

(4.35), i.e. $\langle\!\langle\mathcal{I}|\mathcal{D}_{i_\ell}\mathcal{D}_{i_r}|\psi_{gs}\rangle\!\rangle$, where $\mathcal{D}_i = \prod_{j\le i}\mathcal{C}_{\ell,j}$. Unlike in the trivial phase, the $\mathcal{S}_2$ domain walls are not individually condensed in the effective ground state. So, one might be tempted to conclude that the overlap decays exponentially, implying a volume-law state. However, the area law is saved by the fact that the reference state $\langle\!\langle\mathcal{I}|$ breaks the $\hat{\Pi}_L$ symmetry, i.e. it is a condensate of the respective charge $\mathcal{Q}_{1,j}$. This allows us to extract such charges from the condensate and write

$$e^{-S^{(2)}(A)} = \frac{\langle\!\langle\mathcal{I}|\mathcal{D}_{i_\ell}\mathcal{D}_{i_r}|\psi_{gs}\rangle\!\rangle}{\langle\!\langle\mathcal{I}|\psi_{gs}\rangle\!\rangle} \qquad (4.38)$$

$$= \frac{\langle\!\langle\mathcal{I}|(\mathcal{Q}_{1,i_\ell}\mathcal{D}_{i_\ell})(\mathcal{Q}_{1,i_r}\mathcal{D}_{i_r})|\psi_{gs}\rangle\!\rangle}{\langle\!\langle\mathcal{I}|\psi_{gs}\rangle\!\rangle} \to \text{const.}$$

In the last line, we used the fact that the $\mathcal{S}_2$ domain wall coupled to the $\hat{\Pi}_L$ charge (i.e. $\mathcal{Q}_{1,j}$) is condensed in the ground state.

Finally we note that these SPT phases cannot be distinguished from their trivial counterparts using the bulk probes discussed above. We can show that the subsystem parity variance $\Pi_A^{(2)}$ is non-decaying using the dual argument to that used for the purity. $\Pi_A^{(2)}$ is given as a boundary matrix element of the $\hat{\Pi}_L$ string operator $\prod_{j\in A}\hat{\Pi}_{L,j}$, which creates a pair of domain walls on the two ends of subsystem A. While these domain walls are not individually condensed, a bound state of a $\hat{\Pi}_L$ domain wall and an $\mathcal{S}_2$ charge is condensed. Since $\langle\!\langle\mathcal{I}|$ breaks the $\mathcal{S}_2$ symmetry, when calculating the matrix element we can always extract $\mathcal{S}_2$ charges $\langle\!\langle\mathcal{I}|$ and attach to the domain walls. This implies non-decaying subsystem parity. Note that this argument implies that the parity string is identical to the string order parameter due to the broken symmetry in the reference state. Thus string order parameters are also ruled out as diagnostics to distinguish the SPT and trivial phases.

Nor do the EA correlations able to distinguish the SPT phases from the trivial ones. The EA correlations decay exponentially in the symmetric SPT phase, as in the trivial state, because both the ground state and the reference state $\langle\!\langle\mathcal{I}|$ are symmetric under $\hat{\Pi}_1$, while the EA order parameter is odd under this symmetry. In the "coexistence" SPT phase the order parameter $(XIXI)_j$ is condensed leading to nondecaying EA correlations, as in the trivial coexistence phase.

We conclude that the SPT phases cannot be distinguished by bulk probes. In Section 4.3 we show that a different type of diagnostic, when applied to the edge of the system, allows to distinguish between the SPT and trivial phases.

Volume-law phases

Based on the criterion we developed above for establishing an area-law phase, we expect that a volume-law phase is established if the $\mathcal{S}_2$ permutation symmetry is broken along with all composite symmetries $g_\mathcal{I}\mathcal{C}_\ell$, where $g_\mathcal{I}$ is a symmetry present in the reference state $\langle\!\langle\mathcal{I}|$. One example of such composite symmetry is $\hat{\Pi}_1\mathcal{C}_\ell$.

To identify the volume-law phases, we start from the fully symmetric area-law phase with the effective D_4 symmetry and determine the possible charges that can be condensed to reduce the symmetry in a way that $\mathcal{S}_2$ and required composite symmetries are broken.

The most straightforward option to break symmetry is to condense the $\mathcal{S}_2$ charges that are neutral under the parity symmetries $\hat{\Pi}_1$ and $\hat{\Pi}_L$. This gives the symmetric volume-law phase with a residual symmetry $\mathbb{Z}_2^{\Pi_L} \times \mathbb{Z}_2^{\Pi_1}$. Due to the presence of the symmetries $\hat{\Pi}_L$ and $\hat{\Pi}_1$, the EA order and parity variances behave exactly as they do in the symmetric area-law phase.

One way to further break symmetry is to condense the pair of charges $(XXII)_j$ and $(IIXX)_j$, which are related by the local conserved parities $\mathcal{X}_j$. A second way is to condense the charges $(XIIX)_j$ and $(IXXI)_j$, similarly related by $\mathcal{X}_j$. Recall that in the area-law phase the first pair of charges was related to the second pair by the $\mathcal{S}_2$ permutation symmetry, which is broken in the volume-law phase. Thus, the phase transition, which in the area-law phase involved simultaneous condensation of all four charges, generically splits into two transitions. Which intermediate phase is established between the symmetric and the broken symmetry volume-law states depends on which pair of charges condenses first.

Yet another way to break symmetry, starting from the symmetric volume-law phase, is to condense the charges $XIXI$ and $IXIX$ to establish a third distinct intermediate phase. These three routes of breaking successive symmetries starting from $\mathbb{Z}_2^{\Pi_L} \times \mathbb{Z}_2^{\Pi_1}$ are summarized as follows

$$
\begin{aligned}
&1)\, \mathbb{Z}_2^{\Pi_L} \times \mathbb{Z}_2^{\Pi_1} && \rightarrow\ \mathbb{Z}_2^{\Pi_1} && \rightarrow\ \emptyset, \\
&2)\, \mathbb{Z}_2^{\Pi_L} \times \mathbb{Z}_2^{\Pi_1} && \rightarrow\ \mathbb{Z}_2^{\Pi_1 \Pi_L} && \rightarrow\ \emptyset, \\
&3)\, \mathbb{Z}_2^{\Pi_L} \times \mathbb{Z}_2^{\Pi_1} && \rightarrow\ \mathbb{Z}_2^{\Pi_L} && \rightarrow\ \emptyset.
\end{aligned} \tag{4.39}
$$

We note that these phases are not necessarily realized in a given model, and one may be able to make physical arguments why certain phases can be hard or even impossible to realize in the quantum circuit.

Route 1 is realized if, starting from the symmetric volume-law phase, $XXII$ and $IIXX$ are condensed first. Because this condensate breaks the $\hat{\Pi}_L$ and $\hat{\Pi}_1\hat{\Pi}_L$ symmetry, the subsystem parity variance decays exponentially in this phase. Furthermore, we cannot create the EA order parameter $XIXI$ out of any pair of condensed charges. Hence, the EA order also vanishes. We therefore term this phase the featureless volume-law phase. It is worth pointing out that this state has exactly the same symmetry breaking pattern as the maximally mixed state $|\mathcal{I}\rangle\rangle = \mathbb{1}^{\otimes 2}$. Hence, we can view this state as being smoothly connected to a conventional thermal state. From this phase, the system can go into the broken symmetry volume-law phase by condensing the charges $XIIX$ and $IXXI$.

Route 2 is realized if the charges $XIIX$ and $IXXI$ are the first to condense starting from the symmetric volume-law phase, leaving the symmetry generated by $\hat{\Pi}_1\hat{\Pi}_L$ intact. The ensuing intermediate phase exhibits both long-range EA order and nondecaying parity variance. The former is seen by writing the EA order parameter as the product $XIXI = (XXII)(IXXI)$. The first factor is condensed in $\langle\langle\mathcal{I}|$, whereas the second factor is condensed

in $|\psi_{gs}\rangle\rangle$. The latter is seen by factoring $\hat{\Pi}_L(A) = \hat{\Pi}_1(A)(\hat{\Pi}_1(A)\hat{\Pi}_L(A))$. We call this phase the volume-law coexistence phase I. The broken symmetry phase is reached from here by further condensing the charges $XXII$ and $IIXX$

Finally, route 3 is realized, starting from the symmetric volume-law phase, by condensing the charges $XIXI$ and $IXIX$. As in the area-law case, this again gives rise to coexistence of long-range EA order and nondecaying parity variance. We thus term this phase the volume-law coexistence phase II.

There is yet one more volume-law phase, obtained from the symmetric *area-law* phase by breaking the $\mathcal{S}_2$ symmetry while retaining a composite $\mathbb{Z}_2$ symmetry generated by $\mathcal{C}_\ell\hat{\Pi}_L$. This is achieved by condensing the order parameter $ZYXI$ symmetrized over the residual symmetry $\mathcal{C}_\ell\hat{\Pi}_L$ and the local symmetries. This "composite" volume-law phase, as we term it, exhibits an exponentially decaying parity variance because the ground state breaks the $\hat{\Pi}_L$ symmetry along with all the composite symmetries $g_{\mathcal{I}}\hat{\Pi}_L$. At the same time, there is a long-range EA order, which can be seen by factoring $XIXI = (YYII)\mathrm{i}(ZYXI)$. The first factor is condensed in $\langle\langle\mathcal{I}|$. The second is a component of the order parameter of this phase. Further reducing the residual symmetry leads to the broken symmetry volume-law phase.

Fisher Information as a probe of circuit states

So far we have considered equal-time properties of the output state, which translate to boundary matrix elements in the effective model. An alternative diagnostic approach, which is more natural to implement experimentally, focuses on the probability distribution of measurement outcomes obtained along the time evolution. In Ref. [18], we showed that the sensitivity of the measurement outcome distribution to changes in the initial state is a direct probe of the emergence of an encoding state. This sensitivity to initial conditions, is measured by a quantity known as the Fisher information in the distribution. The Fisher information is depressed below its maximal attainable value upon entering the volume-law phase, indicating that information about the perturbation to the initial state remains partially hidden and thus protected from the measurements. Within the effective model of random unitary circuits, the behavior of the Fisher information is a direct probe of spontaneous breaking of the $\mathcal{S}_n$ permutation symmetries established in the volume-law phases [18].

The Fisher information probe can be adapted to characterize the symmetry enriched phases of the circuit. Specifically, we consider the sensitivity of the measurement outcome distribution to a symmetry breaking perturbation of the initial state. We will show that the corresponding Fisher information allows to distinguish between different broken symmetry states and even identify SPT phases.

Let us start by giving a precise definition of the probing scheme. In the first, initialize the system in a pure state with definite parity $|\psi_0\rangle = \bigotimes_{j=1}^{L}|0\rangle$. The next step is to apply a weak parity changing perturbation at site i, $U_{\theta,i} = e^{-\mathrm{i}\theta X_i}$. Then operate the hybrid circuit on this state. We denote by $p_{\theta,m}$ the distribution of measurement outcomes resulting from the initial state perturbed by U_θ, dropping the site index i for simplicity. The Fisher information, which quantifies the sensitivity of the measurement outcome distribution to the perturbation

θ is defined as

$$F = \frac{\mathrm{d}^2}{\mathrm{d}\theta^2} D_{KL}(p_{0,m}||p_{\theta,m})\Big|_{\theta=0}. \tag{4.40}$$

D_{KL}, the Kullback-Leibler (KL) divergence, measures the distinguishability of two probability distributions $D_{KL}(p_{0,m}||p_{\theta,m}) = \sum_m p_{0,m} \log(p_{0,m}/p_{\theta,m})$. The first order derivative of D_{KL} is zero as D_{KL} is non-negative and vanishes at $\theta = 0$.

In close analogy with the von-Neumann entropy we analyze KL divergence by defining a replica sequence

$$D^{(n)} \equiv \frac{1}{1-n} \log \left(\frac{\sum_m p_{0,m} p_{\theta,m}^{n-1}}{\sum_m p_{0,m}^n} \right), \tag{4.41}$$

where D_{KL} is recovered in the replica limit $n \to 1$, i.e. $D_{KL} = \lim_{n \to 1} D^{(n)}$. The $n = 2$ replica quantity $D^{(2)}$ can be formulated in our framework as

$$\begin{aligned} D^{(2)} &= \lim_{t \to \infty} -\log \left(\frac{\langle\!\langle \mathcal{I} | e^{-tH_{\text{eff}}} \mathcal{U}_{\theta,X} | \psi_0 \rangle\!\rangle}{\langle\!\langle \mathcal{I} | e^{-tH_{\text{eff}}} | \psi_0 \rangle\!\rangle} \right) \\ &= -\log \left(\frac{\langle\!\langle \psi_{gs}^{\mathcal{I}} | \mathcal{U}_{\theta,X} | \psi_0 \rangle\!\rangle}{\langle\!\langle \psi_{gs}^{\mathcal{I}} | \psi_0 \rangle\!\rangle} \right), \end{aligned} \tag{4.42}$$

where $|\psi_0\rangle\!\rangle = \bigotimes_{j=1}^{L} |0000\rangle\!\rangle$ represents the initial state $|\psi_0\rangle$ in the duplicated Hilbert space $\mathcal{H}^{(2)}$, and $\mathcal{U}_{\theta,X} = \mathbb{1} \otimes \mathbb{1} \otimes U_{\theta,i} \otimes U_{\theta,i}^*$ is the unitary operation in $\mathcal{H}^{(2)}$ generated by the single-qubit rotation $U_{\theta,i}$ acting on one copy of the density matrix. The ground state $\langle\!\langle \psi_{gs}^{\mathcal{I}} | = \lim_{t \to \infty} \langle\!\langle \mathcal{I} | e^{-tH_{\text{eff}}}$ is obtained from long imaginary time evolution of the reference state. We distinguish this state by the superscript $\mathcal{I}$ from the ground state obtained by evolving the initial state $|\psi_0\rangle\!\rangle$. There is a subtle difference between these two states in the broken symmetry phase. Because the reference state $\langle\!\langle \mathcal{I} |$ has broken symmetries, the ground state evolved from it can break symmetries explicitly. By contrast, the state $|\psi_{gs}\rangle\!\rangle$ in the broken symmetry phase is a macroscopic superposition of the two broken-symmetry states (i.e. a cat state).

From the KL divergence, we define the n-th Fisher information as $F^{(n)} \equiv \mathrm{d}_\theta^2 D^{(n)}|_{\theta=0}$. Thus, the second Fisher information $F^{(2)}$ is given by a boundary matrix element

$$\begin{aligned} F^{(2)} \equiv \mathrm{d}_\theta^2 D^{(2)} &= 2 \frac{\langle\!\langle \psi_{gs}^{\mathcal{I}} | 1 - \mathcal{O}_{X,i} | \psi_0 \rangle\!\rangle}{\langle\!\langle \psi_{gs}^{\mathcal{I}} | \psi_0 \rangle\!\rangle} \\ &= 2 \left(1 - \frac{\langle\!\langle \psi_{gs}^{\mathcal{I}} | \widetilde{\mathcal{O}}_{X,i} | \psi_0 \rangle\!\rangle}{\langle\!\langle \psi_{gs}^{\mathcal{I}} | \psi_0 \rangle\!\rangle} \right). \end{aligned} \tag{4.43}$$

Here $\mathcal{O}_{X,i} = [(IIXX)_i + (XXII)_i]/2$ and in the last equality we claim that $\mathcal{O}_{X,i}$ can be replaced with the operator $\widetilde{\mathcal{O}}_{X,i} = [(IIXX)_i + (XXII)_i + (XIIX)_i + (IXXI)_i]/2$ without

changing the Fisher information. This is because $XIIX$ and $IXXI$ are odd under the symmetry $\hat{\Pi}_1$, whereas $\langle\!\langle\mathcal{I}|$, $|\psi_0\rangle\!\rangle$ and $\exp(-tH_{\text{eff}})$ are even. Therefore, the matrix element of these components vanishes.[3]

For convenience, we define the "order parameter"

$$\Phi^{(2)} \equiv 1 - \frac{1}{2}F^{(2)} = \frac{\langle\!\langle\psi_{gs}^{\mathcal{I}}|\widetilde{\mathcal{O}}_{X,i}|\psi_0\rangle\!\rangle}{\langle\!\langle\psi_{gs}^{\mathcal{I}}|\psi_0\rangle\!\rangle}. \tag{4.44}$$

Because $\widetilde{\mathcal{O}}_{X,i}$ is symmetric under both left and right swap, while it is odd under $\hat{\Pi}_L$, the order parameter can detect breaking of circuit symmetries that anti-commute with $XXII$ and $IIXX$, while it is insensitive to breaking of the $\mathcal{S}_2$ permutation symmetry.

It is important to note that this behavior is special to circuits with physical $\mathbb{Z}_2$ symmetry. In particular, the replacement of $\mathcal{O}_{X,i}$ with $\widetilde{\mathcal{O}}_{X,i}$ can be made only if H_{eff} inherits the Ising symmetry $\hat{\Pi}_1$ from the circuit. To define a probe that differentiates between area-law and volume-law phases as in Ref. [18], we would need to consider the Fisher information, which measures the sensitivity of the measurement outcomes to a different perturbation, which respects the circuit symmetries. Note also that the matrix element $\Phi^{(2)}$ is necessarily positive in the broken symmetry state because $\langle\!\langle\psi_{gs}^{\mathcal{I}}|$ breaks the symmetry in a definite way inherited from $\langle\!\langle\mathcal{I}|$, which is a positive weight superposition of symmetric and anti-symmetric states.

The behavior of $\Phi^{(2)}$ in the different phases is summarized in Table 4.1. From the information theoretical perspective, $\Phi^{(2)} > 0$ (i.e. Fisher information below its maximal value) means that the information about the perturbation to the initial state remains partially hidden from the measurement results.

The Fisher information can furthermore allow detection of the SPT area-law phases by directly probing edge states. Recall that the reference state $\langle\!\langle\mathcal{I}|$ provides symmetry breaking initial conditions to the imaginary time evolution $\langle\!\langle\mathcal{I}|e^{-tH_{\text{eff}}} \to \langle\!\langle\psi_{gs}^{\mathcal{I}}|$. In the SPT phase, the broken symmetry can propagate to infinite time by coupling to the edge zero mode. This implies the order parameter has a spatial dependence, and $\Phi_i^{(2)} > 0$ for i near the edge, but decaying exponentially into the bulk of the qubit chain. It is also possible to probe the broken permutation symmetry at the edge of the SPT phase by measuring the Fisher information associated with a perturbation that respects the physical circuit symmetry.

Crucially, this detection scheme for the edge modes of the SPT phase is efficient and scalable in the sense that the number of repetitions of the experiment needed to gather enough data does not grow with the system size. Since we are probing a gapped state with a finite correlation length ξ in space and time, the natural expectation is that it is enough to produce the Fisher information from a partial measurement record including only a finite space-time bubble of radius $r \gg \xi$ away from the perturbation. Indeed, within the effective theory, discarding measurement results creates a bulk field that breaks the $\mathcal{S}_2$ symmetry in the discarded region outside of the bubble [18]. The effect of these symmetry breaking

---

[3]Note that even if the ground state spontaneously breaks the $\hat{\Pi}_1$ symmetry, it manifests in $\langle\!\langle\psi_{gs}^{\mathcal{I}}|$ through emergence of a cat state because the reference state is symmetric under $\hat{\Pi}_1$.
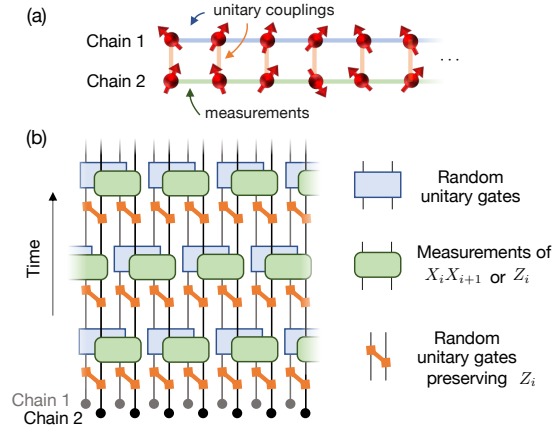
Figure 4.2: (a) Two chain model investigated numerically. Internal dynamics of chain-1 is generated by purely unitary two-qubit gates, while that of chain-2 by pure projective measurements (of Z_i or $X_i X_{i+1}$). The two chains are coupled by random unitary gates applied with probability q. All gates and measurements commute with the $\mathbb{Z}_2$-parity symmetry of chain 2. (b) Circuit diagram for the model. Every time step consists of three types of operations: two-qubit unitary gates within chain-1 (blue boxes) are randomly drawn from the Clifford group; measurements in $X_i X_{i+1}$- or Z_i-basis are performed on chain-2 (green boxes with rounded corners) with the probabilities r and $1-r$, respectively; and the inter-chain gates (orange bonds) are randomly drawn from the Clifford elements preserving Z_i on the chain-2 and applied to the circuit with the probability q.

conditions on the perturbed site in the bubble decays exponentially with r/ξ, leading to a correspondingly small effect on the Fisher information. Thus, the required number of repetitions is expected to scale as e^ξ, allowing an efficient detection.

Numerical demonstration of transitions between volume-law phases

Having classified the possible phases of quantum circuits enriched by the physical $\mathbb{Z}_2$ circuit symmetry, we now demonstrate that parts of this phase structure is realized in a concrete circuit model illustrated in Fig. 4.2. We simulate the circuit directly without relying on replica tricks. The results therefore give further confidence that the effect of the enlarged dynamical symmetry persists to the physical replica limit $n \to 1$.

Our model consists of two coupled L-qubit chains in a ladder geometry, undergoing a hybrid dynamics that consists of unitary gates and projective measurements. We restrict the set of unitary gates to the elements of the two-qubit Clifford group, which allows efficient simulation of large systems [1]. This restriction should not affect any qualitative features of our analysis as Clifford gates are statistically indistinguishable from Haar random unitary gates up to third moments, i.e. Clifford group forms unitary 3-design [264].
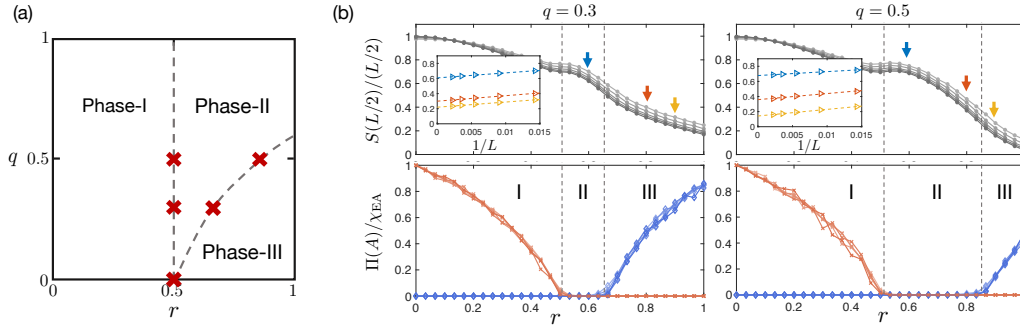
Figure 4.3: (a) Phase diagram of the two chain model. q is the inter-chain coupling. r is the probability of measuring $X_i X_{i+1}$ on chain 2 (versus $1 - r$ of measuring Z_i). The red crosses indicate phase boundaries extracted from the numerics. All three phases exhibit volume-law entanglement. (b) Numerical simulation results. Top panels: Half-chain entanglement entropy normalized by volume. Insets: system size dependence of the entanglement entropy density at points $r = 0.6, 0.8, 0.9$ (indicated by arrows) indicates convergence to a non-vanishing value as $L \to \infty$. Bottom: Behavior of the Edwards-Anderson correlation function $\chi_{EA}(L/2)$ (blue diamonds) and parity variance $\Pi(A = L/2)$ (red crosses) as a function of r for two values of q. The nearly overlapping lines correspond to different system sizes $L = 70, 110, 180, 280, 450$.

The circuit dynamics can be summarised as follows. First, all unitary gates and measurements respect the global $\mathbb{Z}_2$ symmetry generated by $\hat{\pi} = \prod_j Z_j$, where Z_j are the Pauli-Z operators acting on the qubit at site j in chain-2. Thus, the qubits of chain-1 are neutral with respect to the $\mathbb{Z}_2$ symmetry. The time evolution internal to chain-1 is generated purely by unitary gates, which are unrestricted by symmetry. The time evolution internal to chain-2 is generated purely by measurements: with probability r a pair of qubits at sites j and $j + 1$ are measured in the $X_j X_{j+1}$-basis or, with probability $1 - r$ the qubit at site j is measured in the Z_j-basis. These measurements are denoted by the green boxes in the figure. Finally, a coupling between the two chains is implemented by two-qubit unitary gates on the rungs of the ladder, applied with probability q per gate at each time step. These gates, represented by orange rungs in Fig. 4.2, are drawn uniformly from one of the 384 elements in the Clifford group that commute with Z_j in the chain-2. Thus, the parameter q controls the unitary coupling strength between two chains, and r tunes the ratio between different kinds of measurements on chain-2. The system is initialized in the state $|\psi_0\rangle = |0\rangle^{\otimes 2L}$, and we are interested in its steady-state properties.

We can easily understand the steady-state behavior of our model in the decoupled chains limit $q = 0$. In this case, chain-1 evolves as a random unitary circuit, in which the entanglement entropy of any subsystem grows linearly until it saturates to its maximum [186, 140]. In contrast, chain-2 undergoes measurement-only dynamics. Numerical simulations and analytical arguments in Ref. [224] have shown that this leads to two area-law phases

separated by a phase transition at $r_c = 1/2$. For $r < r_c$, chain-2 is in the symmetric area-law phase characterized by nondecaying parity variance and exponentially decaying EA correlations. Chain-2 with $r > r_c$ realizes the broken symmetry area-law phase with long-range EA correlations and exponentially decaying parity variance.

When the two decoupled chains are considered as a single system, they trivially realize a volume-law entanglement scaling (due to chain-1), which undergoes $\mathbb{Z}_2$ symmetry breaking phase transition (due to chain-2) at $r = r_c$. Within our formalism these two volume-law phases are represented by gapped ground states of an effective Hamiltonian. Thus, they are expected to be robust to (at least) weak coupling between the chains.[4] Furthermore, we can use the symmetry analysis of Section 4.3 to predict which phases would be realized.

Since chain-1 has broken $\mathcal{S}_2$ symmetry, its leading effect at weak coupling $q \ll 1$ is to exert an effective $\mathcal{S}_2$-symmetry breaking field on chain-2, which does not affect the properites associated with the parity symmetry. Thus, from the symmetry perspective the state established for $r < r_c$ at an infinitesimal coupling is identical to the symmetric volume-law phase (row 5 in Table 4.1). Similarly, the state established for $r > r_c$ at an infinitesimal coupling is identical to the broken symmetry volume-law phase (row 9 in Table 4.1).

Finally, coupling to the symmetry breaking field produced by chain-1 is relevant at the critical point separating the two area-law phases of chain-2. As discussed in subsection 4.3, the critical point at $q = 0$ is characterized by condensation of the charges $\mathcal{Q}_1 = XXII$ and $\mathcal{Q}_2 = IIXX$ together with $\mathcal{Q}'_1 = IXXI$ and $\mathcal{Q}'_2 = XIIX$. Because the two pairs of charges are connected by the $\mathcal{S}_2$ symmetries, they must condense together when these symmetries are present. However, once we turn on the field breaking the $\mathcal{S}_2$ symmetries, the critical point will generically split into two critical points, one involving condensation $\mathcal{Q}_1$ and $\mathcal{Q}_2$ and the other involving condensation of $\mathcal{Q}'_1$ and $\mathcal{Q}'_2$. This gives rise to an intermediate phase in which only one of the two pairs of charges is condensed (the featureless phase in row 6 or the coexistence phase I in row 7 of Table 4.1). Which intermediate phase is realized depends on the charges that acquire a lower energy, which in turn may depend on the details of the model.

The persistence of the two distinct volume-law phases and the emergence of an intermediate phase between them in the coupled-chain model are nontrivial predictions of the effective theory, which we now turn to test numerically. To this end, we simulate the time evolution of systems with length $L \leq 450$. We evaluate $\Pi(A)$, χ_{EA}, and the volume-normalized half-system entanglement entropy, $S(L/2)/(L/2)$ averaged over ~ 500 random circuit realizations. To focus on the long-range and late-time behaviors, we use $i_\ell \approx L/3$ and $i_r \approx 2L/3$ for evaluating $\chi_{EA}(i_\ell, i_r)$ and $\Pi(A)$ (as the left and right edges of A) and we evaluate all quantities at time $T \approx 3L$.[5]

---

[4]By the same token, the phases are also robust to any other small perturbation to the circuit, which respects the symmetry.

[5]More precisely, we choose $T = 3L + 1 - a$ with $a = 0$ or $a = 1$ depending on whether L or $L + 2$ is a multiple of 4, respectively. We always choose even L. This choice is introduced in order to avoid artifacts associated the gates acting across the half-chain boundaries at the very last time step. We did similar regularizations for the choice of i and j for $\Pi(A)$ and χ_{EA}.

The results of our numerical simulations are summarized in Fig. 4.3. For the decoupled chains ($q = 0$), we find, as expected, a single phase transition tuned by the ratio r of bond to site measurements. Upon increasing the inter-chain coupling to $q = 0.3$ and $q = 0.5$, we observe a splitting into two critical points and emergence of an intermediate phase. As seen in the bottom of panel (b), the intermediate phase is characterized by vanishing of both the the EA correlations and the parity variance, consistent with the featureless phase in row 6 of Table 4.1. Physically, this may be interpreted as a result of the unitary inter-chain coupling countering the effect of the $X_i X_{i+1}$ measurements, favoring the state without long-range order. We see that for sufficiently large q there is no broken symmetry state for any value of r. At the same time, the unitary coupling q involving a single-site Z_i operator on chain 2 commutes with the sub-system parity. Therefore introducing this coupling does not change the point at which non-decaying sub-system parity variance is established. It would be interesting to check if coupling the chains by various measurements that preserve the $\mathbb{Z}_2$ symmetry instead of unitary gates could favor a volume-law coexistence state (row 7 in Table 4.1) as the intermediate phase.

The top panels of Fig. 4.3(b) confirm that all the observed phases are indeed characterized by volume-law scaling of the entanglement entropy. For large values of r, we observe a slow drift of the entropy-density $S(L/2)/(L/2)$ as a function of system sizes [inset of Fig. 4.3(b)]. We attribute this drift to the additive contribution S_0 of chain-2 to $S(L/2)$. Indeed, plotted as a function of $1/L$, the entanglement entropy density shows a clear linear dependence, $S(L/2)/(L/2) = 2S_0/L + s$ with a finite entropy density $s > 0$ in the limit $L \to \infty$ (the dotted lines in the inset).

The establishment of long-range order in a one-dimensional system with extensive entropy, may appear, at first sight, contradictory to theorems prohibiting such order at any non-vanishing temperature. But, this is not a thermal system.

As we mentioned above, an appropriate description of the volume-law phase at weak coupling ($q \ll 1$) is to replace chain-1 by an effective field that breaks the $\mathcal{S}_2$ permutation symmetries. In the physical circuit, this corresponds to coupling chain-2 to an effective infinite temperature bath in place of chain-1. We are then interested in the trajectories of the mixed state in chain-2, connected by coupling q to an infinite temperature bath and subject to local measurements. For each individual trajectory, the measurements act as couplings to zero temperature bath, wherein the measurement projection collapse the local wave function into a definite quantum state with zero entropy. Because of this coupling to two very different baths, each trajectory is very far from being in thermal equilibrium and establishment of long-range order is not prohibited.

One of the nontrivial results of this section is that measurements can facilitate the establishment of quantum order in one dimension, even in states with volume-law entanglement entropy. We may further argue that this protection extends also to topological order and edge states. To this end, we note that our model can be also interpreted as the system of Majorana fermions on chain-2 via Jordan-Wigner transformation. On-site Z measurements map to measurement of the Majorana parity $i\gamma_{2i-1}\gamma_{2i}$ on odd bonds, whereas the XX measurements map to measurements of parity on even bonds $i\gamma_{2i}\gamma_{2i+1}$. Chain-1 is coupled to chain-2 with

unitary coupling q to the Majorana bond parities. The broken symmetry volume-law phase of the qubit system (phase III in Fig. 4.3) translates to a topological volume-law state with free Majorana edge modes. The symmetric volume-law phase (phase I in Fig. 4.3) translates to a volume-law phase which is distinct from a thermal state by having subsystem fermion-parity variance that is nondecaying with subsystem size. Finally, phase II in Fig. 4.3 is smoothly connected to the conventional thermal phase of the Majorana system, where there is no long-range correlation and the fermion parity of a subsystem fluctuates.

4.4 Gaussian fermionic circuits

We turn to investigate hybrid quantum circuits that operate on fermionic degrees of freedom rather than on qubits. Specifically we consider quadratic gates and measurements that preserve the Gaussianity of the fermionic wave function. Such circuits cannot sustain a volume-law state for any finite rate of measurements [55, 87]. However, recent numerical work indicated that a critical phase with entanglement that scales as $\log(L)$ is established at low measurement rates [8, 225].

Here, we provide a simple description of this critical phase using the framework developed in Section 4.2 to map the dynamics to an effective ground state problem. While we describe the general structure of the theory for any number of replicas n, we carry out a more detailed study only of the case of $n = 2$. This theory predicts a measurement-induced Kosterlitz-Thouless (KT) transition from the critical phase into two area-law phases, which are distinguished by the sign of the vortex fugacity. These are identified as a trivial and a topological area-law phase. We map pertinent properties of the circuit dynamics to universal boundary operators in this theory, thus facilitating a detailed comparison to exact numerical simulations of the circuit. The numerical results, obtained for systems of size $L \leq 160$, are consistent with a KT transition.

Before proceeding we note that the two area-law phases, a topological and a trivial phase have been previously discussed in the context of measurement only models [182, 154]. Furthermore, Sang et al. [225] argued that adding a specific set of gates to the measurement only model, allows a mapping to the completely packed loop model with crossings [184], which also hosts a critical state known as the Goldstone phase. We comment on the connections of our results to these loop model predictions at the end of the section.

Model

The general structure of the circuits we consider here is shown in Fig. 4.4. Circuit elements are operating on a one-dimensional chain of Majorana modes γ_{2j-1} and γ_{2j}. We view such pairs of "Majorana sites" $(2j-1, 2j)$ as making up a single "physical site" j, hosting a single complex fermion $f_j = (\gamma_{2j-1} + \mathrm{i}\gamma_{2j})/2$ on site j. For simplicity, we take the initial state to be the vacuum of all fermionic modes, i.e. $f_j|\mathrm{vac}\rangle_f = 0 \;\; \forall j$.
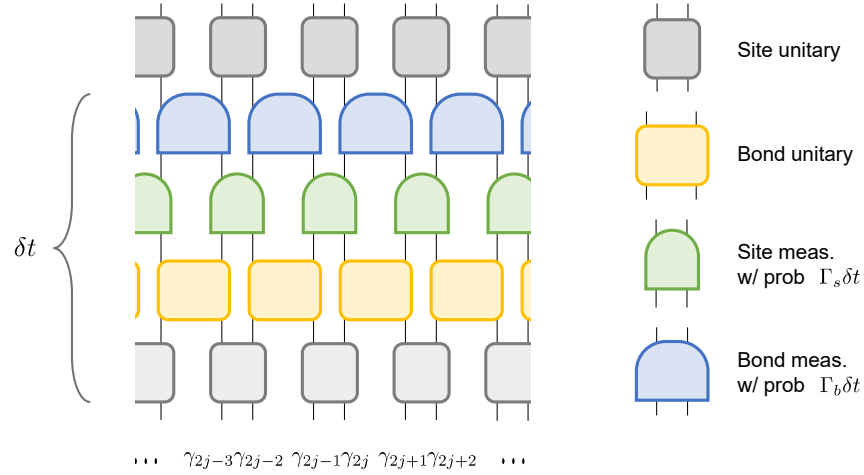
Figure 4.4: Gaussian fermionic circuit. Each time step δt consists of sequential application of one layer of site unitary gates, bond unitary gates, site measurements, and bond measurements. The quadratic site and bond parity measurements are applied with probabilities $\Gamma_s \delta t$ and $\Gamma_b \delta t$ respectively.

The unitary elements of the circuit are generic Gaussian gates operating on the nearest neighbor Majorana pairs

$$U_{s,j} = e^{\theta_{s,j}\gamma_{2j-1}\gamma_{2j}}, \quad U_{b,j} = e^{\theta_{b,j}\gamma_{2j}\gamma_{2j+1}}. \tag{4.45}$$

We call $U_{s,j}$ the site unitary and $U_{b,j}$ the bond unitary as they operate on physical sites and bonds, respectively. These gates are depicted as gray and yellow boxes in Figure 4.4.

Similar to the qubit circuits discussed in the previous section, drawing the couplings $\theta_{s,j}$ and $\theta_{b,j}$ from symmetric distributions ensures a mapping to imaginary time evolution with an effective Hermitian Hamiltonian. Here, we shall draw the bond coupling $\theta_{b,j}$ from a Gaussian distribution $N(0, \sigma_J^2)$ with zero mean and variance σ_J^2, while the site coupling $\theta_{s,j}$ is taken from a uniform distribution over $[0, 2\pi)$. We note that this specific choice of the distributions is made to simplify the exact mapping and the resulting effective Hamiltonian, and it is not crucial for our general discussion in this section.

After each layer of unitary gates in the circuit, measurements are made on a certain fraction of the fermion parity operators defined on sites and bonds:

$$\hat{\pi}_{s,j} = -\mathrm{i}\gamma_{2j-1}\gamma_{2j}, \quad \hat{\pi}_{b,j} = -\mathrm{i}\gamma_{2j}\gamma_{2j+1}. \tag{4.46}$$

Measurements of the site parity are performed with a probability p_s at each time step and those of bond parity with probability p_b. Upon the measurement of $\hat{\pi}_{a,j}$ with $a \in \{s, b\}$, the quantum state evolves according to the Born rules: projection onto a definite parity eigenstate $P_\pm|\Psi\rangle/\sqrt{\langle\Psi|P_\pm|\Psi\rangle}$ with probability $\langle\Psi|P_\pm|\Psi\rangle$, where $P_\pm = (1 \pm \hat{\pi}_{a,j})/2$.

We investigate the quantum state at the output of this circuit after a long time evolution of $N_T \gg 1$ steps. As before, we are interested in quantities that are nonlinear in the system density matrix, such as the entanglement entropy of a subsystem A or the variance of fermion parities taken over the ensemble of trajectories:

$$\Pi_{a,A} \equiv \overline{\sum_m p_m \Big\langle \prod_{j \in A} \hat{\pi}_{a,j} \Big\rangle_m^2}. \tag{4.47}$$

The sum is over different trajectories (runs of the circuit) characterized by a specific set of measurement outcomes m and the angled brackets represent a quantum expectation value in the output state of that trajectory.

Enlarged Symmetry

The entanglement entropy and other quantities that depend on high moments of observables can be derived from the average replicated density matrix $|\tilde{\rho}^{(n)}\rangle\rangle$. Thus, it is important to identify the symmetry of the dynamics of n replicas, which will allow us to classify distinct steady state phases. Due to the special structure of Gaussian fermionic circuits, this symmetry is different from the dynamical symmetry identified for the qubit circuits in Section 4.2.

To facilitate the analysis, we introduce second quantized operators acting in the duplicated Fock space. The Majorana operators γ_j acting on the wave-function of the physical circuit are extended to $\gamma_{j,\alpha\sigma}$, where $\alpha \in \{1, 2, \ldots, n\}$ indicates the replica on which this Majorana operates and $\sigma \in \{\uparrow, \downarrow\}$ indicates forward and backward branch of the evolution, respectively. Note that the mapping from tensor product operators, such as $\gamma_j \otimes \mathbb{1} \otimes \mathbb{1} \otimes \mathbb{1}$ or $\mathbb{1} \otimes \gamma_j \otimes \mathbb{1} \otimes \mathbb{1}$ to the second quantized operators in the duplicated Hilbert space requires extra phase factors to ensure anti-commutation relations between all fermionic operators. The precise mapping is given in Appendix C.5.

The evolution of the replicated density matrix in a single time step of the fermionic circuit in Fig. 4.4 is given by

$$|\tilde{\rho}^{(n)}(t + \delta t)\rangle\rangle = \mathcal{M}_b^{(n)} \mathcal{M}_s^{(n)} \mathcal{U}_b^{(n)} \mathcal{U}_s^{(n)} |\tilde{\rho}^{(n)}(t)\rangle\rangle. \tag{4.48}$$

As discussed in Section 4.2, $\mathcal{M}_{s/b}^{(n)}$ is a linear operation on the unnormalized quantum state $|\tilde{\rho}^{(n)}\rangle\rangle$ generated by a layer of site/bond measurements performed with probabilities $p_{s/b}$.

We first focus on the the dynamical symmetry in the case of pure unitary evolution, i.e. when $p_s = p_b = 0$. The generators of the unitary time steps take the form of decoupled quadratic Majorana Hamiltonians in the duplicated Fock space:

$$h_s^{(n)} = \sum_{\alpha=1}^n \sum_{j=1}^L i\theta_{s,j} \left(\gamma_{2j-1,\alpha\uparrow}\gamma_{2j,\alpha\uparrow} - \gamma_{2j-1,\alpha\downarrow}\gamma_{2j,\alpha\downarrow} \right),$$

$$h_b^{(n)} = \sum_{\alpha=1}^n \sum_{j=1}^L i\theta_{b,j} \left(\gamma_{2j,\alpha\uparrow}\gamma_{2j+1,\alpha\uparrow} - \gamma_{2j,\alpha\downarrow}\gamma_{2j+1,\alpha\downarrow} \right). \tag{4.49}$$

Using the Majorana operators of the $2n$ chains, it is natural to construct a local $so(2n)$ algebra on every Majorana site ℓ, generated by $\Gamma_\ell^{\alpha\sigma,\beta\sigma'} = \frac{i}{4}[\gamma_{\ell,\alpha\sigma}, \gamma_{\ell,\beta\sigma'}]$. From these local objects, we construct a global $so(2n)$ algebra with elements

$$\Gamma^{\alpha\sigma,\beta\sigma'} = \sum_{j=1}^{L} \left(\sigma\sigma'\Gamma_{2j-1}^{\alpha\sigma,\beta\sigma'} + \Gamma_{2j}^{\alpha\sigma,\beta\sigma'} \right), \tag{4.50}$$

which commute with the generators (4.49) of the unitary dynamics. Note that here and below $\sigma = \uparrow$ ($\sigma = \downarrow$) is identified with $\sigma = +1$ ($\sigma = -1$).

The Γ matrices generate proper rotations among the $2n$ species of Majorana fermions. In addition we have the single-branch fermion parity symmetries $\hat{\Pi}_{\alpha,\sigma} = \prod_{j=1}^{L} i\gamma_{2j-1,\alpha,\sigma}\gamma_{2j,\alpha,\sigma}$, which constitute improper rotations, e.g. $\hat{\Pi}_{1,\uparrow}$ that maps $\gamma_{j,1,\uparrow} \mapsto -\gamma_{j,1,\uparrow}$. Thus, altogether the purely unitary dynamics on n copies have an $O(2n)$ symmetry.

In addition, the Hamiltonian admits a fermionic time-reversal symmetry $\mathbb{T}$, under which $\mathbb{T}\gamma_{\alpha,\uparrow}\mathbb{T}^{-1} = \gamma_{\alpha,\downarrow}$, $\mathbb{T}\gamma_{\alpha,\downarrow}\mathbb{T}^{-1} = -\gamma_{\alpha,\uparrow}$, and $\mathbb{T} i \mathbb{T}^{-1} = -i$. We conclude that the unitary dynamics exhibits the symmetry $O(2n) \rtimes \mathbb{Z}_2^{\mathbb{T}}$. Note that the effective time-reversal symmetry is not exactly the Hermiticity symmetry, which appears as a nonlocal transformation in the fermionic duplicated Hilbert space (see Appendix C.5).

Adding measurements reduces the symmetry. Only the subset of the generators (4.50) having $\sigma = \sigma'$ commute with the measurement operators. These generators, supported only on either the forward or the backward branches, form a $so(n) \oplus so(n)$ algebra and give rise to a $O(n) \times O(n)$ symmetry. Together with fermionic time reversal, the symmetry of the n-copy unitary evolution with measurements is $[O(n) \times O(n)] \rtimes \mathbb{Z}_2^{\mathbb{T}}$.

It is worth pointing out that the dynamical symmetry of the pure unitary evolution is the same as the static symmetry in the case of free fermions in the symplectic class AII [222, 93]. Moreover, the addition of measurements here breaks the $O(2n)$ symmetry in the same way as adding a non-Hermitian quadratic coupling does in the free fermion problem. There is, however, an important difference in taking the replica limit, which in our case is $n \to 1$, whereas it is $n \to 0$ for the disordered fermion ground state problem.

We note on passing that a measurement-only model (i.e. no unitary gates) also has an enlarged dynamical symmetry $O(2n) \rtimes \mathbb{Z}_2^{\mathbb{T}}$ like the purely unitary model. In this case, the $O(2n)$ symmetry generators are given as simple zero momentum sums of the local generators. That is, the first term in Eq. (4.50) does not have an additional sign $\sigma\sigma'$.

Similar to the case of the qubit circuits considered in Section 4.3, the effective global symmetry is reduced when we account for the presence of local integrals of motion. Specifically, the fermion gates and measurements commute with all the local operators $\mathcal{R}_\ell = \prod_{\alpha=1}^{n} i\gamma_{\ell,\alpha\uparrow}\gamma_{\ell,\alpha\downarrow}$ that measure the total parity of fermions from all species at Majorana site ℓ (see Appendix C.1). Thus $|\tilde{\rho}^{(n)}\rangle\rangle$ evolves to a ground state of H_{eff} with definite eigenvalues of $\mathcal{R}_\ell$. Such a state necessarily breaks the single branch parity symmetries that anti-commute with the $\mathcal{R}_\ell$.

Having removed the improper rotations generated by the single-branch parities, we are left with the effective symmetry $SO(2n) \rtimes \mathbb{Z}_2^{\mathbb{T}}$ for the purely unitary circuit. With measurements,

the effective symmetry is reduced to $\mathcal{G}_{f,\text{eff}}^{(n)} \equiv (SO(n) \times SO(n)) \rtimes (\mathbb{Z}_2 \times \mathbb{Z}_2^{\mathbb{T}})$, where the first $\mathbb{Z}_2$ is generated by fermion parity in both the forward and backward branch of the first copy, i.e. $\hat{\Pi}_1 = \hat{\Pi}_{1\uparrow}\hat{\Pi}_{1\downarrow}$. Finally, we note that the global symmetry $\prod_{\alpha=1}^{n} \hat{\Pi}_\alpha = \prod_\ell \mathcal{R}_\ell$, which is part of $\mathcal{G}_{f,\text{eff}}^{(n)}$, cannot be broken because it is a product of local integrals of motion.

We now elaborate on how this scheme applies to the case of two replicas. The dynamical $O(2) \times O(2)$ symmetry in presence of measurements, implies two conserved $U(1)$ charges, which we can write as the total occupation numbers of complex fermion modes

$$N_\sigma = \sum_{j=1}^{L} N_{\sigma,j} = \sum_{j=1}^{L} c_{2j-1,\sigma}^\dagger c_{2j-1,\sigma} + c_{2j,\sigma}^\dagger c_{2j,\sigma}, \tag{4.51}$$

The complex fermions are not local to a single copy of the system and are rather defined as superpositions of Majorana modes on the two copies:

$$c_{2j-1,\uparrow} = \frac{\gamma_{2j-1,1\uparrow} + i\gamma_{2j-1,2\uparrow}}{2}, c_{2j,\uparrow} = \frac{\gamma_{2j,2\uparrow} - i\gamma_{2j,1\uparrow}}{2},$$
$$c_{2j-1,\downarrow} = \frac{\gamma_{2j-1,1\downarrow} - i\gamma_{2j-1,2\downarrow}}{2}, c_{2j,\downarrow} = \frac{\gamma_{2j,2\downarrow} + i\gamma_{2j,1\downarrow}}{2}. \tag{4.52}$$

The $U(1)$ symmetries are supplemented by the single branch $\mathbb{Z}_2$ parity symmetries to give the two copies of $O(2) = U(1) \rtimes \mathbb{Z}_2$. These parity transformations act on the two conserved fermion species independently as particle-hole transformations, namely $c_{j,\sigma} \mapsto (-1)^j c_{j,\sigma}^\dagger$. Together with the time-reversal we have the full symmetry $\mathcal{G}_f^{(2)} \equiv [O(2) \times O(2)] \rtimes \mathbb{Z}_2^{\mathbb{T}}$.

For purely unitary dynamics, the symmetry is enlarged to $O(4) \rtimes \mathbb{Z}_2^{\mathbb{T}} = (SO(4) \rtimes \mathbb{Z}_2) \rtimes \mathbb{Z}_2^{\mathbb{T}}$. The $SO(4)$ symmetry has a useful and intuitive representation in terms of two $SU(2)$ symmetries, which stems from the isomorphism $SO(4) \cong [SU(2) \times SU(2)]/\mathbb{Z}_2$. One of the $SU(2)$ symmetries is associated with rotations between the forward and backward branches, labeled as up and down spins. We call this the Σ spin symmetry. The other $SU(2)$ symmetry is a charge "η-symmetry" [276]. The respective generators of the spin and charge symmetries can be written explicitly as

$$\Sigma_j^+ \equiv c_{2j-1,\uparrow}^\dagger c_{2j-1,\downarrow} + c_{2j,\uparrow}^\dagger c_{2j,\downarrow}, \tag{4.53a}$$

$$\Sigma_j^- \equiv \left(\Sigma_j^+\right)^\dagger, \tag{4.53b}$$

$$\Sigma_j^z \equiv \frac{1}{2} \sum_\sigma \sigma \left(c_{2j-1,\sigma}^\dagger c_{2j-1,\sigma} + c_{2j,\sigma}^\dagger c_{2j,\sigma}\right), \tag{4.53c}$$

$$\eta_j^+ \equiv -c_{2j-1,\uparrow}^\dagger c_{2j-1,\downarrow}^\dagger + c_{2j,\uparrow}^\dagger c_{2j,\downarrow}^\dagger, \tag{4.53d}$$

$$\eta_j^- \equiv \left(\eta_j^+\right)^\dagger, \tag{4.53e}$$

$$\eta_j^z \equiv \frac{1}{2} \sum_\sigma \left(c_{2j-1,\sigma}^\dagger c_{2j-1,\sigma} + c_{2j,\sigma}^\dagger c_{2j,\sigma} - 1\right). \tag{4.53f}$$

Here, the ladder operators $\Sigma_j^\pm = \Sigma_j^x \pm i\Sigma_j^y$ and $\eta_j^\pm = \eta_j^x \pm i\eta_j^y$. The $SU(2) \times SU(2)$ is quotient by $\mathbb{Z}_2$ because the total η and Σ spins must add to an integer spin representation to give the

required $SO(4)$ symmetry. Finally, the $SO(4)$ symmetry is supplemented by the time-reversal symmetry and the single branch parity symmetry to complete the full $O(4) \rtimes \mathbb{Z}_2^{\mathbb{T}}$ symmetry.

When acting on the spin and η-operators, the single-branch fermion parity transformation exchanges two sets of $SU(2)$ generators, i.e. $\Sigma_j^{\pm,z} \mapsto \eta_j^{\pm,z}$ and $\eta_j^{\pm,z} \mapsto \Sigma_j^{\pm,z}$, and the time reversal flips the sign of spin operators, while keeping charge η-operators invariant, i.e. $\mathbb{T}\Sigma_j^{\pm,z}\mathbb{T}^{-1} = -\Sigma_j^{\pm,z}$ and $\mathbb{T}\eta_j^{\pm,z}\mathbb{T}^{-1} = \eta_j^{\pm,z}$.

As explained above, the ground state of the effective Hamiltonian must break the single-branch symmetries and thus exhibits a reduced effective symmetry. For purely unitary dynamics, the full symmetry $O(4) \rtimes \mathbb{Z}_2^{\mathbb{T}}$ is thus reduced to $SO(4) \rtimes \mathbb{Z}_2^{\mathbb{T}}$. With measurements, the reduced symmetry is $\mathcal{G}_{f,\text{eff}}^{(2)} \equiv (U(1) \times U(1)) \rtimes (\mathbb{Z}_2 \times \mathbb{Z}_2^{\mathbb{T}})$. Here the first $\mathbb{Z}_2$ is generated by the particle-hole transformation $\mathbb{P}$ for both conserved fermion species, which maps $\mathbb{P}\eta_j^{\pm,z}\mathbb{P}^{-1} \mapsto -\eta_j^{\mp,z}$ and $\mathbb{P}\Sigma_j^{\pm,z}\mathbb{P}^{-1} \mapsto -\Sigma_j^{\mp,z}$.

Effective 1D quantum Hamiltonian

We now carry out the program developed in Section 4.2 to map the dynamics of the averaged replicated density matrix $|\tilde{\rho}^{(2)}\rangle\rangle$ to effective imaginary time evolution with a one-dimensional quantum Hamiltonian. Almost everything proceeds exactly as detailed in Section 4.2 for qubit circuits. Here we elaborate on distinct features in our fermionic model related to the enlarged dynamical symmetry.

As a first step in the program, we consider averaging over probabilistic measurements and bond unitary gates. The site unitary gates, designed in this model to project onto a reduced Hilbert space, will be considered later. It is straightforward to integrate over the Gaussian distribution of the bond coupling $\theta_{b,j}$ to obtain the averaged bond unitary acting on the doubled density matrix

$$\mathcal{U}_{b,j} = \exp\left[-\frac{J_b \delta t}{2}\left(\sum_{\alpha,\sigma} \sigma\, \mathrm{i}\gamma_{2j,\alpha\sigma}\gamma_{2j+1,\alpha\sigma}\right)^2\right], \tag{4.54}$$

where we have denoted the variance $\overline{\theta_{b,j}^2} \equiv J_b \delta t$. The averaged measurement in the duplicated Hilbert space takes the form

$$\mathcal{M}_{a,j} = (1 - \Gamma_a \delta t) + \Gamma_a \delta t \sum_{m=\pm} P_{a,j,m}^{\otimes 4}, \tag{4.55}$$

where $a \in \{s, b\}$ indicates the site and bond measurements implemented by the projections $P_{s,j,\pm} = (1 \pm \hat{\pi}_{s,j})/2$ and $P_{b,j,\pm} = (1 \pm \hat{\pi}_{b,j})/2$ on measurement outcomes $m = \pm$. Γ_a is the measurement rate so that the measurement probability in a time step is $p_a = \Gamma_a \delta t$. Crucially, the evolution operators $\mathcal{U}_{b,j}$ and $\mathcal{M}_{a,j}$ are both Hermitian. Thus in the limit $\delta t \to 0$ they describe imaginary time evolution over an infinitesimal time step, generated by an effective quantum Hamiltonian $H_{\text{eff}} = H_{\mathcal{U}} + H_{\mathcal{M}}$.

We could have also included site unitary gates

$$\mathcal{U}_{s,j} = \overline{\exp\left[\sum_{\alpha,\sigma} \theta_{s,j}\sigma \mathrm{i}\gamma_{2j-1,\alpha\sigma}\gamma_{2j,\alpha\sigma}\right]} \tag{4.56}$$

on the same footing in this program, averaging over $\theta_{s,j}$ drawn from a Gaussian distribution of coupling constants. This would result in a complete effective Hamiltonian written in terms of the Majorana operators on the four chains. However, to obtain a simpler effective model without changing the essential structure and symmetries of the problem, we choose the site coupling constants $\theta_{s,j}$ to be uniformly distributed on $[0, 2\pi)$. In this case, exactly as in Section 4.2, averaging over the site unitaries implements a projection on a six-dimensional local Hilbert space on physical sites (i.e. Majorana sites $2j-1, 2j$). However, in the fermionic system, it is advantageous to use a different basis of the reduced Hilbert space, which makes use of the fermionic symmetries.

We recall the above observation that unitary gates, including the single-site gates, commute with generators of the $SU(2)$ spin (Σ) and $SU(2)$ charge (η) symmetry. Therefore, the basis of the projected Hilbert space can be organized into multiplets of the Σ and η spins on each physical site j. Three of the basis states $|m\rangle\!\rangle_\eta$ with $m = \pm 1, 0$ form the η triplet which transform as the Σ singlet. The other three states $|m\rangle\!\rangle_\Sigma$ with $m = \pm 1, 0$ form the Σ triplet and transform as the η singlet. These basis states can be written explicitly in terms of the second quantized conserved fermion operators defined in Eq. (4.52):

$$|-\rangle\!\rangle_\eta = |\mathrm{vac}\rangle\!\rangle, \tag{4.57a}$$

$$|0\rangle\!\rangle_\eta = \frac{1}{\sqrt{2}}\left(c^\dagger_{2j-1,\uparrow}c^\dagger_{2j-1,\downarrow} - c^\dagger_{2j,\uparrow}c^\dagger_{2j,\downarrow}\right)|\mathrm{vac}\rangle\!\rangle, \tag{4.57b}$$

$$|+\rangle\!\rangle_\eta = c^\dagger_{2j-1,\uparrow}c^\dagger_{2j,\uparrow}c^\dagger_{2j-1,\downarrow}c^\dagger_{2j,\downarrow}|\mathrm{vac}\rangle\!\rangle, \tag{4.57c}$$

$$|-\rangle\!\rangle_\Sigma = c^\dagger_{2j-1,\downarrow}c^\dagger_{2j,\downarrow}|\mathrm{vac}\rangle\!\rangle, \tag{4.57d}$$

$$|0\rangle\!\rangle_\Sigma = \frac{1}{\sqrt{2}}\left(c^\dagger_{2j-1,\downarrow}c^\dagger_{2j,\uparrow} + c^\dagger_{2j-1,\uparrow}c^\dagger_{2j,\downarrow}\right)|\mathrm{vac}\rangle\!\rangle, \tag{4.57e}$$

$$|+\rangle\!\rangle_\Sigma = c^\dagger_{2j-1,\uparrow}c^\dagger_{2j,\uparrow}|\mathrm{vac}\rangle\!\rangle, \tag{4.57f}$$

where $|\mathrm{vac}\rangle\!\rangle$ is defined by the annihilation $c_{j,\sigma}|\mathrm{vac}\rangle\!\rangle = 0$. Intuitively we can view the system as hosting on each physical site a single spin-1 particle, which can be either an η or a Σ spin. The occupation of η or Σ triplet at site j corresponds to distinct eigenvalues of the local conserved quantities: $\mathcal{R}_{2j-1} = \mathcal{R}_{2j} = \pm 1$ for η and Σ, respectively.

The effective Hamiltonian that generates the imaginary time evolution directly follows from Eqs. (4.54) and (4.55) projected on the reduced six-dimensional local Hilbert space. After straightforward algebra, we find that H_{eff} simplifies to

$$H_{\mathrm{eff}} = H_{\mathrm{eff},\eta} + H_{\mathrm{eff},\Sigma}, \tag{4.58}$$

where each term in $H_{\text{eff},\eta}$ ($H_{\text{eff},\Sigma}$) acts nontrivially only for η-spins (Σ-spins) and otherwise annihilates the wave function. We can write this explicitly as

$$H_{\text{eff},\kappa} = \sum_j \Delta \left(S^z_{\kappa,j}\right)^2 - \sum_j J_\perp \left(S^x_{\kappa,j} S^x_{\kappa,j+1} + S^y_{\kappa,j} S^y_{\kappa,j+1}\right) + J_z S^z_{\kappa,j} S^z_{\kappa,j+1}, \qquad (4.59)$$

where the spin-1 operators $\vec{S}_{\kappa,j} = (S^x_{\kappa,j}, S^y_{\kappa,j}, S^z_{\kappa,j})$ annihilate the singlet state of the species $\kappa = \eta, \Sigma$. The coupling constants in this Hamiltonian are determined from the parameters of the unitary gates and the measurements as follows: $\Delta = \Gamma_s$, $J_\perp = 2J_b + \Gamma_b/4$, and $J_z = 2J_b - \Gamma_b/4$.

Let us make a few remarks on the effective Hamiltonian. First, H_{eff} conserves the total z components as well as the parities associated with $S^z_{\kappa,j} \mapsto -S^z_{\kappa,j}$ transformation of η and Σ spins, separately. Besides, H_{eff} is the same in η and Σ sector and therefore invariant under the exchange of η and Σ spins. Thus, H_{eff} respects the symmetry $[(U(1) \rtimes \mathbb{Z}_2) \times (U(1) \rtimes \mathbb{Z}_2)] \rtimes \mathbb{Z}_2^{\mathbb{T}}$ as expected. Second, the occupation of η and Σ triplet states is locally conserved at every site. Note that the number of local integrals of motion is reduced from $2L$ to L upon averaging over the unitary gates and projection unto the six-dimensional local Hilbert space $\mathcal{P}\mathcal{R}_{2j-1}\mathcal{P} = \mathcal{P}\mathcal{R}_{2j}\mathcal{P}$. Accordingly, the dynamics is partitioned into 2^L sectors corresponding to configurations of the η and Σ occupations.

In our case, the physical circuit is initialized in the vacuum state of the fermions f_j. When extended to the duplicated Hilbert space, this state can be written using the conserved fermions as

$$|\rho_0\rangle\!\rangle_j = \frac{1}{2} \left(c^\dagger_{2j-1,\uparrow} + c^\dagger_{2j,\uparrow}\right) \left(c^\dagger_{2j-1,\downarrow} - c^\dagger_{2j,\downarrow}\right) |\text{vac}\rangle\!\rangle_j$$

$$= \frac{1}{\sqrt{2}} \left(|0\rangle\!\rangle_\eta - |0\rangle\!\rangle_\Sigma\right). \qquad (4.60)$$

We see that the initial state is already in the reduced Hilbert space and equally populates both η and Σ triplet states at every site.

In the long imaginary time evolution, the wave function is dominated by the global ground states of the Hamiltonian (4.58) among all 2^L sectors. The ground states are found in the two uniform sectors, i.e. the η sector with all sites occupied by η spins ($\mathcal{R}_\ell = 1$) and the Σ sector with all sites occupied by Σ spins ($\mathcal{R}_\ell = -1$). Thus, the $\lim_{t\to\infty} |\rho(t)\rangle\!\rangle \approx |\psi_{gs}\rangle\!\rangle_\eta + |\psi_{gs}\rangle\!\rangle_\Sigma$

The steady state phases of the circuit can be classified based on the reduced effective symmetry within either one of the two relevant sectors. The symmetry is reduced because in each sector the two $U(1)$ charges are not independent. In the η sector every site is a sigma singlet with $N_{\uparrow,j} = N_{\downarrow,j}$, so only $N_\uparrow + N_\downarrow$ is a non trivial charge. In the Σ sector two fermions occupy each site, so $N_{\uparrow,j} + N_{\downarrow,j} = 2$, so only $N_\uparrow - N_\downarrow$ is a non trivial charge. Hence, either sector only forms a faithful representation of $U(1) \rtimes (\mathbb{Z}_2 \times \mathbb{Z}_2^{\mathbb{T}})$, which is a subgroup of $\mathcal{G}^{(2)}_{f,\text{eff}}$. One can verify $U(1) \rtimes (\mathbb{Z}_2 \times \mathbb{Z}_2^{\mathbb{T}})$ is exactly the symmetry of H_{eff} in either sector. For vanishing measurement rates, owing to local conserved quantities, each sector only forms a faithful representation of either $SU(2)$ spin or charge symmetry, reducing the effective

symmetry down to $O(3) = SO(3) \rtimes \mathbb{Z}_2^{\mathbb{T}}$.[6] Indeed in this limit the effective Hamiltonian in each of the two sectors is the Heisenberg ferromagnet, which manifests the $O(3)$ symmetry.

Finally, we establish the correspondence between the ground state properties of H_{eff} and the steady states of quantum circuits by mapping various physical observables measured on the circuit to the matrix elements of different boundary operators in the effective spin model. As explained in Section 4.2, properties related to the second moments of the density matrix (conditional on the measurement device) generally take the form

$$O^{(2)} \leftrightarrow \frac{\langle\!\langle \mathcal{I}|\mathcal{O}|\rho^{(2)}\rangle\!\rangle}{\langle\!\langle \mathcal{I}|\rho^{(2)}\rangle\!\rangle}, \tag{4.61}$$

where $\langle\!\langle \mathcal{I}|$ is the reference state that implements the (doubled) trace operation in the duplicated Hilbert space, i.e. $\langle\!\langle \mathcal{I}|\rho^{(2)}\rangle\!\rangle = \text{tr}\, \rho^{(2)}$.

Within the effective description, the state $\langle\!\langle \mathcal{I}|\mathcal{O}$ can be viewed as the boundary condition to the imaginary time evolution at the latest time. The action of $\mathcal{O}$ to the left transforms the boundary conditions set by the reference state $\langle\!\langle \mathcal{I}|$ in the region on which $\mathcal{O}$ is supported. The kind of boundary condition imposed is dictated by the symmetries of $\langle\!\langle \mathcal{I}|$. We show in appendix C.6 that the reference state breaks the $U(1)$ symmetry in both the η and Σ sector, exhibiting the long range order $\langle\!\langle \mathcal{I}|\eta_i^y \eta_j^y|\mathcal{I}\rangle\!\rangle \to c$ and $\langle\!\langle \mathcal{I}|\Sigma_i^y \Sigma_j^y|\mathcal{I}\rangle\!\rangle \to c$ as $|i - j| \to \infty$. Thus, $\langle\!\langle \mathcal{I}|$ effectively imposes a symmetry breaking boundary condition on the imaginary time evolution by H_{eff} [see Fig. 4.5(a)].

The various operators we use to probe the circuit transform the broken symmetry boundary conditions in different ways. Consider first the site parity variance $\Pi_{s,A}^{(2)}$ on subsystem A, which is mapped to the boundary matrix element (4.61) of the operator

$$\hat{\Pi}_{s,A} = \prod_{j \in A} (-i\gamma_{2j-1,1,\uparrow}\gamma_{2j,1,\uparrow})(-i\gamma_{2j-1,2,\uparrow}\gamma_{2j,2,\uparrow})$$

$$= \prod_{j \in A} e^{-i\pi(\eta_j^z + \Sigma_j^z)}. \tag{4.62}$$

This operator rotates the $U(1)$ order parameters for both η and Σ spins by π everywhere in subsystem A. The ensuing boundary condition is illustrated schematically in Fig. 4.5(b). We'll see that this is equivalent to inserting a pair of topological defects (vortices) at the edges of the region A.

The bond parity variance operator $\hat{\Pi}_{b,A}$ can be obtained by simply translating $\hat{\Pi}_{s,A}$ by half of a physical site (one Majorana site). Thus, the operator leads to the same π rotation of the $U(1)$ orders of the boundary state within region A, but it is bound to a $\mathbb{Z}_2$ charge (of the symmetry $\phi \to -\phi$) on each edge of the region [see Fig. 4.5(c)]. As we will see in the next section, this difference has nontrivial implications on the behavior of the bond parity variance in the different phases.

---

[6]The symmetry is $SO(3)$ rather than $SU(2)$ because the ground state occupies an integer representation.
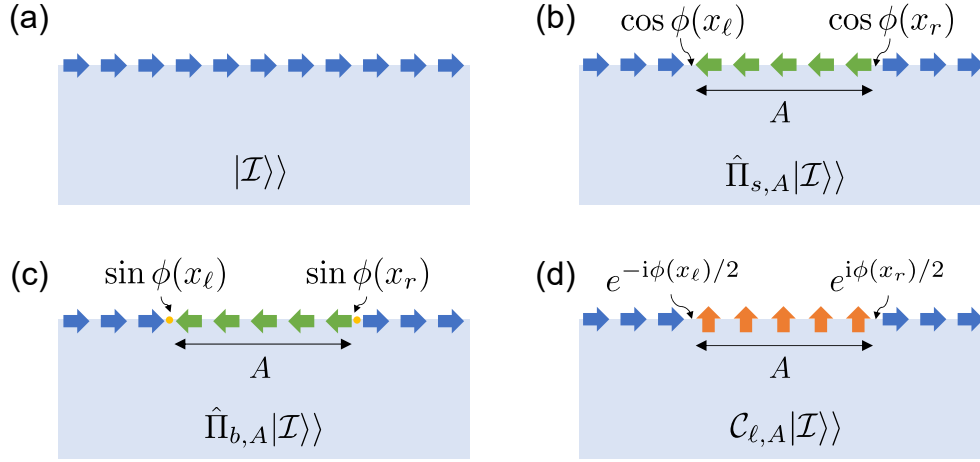
Figure 4.5: Boundary conditions imposed on the $U(1)$ phase by the boundary operators corresponding to different probes. (a) The reference state $|\mathcal{I}\rangle\rangle$ imposes a symmetry breaking state with $U(1)$ phase locked to zero (blue arrows). (b) The site parity variance $\hat{\Pi}_{s,A}$ rotates the phase by π-phase in region A, which creates a vortex anti-vortex pair at the edges of the region. (c) The bond parity variance $\hat{\Pi}_{b,A}$ similarly affects a π phase rotation, creating a vortex anti-vortex pair at the edges of A. However, in this case, the vortex creation operators are bound to a $\mathbb{Z}_2$ charge (of the symmetry $\phi \to -\phi$). (d) The swap operator $\mathcal{C}_{\ell,A}$ rotates the phase in A by $\pi/2$ (orange arrows), creating a pair of half-vortices at edges of the region.

The entanglement entropy of a subsystem is associated with the matrix element of a swap operator $\mathcal{C}_{\ell,A}$ as discussed in Section 4.2. Because $\mathcal{C}_{\ell,A}$ is nonlocal when written in terms of fermionic operators, we replace it with a local operator $\widetilde{\mathcal{C}}_{\ell,A}$ which has exactly the same action as $\mathcal{C}_{\ell,A}$ on the reference state, namely $\widetilde{\mathcal{C}}_{\ell,A}|\mathcal{I}\rangle\rangle = \mathcal{C}_{\ell,A}|\mathcal{I}\rangle\rangle$ (see Appendix C.7). The operator $\widetilde{\mathcal{C}}_{\ell,A}$ can be simply expressed in terms of the f-fermions defined on the forward branches and in terms of the η and Σ spins,

$$
\begin{aligned}
\widetilde{\mathcal{C}}_{\ell,A} &= \prod_{j\in A} f^{\dagger}_{j,1,\uparrow}f_{j,2,\uparrow} + f_{j,1,\uparrow}f^{\dagger}_{j,2,\uparrow} + \frac{1}{2}\left(1 + \hat{\Pi}_{j,1,\uparrow}\hat{\Pi}_{j,2,\uparrow}\right) \\
&= \prod_{j\in A} e^{-\mathrm{i}\frac{\pi}{2}(\Sigma^z_j + \eta^z_j)},
\end{aligned}
\tag{4.63}
$$

where $\hat{\Pi}_{j,\alpha,\uparrow} = 1 - 2f^{\dagger}_{j,\alpha,\uparrow}f_{j,\alpha,\uparrow}$ is the fermion parity in the forward branch of copy α at site j. Since $\widetilde{\mathcal{C}}_{\ell,A}$ only operates on the forward branches, it naturally breaks the time-reversal symmetry of spin-1/2 fermions. Specifically, the unitary operator $\widetilde{\mathcal{C}}_{\ell,A}$ rotates both $U(1)$ order parameters in the region A by an angle $\pi/2$. We'll see below that this is equivalent to inserting a pair of half vortices at the edges of region A leading to the boundary state illustrated in Fig. 4.5(d).

Phases of the effective model

The effective Hamiltonian H_{eff} consists of two identical and decoupled spin-1 Hamiltonians $H_{\text{eff},\kappa}$, each acts on the $\kappa = \eta, \Sigma$ sectors. The ground states and phase transitions of $H_{\text{eff},\kappa}$ have been extensively investigated numerically [60] and admit a simple long-wavelength description [229].

In the physically relevant parameter regimes, $\Gamma_b, \Gamma_s, J_b \geq 0$, the ground state phase diagram of $H_{\text{eff},\kappa}$ contains three phases, as illustrated schematically in Fig. 4.6(a). For vanishing measurement rates, $H_{\text{eff},\kappa}$ is a $O(3)$ ferromagnet, which admits a fluctuation-free broken symmetry state. This is a singular point in the phase diagram corresponding to the volume-law state established for purely unitary dynamics of free fermions. For any non-zero measurement rate, the $O(3)$ symmetry is broken down to $U(1) \rtimes (\mathbb{Z}_2 \times \mathbb{Z}_2^{\mathbb{T}})$ leading to a critical phase with algebraic long-range order. Increasing the measurement rates Γ_s and Γ_b beyond a critical threshold leads to two possible gapped phases, depending on the ratio between the two measurement processes. The site measurements Γ_s contribute to the Δ-term (also known as single-ion anisotropy), leading to a trivial gapped phase when they are dominant. The bond measurements Γ_b, on the other hand, leads to the Haldane gapped phase, which is an SPT phase of the spin-1 model.

The above phases and phase transitions can be captured within a long wavelength theory. First, note that the imaginary time evolution with the effective Hamiltonian has a coarse-grained description in terms of the 2d XY model $S_{XY} = \frac{K}{2} \int dx d\tau (\nabla \theta)^2$ with $\theta = \theta + 2\pi$. We can gain even more insight, however, by framing the long-wavelength theory of the XY model in the form of the one-dimensional sine-Gordon Hamiltonian

$$H = \frac{1}{2} \int dx \left[K(\nabla \hat{\theta})^2 + \frac{1}{K}(\nabla \hat{\phi})^2 \right] - g \int dx \cos\left(2\hat{\phi}\right). \tag{4.64}$$

Here, $\hat{\theta}$ is related to the $U(1)$ phase in the XY model (though it is not compact). $\nabla \hat{\phi}/\pi$ is the long wavelength fluctuation of the conserved charge conjugate to $\hat{\theta}$, so that $[\hat{\theta}(x), \hat{\phi}(x')] = i\pi\Theta(x - x')$. The coupling g is related to the vortex fugacity implicit in the XY model. This model is invariant to a shift of $\hat{\phi} \to \hat{\phi} + \pi$, which corresponds to a translation by a lattice constant, and to $\hat{\phi} \to -\hat{\phi}$ related to the $\mathbb{Z}_2$ "particle-hole" symmetry.

In the critical phase of the spin-1 Hamiltonian, the renormalized Luttinger parameter $K > 2$ and the coupling g is irrelevant in the long wavelength limit. As the microscopic parameters are varied, the system eventually undergoes a Kosterlitz-Thouless transition into a gapped phase at a critical universal value $K_c = 2$. The long wavelength theory distinguishes the two gapped phases through the sign of the coupling g. If $g > 0$, the dual field $\hat{\phi}$ is locked to $\phi = 0$ giving rise to a trivial gapped phase. If $g < 0$, then $\hat{\phi}$ is locked to $\phi = \pi/2$, which corresponds to the SPT (Haldane) phase. Note that the two phases are related through a shift by half a lattice constant (equivalently, one Majorana site).

We now turn to discuss how the different phases of the effective model are probed by the boundary operators. As noted in the previous section, the action of these operators on the boundary state imposes the boundary conditions depicted in Fig. 4.5. Hence, they correspond

to boundary condition changing operators in the long wavelength theory. The logarithm of the boundary overlap (4.61) is directly related to the excess free energy of the effective 2d XY model with the modified boundary conditions relative to the free energy with the uniform boundary conditions set by the reference state.

Consider first the parity string operators $\hat{\Pi}_{s,A}$ and $\hat{\Pi}_{b,A}$, which enter the calculation of the parity variances. These operators affect a π-phase flip on region A, which creates a pair of vortices on the boundary of the 2d XY model. In the long wave length limit, the vortex insertion is affected by the operators $e^{\pm i\hat{\phi}}$. To compute the site parity string $\hat{\Pi}_{s,A}$, we must choose the symmetric combination $\cos\hat{\phi}(x)$ at each end because the site parity string preserves the particle-hole symmetry on every site. Thus, in the long wavelength limit we can write $\hat{\Pi}_{s,A} \sim \cos\phi(x_\ell)\cos\phi(x_r)$, where x_ℓ, x_r are the two ends of the region A. The bond parity string is obtained from the site parity string through translation by half a physical site (one Majorana site), implemented by a shift $\hat{\phi} \to \hat{\phi} + \pi/2$ in the long wavelength theory. Thus, $\hat{\Pi}_{b,A} \sim \sin\phi(x_\ell)\sin\phi(x_r)$. This is consistent with the fact that, on each end of the region A, the bond parity string carries a residual parity operator of half a physical site, which is anti-symmetric with respect to the particle-hole symmetry. The swap string, which enters the calculation of the entanglement entropy, affects a $\pi/2$ rotation of the $U(1)$ phase, which creates a pair of half-vortices on the boundary of the 2d XY model. In the long wavelength theory, this is achieved by the operators $\widetilde{\mathcal{C}}_{\ell,A} \sim e^{-i\phi(x_\ell)/2}e^{i\phi(x_r)/2}$.

Having established the long wavelength form of the operators associated with the different boundary observables, we can determine the behavior of the boundary matrix element in the different phases. In the critical phase, the distinction between the site and bond parity strings is not important. Both decay as a power law, dictated by the scaling dimensions of boundary vortex insertions $\Pi_{a,A}^{(2)} \sim |x_\ell - x_r|^{-K/4}$ [97]. The behavior of the entanglement entropy on the other hand is dictated by a pair of half-vortex insertions at the boundary, each having half the scaling dimension of a vortex insertion. Thus, we expect $e^{-S_A^{(2)}} \sim |x_\ell - x_r|^{-K/16}$. So, while the decay exponents vary continuously in the the long wavelength theory, the theory predicts a universal ratio of 4 between the decay exponent of the parity variance and that of $\exp\left(-S_A^{(2)}\right)$ in the critical phase. Furthermore, the KT transition is expected to occur at a universal value of the stiffness $K_c = 2$, which implies a critical exponent $\alpha_\Pi^c = 1/2$ for the decay of the parity variance and $\alpha_S^c = 1/8$ for $\exp\left(-S_A^{(2)}\right)$.

In the low energy fixed points corresponding to gapped ground states, $\hat{\phi}(x)$ is nonfluctuating; it is locked to $\phi = 0$ in the trivial phase and to $\phi = \pi/2$ in the SPT phase. Hence, we can immediately deduce the action of parity and swap strings on the ground states. The swap does not vanish in either phase, thus giving $\exp\left(-S_A^{(2)}\right) \to$ const at long distances in both the trivial and SPT state. The two phases are distinguished by the action of the parity strings. The site parity string, which involves $\cos\hat{\phi}$, acts as a constant on the trivial ground state and vanishes on the SPT ground state at the fixed point. Conversely, the bond parity string acts as a constant on the SPT ground state and vanishes on the trivial ground state. Therefore, in the trivial phase, we expect $\Pi_{s,A}^{(2)} \to$ const and $\Pi_{b,A}^{(2)} \to \exp(-|x_\ell - x_r|/\xi)$. In
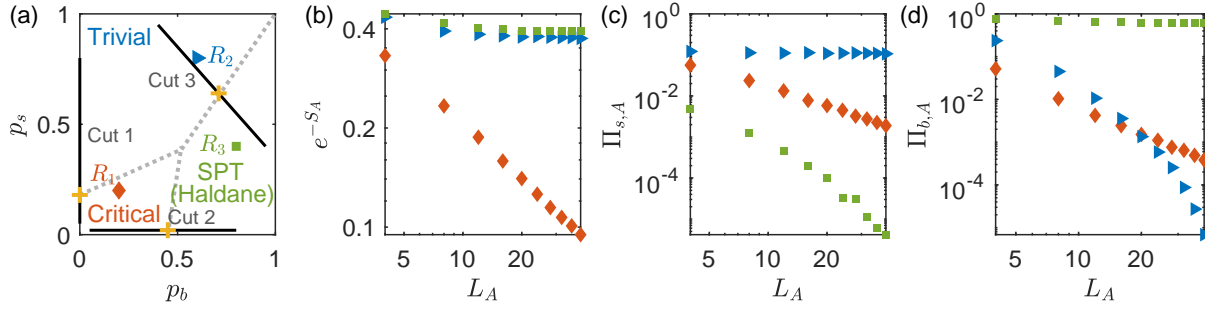
Figure 4.6: Entanglement entropy and subsystem parity variances in three phases of Gaussian fermionic circuits. (a) Schematic phase diagram in the space of bond measurement versus site measurement probabilities (p_b v.s. p_s). Yellow markers represent numerically extracted critical points along marked cuts. (b-d) Results for representative points of the three phases $R_1 : (0.2, 0.2)$, $R_2 : (0.6, 0.8)$, $R_3 : (0.8, 0.4)$ shown on the phase diagram. (b) Entanglement entropy e^{-S_A} shows power-law decay (logarithmic entanglement scaling) with subsystem size L_A in the critical phase (R_1, red diamonds) and a constant (area law) in the trivial and SPT phases. (c) Subsystem site parity variance $\Pi_{s,A}$ shows a power-law decay with L_A in the critical phase (red diamonds), faster than power-law in the SPT phase (green squares) and is nondecaying in the trivial phase (blue triangles). (d) Subsystem bond-parity variance $\Pi_{b,A}$ shows a power-law decay in the critical phase (red diamonds), exponential decay in the trivial phase and is nondecaying in the SPT phase. The numerical results are obtained with system size $L = 160$ and averaged over 400 random circuit realizations and measurement outcomes.

the SPT phase, this is inverted, $\Pi_{b,A}^{(2)} \to$ const, whereas $\Pi_{s,A}^{(2)} \to \exp(-|x_\ell - x_r|/\xi)$. In the following section, we examine the predictions of the long wave-length theory for the various phases by numerically simulating the quantum circuit.

Numerical simulation in Gaussian fermionic circuits

The fermions circuit defined in Section 4.4 can be simulated efficiently because it preserves the Gaussianity of the wave function in each quantum trajectory [248]. This allows us to test the predictions of the effective model by direct numerical calculation of the circuit dynamics. Technically, it is enough to propagate the $O(N^2)$ two point functions $G_{ij} \equiv \langle\Psi|i\gamma_i\gamma_j|\Psi\rangle - i\delta_{ij}$, which fully determine the Gaussian wave function. Indeed, all quantities of interest, including the subsystem entanglement entropy S_A and parity variances $\Pi_{s,A}$ and $\Pi_{b,A}$, can be directly read out from G_{ij}. We perform the calculation with system sizes of up to $L = 160$ sites using periodic boundary conditions to facilitate better finite size scaling. We operate the circuit to depth $3L$ to achieve a steady state.

We explore a two-dimensional phase space defined by the site and bond measurement probabilities as illustrated in Fig. 4.6(a). The behavior of the three observables we extract
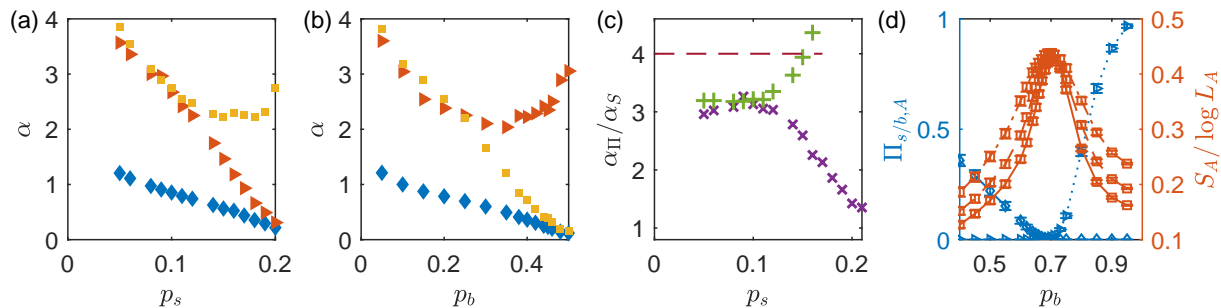
Figure 4.7: Tuning across the critical points on the three cuts shown in Fig. 4.6(a): cut 1 ($p_b = 0$), 2 ($p_s = 0.02$), 3 ($p_b + p_s = 1.35$). (a, b) Fitted power-law decay exponent of e^{-S_A} (α_S, blue diamonds), site parity variance ($\alpha_{\Pi,s}$, red triangles), and bond parity variance ($\alpha_{\Pi,b}$, yellow squares) along cut 1 [panel (a)] and cut 2 [panel (b)]. The horizontal axis represents the tuning parameter along each cut. The exponents are extracted from simulations with the system size $L = 160$ averaged over 400 random circuit realizations and measurement outcomes. (c) Ratio between exponents $\alpha_{\Pi,s}/\alpha_S$ and $\alpha_{\Pi,b}/\alpha_S$ along cut 1. Results for $\alpha_{\Pi,s}/\alpha_S$ (purple crosses) and $\alpha_{\Pi,b}/\alpha_S$ (green "+"). The red dashed line represents the prediction of the two-replica model for the critical phase: $\alpha_\Pi/\alpha_S = 4$. (d) Parity variances (blue, left vertical axis) and normalized entanglement entropy (red, right vertical axis) along cut 3 from $(p_b, p_s) = (0.4, 0.95)$ to $(0.95, 0.4)$. $\Pi_{s,A}$ (blue dashed line) and $\Pi_{b,A}$ (blue dotted line) are for $L_A = L/2$. The plotted entanglement entropy is taken for subsystem size $L_A = L/2$ and normalized by $\log L_A$. The three red lines correspond to system sizes $L = 40, 80, 160$; the peak gets sharper with increasing system size and indicates logarithmic entanglement scaling only at the critical point. The numerical results are averaged over 400 random circuit realizations and measurement results.

indicates the establishment of three phases. Panels (b-d) of the figure demonstrate this for three representative points in the phase diagram. At the point $(p_b, p_s) = (0.2, 0.2)$ (red diamond), we observe the expected behavior of the critical phase with entanglement entropy scaling as $\log L_A$ and power-law decay of the parity variances. The point $(p_b, p_s) = (0.6, 0.8)$ (blue triangle) exhibits the behavior we expect in the trivial phase with entanglement entropy and the site parity variance saturating to a constant, while the bond parity variance decaying exponentially. Finally, the point $(p_b, p_s) = (0.8, 0.4)$ (green square) shows a constant entanglement entropy and bond parity variance as well as an exponential decaying site parity variance, as expected in the SPT phase.

Having confirmed these basic behaviors, we turn to investigate the critical phase and the transitions from this phase into the two gapped states. To this end, we vary the measurement probabilities p_s and p_b along the two cuts depicted as cut 1 and cut 2 in Fig. 4.6(a). Along these cuts, we aim to fit the subsystem size dependence of $\Pi_{s,A}$, $\Pi_{b,A}$ and $\exp(-S_A)$ to a power law of L_A. More precisely, since we anticipate that the critical phase has a conformal

field theory description, we can account for the finite system size and periodic boundary conditions by fitting the decay of these objects to a power law of the conformal coordinate $z_A = L\sin(\pi L_A/L)$. Figure 4.7(b,c) shows the variation of the fitted exponents $\alpha_{\Pi,s}$, $\alpha_{\Pi,b}$, and α_S along the cuts. We see that the exponents $\alpha_{\Pi,s}$ and $\alpha_{\Pi,b}$ coincide and decrease together on increasing the measurement rate toward the transition, as expected in the critical phase. The exponents then start to deviate, presumably near the critical point, in order to match the opposite behavior of the two parities in the gapped phases. For example, in the trivial phase, we expect $\alpha_{\Pi,s} \to 0$, which encodes $\Pi_{s,A} \to$ const, and $\alpha_{\Pi,b} \to \infty$ in order to mimic $\Pi_{b,A} \sim \exp(-L_A/\xi)$.

In the range of tuning parameter, where the two parity exponents coincide, we find that the ratio between these exponents and the one controlling the decay of $\exp(-S_A)$ is pinned to a constant value. The ratio, as seen in Fig. 4.7(c), is pinned to $\alpha_\Pi/\alpha_S \approx 3$, which deviates from the ratio of 4 predicted by the low energy effective theory. This discrepancy could be related to the difference between the von Neumann entropy computed here and the second conditional Rényi entropy calculated in the effective model.

We now focus on the phase transition from the critical phase to the trivial phase along cut 1 in Fig. 4.6(a). To establish the universality class, we analyze the behavior of the correlation length and compare it to the hallmark exponential divergence associated with a KT transition.

We extract the correlation length ξ from the behavior of the entanglement entropy in the area-law phase near the transition since it gives much cleaner data than the parity variances. On distances small compared to the correlation length, i.e. $L_A \ll \xi$, we expect the critical behavior

$$S(z_A, p_s, L) = b(p_s) + \alpha_S(p_s)\log z_A, \tag{4.65}$$

while for $L_A \gg \xi$ we should see a saturation to $b(p_s) + \alpha_S(p_s)\log(z_\xi)$. Here, $z_\xi = L\sin(\pi\xi/L)$ is the conformal coordinate for the correlation length ξ.

To accurately obtain ξ, we first fit $b(p_s)$ and $\alpha_S(p_s)$ from the short distance behavior of $S(z_A, p_s, L)$. We then use the interpolating function

$$S(z_A, p_s, L) = \frac{\alpha_S(p_s)}{\beta}\log\left(z_\xi^\beta \tanh\frac{z_A^\beta}{z_\xi^\beta}\right) + b(p_s) \tag{4.66}$$

to obtain $\xi(p_s, L)$ for different values of p_s and system sizes $L = 40, 80, 160$. The parameter β is added to improve the fit and details of the procedure are given in Appendix C.8.

The fitted values of the correlation length are presented in Fig. 4.8 at all points for which $\xi \le L/2$. We find that $\xi(p_s, L)$ fall close to the same curve for the different values of L. The figure shows a fit of the data for the largest length $L = 160$ to the KT form of the correlation length $\xi(p_s) = \exp(A/\sqrt{p_s - p_{s,c}} + B)$.

The results are consistent with a KT transition within the range of system sizes reached and also provide an estimate of the critical point $p_{s,c} = 0.17$. We note that the finite size

corrections to the critical stiffness K_c in the KT transition exhibit a slow logarithmic decay with system size. Therefore, it is not surprising that the critical exponents governing the decay of the various boundary correlations are larger than the expected thermodynamic value.

Having analyzed the critical phase and the phase transition into the area-law phases, we turn to the phase transition between the two area-law states along cut 3 in Fig. 4.6(a). The variation of the half system entanglement entropy normalized by $\log(L/2)$ is shown by the red curves in Fig. 4.6(d) for the three system sizes $L = 40, 80, 160$. The normalized value is seen to be size independent at a single point and the curve appears to sharpen with increasing system size. This gives strong evidence for single critical point along the cut as expected from the $O(2)$ long-wavelength description (4.64). Thus we do not find an indication of a generic critical phase intervening between the two area-law phases as suggested based on a relation to the completely packed loop model [225].

The details of the transition, however, also do not precisely match the predictions of the effective theory (4.64). On the critical line separating the two area-law phases, the effective theory predicts a stiffness constant $K < 2$, which is continuously decreasing with increasing measurement rate along this line. Accordingly the coefficient of the logarithmic half-system entropy is expected to be $\alpha_S < 1/8$, which is violated by the observed value of $\alpha_S \approx 0.43$.

The variation of the half-system site and bond parity variances across the transition behave broadly as expected, but again show a mismatch with the effective theory upon more detailed comparison. These variations are shown by the blue curves in the figure for a single system size of $L = 160$. The two string "order parameters" are seen to switch roles between the two phases, as expected. However, the sharp suppression of both order parameters at the critical point is unexpected. The effective model implies a slow decay of the parity variance with an exponent $\alpha_\Pi < 1/2$. This should produce a rather broad finite size coexistence region of the two "order parameters" [28], which is not observed in the numerical results.

Beyond the two-replica theory

In our analysis of the Gaussian fermion circuits we focused on the two-replica theory without taking the replica limit $n \to 1$. Nonetheless, several key predictions of this model are supported by the numerical results obtained from direct simulation of fermion circuits. These includes the establishment of a critical phase characterized by logarithmic entanglement entropy with variable coefficient α_S, the connection between α_S and the power-law decays of the site and bond parity variances, and the KT transition separating the critical phase from the area-law states. At the same time, the numerical results suggest that the phase transition between the two area-law states is not captured correctly within the two-replica model.

To gain insights into the success and the limitations of this model, we consider an approximate scheme to evaluate O_2 in Eq. (4.13) in terms of a statistical mechanics model

with quenched disorder. The second moment O_2 is again given by

$$O_2 = \overline{\sum_m p_m(U) \left(\frac{\text{tr}\left(\hat{O}\, \tilde{\rho}_m(U) \right)}{\text{tr}\left(\tilde{\rho}_m(U) \right)} \right)^2}. \tag{4.67}$$

Here U runs over the different realizations of unitary gates, and we explicitly note the dependence of the trajectory state $\tilde{\rho}_m(U)$ on U.

Now, if $p_m(U) \equiv \text{tr}\left(\tilde{\rho}_m(U) \right)$ has a narrow distribution over U, we can approximate it by its average $p_m = \overline{p_m(U)}$ and perform the average over unitaries in Eq. (4.67) before averaging over measurement outcomes to obtain

$$O_2 \approx \sum_m p_m \frac{\langle\!\langle \mathcal{I}|\mathcal{O}^{(2)}|\rho_m^{(2)} \rangle\!\rangle}{\langle\!\langle \mathcal{I}|\rho_m^{(2)} \rangle\!\rangle}. \tag{4.68}$$

In this expression the measurements enter as quenched disorder. Typical trajectories m consist of imaginary time evolution with an effective Hamiltonian generated by the averaged unitary dynamics, interrupted by isolated measurements located in random space-time positions. The isolated measurements reduce the $O(3)$ symmetry of the Heisenberg ferromagnet down to $O(2)$. We note that a similar scheme, which avoids the replica limit at the expense of introducing disorder, was considered in Ref. [283] for purely unitary circuits.

Such a model with quenched disorder has a true symmetry $O(2)$. In the case of low measurement rates, the stiffness is large enough such that the only relevant effect of the disorder is the reduction of the symmetry from $O(3)$ to $O(2)$; the space-time randomness is expected to be irrelevant in the ensuing $O(2)$ critical phase. In contrast the disorder does become relevant beyond the KT transition. Thus, taking a proper replica limit may be important for describing the transition between the two area-law states, which explains the failure of the two-replica theory to describe this critical behavior correctly.

It remains an interesting challenge to evaluate the second moment O_2 in the proper replica limit $n \to 1$. One perturbative approach to the problem suggested in Ref. [93] in the context of disordered fermion models, is through an expansion of the $O(n)$ nonlinear sigma model in $\epsilon = 2 - n$. Alternatively, Sang et al. [225] proposed to utilize a mapping of certain Majorana fermion circuits to the completely packed loop model with crossings [184]. Although the more generic model we considered does not map exactly to the loop model, it is possible that the two models are in the same universality class. The numerical results at the available system sizes do not appear consistent with this possibility. These results indicate a direct transition between the two area-law states, while in the loop model the two area-law states are generically separated by a finite region of the critical phase.

4.5   Discussion

The quantum circuits we have considered in this Chapter generate the time evolution of many-body wave-functions or density matrices through a series of unitary gates and local
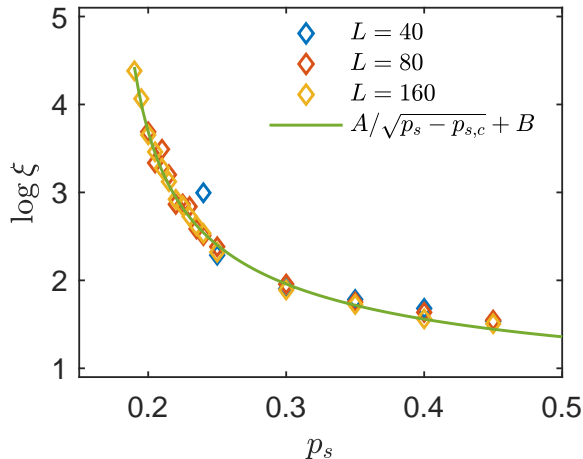
Figure 4.8: Correlation length ξ in the trivial area-law phase along cut 1 indicated on Fig. 4.6(a). The green line represents the fitted correlation length according to the scaling $\log \xi(p_s) = A/\sqrt{p_s - p_{s,c}} + B$ in the KT transition with $A = 0.58$, $p_{s,c} = 0.17$, and $B = 0.34$. The results for $L = 40, 80, 160$ are denoted by blue, red, and yellow diamonds, respectively. The data used to extract $\xi(p_s)$ is presented in Appendix C.8.

measurements. Such a time evolution gives rise to a special kind of ensemble, whose members are the quantum states corresponding to all possible histories of measurement outcomes. Our goal has been to characterize the phases that can emerge as steady states in this new kind of ensemble. A key observation of this work is that, unlike in thermal equilibrium or in quantum ground states, the symmetry that governs the classification of phases in quantum circuits is not simply the symmetry of the physical interactions imposed by the circuit elements. Rather, many statistical properties of the ensemble in steady states are dictated by an enlarged symmetry group, which combines the physical circuit symmetry with intrinsic dynamical symmetries of the problem.

The enlarged symmetry emerges because distinctive properties of the circuit steady state can be seen only in the fluctuations of physical observables over the different measurement histories, while a simple average over all possible measurement outcomes looks trivial. In particular, the variance of physical observables, which is the minimal nontrivial fluctuation, is encoded in the time evolution of two identical copies of the density matrix. A symmetry to permute quantum states between the two copies naturally arises and combines with the physical circuit symmetries.

This symmetry enlargement has an illuminating analogy in Anderson's pioneering work on spin glasses (see also Ref. [185]). Edwards and Anderson famously pointed out that spin glass order is characterized by the random frozen magnetic moment, which can be diagnosed by the variance of the spin moment over the ensemble of random samples $q_{EA} = \overline{\langle s_i \rangle^2}$ [81]. In close analogy with the diagnostics, we considered for the quantum circuits, the EA order

parameter can be expressed as a standard average (correlation function) in an effective probability distribution constructed from two identical copies of the system. This doubling naturally gives rise to a permutation symmetry between replicas, which is reminiscent of the permutation symmetries in our system.

The analogy with the spin glass also extends to information theoretic aspect of the problem. We have shown that broken symmetry phases of the circuit are states that encode and protect information on symmetry breaking in the initial state. Similarly, the onset of an EA order parameter in a spin glass signals the emergence of an error correcting code, allowing to encode information in random broken symmetry spin configurations [240, 195].

There is however a fundamental difference between the quantum measurement ensemble and the spin glass problem. Due to the quantum nature of the circuit, fluctuations in the measurement ensemble are obtained from the time evolution of doubled density operators rather than from (static) probability distributions. This leads to a richer symmetry, since the forward (ket) and backward (bra) evolution of the density operators are associated with independent permutation symmetries. Spontaneous breaking of these inherently quantum symmetries signals a capacity to encode quantum information [65, 104, 18, 85, 127].

To facilitate the classification of phases, we formulated a mapping between the steady states of the circuit ensemble and the ground states of an effective Hamiltonian, which inherits the enlarged dynamical symmetry. This leads to establishment of phases that would not have been possible in presence of the physical circuit symmetry alone. Here is a summary of the most striking consequences. (i) A topological area-law phase can form in a one-dimensional model with only $\mathbb{Z}_2$ physical circuit symmetry, owing to protection from an enlarged symmetry $\mathbb{Z}_2 \times \mathcal{S}_2$ that combines the circuit symmetry and the dynamical permutation symmetry between trajectories. We argued that this state admits an efficient experimental detection scheme using the Fisher information associated with perturbations applied at the edge. Demonstrating the existence of this state in a numerical simulation of a concrete model, or alternatively showing a fundamental obstruction to realize it, remains a challenge for future work. (ii) Several distinct volume-law phases, characterized by different broken symmetry patterns, arise as ground states of a circuit with $\mathbb{Z}_2$ symmetry. We demonstrate the existence of three of these volume-law entangled states in numerical simulations of a one-dimensional model. An interesting conclusion from this result is that the quantum measurements allow to stabilize orders, which could not have existed in a finite entropy equilibrium state. We argue, as a corollary, that measurements can even facilitate the establishment of topological order and protected edge modes in a state with volume-law entanglement. (iii) A Gaussian fermionic circuit with only $\mathbb{Z}_2$ fermion parity conservation exhibits a critical phase facilitated by a $U(1)$ dynamical symmetry of two copies of the density matrix. We predict a Kosterlitz-Thouless transition to area-law states above a critical rate of measurement. We show numerical evidence supporting this transition.

It is worth noting that the predictions of the effective model rely on analysis of quantum dynamics with two replicas without taking the formal replica limit $n \to 1$. The rather detailed agreement with exact numerical results may suggest that two replicas play a special role in this problem because the minimal diagnostics of the ensemble are fundamentally second

moments. It is worth exploring alternative schemes to average over the ensemble, which avoid introducing auxiliary replicas, possibly at the expense of retaining space-time disorder [283]. We also remark that our classification of phases in this Chapter was based on symmetry alone. It would be important to understand if additional constraints on the dynamics, such as the complete positivity of quantum channels, could inhibit the establishment of certain states.

Arguably the most pressing challenge for the theory right now is to connect with the rapidly advancing experimental work on quantum circuits. An important first step would be to extend the theoretical framework to more realistic models, which include, at a minimum, decoherence and possibly other dissipative processes in addition to unitary gates and measurements. Such an extension would also be interesting from the theoretical perspective because decoherence changes the symmetry of the problem. Any weak coupling to the environment explicitly breaks the independent permutation symmetries among replicated quantum states propagating forward or backward, and it only respects simultaneous permutations of forward and backward states. We have noted that the separation of the two permutation symmetries is a signature of quantumness that is absent in classical settings, such as the replica theory of a spin glass. Nonetheless, the universal behavior and encoding power may not immediately collapse to that of a classical circuit. There is another quantum symmetry associated with the exchange between forward and backward propagating states, namely the hermiticity of the density matrix, which is neither removed nor trivialized immediately by the addition of decoherence. A nontrivial hermiticity symmetry, in principle distinguishes the quantum dynamics of density matrices from classical probability distributions even in the presence of decoherence. It would be interesting to explore under what conditions the hermiticity symmetry can be spontaneously broken and to understand the implications of such order on the capacity for encoding quantum information.

We close by recalling a dialogue that had not occurred in Paris in the 1920s. Hopefully it sums up our message clearly:

FITZGERALD: Quantum circuits are different from spin glasses.

HEMINGWAY: Yes, they have more symmetry.

Chapter 5

Finite-time teleportation phase transition in random quantum circuits

5.1 Introduction

The dynamics of entanglement in many-body time evolution and in quantum circuits is the focus of intense theoretical [143, 186, 239, 163] and experimental interest [136, 15, 64, 197]; indeed, it provides crucial insights for understanding the capacity of physical systems to process quantum information as well as the computational complexity involved in simulating their dynamics [258]. In generic unitary evolution with short-range interactions, the Lieb-Robinson bound [167] ensures that quantum entanglement propagates along light cones. Thus, two degrees of freedom separated by a distance L take a time of order L to get entangled.

Entanglement can be created much faster by supplementing unitary evolution with measurements [46, 164, 70]. As a simple example, we consider a chain of qubits initialized in a product of Bell pairs on the *odd* links, which can be prepared from a product state by a single layer of two-qubit gates. By performing Bell measurements on the *even* links, one can create a Bell pair of the (unmeasured) first and last qubit. As another example, a two-dimensional cluster state can be used for measurement-based quantum computation [217]; one can create any desired entangled state by appropriate local measurements.

In the schemes described above, entanglement is generated over arbitrarily long distances using a unitary circuit of constant depth followed by a single layer of measurements. These states are said to possess finite localizable entanglement and infinite entanglement length [257, 209]. However, the examples above are highly fine-tuned. It is natural to ask how long it would take to create quantum correlations between distant qubits using generic unitary evolution followed by local measurements.

In this Chapter, we show that the creation of infinite range entanglement, i.e. states with infinite entanglement lengths, can occur as a phase transition at a critical time of order one. In the simplest setup, an initial product state is evolved for a time t, after which all but two infinitely separated qubits are measured. In two (or higher) dimensional systems with
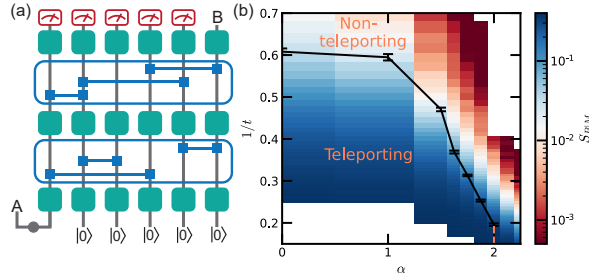
Figure 5.1:   (a) Random quantum circuit on N qubits. In each time step δt, we apply
single-qubit Haar random gates to every qubit followed by $N\delta t$ two-qubit Haar random
gates. The distribution of two-qubit gates is determined by the geometry of the circuit.
The first qubit is maximally entangled with a reference qubit A, while the remaining qubits
are prepared in $|0\rangle$. We consider the mutual information between A and an output qubit
B, conditioned on local measurements on the rest of the qubits. (b) Phase diagram of
one-dimensional long-range unitary circuits with power-law decaying interaction. The black
markers represent the inverse critical time $1/t_c$ as a function of power-law exponent α. The
transition requires $\alpha \leq 2$, indicated by the pink dotted line. When $t > t_c$, the output state is
in the teleporting phase, corresponding to the low-temperature ferromagnetic phase of the
effective quantum Hamiltonian. The color indicates the conditional entropy $S_{B|M}$.

short-range interactions, entanglement between the two distant qubits onsets at a critical time
t_c. The same is true for one-dimensional systems with sufficiently long-range interactions.
An equivalent scheme, shown in Fig. 5.1(a), is to consider the teleportation from an input
qubit to an infinitely distant output qubit after measuring all other output qubits, which can
be achieved with nonvanishing fidelity after time t_c.

    We provide a theoretical picture of this transition by mapping the random circuit evolution
to an effective equilibrium problem. This approach builds on recent developments in describing
entanglement dynamics through mapping circuits consisting of random unitaries to the
statistical mechanics of classical spins located at the space-time positions where the gates
operate [115, 183, 253, 18, 130]. In the case of continuous time evolution, the classical
spin model can be viewed as imaginary time evolution generated by an effective quantum
Hamiltonian [17, 33].

    Previously, this mapping was primarily applied to understand the steady-state entangle-
ment properties, which are determined by the ground state of the effective Hamiltonian (i.e.
infinite imaginary time evolution). Similarly, the finite-time evolution, which we consider
here, is related to a thermal state of the effective Hamiltonian (i.e. finite imaginary time
evolution). The key point is that a finite-temperature transition in the thermal state indicates
a finite real-time transition in the circuit.

    We demonstrate this phenomenon by considering the transition in continuous-time random
unitary circuits (RUC) with different architectures including: two-dimensional short-range

systems, all-to-all coupled systems, and one-dimensional long-range systems with power-law decaying interactions. In the last case, our theory predicts a finite-time transition for power-law exponent $\alpha \leq 2$, and specifically a Kosterlitz-Thouless (KT) like transition at $\alpha = 2$. We corroborate these predictions with numerical simulations of random Clifford circuits.

Before proceeding, we remark on a related paper by Napp et al. [189] dealing with the sampling complexity of shallow two-dimensional brick-layer RUCs. This work claimed and provided evidence that approximate sampling from such circuits is hard if the depth t is above a threshold t_c of $O(1)$ while it is easy for $t < t_c$. Sampling requires measuring all qubits following the final layer of unitary gates. The essence of the argument is that this network can be contracted sideways, showing it is equivalent to simulating the dynamics of a one-dimensional quantum circuit with measurements. Hence, one expects a phase transition in sampling complexity in shallow two-dimensional RUCs which is of the same universality as the measurement-induced transition in one dimension [163, 239, 162, 65, 104]. In our discussion, we argue heuristically that this sampling transition can be understood as a specific example of the teleportation transition, and may therefore occur in a broad class of systems for which the effective Hamiltonian exhibits a finite-temperature transition.

5.2   Setup and theoretical framework

Our model consists of N qubits with $N - 1$ qubits initialized in a product state and a single qubit prepared in a maximally entangled state with the reference A. In each time step δt, we apply a layer of single-qubit Haar random unitary gates followed by $N \delta t$ two-qubit Haar random unitary gates [Fig. 5.1(a)]. The sites (i, j) on which each two-qubit gate operates are drawn independently from a distribution $P(i, j)$, which depends on the specific models we discuss below. The single-qubit gates do not generate entanglement and are introduced only for analytical convenience [1]. After evolving for time t, we measure all $N - 1$ qubits except for a distant qubit B.

The resulting fidelity of teleportation between qubits A and B is quantified by the entanglement entropy of B, conditioned on outcomes of the measured qubits M (see Appendix D). To analytically determine the conditional entropy $S_{B|M}$ averaged over circuit realizations and measurement outcomes, we formulate it as the $n \to 1$ limit (replica limit) of the quantities [18]

$$S_{B|M}^{(n)} = \frac{1}{1-n} \log \frac{\overline{\sum_m \text{tr}\, \tilde{\rho}_{B,m}^n}}{\overline{\sum_m \text{tr}\, \tilde{\rho}_m^n}}, \tag{5.1}$$

where $\tilde{\rho}_m := \hat{P}_m \rho \hat{P}_m$ is the projection of the density matrix onto the set of measurement outcomes labeled by m, and the overline indicates the average over the Haar ensemble. Accordingly, the probability for this set of measurement outcomes is $p_m = \text{tr}\left(\rho \hat{P}_m\right) = \text{tr}\, \tilde{\rho}_m$,

---

[1]We note that single-qubit gate on site i can in principle change the circuit ensemble provided that no two-qubit Haar random gate acts on i.
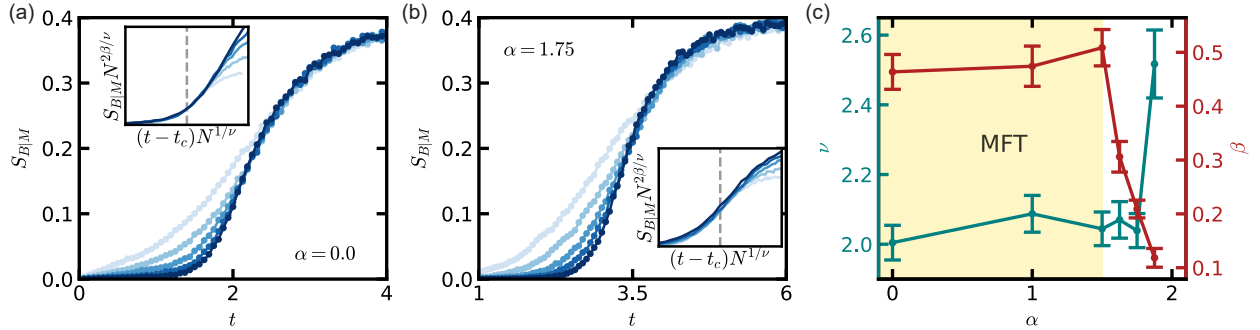
Figure 5.2: Finite-time transition in one-dimensional long-range interacting random circuits. (a,b) The conditional entropy $S_{B|M}$ in circuits with power-law exponents $\alpha = 0$ [all-to-all, panel (a)] and $\alpha = 1.75$ [panel (b)] plotted as a function of time t for various system sizes N from 32 to 512 indicated by increasing opacity. (inset) Finite-size scaling collapse using Eq. (5.3). The grey dotted line indicates t_c. For the all-to-all circuit ($\alpha = 0$), we obtain critical exponents $\nu \approx 2.0$, $\beta \approx 0.46$, and critical time $t_c \approx 1.6$. For $\alpha = 1.75$, we obtain $\nu \approx 2.0$, $\beta \approx 0.20$, and critical time $t_c \approx 2.1$. (c) Critical exponents ν and β for $\alpha < 2$. The exponents agree with mean-field theory (MFT) for $\alpha \leq 1.5$. Moreover, near $\alpha = 2$, ν begins to diverge, as expected near a KT-like transition. The finite-time transition does not exist for $\alpha > 2$. The numerical results are averaged over $1.5 \cdot 10^4$ random circuit realizations.

and the normalized density matrix is $\rho_m = \tilde{\rho}_m / p_m$. We note that the $S_{B|M}^{(n)}$ are not precisely the conditional Rényi entropies because the average is taken inside the logarithm.

The simplest quantity that captures the qualitative features of $S_{B|M}$ is $S_{B|M}^{(2)}$, although the critical exponents of their respective transitions may be different [253, 18, 130]. The quantity $S_{B|M}^{(2)}$ involves the second moments of the density matrix, which can be determined from the double density matrix $\rho \otimes \rho$. Formally, $\rho \otimes \rho$ can be represented as a state vector $|\rho\rangle\!\rangle$ in the replicated Hilbert space $\mathcal{H}^{(2)} := (\mathcal{H} \otimes \mathcal{H}^*)^{\otimes 2}$, where $\mathcal{H}$ ($\mathcal{H}^*$) denotes the ket (bra) Hilbert space. A unitary gate U in the circuit acts as $\mathcal{U} = (U \otimes U^*)^{\otimes 2}$ on $|\rho\rangle\!\rangle$. Hence, the replicated density matrix undergoes unitary evolution $|\rho(t)\rangle\!\rangle = \prod_{\tau=1}^{N_t} \mathcal{U}_{2,\tau} \mathcal{U}_{1,\tau} |\rho(0)\rangle\!\rangle$, where $\mathcal{U}_{1,\tau}$ and $\mathcal{U}_{2,\tau}$ denote the layer of single- and two-qubit gates in each time step τ, respectively.

The average dynamics of the double density matrix can be analytically mapped to imaginary time evolution under an effective Hamiltonian [17, 33]. First, the average over single-qubit gates effects a projection from a sixteen-dimensional local Hilbert space to the two-dimensional Hilbert space of a spin-1/2 (see Appendix D). Then, the layer of two-qubit gates reduces to a transfer matrix for the transition amplitude between the spin-1/2 configurations in consecutive time steps, $\mathcal{T} = \mathbb{1} + N\delta t \sum_{ij} P(i,j)\overline{\mathcal{U}_{2,\tau}(i,j)}$.

The transfer matrix $\mathcal{T}$ can be viewed as the infinitesimal imaginary time evolution generated by an effective quantum Hamiltonian operating on spin-1/2 degrees of freedom,

$\mathcal{T} = e^{-\delta t H_{\text{eff}}}$. For our circuit, the effective Hamiltonian takes the form

$$H_{\text{eff}} = \sum_{i,j} J_{ij} \left[-\frac{2}{5}\sigma_i^z \sigma_j^z - \frac{1}{10}\sigma_i^y \sigma_j^y - \frac{1}{5}(\sigma_i^x + \sigma_j^x) \right], \tag{5.2}$$

where the coupling $J_{ij} = NP(i,j)$ is given by the average number of two-qubit gates acting
between qubit i and j in every unit time [2]. Accordingly, the replicated, un-normlized, density
matrix evolves as $|\rho(t)\rangle\rangle = e^{-tH_{\text{eff}}}|\rho(0)\rangle\rangle$. We note that the Hamiltonian exhibits a global Ising
symmetry generated by $\prod_i \sigma_i^x$, which stems from the invariance of $\mathcal{U}$ under the permutation
of two copies of ket (or bra) Hilbert space.

The effective imaginary time evolution above yields a thermal state of the ferromagnetic
Ising Hamiltonian in Eq. (5.2) at inverse temperature t. For two-dimensional RUCs, the
associated two-dimensional Ising model will undergo a ferromagnetic transition at a tem-
perature corresponding to a finite critical time t_c. Similarly, for one-dimensional RUCs, the
associated one-dimensional Ising model can exhibit a finite-temperature transition provided
the unitary couplings decay with a sufficiently small power of distance $\alpha \leq 2$ [221, 79, 249,
13]. This finite-temperature phase transition implies a transition in the output state of the
circuit occurring at a finite time.

This transition indeed manifests in the conditional entropy $S_{B|M}^{(2)}$. The projective mea-
surements of the output state play a crucial role in revealing the transition: they impose
a boundary condition in the finite imaginary time evolution that preserves the Ising sym-
metry [18, 130]. In more detail, $S_{B|M}^{(2)}$ is mapped to the excess free energy associated with
imposing symmetry-breaking fields only at the space-time locations of qubit A and B.
This can be further reduced to the imaginary time order parameter correlation function,
$S_{B|M}^{(2)} \sim \langle \sigma_B^z(t)\sigma_A^z(0) \rangle$ (see Appendix D). Consequently, $S_{B|M}^{(2)}$ is non-decaying in the ordered
phase $(t > t_c)$ due to the long-range order in the Ising model, whereas $S_{B|M}^{(2)}$ rapidly decays
to zero in the disordered phase $(t < t_c)$.

We remark that the finite-time transition cannot be detected in the purity (or entanglement
entropy) of an an extensive subsystem of the output state. Indeed, in the imaginary time
evolution, this quantity involves breaking of the Ising permutation symmetry through the
boundary condition at the final time [115, 183, 253]. Since the symmetry-breaking boundary
conditions are imposed on the top of a slab of finite thickness (time), they eliminate the
transition in the bulk.

5.3   Examples and numerical results

We demonstrate the finite-time teleportation transition predicted above in three exemplary
models: (1) all-to-all interacting quantum circuits, (2) one-dimensional quantum circuits with
power-law decaying long-range interactions, and (3) two-dimensional quantum circuits with

---

[2]We note that because only N gates are applied per unit time, $\sum_{(i,j)} J_{ij} = N$, and therefore the energy
of the Ising model is always extensive.

short-range interactions. To verify the predictions obtained from the approximate mapping
of these circuits to finite-temperature quantum states, we compute the conditional entropy in
random Clifford circuits, which can be efficiently simulated [100, 1]. While these circuits are
not generic, they form a unitary 3-design [264] and are therefore expected to give the same
qualitative results as circuits of Haar random unitaries.

As the first example, we consider the circuit with all-to-all unitary gates. Within a time
step δt, each two-qubit gate is drawn independently and operates on a random pair of qubits
(i, j) with equal probability. Hence, the effective quantum Hamiltonian that describes $S_{B|M}^{(2)}$
has all-to-all couplings $J_{ij} \sim 1/N$ (see Appendix D). In the limit $N \to \infty$, the Ising phase
transition in this Hamiltonian is described exactly by mean-field theory, which predicts critical
exponents $\nu_{MF} = 2, \beta_{MF} = 0.5$, and a critical time $t_c^{(2)} = 2.0$ (see Appendix D). We note
that the mean-field theory does not yield a reliable t_c for $S_{B|M}$ as the effective Hamiltonian
is derived for an approximate quantity $S_{B|M}^{(2)}$.

To characterize the transition of the conditional entropy $S_{B|M}$, we simulate this quantity
in all-to-all Clifford circuits of system sizes up to $N = 512$ as shown in Fig. 5.2(a) [3] [4]. We
perform a finite-size scaling analysis using the scaling formula to extract critical exponents
(see Appendix D):

$$S_{B|M}(t, N) = N^{-2\beta/\nu} \mathcal{F}((t - t_c)N^{1/\nu}). \tag{5.3}$$

This analysis yields critical exponents $\nu = 2.1 \pm 0.2, \beta = 0.4 \pm 0.1$, which are in close agreement
with the predictions of the mean-field theory, and also the critical time $t_c \approx 1.6$.

As a second example, we consider a one-dimensional array of N qubits evolving with
power-law decaying couplings and periodic boundary conditions. Here, for each two-qubit gate,
we independently choose a random pair of sites (i, j) with a probability $P(i, j) \propto 1/|i - j|^\alpha$.
The effective model for this circuit is a one-dimensional finite-width classical Ising model
with long-range coupling $J_{ij} \sim 1/|i - j|^\alpha$.

This model is in the same universality class as the one-dimensional long-range classical
Ising chain at finite temperature, which has been extensively studied and shown to have
an ordering transition when $\alpha \leq 2$ [221, 79, 249, 13], with Kosterlitz-Thouless universality
at $\alpha = 2$ [150, 57, 30, 31, 126, 173]. Furthermore, for $3/2 < \alpha < 2$, the transition features
continuously varying critical exponents, whereas for $\alpha \leq 3/2$, it is described by mean-field
theory with α-independent exponents [150].

These predictions from the classical Ising chain are borne out clearly in our Clifford
numerics. For $\alpha \leq 2$, we simulate $S_{B|M}$ for A and B separated by $N/2$ sites and observe
a crossing for various N, as exemplified at $\alpha = 1.75$ in Fig. 5.2(b) and Appendix D. This
indicates the finite-time transition and enables using finite-size scaling to extract critical
exponents. For $\alpha \leq 3/2$ we find approximately constant critical exponents, consistent with
mean-field theory. In contrast, for $3/2 < \alpha < 2$ we obtain continuously varying critical

---

[3]We ignore the single-qubit gates in the Clifford simulation as they do not affect the information dynamics.
[4]We note that $I_{A:B|M}$ saturates to a maximum value 0.8 in the long time limit, which is universal for
random Clifford evolution [70].
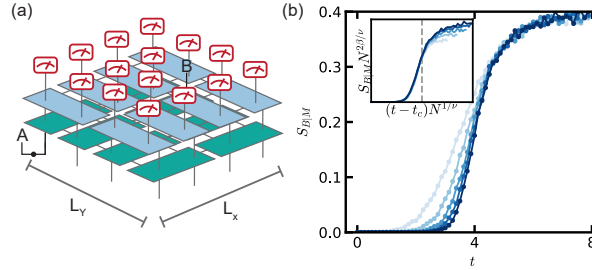
Figure 5.3: Finite-time teleportation transition in two-dimensional short-range random circuits. (a) Schematic of a finite-time two-dimensional random circuit of size $L_x = L_y = L$. We use periodic boundary conditions and consider reference A to be entangled with an input qubit separated from output qubit B by $L/2$ in both directions. (Inset) A realization of $N\delta t$ gates within a time step δt. (b) The conditional entropy $I_{B|M}$ plotted as a function of time t for various system sizes L from 8 to 24 indicated by increasing opacity. (Inset) Finite-size scaling collapse using Eq. (5.3). We obtain $\nu \approx 1.2 \pm 0.1$, $\beta \approx 0.11 \pm 0.03$, and critical time $t_c \approx 4.2$ (indicated by the grey dashed line). The numerical results are averaged over 9000 random circuit realizations.

exponents as shown in Fig. 5.2(c). On the other hand, we observe no evidence of a finite-time transition in $S_{B|M}$ for $\alpha > 2$ (see Appendix D). A phase diagram is presented in Fig. 5.1(b).

The point $\alpha = 2$ requires special attention. In this case, the effective model exhibits a finite-temperature KT transition, which does not admit single-parameter scaling as postulated in Eq. (5.3). The exponential divergence of the correlation length can be viewed as having $\nu \to \infty$. Indeed Fig. 5.2(c) shows a sharp increase of ν upon approaching $\alpha = 2$. At $\alpha = 2$ we compare the observed scaling of $S_{B|M}(t, N)$ to the scaling form $a \exp[1/(\log N + b)]$ expected in an Ising chain with inverse square interaction [30]. We find an accurate fit at the critical time $t_c \approx 5.0$ (see Appendix D), which provides circumstantial evidence for a KT-like transition. However, simulations on larger system sizes are needed to precisely determine the universality of this transition. Altogether, the qualitative understanding gleaned from the effective spin model agrees with our numerical findings.

In the last example, we consider the finite-time transition in short-range interacting circuits in higher dimension ($d \geq 2$). Specifically, we consider $P(i, j)$ to be uniformly distributed over pairs of nearest-neighbor qubits. The critical exponents extracted from the two-dimensional Clifford simulation are $\nu \approx 1.2$, $\beta \approx 0.11$ [Fig. 5.3(b)]. These exponents are in agreement with the exponents found in the measurement-induced entanglement transition [278] [5]. This result is indeed expected by mapping the dynamics of a finite depth two-dimensional brick-layer RUC with final-time measurements to hybrid quantum dynamics (i.e. unitary and measurement) in one dimension [189].

---

[5]The anomalous dimension in two dimensions is given by $\eta = 2\beta/\nu \approx 0.2$ in agreement with the result of [278].

5.4   Discussion

The above analysis of two-dimensional circuits suggests that the finite-time teleportation transition may generally correspond to a transition in approximate sampling complexity [189, 177]. Specifically, we consider the problem of sampling measurement outcomes from N qubits initialized in a product state and evolved under a finite-time RUC. To draw a connection to the teleportation transition, we divide the output qubits into three regions: $\mathcal{A}$ and $\mathcal{B}$, each with a sub-extensive number of qubits N^γ with $0 < \gamma < 1$, and M, the remaining qubits.

In the teleporting phase ($t > t_c$), measurements on M generate long-range entanglement between subsystems $\mathcal{A}$ and $\mathcal{B}$. In the spin model, $S_{\mathcal{B}|M}$ is the excess free energy of imposing a domain wall separating $\mathcal{A}$ from $\mathcal{B}$, which scales as a power law of $\min(|\mathcal{A}|, |\mathcal{B}|)$ in the ordered phase [6]. Thus, we expect approximate sampling from the pure joint state $|\psi_\mathcal{A}\psi_\mathcal{B}\rangle$ to be as complex as sampling from a Haar-random state of a sub-extensive power-law number of qubits, which is believed to be classically hard [38].

On the other hand, in the non-teleporting phase ($t < t_c$), the classical spin model has a finite correlation length ξ, i.e. sampling from a given qubit is independent from sufficiently distant qubits. Indeed, it has been shown for brick-layer circuits that approximate sampling can be achieved by patching simulations of sub-regions of size $O((\log N)^d)$ together, resulting a $\mathrm{Poly}(N)$ runtime in two dimensions and quasi-$\mathrm{Poly}(N)$ runtime in higher dimensions [189]. However, establishing a rigorous connection between finite-time teleportation in Haar-random circuits with arbitrary connectivity and sampling complexity remains an open question for future work.

Although 1d short-range RUCs do not feature a finite-time transition, the spin model mapping indicates an exponentially diverging correlation length $\xi \sim \exp(Jt)$ with circuit depth t. This results from the correlation length $\xi \sim \exp(J/T)$ in the 1d quantum Ising model at temperature T with coupling J. Therefore, one can teleport qubits over a distance N in circuits of depth $t \sim \log N$ [7].

The teleportation transition we describe can potentially be realized on leading quantum simulation platforms, such as trapped-ion systems, which feature tunable long-range interactions [210], and two-dimensional superconducting circuits [15, 226]. We note, however, that obtaining the conditional entropy in experiments is challenging as naive evaluation of $S_{B|M}$ requires post-selection on an extensive number of qubits. Alternatively, one can verify the entanglement by decoding from the output qubit, which is a topic of ongoing research for generic evolution beyond Clifford circuits [105, 197]. We remark our protocol demonstrates a distinct teleportation mechanism from those inspired by quantum gravity [114, 153, 49, 232], in which the teleportation distance is limited by the lightcone of the evolution.

Our framework is also applicable to studying finite-time transitions in circuit ensembles beyond Haar-random unitary circuits. In particular, in circuits with conserved quantities, the

---

[6]The sub-extensive symmetry breaking boundary conditions on $\mathcal{A}$, $\mathcal{B}$ do not destroy the long-range order in the effective spin model.

[7]However, the approximate sampling from $\log N$-depth 1d RUCs is tractable since $I_{A:B|M} = O(\log N)$ [205].

effective Hamiltonian is governed by an enlarged symmetry allowing a richer phase structure at finite times [17]. For example, in free fermion dynamics that conserve fermion parity, the effective Hamiltonian exhibits a continuous $U(1)$ symmetry. In two dimensions, the effective model undergoes a finite-time KT transition and can support power-law decaying $S_{B|M}$, while in dimension $d \geq 3$, the continuous symmetry can be broken, leading to non-decaying $S_{B|M}$. Moreover, we note that the key dynamical feature that enables the teleportation transition is the protection of quantum information against local measurements. Thus, we conjecture that the transition can also occur in non-random chaotic Hamiltonian dynamics in which local scrambling protects information.

Chapter 6

The errorfield double formulation of mixed-state topological order

6.1   Introduction

Recent experiments in many-body quantum simulation platforms, such as arrays of Rydberg atoms and superconducting qubit systems, have shown compelling evidence for the establishment of topological order [234, 34, 226, 5]. While these platforms offer a high degree of control, the state preparation is subject to inevitable decoherence, leading ultimately to a mixed state. Experimental probes of topological order have a long history in the context of the fractional quantum Hall effect in semiconductors [250, 21, 187]. In this case, it is understood that the imperfection due to non-vanishing temperature broadens the signatures of topological order [265, 200, 201, 41, 152, 50]. However, the states prepared in these new platforms do not have time to reach thermal equilibrium before they are probed and therefore cannot be described as Gibbs states. Instead, they are better modeled as a topologically ordered pure state corrupted by local channels describing decoherence for a finite time. It is natural to ask how to characterize the topological order in such corrupted topological states.

Different perspectives on this problem suggest seemingly conflicting answers. On one hand, the operation of the local quantum channels has an equivalent description as a finite-depth unitary process in an extended Hilbert space that includes an ancilla qubit for every system qubit. This finite-depth unitary circuit cannot lead to a singular change in the expectation value of any conventional diagnostic used to probe topological order, such as Wilson loops or open string operators [88], which support in a finite region. From this perspective, the topological order persists for any strength of decoherence, short of full dephasing or depolarization.

On the other hand, we can assess the effect of decoherence on the topological order through its ability to destroy the protection of quantum information encoded in the degenerate ground-state subspace [145, 43]. In this vein, Dennis et al. [74] calculate a finite error threshold for the Toric code subject to local Pauli X and Z errors. These errors create pairs of syndromes

(i.e. anyon excitations) detected by stabilizer measurements. The recovery scheme is an algorithm for annihilating the syndromes in pairs, which fails when the error rate exceeds the threshold. The existence of a recovery threshold strongly suggests that there is an underlying decoherence-induced transition in the intrinsic properties of the mixed state, which is not captured by standard probes used to detect ground-state topological order. We note, however, that the recovery fidelity itself is not an intrinsic property as it may depend on the recovery algorithm. Furthermore, theories of recovery thresholds are limited to solvable topological stabilizer codes and do not offer insight into the effect of decoherence on topologically ordered states more generally.

In this Chapter, we develop a universal description of topological order and decoherence-induced transitions in corrupted mixed states that is based on the underlying topological quantum field theory (TQFT). A key step is treating the density matrix as a state vector in a double (ket and bra) Hilbert space, $|\rho\rangle\!\rangle = \mathcal{N} |\Psi_0\rangle \otimes |\Psi_0^*\rangle$. The action of the decoherence channel $\mathcal{N}$, which couples the ket and bra states, can induce anyon condensation in the double space. We argue that this transition is described in terms of boundary criticality in close analogy to the effect of measurement on quantum ground states analyzed in Ref. [95].

To derive an effective theory of the decoherence-induced transition, we utilize the description of the state $|\Psi_0\rangle$ as a (2+1)-dimensional TQFT. Then, $|\rho\rangle\!\rangle$ is given as a double TQFT coupled by the quantum channel $\mathcal{N}$ only at the temporal boundary $\tau = 0$, and the induced transition corresponds to anyon condensation on the boundary. Accordingly, the distinct decoherence-induced phases are classified by the possible boundary anyon condensates [158, 20, 263]. We note that the description in terms of boundary phase transitions explains why the error threshold transitions in stabilizer models invariably map to transitions in 2D classical statistical mechanics or (1+1)D quantum models despite representing transitions in 2D quantum states [74, 262, 135, 36, 151, 66, 58, 254, 24].

6.2 Errorfield double state

The basic subject for our analysis is a topologically ordered state $|\Psi_0\rangle$ affected by local decoherence channels $\mathcal{N}_i$:

$$\rho = \prod_i \mathcal{N}_i[|\Psi_0\rangle \langle \Psi_0|], \tag{6.1}$$

where i is a site index. The local channel $\mathcal{N}_i[\cdot] := \sum_k \mathcal{K}_{k,i}(\cdot)\mathcal{K}_{k,i}^\dagger$ is defined by the Kraus operators $\mathcal{K}_{k,i}$, which satisfy $\sum_k \mathcal{K}_{k,i}^\dagger \mathcal{K}_{k,i} = \mathbb{1}$; they create different kinds of errors in the state. For example, the channel that causes bit-flip errors consists of two Kraus operators $\mathcal{K}_{1,i} = \sqrt{1-p}\,\mathbb{1}$ and $\mathcal{K}_{2,i} = \sqrt{p}X_i$, where p is the error rate.

To understand the effect of decoherence on a quantum ground state, it is convenient to express the Kraus operators in terms of the quasiparticles they create. In particular, a Kraus operator acting on a topological state generally creates a superposition of different clusters of anyons, i.e. $\mathcal{K}_{k,i} = \sum_\alpha c_{k,\alpha} \mathcal{A}_i[\alpha]$, where $c_{k,\alpha}$ is a complex coefficient, and $\mathcal{A}_i[\alpha]$
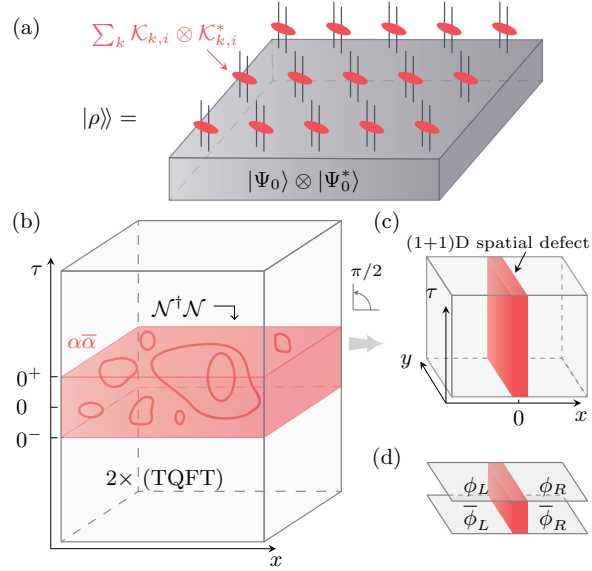
Figure 6.1: (a) Errorfield double state $|\rho\rangle\!\rangle$ describing a topologically ordered pure state corrupted by local errors (red dots). (b) Path integral representation of the norm $\langle\!\langle\rho|\rho\rangle\!\rangle$. Two path integrals in the past ($\tau < 0$) and the future ($\tau > 0$) prepare the double ground states at $\tau = 0^-$ and 0^+. The states are coupled by the quantum channel $\mathcal{N}^\dagger\mathcal{N}$ (red cuboid). Red lines represent the worldlines of anyon $\alpha\bar{\alpha}$ created by the incoherent errors. (c) The $\pi/2$ rotation converts the 2D temporal defect at $\tau = 0$ to a (1+1)D spatial defect at $x = 0$. (d) The rotated path integral represents the norm of the ground state of double 2D topological order with a 1D defect.

creates a cluster of anyons in the vicinity of site i [1]. Here, we focus on Kraus operators that are dominated by a single term rather than a coherent superposition, i.e. $\mathcal{K}_{k,i}$ is approximately proportional to a certain $\mathcal{A}_i[\alpha]$. Such Kraus operators are said to create incoherent errors [2]. The resulting mixed state is an incoherent mixture of states with different anyon configurations.

An essential step in characterizing the phases of the corrupted state is to regard the density matrix as a state vector in a double Hilbert space, i.e.

$$|\rho\rangle\!\rangle = \mathcal{N} |\Psi_0\rangle \otimes |\Psi_0^*\rangle = \prod_i \sum_k \mathcal{K}_{k,i} \bar{\mathcal{K}}_{k,i} |\Psi_0\rangle \otimes |\Psi_0^*\rangle , \qquad (6.2)$$

---

[1] Strictly speaking, such a decomposition is well-defined for fixed-point states where the sizes of anyons are zero. In more general situations, e.g., Laughlin states, one can regard this decomposition as a *definition* of phenomenological error models that we choose to work with.

[2] For example, one type of incoherent error creates a single anyon pair, an anyon and its anti-particle, on neighboring sites.

where we define barred operators as acting on the bra space, e.g. a super-operator $\mathcal{K}(\cdot)\mathcal{K}^\dagger$ acting on a density matrix is denoted as $\mathcal{K}\bar{\mathcal{K}}$ when acting on $|\rho\rangle\rangle$. We refer to $|\rho\rangle\rangle$ as an *errorfield double* (EFD) because of its analogy to the thermofield double state [106].

In absence of decoherence, $|\rho\rangle\rangle$ contains two decoupled copies of conjugate topologically ordered states. The non-unitary evolution affected by the operator $\mathcal{N}$ can induce phase transitions at finite error rates that can be diagnosed by operator expectation values in the EFD. Up to normalization, these expectation values are of the form $\langle\langle\rho|O\,\bar{O}|\rho\rangle\rangle = \mathrm{tr}\big(\rho O\rho O^\dagger\big)$. This object is the overlap between ρ and $\rho' = O\rho O^\dagger$, which measures the distinguishability between these two states.

6.3 Decoherence-induced transition as anyon condensation

To begin, we consider the example of the Toric code [145] subject to bit-flip errors. The Kraus operator $X_i = m_r m_{r'}$ is incoherent and creates two m anyons at neighboring locations r, r'. In the EFD, the corresponding super-operator creates two neighboring anyon pairs, $X_i \bar{X}_i = (m\bar{m})_r (m\bar{m})_{r'}$, where each pair $m\bar{m}$ creates an anyon of the double Toric code. The resulting EFD is given by

$$|\rho\rangle\rangle = \exp\left(\mu \sum_{\langle rr'\rangle} (m\bar{m})_r (m\bar{m})_{r'}\right) |\Psi_0\rangle \otimes |\Psi_0^*\rangle, \tag{6.3}$$

where $\mu = \tanh^{-1}[p/(1-p)]$. The operation of the error channel generates an effective imaginary time evolution of the pure topological state. As shown in Appendix E, this leads to anyon condensation of $m\overline{m}$ at $p_c^{(2)} = 0.178$, with the solvable transition in the 2D (classical) Ising universality class [3].

The anyon condensation can be detected by the open string operator

$$\langle\langle W_{m\overline{m}}(\mathcal{P})\rangle\rangle := \frac{\langle\langle\rho|W_{m\overline{m}}(\mathcal{P})|\rho\rangle\rangle}{\langle\langle\rho|\rho\rangle\rangle} = \frac{\mathrm{tr}\,\rho\,w_m(\mathcal{P})\,\rho\,w_m^\dagger(\mathcal{P})}{\mathrm{tr}\,\rho^2}, \tag{6.4}$$

where $w_m(\mathcal{P}) := \prod_{i\in\mathcal{P}} X_i$, and $W_{m\bar{m}} = w_m \otimes w_m^*$ creates the paired anyon $m\overline{m}$ at each end of the open path $\mathcal{P}$ [4]. In the topological phase, this quantity decays exponentially with the distance between two endpoints. In other words, the density matrix obtained by injecting an extra pair of far-separated anyons into ρ is orthogonal to ρ and hence distinguishable

---

[3]The superscript of $p_c^{(2)}$ indicates the transition in EFD is detected by the quadratic function of the density matrix. For the general n-th moment of the density matrix, the critical point $p_c^{(n)}$ depends on n. It approaches the error-correction threshold $p_c = 0.109$ in the replica limit $n \to 1$ (see Chapter 7).

[4]We remark that the condensate can also be generally probed by the Fredenhagen-Marcu (FM) order parameter of $m\bar{m}$ [89, 90, 91, 101, 255].

from it. In this sense, the m anyons remain well-defined excitations. Once the paired anyon condenses, the open string saturates to a non-vanishing value at a long distance.

Other types of incoherent errors in the Toric code, i.e. Pauli-Y and -Z errors, can induce distinct phases with condensed fermion pairs $f\bar{f}$ and electric anyon pairs $e\bar{e}$, respectively. All of these transitions are mutually independent because the paired anyons are mutual bosons, and they occur at the same $p_c^{(2)}$. If two types of paired anyons condense simultaneously, it implies a condensate of the third type as well because each two are equivalent (i.e. fuse) to the third type, e.g. $e \times m = f$.

We remark that the anyon condensation can be also probed by the topological entanglement entropy (TEE) of the EFD [146, 160], which changes discontinuously at the transition. In the toric code without decoherence, the TEE is $2\log 2$, with each of the two states contributing $\log 2$. The condensation of $m\bar{m}$ reduces the TEE to $\log 2$, and further condensing also $e\bar{e}$ completely removes the TEE (see Appendix E).

The results in the above example can be readily extended to general Abelian topological orders subject to incoherent errors. The paired anyon $\alpha\bar{\alpha}$ in the EFD are self-bosons and may condense at a large error rate. Moreover, different types of paired anyons, $\alpha\bar{\alpha}$ and $\beta\bar{\beta}$, are always mutual bosons and can condense independently.

Anyon condensation in the EFD affects the information encoding in the corrupted state. In topological quantum memory, the information is manipulated by the logical operator $w_\alpha(\ell)$ that moves an anyon α along non-contractible loops $\ell = \ell_1, \ell_2$ on the torus. These logical operators are non-commuting and therefore encode quantum information.

In the condensed phase of $\alpha\bar{\alpha}$, $W_{\alpha\bar{\alpha}}$ acting on the EFD does not produce an orthogonal state, i.e. two states have a finite overlap, indicating the loss of information encoded in w_α. Furthermore, the condensation identifies $W_{\beta\bar{\beta}}$ with $W_{\eta\bar{\eta}}$ provided that $\alpha \times \beta = \eta$. Thus, two logical operators $w_\beta(\ell)$ and $w_\eta(\ell)$ are no longer independent. By analyzing the commutation relations between independent logical operators, one can determine the encoding ability. If the remaining operators are non-commuting, the corrupted state remains a quantum memory, otherwise, only classical information can be encoded. The memory is completely destroyed if no operators remain.

6.4   Effective field theory

To generalize the decoherence-induced transitions to other topologically ordered states and gain insight into the nature of the ensuing phases, we formulate the problem within an effective field theory. To this end, we employ the path integral representation of the normalization

$$\langle\!\langle \rho | \rho \rangle\!\rangle = \langle\!\langle \rho_0 | \, \mathcal{N}^\dagger \mathcal{N} \, | \rho_0 \rangle\!\rangle, \tag{6.5}$$

which plays the role of a generating function for expectation values in the EFD. Since $|\rho_0\rangle\!\rangle = |\Psi_0\rangle \otimes |\Psi_0^*\rangle$ is a double topologically ordered state, it is given as a double TQFT in the Euclidean half spacetime $\tau < 0$. Similarly, $\langle\!\langle \rho_0 |$ is represented by a double TQFT in $\tau > 0$. Therefore, in absence of decoherence, the norm $\langle\!\langle \rho_0 | \rho_0 \rangle\!\rangle$ is represented by two

decoupled TQFT in the entire spacetime. The decoherence, represented by $\mathcal{N}^\dagger\mathcal{N}$, creates a
temporal defect in the double TQFT, which couples the conjugate copies on the plane $\tau = 0$
[Fig. 6.1(b)]. We note that the effect of measurements on a quantum ground state is similarly
represented by a temporal defect in the Euclidean action [95].

The transition induced by the coupling at $\tau = 0$ must be a boundary transition. This
renders a distinction between the condensation of $\alpha\bar{\alpha}$ in the EFD and that in a quantum
ground state. The latter involves the proliferation of $\alpha\bar{\alpha}$ loops of arbitrary size in the $(2+1)$D
spacetime, while the former is marked by the proliferation of small loops of the condensed
object $\alpha\bar{\alpha}$, fluctuating near $\tau = 0$ [Fig. 6.1(b)]. The distinction has consequences on the
signatures of the decoherence-induced anyon condensate.

In the Toric code example, the usual ground-state condensation of $m\bar{m}$ would lead to
confinement of anyon e that has non-trivial mutual statistics with $m\bar{m}$ [52]. This would be
detected, for example, by the Wilson loop $W_e(\mathcal{C}) := \prod_{i\in\mathcal{C}} Z_i \otimes 1\!\!\!/\!\!\!1$ along a contractible loop $\mathcal{C}$.
Once $m\bar{m}$ is condensed, $W_e(\mathcal{C})$ is affected by a finite density of large $m\bar{m}$ loops that pierce $\mathcal{C}$,
leading to exponential decay of $W_e(\mathcal{C})$ with an area law, i.e. $W_e(\mathcal{C}) \sim e^{-b\mathrm{Area}(\mathcal{C})}$. By contrast,
the decoherence-induced condensate only involves the proliferation of small $m\bar{m}$ loops that
only affect $W_e(\mathcal{C})$ along its perimeter leading to perimeter-law scaling, $W_e(\mathcal{C}) \sim e^{-a|\mathcal{C}|}$,
regardless of the error rate. Thus, the anyon condensation in the EFD does not lead to
confinement, and the Wilson loop cannot probe the transition.

6.5 Mapping to (1+1)D boundary phases

To classify the possible decoherence-induced phases it is convenient to perform a $\pi/2$-spacetime
rotation of the $(2+1)$D TQFT, $\tau \to -x$ and $x \to \tau$. The bulk action is invariant under this
rotation [272, 86, 235], whose sole effect is therefore to convert the temporal defect to a
spatial defect in a quantum ground state [Fig. 6.1(c)]. Thus, the decoherence-induced phases
are mapped to the quantum phases of a 1D defect in a double topologically ordered state
[Fig. 6.1(d)], which can be equivalently formulated as boundary phases [25, 133] (see also
Appendix E).

The possible phases can be understood using the field theory description. The Lagrangian
characterizing the low-energy physics has three contributions

$$\mathcal{L} = \mathcal{L}_0 + \mathcal{L}_1 + \mathcal{L}_\mathcal{N}. \tag{6.6}$$

$\mathcal{L}_0$ describes the low-energy excitation in the TQFT, which involves only the edge degrees of
freedom since the bulk is gapped. $\mathcal{L}_1$ represents the coupling between the edge modes on the
left and right of the defect in Fig. 6.1(d), which stems from the continuity of the TQFTs in
the two half spacetimes before the rotation. This is the coupling ensuring that the system
before decoherence is described by a gapped theory without temporal boundaries. Lastly,
$\mathcal{L}_\mathcal{N}$ represents the effect of the error channels, which couple the edge modes in the ket and
bra copies.

We now focus on the case of Abelian topological order, which is captured by Abelian Chern-Simons theories. The low-energy excitations are described by a theory of compact bosons on the edge [83, 267]

$$\mathcal{L}_0[\phi] = \frac{1}{4\pi} \sum_{I,J} \mathbb{K}_{IJ}^{(2)} i\partial_\tau \phi^I \partial_y \phi^J - \mathbb{V}_{IJ}^{(2)} \partial_y \phi^I \partial_y \phi^J, \tag{6.7}$$

where $\phi := [\bar{\phi}_R, \phi_R, \phi_L, \bar{\phi}_L]$, ϕ_s and $\bar{\phi}_s$ are the field variables in the ket and bra Hilbert spaces, respectively, while $s = L, R$ denote the two copies of the EFD. A central object of the theory is the K-matrix $\mathbb{K}^{(2)} = K \oplus (-K) \oplus K \oplus (-K)$ with K an integer-valued matrix. $\mathbb{V}^{(2)} = V \oplus V \oplus V \oplus V$ with V a non-universal positive definite matrix. In this theory, $\mathcal{L}_1$ is a non-linear coupling of ϕ_L to ϕ_R and $\bar{\phi}_L$ to $\bar{\phi}_R$, and $\mathcal{L}_\mathcal{N}$ couples field variables within the same copy of the EFD, i.e. ϕ_s and $\bar{\phi}_s$.

The gapped phase of the defect is obtained by condensing bosonic excitations. The excitations in $\mathcal{L}_0$ are of the form $e^{i\boldsymbol{l}^T \cdot \phi}$ labeled by an integer vector $\boldsymbol{l}$. Such excitations are bosonic if their self statistics $\theta_{\boldsymbol{l}} := \pi \boldsymbol{l}^T (\mathbb{K}^{(2)})^{-1} \boldsymbol{l} = 0 \mod 2\pi$. For Abelian topological order, the condensed bosonic excitations on the edge form a group termed the Lagrangian subgroup [158, 20, 263].

The possible edge phases are classified by inequivalent Lagrangian subgroups $\mathcal{M}$. In our case, the allowed subgroup is subject to symmetry constraints, i.e. it is invariant under the global symmetry $\mathcal{G}^{(2)} = \mathbb{Z}_2 \times \mathbb{Z}_2^{\mathbb{H}}$ of the defect theory. Here, $\mathbb{Z}_2$ is an anti-unitary symmetry associated with the Hermitian conjugation in the double Hilbert space, i.e. $\phi_R^I(\bar{\phi}_R^I) \leftrightarrow \phi_L^I(\bar{\phi}_L^I)$ and $i \leftrightarrow -i$, and $\mathbb{Z}_2^{\mathbb{H}}$ is an anti-unitary symmetry originated from the hermiticity of density matrix and acts as $\phi_s^I \leftrightarrow \bar{\phi}_s^I$ with $s = L, R$ and $i \leftrightarrow -i$ [5][6]. Furthermore, the interaction only creates specific excitations: paired anyon $\alpha_s \bar{\alpha}_s = e^{i\boldsymbol{l}^T \cdot (\phi_s - \bar{\phi}_s)}$ by the incoherent errors, and $\alpha_L \alpha_R' = e^{i\boldsymbol{l}^T \cdot (\phi_L + \phi_R)}$, $\bar{\alpha}_L \bar{\alpha}_R' = e^{-i\boldsymbol{l}^T \cdot (\bar{\phi}_L + \bar{\phi}_R)}$ by $\mathcal{L}_1$. This requires the condensed object in $\mathcal{M}$ to be the fusion of such paired anyons.

The Lagrangian subgroup $\mathcal{M}$ therefore must satisfy the following criteria:

1. $e^{i\theta_{\boldsymbol{mm'}}} = 1, \forall \boldsymbol{m}, \boldsymbol{m'} \in \mathcal{M}$;

2. $\forall \boldsymbol{l} \notin \mathcal{M}, \exists \boldsymbol{m}$ s.t. $e^{i\theta_{\boldsymbol{ml}}} \neq 1$;

3. $\forall \boldsymbol{m} \in \mathcal{M}, g\boldsymbol{m}g^{-1} \in \mathcal{M}, \forall g \in \mathcal{G}^{(2)}$;

4. (Incoherent error) $[\boldsymbol{1}, \boldsymbol{1}, -\boldsymbol{1}, -\boldsymbol{1}]^T \cdot \boldsymbol{m} = 0 \mod \mathbb{K}^{(2)}\Lambda, \forall \boldsymbol{m} \in \mathcal{M}$ [7].

---

[5] The K-matrix $\mathbb{K}^{(2)}$ flips sign under the anti-unitary symmetry, however, the Lagrangian $\mathcal{L}_0$ is invariant as the minus sign cancels that from the imaginary identity.

[6] The effective theory for the norm of the EFD $\langle\!\langle\rho|\rho\rangle\!\rangle = \operatorname{tr}\rho^2$ is expected to have a $\mathbb{Z}_2$ unitary symmetry permuting two copies of density matrix. This permutation is a combination of the Hermitian conjugation of the EFD and that of the density matrix and thus is included in $\mathcal{G}^{(2)}$.

[7] The equation is held modulo physical excitations, where Λ is an integer vector. $\boldsymbol{1}$ is a vector with each component being 1 and of the same dimension as the matrix K.

Here, $\theta_{\boldsymbol{ml}} := 2\pi \boldsymbol{m}^T (\mathbb{K}^{(2)})^{-1} \boldsymbol{l}$ characterizes the mutual statistics between two anyons. In three examples, the Toric code, double semion model [159], and $\nu = 1/3$ Laughlin state [155], we enumerate the possible phases (i.e. Lagrangian subgroups) summarized in Table 6.1 (see Appendix E).

6.6   Discussion

We have introduced the errorfield double formulation to characterize the breakdown of quantum memories described by Abelian topological orders, generalizing error recovery transitions in specific quantum codes. We showed that the breakdown of quantum memories corresponds to a boundary transition in a replicated theory consisting of $n \geq 2$ copies of the topological order and its conjugate. We focused on the $n = 2$ case and incoherent errors and classified the possible phases. Our results are ripe for multiple lines of generalization.

One useful extension is to characterize the effect of quantum channels that include coherent errors [42, 123, 128, 254, 24]. A physically important example is provided by amplitude damping errors applied to the toric code [72, 71]. Here, the decoherence involves terms that can drive condensation of anyons in a single-copy Hilbert space (i.e. α or $\bar{\alpha}$). The corresponding Lagrangian subgroup does not need to satisfy the fourth criterion, allowing for the establishment of additional decoherence-induced phases (see Appendix E).

Another future direction is to investigate the effect of decoherence in non-Abelian topologically ordered states. Here, decoherence can affect the capacity to perform protected quantum computation in the fusion space [190]. One complication is that errors are intrinsically "coherent" as incoherent errors can generate anyons in the individual ket or bra copy due to non-Abelian fusion rules.

The existence of an error recovery threshold suggests that the decoherence-induced phases can be characterized by information-theoretic properties. In Chapter 7, we propose information-theoretic diagnostics of the topological order in corrupted mixed states and demonstrate their consistency in a concrete example of the Toric code under incoherent errors. The EFD framework allows computing quadratic functions of the density matrix and therefore correspond to second Rényi versions of the information-theoretic quantities. However, the framework is generalizable to a replicated theory of the (1+1)D defect, allowing us to analyze the n-th moment of ρ (see Appendix E). The information-theoretic quantities is obtained in the limit $n \to 1$. We expect that the classification in Table 6.1 still holds in this limit (see Appendix E).

Finally, the EFD formalism can be applied to the investigation of mixed states beyond topologically ordered systems. Decoherence-induced transitions may occur in other states that encode information nonlocally, such as fracton systems [107, 261] and quantum low-density parity check codes [45]. The recently proposed average symmetry-protected topological phases [176, 157, 280] is another problem that can be possibly characterized in the EFD formulation.

Model	Memory	Edge condensate (generators of Lagrangian subgroup)		Error that realizes the phase
Toric code $K_{\mathrm{TC}} = \begin{pmatrix} 0 & 2 \\ 2 & 0 \end{pmatrix}$	Quantum	I	$e_L \bar{e}_R,\ \bar{e}_L \bar{e}_R,\ m_L m_R,\ \bar{m}_L \bar{m}_R$	No error
	Classical	II	$e_L \bar{e}_L,\ e_R \bar{e}_R,\ e_L \bar{e}_R,\ m_L \bar{m}_L m_R \bar{m}_R$	Incoherent e error
	Classical	III	$m_L \bar{m}_L,\ m_R \bar{m}_R,\ m_L \bar{m}_R,\ e_L \bar{e}_L e_R \bar{e}_R$	Incoherent m error
	Classical	IV	$f_L \bar{f}_L,\ f_R \bar{f}_R,\ f_L \bar{f}_R,\ e_L \bar{e}_L e_R \bar{e}_R$	Incoherent f error
	Trivial	V	$e_L \bar{e}_L,\ e_R \bar{e}_R,\ m_L \bar{m}_L,\ m_R \bar{m}_R$	Any two types of incoherent errors
Double semion $K_{\mathrm{DS}} = \begin{pmatrix} 2 & 0 \\ 0 & -2 \end{pmatrix}$	Quantum	I	$m_{aL} m_{aR},\ \bar{m}_{aL} \bar{m}_{aR},\ m_{bL} m_{bR},\ \bar{m}_{bL} \bar{m}_{bR}$	No error
	Quantum	II	$m_{aL} \bar{m}_{aL},\ m_{aR} \bar{m}_{aR},\ m_{bL} m_{bR},\ \bar{m}_{bL} \bar{m}_{bR}$	Incoherent m_a error
	Quantum	III	$m_{bL} \bar{m}_{bL},\ m_{bR} \bar{m}_{bR},\ m_{aL} m_{aR},\ \bar{m}_{aL} \bar{m}_{aR}$	Incoherent m_b error
	Quantum	IV	$b_L \bar{b}_L,\ b_R \bar{b}_R,\ b_L b_R,\ m_{aL} \bar{m}_{aL} m_{aR} \bar{m}_{aR}$	Incoherent b error
	Trivial	V	$m_{aL} \bar{m}_{aL},\ m_{aR} \bar{m}_{aR},\ m_{bL} \bar{m}_{bL},\ m_{bR} \bar{m}_{bR}$	Any two types of incoherent errors
Laughlin state $\nu = 1/3$, $K_{1/3} = (3)$	Quantum	I	$\eta_L^2 \eta_R^2,\ \bar{\eta}_L^2 \bar{\eta}_R^2$	No error
	Trivial	II	$\eta_L \bar{\eta}_L,\ \eta_R \bar{\eta}_R$	Incoherent error for quasiparticles

Table 6.1: Decoherence-induced phases in the Toric code, double semion model, and $\nu = 1/3$ Laughlin state subject to incoherent errors. Distinct phases are labeled by Lagrangian subgroups. The Toric code model contains four superselection sectors, $\{1, e, m, f\}$, where the anyon e and m are self-bosons and mutual semions, and $e \times m = f$ is a fermion. The double-semion model also has four sectors $\{1, m_a, m_b, b\}$, where m_a, m_b are semion and anti-semion, and their fusion $m_a \times m_b = b$ is a boson. The $\nu = 1/3$ Laughlin state has three sectors $\{1, \eta, \eta^2\}$, where η and η^2 are the quasiparticle and quasihole, respectively. α_s and $\bar{\alpha}_s$ denote the anyon α in the ket and bra Hilbert space, while $s = L, R$ represent the left and right copy. Here, only the generators of the Lagrangian subgroup are listed. The fusion of any two generators is also in the subgroup and is condensed on the edge. In the last column, we comment on the error channel that realizes each phase.

Chapter 7

Diagnostics of mixed-state topological order

7.1   Introduction

The major roadblock to realizing quantum computers is the presence of errors and decoherence from the environment which can only be overcome by adopting quantum error correction (QEC) and fault tolerance [98]. A first step would be the realization of robust quantum memories [53, 242, 247]. Topologically ordered systems in two spatial dimensions, owing to their long-range entanglement and consequent degenerate ground states, serve as a promising candidate [190, 265, 145, 94]. A paradigmatic example is the surface code [43, 74], whose promise as a robust quantum memory has stimulated recent interest in its realization in near-term quantum simulators [193, 226, 255, 234, 34, 5, 11].

One of the central quests is to analyze the performance of topological quantum memory under *local* decoherence. In the case of surface code with bit-flip and phase errors, it has been shown that the stored information can be decoded reliably up to a finite error threshold [74]. Namely, as the error rate increases, the success probability of the decoding algorithm drops to zero at a critical value that depends on the choice of the algorithm. These decoding transitions imply an error-induced singularity in the mixed state of the system. The algorithmic dependence of the error thresholds is a mere reflection of the suboptimality of specific algorithms. It is then natural to inquire how this transition can be probed through the behavior of intrinsic properties of the quantum state.

Such a characterization has at least two important consequences. First, the critical error rate for the intrinsic transition should furnish an upper bound for decoding algorithms, saturating which implies that the optimal decoder has been found. Second, the correspondence between successful decoding and intrinsic properties of the quantum state acted upon by errors points to the existence of topologically distinct mixed states. In another word, answering this question amounts to relating the breakdown of topological quantum memory to a transition in the mixed-state topological order. Progress towards this goal lies in quantifying the residual

long-range entanglement in the error-corrupted mixed state. We will consider quantities that are motivated from both perspectives and explore their unison.

In this work, we investigate three information-theoretical diagnostics: (i) quantum relative entropy between the error-corrupted ground state and excited state; (ii) coherent information; (iii) topological entanglement negativity. The first two are natural from the perspective of quantum error correction (QEC). More specifically, the quantum relative entropy quantifies whether errors ruin orthogonality between states [147], and coherent information is known to give robust necessary and sufficient conditions on successful QEC [230, 231, 120]. The third one is a basis-independent characterization of long-range entanglement in mixed states and is more natural from the perspective of mixed-state topological order. This quantity has been proposed to diagnose topological orders in Gibbs states [171, 172], which changes discontinuously at the critical temperature. We borrow and apply this proposal to error-corrupted states. Our transition occurs in two spatial dimensions at a finite error rate, in contrast to the finite temperature transitions in four spatial dimensions.

The presence of three seemingly different diagnostics raises the question of whether they all agree and share the same critical error rate. Satisfyingly, we indeed find this to be the case in a concrete example, surface code with bit-flip and phase errors. The n-th Rényi version of the three quantities can be formulated in a *classical* two-dimensional statistical mechanical model of $(n-1)$-flavor Ising spins, which exhibits a transition from a paramagnetic to a ferromagnetic phase as the error rate increases. The three quantities are mapped to different probes of the ferromagnetic order and must undergo the transition simultaneously, which establishes their consistency in this concrete example.

Interestingly, the statistical mechanical model derived for the information-theoretic diagnostics is exactly dual to the random-bond Ising model (RBIM) that governs the decoding transition of the algorithm proposed in [74]. This duality implies that the error threshold of the algorithm in [74] saturates the upper bound. Therefore, it confirms that this decoding algorithm is optimal, and its threshold reflects the intrinsic properties of the corrupted state. We remark that mappings to statistical mechanical models have been tied to obtaining error thresholds of decoding algorithms [74, 262, 135, 36, 151, 66]. Here such mappings arise from characterizing intrinsic properties of the error corrupted mixed state.

The rest of the Chapter is organized as follows. Sec. 7.2 gives a concrete definition of the error-corrupted states and introduces the three diagnostics. Sec. 7.3 studies the concrete example, the 2D Toric code subject to local bit-flip and phase errors. We close with discussions in Sec. 7.4.

7.2 Setup and diagnostics

In this section, we begin with introducing the error-corrupted mixed state. We show that any operator expectation value in a single-copy corrupted density matrix cannot probe the transition, and instead one needs to consider the non-linear functions of the density matrix. Next, we introduce three information-theoretic diagnostics of the transition: (i) quantum

relative entropy; (ii) coherent information; (iii) topological entanglement negativity. These quantities generalize the diagnostics of ground-state topological order.

Error-corrupted mixed state

The type of mixed state we consider throughout the Chapter describes a topologically ordered ground state $\rho_0 = |\Psi_0\rangle \langle \Psi_0|$ subject to local errors

$$\rho = \mathcal{N}[\rho_0] = \prod_i \mathcal{N}_i[\rho_0], \tag{7.1}$$

where the quantum channel $\mathcal{N}_i$ models the local error at site i and is controlled by the error rate p. We refer to ρ as the error-corrupted mixed state.

The transition in the corrupted state, if exists, cannot be probed by the operator expectation value in a single-copy density matrix. To demonstrate it, we purify the corrupted state by introducing one ancilla qubit prepared in $|0\rangle_i$ for each physical qubit at site i. The physical and ancilla qubits are coupled locally via unitary $U_i(p)$ such that tracing out the ancilla qubits reproduces the corrupted state ρ. This leads to a purification

$$|\Phi\rangle = \prod_i U_i(p) |\Psi_0\rangle (\otimes_i |0\rangle_i), \tag{7.2}$$

which is related to the topologically ordered state by a depth-1 unitary circuit on the extended system [see Fig. 7.1]. It follows that the expectation value of *any* operator supported on a large but finite region of the physical qubits, e.g., a Wilson loop operator, must be a smooth function of the error rate [see Fig. 7.1 for a schematics]. Thus, it is indispensable to consider the non-linear functions of the density matrix, e.g. quantum information quantities, to probe the transition in the corrupted state. This property holds when ρ describes a general mixed state in the ground-state subspace under local errors.

We remark that the above argument does not prevent observables in a single-copy density matrix from detecting topological order in finite-temperature Gibbs states [112]. The key difference is the purifications of the Gibbs states at different temperatures are not necessarily related by finite-depth circuits.

Quantum relative entropy

Anyon excitations are crucial for storing and manipulating quantum information in a topologically ordered state. For example, to change the logical state of the code one creates a pair of anyons out of the vacuum and separates them to opposite boundaries of the system. The first diagnostic tests if the process of creating a pair of anyons and separating them by a large distance gives rise to a distinct state in the presence of decoherence.

Specifically, we want to test if the corrupted state $\rho = \mathcal{N}[\rho_0]$ is sharply distinct from $\rho_\alpha = \mathcal{N}[w_\alpha(\mathcal{P})\rho_0 w_\alpha(\mathcal{P})^\dagger]$. In the second state, $w_\alpha(\mathcal{P})$ is an open string operator that creates
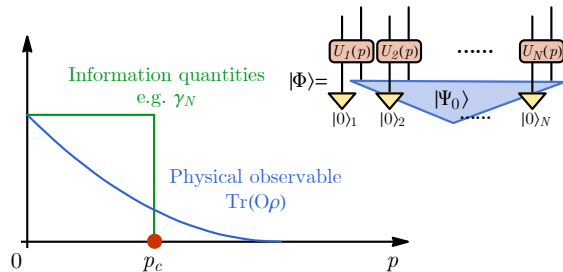
Figure 7.1: Physical observables verses information quantities in error corrupted states. Each error corrupted state can be obtained from applying local unitaries to the system (topological order) plus ancilla qubits (trivial product state). Thus, physical observables must be smooth functions of the error rate p. In contrast, information quantities, e.g. the topological entanglement negativity γ_N, can have discontinuities that identify the many-body singularities.

an anyon α and its anti-particle α' at the opposite ends of the path $\mathcal{P}$. We use the *quantum relative entropy* as a measure for the distinguishability of the two states

$$D(\rho||\rho_\alpha) := \operatorname{tr} \rho \log \rho - \operatorname{tr} \rho \log \rho_\alpha \,. \tag{7.3}$$

In absence of errors the relative entropy is infinite because the two states are orthogonal, and it decreases monotonically with the error rate [168, 14, 169]. Below the critical error rate, however, the states should remain perfectly distinguishable if the anyons are separated by a long distance. Therefore we expect the relative entropy to diverge as the distance between the anyons is taken to infinity. Above the critical error rate on the other hand we expect the relative entropy to saturate to a finite value reflecting the inability to perfectly distinguish between the two corrupted states. In this regard, the relative entropy describes whether anyon excitations remain well-defined and is a generalization of the Fredenhagen-Marcu order parameter for ground state topological order [89, 90, 91, 101].

To facilitate calculations, we consider a specific sequence of the Rényi relative entropies

$$D^{(n)}(\rho||\rho_\alpha) := \frac{1}{1-n} \log \frac{\operatorname{tr} \rho \rho_\alpha^{n-1}}{\operatorname{tr} \rho^n}, \tag{7.4}$$

which recovers $D(\rho||\rho_\alpha)$ in the limit $n \to 1$. In Sec. 7.3 we map the relative entropies $D^{(n)}$ in the corrupted Toric code to order parameter correlation functions in an effective statistical mechanics model, which is shown to exhibit the expected behavior on two sides of the critical error rate.

Coherent information

The basis for protecting quantum information in topologically ordered states is encoding it in the degenerate ground state subspace. The second diagnostic we consider is designed to test the integrity of this protected quantum memory.

We use the *coherent information*, as a standard metric for the amount of quantum information surviving in a channel [230, 231, 120]. In our case, the relevant quantum channel consists of the following ingredients illustrated below. (i) A unitary operator U that encodes the state of the logical qubits in the input R into the ground state subspace. (ii) A unitary coupling U_{QE} of the physical qubits Q to environment qubits E, which models the decoherence. The coherent information in this setup is defined as

$$I_c(R \rangle Q) := S_Q - S_{QR}. \qquad \qquad (7.5)$$

Here S_Q and S_{RQ} are the von Neumann entropies of the systems Q and RQ respectively and we used the Choi map to treat the input R as a reference qubit in the output. It follows from subadditivity that the coherent information is bounded by the amount of encoded information in the degenerate ground state subspace, i.e. $-S_R \leq I_c \leq S_R$. In the absence of errors $I_c = S_R$, and we expect this value to persist as long as the error rate is below the critical value. Above the critical error rate, we expect $I_c < S_R$, indicating the loss of encoded information.

Physically the coherent information is closely related and expected to undergo a transition at the same point as the relative entropy discussed above. The quantum information is encoded by separating anyon pairs across the system. It stands to reason that if this state remains perfectly distinguishable from the original state, as quantified by the relative entropy, then the quantum information encoded in this process is preserved.

The critical error rate for preserving the coherent information is an upper bound for the threshold of any QEC algorithms

$$p_c \geq p_{c,\text{algorithm}}. \qquad \qquad (7.6)$$

The key point is that coherent information is non-increasing upon quantum information processing and cannot be restored once it is lost. Thus, a successful QEC requires $I_c = S_R$. Moreover, the QEC algorithm involves syndrome measurements that are non-unitary and generically do not access the full coherent information in the system giving rise to a lower error threshold.

To facilitate calculations and mappings to a statistical mechanics model we will need the Rényi coherent information

$$I_c^{(n)} := S_Q^{(n)} - S_{RQ}^{(n)} = \frac{1}{n-1} \log \frac{\operatorname{tr} \rho_{RQ}^n}{\operatorname{tr} \rho_Q^n}, \qquad \qquad (7.7)$$

which approaches I_c in the limit $n \to 1$. In the example of Toric code with incoherent errors discussed in Sec. 7.3, we show that $I_c^{(n)}$ takes distinct values in different phases.

Topological entanglement negativity

The topological entanglement entropy provides an intrinsic bulk probe of ground state topological order and does not require a priori knowledge of the anyon excitations. The third diagnostic we consider generalizes this notion to the error-corrupted mixed state.

A natural quantity often used to quantify entanglement in mixed states, is the logarithmic negativity of a sub-region A [206, 119, 260]

$$\mathcal{E}_A(\rho) := \log ||\rho^{T_A}||_1, \tag{7.8}$$

where ρ^{T_A} is the partial transpose on the subsystem A and $|| \cdot ||_1$ denotes the trace (L_1) norm. The logarithmic negativity coincides with the Rényi-1/2 entanglement entropy for the pure state and is non-increasing with the error rate of the channel, a requirement that any measure of entanglement must satisfy [192, 207]. The logarithmic negativity was previously used in the study of ground state topological phases [270, 269, 236] and more recently for detecting topological order in finite temperature Gibbs states [171, 172].

We expect that the universal topological contribution to the entanglement [146, 160] will survive in the corrupted mixed state below a critical error rate and be captured by the logarithmic negativity. Thus, the conjectured form of this quantity is

$$\mathcal{E}_A = c|\partial A| - \gamma_N + \ldots, \tag{7.9}$$

where $|\partial A|$ is the circumference of the region A, c is a non-universal coefficient, and ellipsis denotes terms that vanish in the limit $|\partial A| \to \infty$. The constant term γ_N is the *topological entanglement negativity* of a simply connected subregion A, and is argued to originate from the long-range entanglement [103, 171]. One of the essential reasons for γ_N being topological is the conversion property $\mathcal{E}_A = \mathcal{E}_{\bar{A}}$, i.e. negativity of a subsystem is equal to that of the complement. In contrast, the von Neumann entropy of a subregion in the error-corrupted mixed state exhibits a volume-law scaling, and its constant piece is not topological because of $S_A \neq S_{\bar{A}}$.

To facilitate the calculation of the negativity, we consider the Rényi negativity of even order

$$\mathcal{E}_A^{(2n)}(\rho) := \frac{1}{2 - 2n} \log \frac{\text{tr}\left(\rho^{T_A}\right)^{2n}}{\text{tr}\, \rho^{2n}} . \tag{7.10}$$

The logarithmic negativity is recovered in the limit $2n \to 1$. Here, we choose a particular definition of the Rényi negativity such that it exhibits an area-law scaling in the corrupted state. In Sec. 7.3, we show explicitly that in the Toric code the topological part $\gamma_N^{(2n)}$ of the Rényi negativity takes a quantized value $\log 2$ in the phase where the quantum memory is retained and vanishes otherwise.

To summarize, we expect the topological negativity takes the same universal value as the topological entanglement entropy in the uncorrupted ground state and drops sharply to a lower value at a critical error rate. It is *a priori* not clear, however, that the transition in the

negativity must occur at the same threshold as that marks the transition of the other two diagnostics we discussed. In Sec. 7.3 we show, through mapping to a statistical mechanics model that, in the example of the Toric code, a single phase transition governs the behavior of all three diagnostics.

Diagnostics	Observable	PM	FM
$D^{(n)}$	Logarithm of order parameter correlation function	$O(\|i_l - i_r\|)$	$O(1)$
$I_c^{(n)}$	Related to the excess free energy for domain walls along non-contractible loops	$2\log 2$	0
$\mathcal{E}_A^{(2n)}$	Excess free energy for aligning spins on the boundary of A	$c\|\partial A\|/\xi - \log 2$	$c\|\partial A\|/\xi$

Table 7.1: Dictionary of the mapping. The Rényi-n version of the diagnostics of topological order in error corrupted states and their corresponding observables in $(n-1)$-flavor Ising models are listed in the first and second columns, respectively. We consider 2D Toric code subject to one type of incoherent error (bit-flip or phase errors). The asymptotic behaviors of these diagnostics in the paramagnetic (PM) and ferromagnetic (FM) phases of the spin model are provided.

7.3 Example: Toric code under bit-flip and phase errors

In this section, we use the three information-theoretical diagnostics to probe the distinct error-induced phases in the 2D Toric code under bit-flip and phase errors. In particular, we develop 2D classical statistical mechanical models to analytically study the Rényi-n version of the diagnostics in this example. The statistical mechanical models involve $(n-1)$-flavor Ising spins and undergo ferromagnetic phase transitions as a function of error rates. We show that the three diagnostics map to distinct observables that all detect the ferromagnetic order and undergo the transition simultaneously. We remark that our results also apply to the planar code.

In Sec. 7.3, we introduce the Toric code and the error models. We derive the statistical mechanical models in Sec. 7.3 and analyze the phase transition in Sec. 7.3. Sec. 7.3 discusses the three diagnostics and their corresponding observables in the statistical mechanical models. See Table 7.1 for a summary. We discuss the replica limit $n \to 1$ in Sec. 7.3.

Toric code and error model

We consider the 2D Toric code on an $L \times L$ square lattice with periodic boundary conditions. This code involves $N = 2L^2$ physical qubits on the edges of the lattice, and its code space is given by the ground state subspace of the Hamiltonian

$$H_{\mathrm{TC}} = -\sum_s A_s - \sum_p B_p \,, \tag{7.11}$$

where A_s and B_p are mutually commuting operators associated with vertices and plaquettes

$$A_s = \prod_{\ell \in \mathrm{star}(s)} X_\ell \,, \quad B_p = \prod_{\ell \in \mathrm{boundary}(p)} Z_\ell \,. \tag{7.12}$$

Here, X_ℓ and Z_ℓ denote the Pauli-X and Z operators on edge ℓ, respectively. The ground state satisfying $A_s |\Psi\rangle = B_p |\Psi\rangle = |\Psi\rangle$ is four-fold degenerate and can encode two logical qubits.

We consider specific error channels describing uncorrelated single-qubit bit-flip and phase errors

$$\begin{aligned} \mathcal{N}_{X,i}[\rho] &= (1 - p_x)\rho + p_x X_i \rho X_i \,, \\ \mathcal{N}_{Z,i}[\rho] &= (1 - p_z)\rho + p_z Z_i \rho Z_i \,, \end{aligned} \tag{7.13}$$

where the Pauli-X (Z) operator acting on the Toric code ground state creates a pair of m (e) anyons on the adjacent plaquettes (vertices), p_x and p_z are the corresponding error rates. The corrupted state reads

$$\rho = \mathcal{N}_X \circ \mathcal{N}_Z[\rho_0] \,,$$

where $\mathcal{N}_{X(Z)} = \prod_i \mathcal{N}_{X(Z),i}$. We assume that the error rate is uniform throughout our discussion.

We make a few remarks. First, the error channels in Eq. (7.13) do not create coherent superposition between states with different anyon configurations and are referred to as incoherent errors. Second, Pauli-Y errors create f anyons incoherently and can also be analyzed. It leads to a similar physics and will be not discussed in the work.
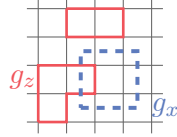
Statistical mechanical models

Here, we map the n-th moment of the corrupted density matrix $\mathrm{tr}\, \rho^n$ to the partition function of the $(n-1)$-flavor Ising model. In this statistical mechanical model, one can analyze the singularity in the Rényi version of the three diagnostics, which will be presented in Sec. 7.3.

To begin, we consider the maximally mixed state in the ground state subspace

$$\rho_0 = \frac{1}{4} \prod_s \frac{1 + A_s}{2} \prod_p \frac{1 + B_p}{2} \,. \tag{7.14}$$

For our purpose here, it is convenient to write ρ_0 in a loop picture

$$\rho_0 = \frac{1}{2^N} \sum_{g_z} g_z \sum_{g_x} g_x \,, \tag{7.15}$$

where g_z and g_x are Z and X loops on the original and dual lattice given by the product of A_s and B_p operators, respectively. The summation runs over all possible loop configurations. In what follows, we will use $g_{x(z)}$ to denote both the operators and the loop configurations. The meaning will be clear in the context.

Two error channels act on the loop operators g_x, g_z by only assigning a real positive weight:

$$\mathcal{N}_{X,i}[g_z] = \begin{cases} (1 - 2p_x)g_z & Z_i \in g_z \\ g_z & Z_i \notin g_z \end{cases},$$

$$\mathcal{N}_{Z,i}[g_x] = \begin{cases} (1 - 2p_z)g_x & X_i \in g_x \\ g_x & X_i \notin g_x \end{cases}.$$

Thus, the corrupted state remains a superposition of loop operators

$$\rho = \frac{1}{2^N} \sum_{g_x, g_z} e^{-\mu_x|g_x| - \mu_z|g_z|} g_x g_z, \tag{7.16}$$

where $|g_{x(z)}|$ denotes the length of the loop, and $\mu_{x(z)} = -\log(1 - 2p_{z(x)})$ can be understood as the line tension. Using Eq. (7.16), it is straightforward to see that the expectation values of operators, such as the Wilson loop and open string, behave smoothly as the error rate increases, in consistence with the general argument in Sec. 7.2.

Using this loop picture Eq. (7.16), we can write the n-th moment as

$$\text{tr}\,\rho^n = \frac{1}{2^{nN}} \sum_{\{g_x^{(s)}, g_z^{(s)}\}} \text{tr}\left(\prod_{s=1}^{n} g_x^{(s)} g_z^{(s)}\right) \tag{7.17}$$

$$e^{\sum_s -\mu_x|g_x^{(s)}| - \mu_z|g_z^{(s)}|},$$

where $g_{x(z)}^{(s)}$, $s = 1, 2, \cdots, n$ is the $X(Z)$ loop operator from the s-th copy of density matrix. The product of loop operators in Eq. (7.17) has a nonvanishing trace only if the products of X and Z loops are proportional to identity individually, which leads to two independent constraints

$$g_a^{(n)} = \prod_{s=1}^{n-1} g_a^{(s)}, \quad a = x, z \,. \tag{7.18}$$

The n-th moment factorizes into a product of two partition functions
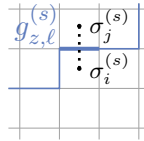
$$\text{tr}\,\rho^n = \frac{1}{2^{(n-1)N}} \mathcal{Z}_{n,x} \mathcal{Z}_{n,z} \,, \tag{7.19}$$

where $\mathcal{Z}_{n,a} = \sum_{\{g_a^{(s)}\}} e^{-H_{n,a}}$ with $a = x, z$ is a statistical mechanics model that describes fluctuating $X(Z)$ loops with a line tension. The Hamiltonian takes the form

$$H_{n,a} = \mu_a \left(\sum_{s=1}^{n-1} |g_a^{(s)}| + |\prod_{s=1}^{n-1} g_a^{(s)}| \right). \tag{7.20}$$

Here, we have imposed the constraints (7.18), and the summation in each partition function runs over the loop configurations only in the first $n - 1$ copies.

The loop model can be mapped to a statistical mechanical model of $n - 1$ flavors of Ising spins with nearest neighbor ferromagnetic interactions. The mapping is established by identifying the loop configuration $g_a^{(s)}$ with $s = 1, 2, \ldots, n - 1$ with domain walls of Ising spins. Specifically, for a Z loop configuration on the original lattice, we associate a Ising spin configuration σ_i on the dual lattice such that

$$\left| g_{z,\ell}^{(s)} \right| = \left(1 - \sigma_i^{(s)} \sigma_j^{(s)} \right) / 2,$$

where i, j are connected by the link dual to ℓ, and $|g_{z,\ell}^{(s)}|$ is a binary function that counts the support of loop on link ℓ. The total length of the loop is given by $|g_z^{(s)}| = \sum_\ell |g_{z,\ell}^{(s)}|$. Similarly, we can define the Ising spins on the original lattice that describe the X loop configuration on the dual lattice.

In terms of the Ising spins, the effective Hamiltonian is given by

$$H_{n,a} = -J_a \sum_{\langle i,j \rangle} \left(\sum_{s=1}^{n-1} \sigma_i^{(s)} \sigma_j^{(s)} + \prod_{s=1}^{n-1} \sigma_i^{(s)} \sigma_j^{(s)} \right) \tag{7.21}$$

with a ferromagnetic coupling $J_{x(z)} = -\log \sqrt{1 - 2p_{z(x)}}$. In what follows, we refer to this model as the $(n - 1)$-*flavor Ising model*. We remark that the model exhibits a global symmetry $G^{(n)} = (\mathbb{Z}_2^{\otimes n} \rtimes \mathcal{S}_n)/\mathbb{Z}_2$, where $\mathcal{S}_n$ is the permutation symmetry over n elements. As is shown below, increasing the error rate the model undergoes a paramagnetic-to-ferromagnetic transition that completely breaks the $G^{(n)}$ symmetry.

Phase transitions

Here, we study the ferromagnetic transition in the $(n - 1)$-flavor Ising model. The transition points depend on n and are determined using both analytical methods (e.g. Kramers-Wannier duality for $n = 2, 3$) and Monte-Carlo simulation (for $n = 4, 5, 6$, etc). The results are presented in Fig. 7.2.

For $n = 2$, the statistical mechanical model is the standard square lattice Ising model:

$$H_{2,a} = -2J_a \sum_{\langle i,j \rangle} \sigma_i \sigma_j. \tag{7.22}$$
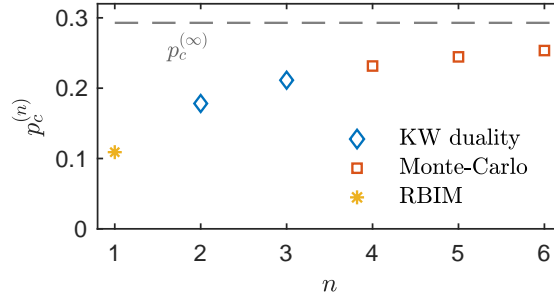
Figure 7.2: Critical error rates for various Rényi index n. $p_c^{(2)} \approx 0.178$ and $p_c^{(3)} \approx 0.211$ are determined by the exact solution (blue diamonds). For $n \geq 4$, $p_c^{(n)}$ is determined by calculating the crossing of the Binder ratio for various system sizes via Monte-Carlo (red squares). $p_c^{(n)}$ in the replica limit $n \to 1$ (the yellow star) is given by the critical point of random-bond Ising model (RBIM) in 2D, $p_c^{(1)} \approx 0.109$, as explained in Sec. 7.3. In the limit $n \to \infty$, the spin model is asymptotically decoupled Ising models with $p_c^{(\infty)} \approx 0.293$ (the grey dashed line).

The critical point is determined analytically by the Kramers-Wannier duality [211, 142]

$$p_c^{(2)} = \frac{1}{2}\left(1 - \sqrt{\sqrt{2}-1}\right) \approx 0.178. \tag{7.23}$$

For $n = 3$, the model becomes the Ashkin-Teller model on 2D square lattice along the $\mathcal{S}_4$ symmetric line. The Hamiltonian is

$$H_{3,a} = -J_a \sum_{\langle i,j \rangle} \sigma_i^{(1)}\sigma_j^{(1)} + \sigma_i^{(2)}\sigma_j^{(2)} + \sigma_i^{(1)}\sigma_i^{(2)}\sigma_j^{(1)}\sigma_j^{(2)}. \tag{7.24}$$

The model is equivalent to the standard four-state Potts model [149] with a critical point determined by the Kramers-Wannier duality

$$p_c^{(3)} = \frac{1}{2}\left(1 - \frac{1}{\sqrt{3}}\right) \approx 0.211. \tag{7.25}$$

For $n \geq 4$, we are not aware of any exact solution and resort to the Monte-Carlo simulation. To locate the transition point p_c, we consider the average magnetization per spin,

$$m := \frac{1}{(n-1)L^2} \sum_{s=1}^{n-1} \sum_i \sigma_i^{(s)}. \tag{7.26}$$

We calculate the magnetization square $\langle m^2 \rangle$ and the Binder ratio $B = \langle m^4 \rangle / \langle m^2 \rangle^2$ numerically and display the results in Fig. 7.3. Assuming a continuous transition, we determine $p_c^{(n)}$ by
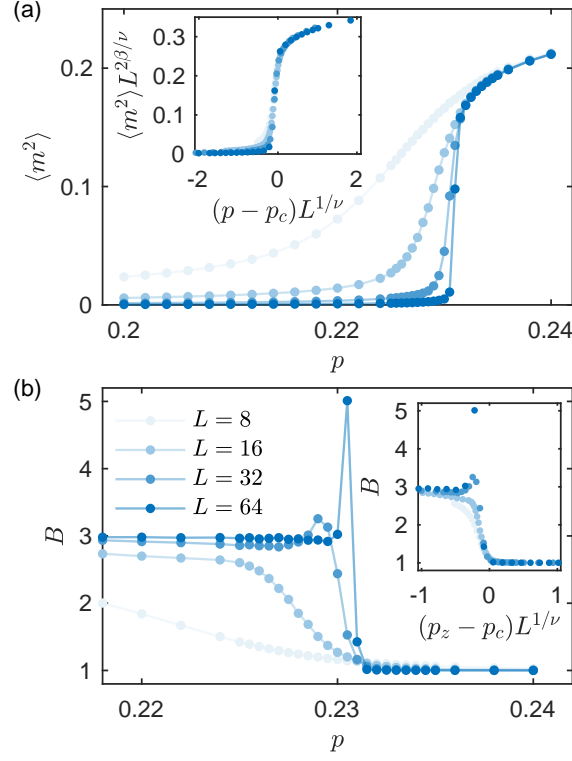
Figure 7.3: Phase transition in the statistical mechanical model for $n = 4$. Magnetization (a) and Binder ratio (b) as a function of error rate p for various system sizes up to $L_x = L_y = L = 64$. The crossing of $B(p, L)$ yields $p_c = 0.231$. The exponents $\nu = 0.74$ and $\beta = 0.04$ are extracted from the finite-size scaling collapse in the insets. The results are averaged over 10^5 independent Monte-Carlo measurements for each of 48 initial configurations.

the crossing point of $B(p, L)$ for various system sizes L and extract the critical exponents using the scaling ansatz $B(p, L) = \mathcal{F}_b((p - p_c)L^{1/\nu})$ and $\langle m^2 \rangle(p, L) = L^{-2\beta/\nu}\mathcal{F}_m((p - p_c)L^{1/\nu})$. The analysis yields $p_c^{(4)} = 0.231$ for $n = 4$. However, the sharp drop of magnetization and the non-monotonic behavior of $B(p, L)$ near $p_c^{(4)}$ hint at a possible first-order transition [32, 125].

The critical error threshold p_c increases monotonically with n and is exactly solvable in the limit $n \to \infty$. In this case, the interaction among different flavors is negligible compared to the two-body Ising couplings. Thus, the critical point is asymptotically the same as that in the Ising model with coupling J_a and is given by

$$p_{a,c}^{(\infty)} = \frac{1}{2}\left(2 - \sqrt{2}\right) \approx 0.293. \tag{7.27}$$

Three diagnostics

The Rényi version of the three information theoretic diagnostics, quantum relative entropy, coherent information, and topological entanglement negativity, translate into distinct physical quantities in the statistical mechanical model. We write these quantities explicitly below and show that all three detect the establishment of ferromagnetic order. Therefore the transition in all three quantities is governed by the same critical point, a fact that is not evident before mapping to statistical mechanical models.

Quantum relative entropy

We start with the Rényi version of the quantum relative entropy given by Eq. (7.4). Let ρ be the corrupted ground state of the Toric code, and $\rho_m = \mathcal{N}[|\Psi_m\rangle \langle\Psi_m|]$ where $|\Psi_m\rangle :=$ $w_m(\mathcal{C}) |\Psi_0\rangle$ has a pair of m-particles at the end of path $\mathcal{C}$. The phase errors do not change the distinguishability between the two states and can be safely ignored here. Only the statistical mechanics model for the Z loops/spins is relevant. Let i_ℓ and i_r denote the positions of two m-particles, we show in Appendix F.1 that the Rényi relative entropy is mapped to a two-point function of the Ising spins

$$D^{(n)}(\rho||\rho_\alpha) = \frac{1}{1-n} \log\langle\sigma_{i_\ell}^{(1)}\sigma_{i_r}^{(1)}\rangle, \tag{7.28}$$

where $\sigma_j^{(1)}$ is the first flavor of the Ising spin at site j, and the subscription z is suppressed.

When the error rate is small and the system is in the paramagnetic phase, the correlation function decays exponentially, and thus $D^{(n)} = O(|i_\ell - i_r|)$ which grows linearly with the distance between i_ℓ and i_r. This indicates that the error-corrupted ground state and excited state remain distinguishable. When the error rate exceeds the critical value and the system enters the ferromagnetic phase, $D^{(n)}$ is of $O(1)$ due to the long-range order, which implies that the error-corrupted ground state and excited state are no longer distinguishable.

Coherent information

Next consider the Rényi version of the coherent information $I_c^{(n)}$ in Eq. (7.7). We let the two logical qubits in the system Q be maximally entangled with two reference qubits R. As detailed in Appendix F.1, $I_c^{(n)}$ can be mapped to the free energy cost of inserting domain walls along non-contractible loops that are related to the logical operators. More explicitly, let $\mathbf{d}_{al}$ with $a = x, z$ and $l = l_1, l_2$ be a $(n-1)$-component binary vector. Each component of $\mathbf{d}_{al}$ dictates the insertion of domain walls for $a = x, z$ spins along the non-contractible loop l, respectively, in $n - 1$ copies of the Ising spins. Here, along the domain walls, the couplings between nearest neighbor spins are flipped in sign and turned anti-ferromagnetic. Then, we have

$$I_c^{(n)} = \frac{1}{n-1} \sum_{a=x,z} \log\left(\sum_{\mathbf{d}_{a1}\mathbf{d}_{a2}} e^{-\Delta F_{n,a}^{(\mathbf{d}_{a1},\mathbf{d}_{a2})}} \right) - 2\log 2, \tag{7.29}$$
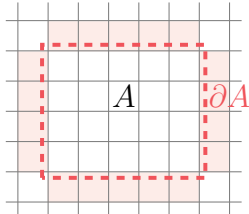
Figure 7.4: Entanglement negativity between region A and its compliment $\bar{A}$ corresponds to the excess free energy for aligning Ising spins on the boundary of A (pink plaquettes) pointing to the same direction.

where $\Delta F_{n,a}^{(\mathbf{d}_{a1}, \mathbf{d}_{a2})}$ is the free energy cost associated with inserting domain walls labeled by binary vectors $\mathbf{d}_{al}$, the sum runs over all possible $\mathbf{d}_{al}$.

   When the error rate is small and the system is in the paramagnetic phase, the domain wall along a non-contractible loop costs nothing, i.e. $\Delta F_{n,a}^{(\mathbf{d}_{a1}, \mathbf{d}_{a2})} = 0$. It follows that the corrupted state retains the encoded information, i.e. $I_c^{(n)} = 2\log 2$. When the error rate exceeds the critical value and the system enters the ferromagnetic phase, inserting a domain wall will have a free energy cost that is proportional to its length. Namely, $\Delta F_{n,a}^{(\mathbf{d}_{a1}, \mathbf{d}_{a2})}$ is proportional to the linear system size unless no defect is inserted. One can deduce $I_c^{(n)} = 0$ when the spin model for either Z or X loop undergoes a transition to the ferromagnetic phase, namely, the corrupted state corresponds to a classical memory. When both spin models are in the ferromagnetic phase, we have $I_c^{(n)} = -2\log 2$, indicating that the system is a trivial memory.

Topological entanglement negativity

The Rényi negativities of even order are given in Eq. (7.10). Let us specialize here to the Toric code with only phase errors. As shown in Appendix F.1, the $2n$-th Rényi negativity of a region A is given by

$$\mathcal{E}_A^{(2n)} = \Delta F_A \,, \tag{7.30}$$

where ΔF_A is the excess free energy associated with aligning a single flavor of Ising spins on the boundary ∂A in the same direction (illustrated in Fig. 7.4).

   The excess free energy ΔF_A, or more precisely, its subleading term can probe the ferromagnetic transition in the statistical-mechanical model. The excess free energy has two contributions. The energetic part is always proportional to $|\partial A|$. The entropic part is attributed to the loss of degrees of freedom due to the constraint. In the paramagnetic phase, the Ising spins fluctuate freely above the scale of the finite correlation length ξ. Hence, enforcing each constraint removes $O(|\partial A|/\xi)$ degrees of freedom proportional to the circumference of A, which yields the leading term (area law). Importantly, there is still one residual degree of freedom, namely, the aligned boundary spins can fluctuate together, which
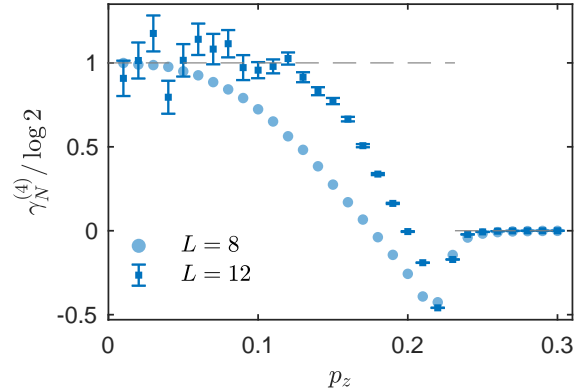
Figure 7.5: Topological negativity $\gamma_N^{(4)}$ as a function of the phase error rate p_z. We consider the subsystems A, B, and C as in Eq. (7.31) and choose the side of the region ABC to be $L/4$. $\gamma_N^{(4)}$ approaches $\log 2$ and zero at small and large p_z, respectively. The curves become steeper as the system size L increases. The dashed line indicates the predicted behavior in the thermodynamic limit. The results are averaged over 10^7 independent Monte-Carlo measurements from each of $48, 96$ random initial configurations for $L = 8, 12$, respectively. The errorbars for $L = 8$ are negligible and thus omitted.

results in a subleading term $\log 2$. Altogether, we have $\mathcal{E}_A^{(2n)} = c|\partial A|/\xi - \log 2$. Here, it is an interesting question to verify whether the prefactor c is universal or not [179], and we leave it for future study [1]. In the ferromagnetic phase, the finite correlation length ξ sets the scale of the critical region, below which the spins can fluctuate. Thus, imposing each constraint removes $O(|\partial A|/\xi)$ degrees of freedom. However, the aligned boundary spins should also align with the global magnetization resulting in a vanishing subleading term in the excess free energy. Hence, the negativity $\mathcal{E}_A^{(2n)}$ exhibits a pure area law without any subleading term.

To support our analytical argument, we also numerically calculate the Rényi-4 negativity (the Rényi-2 negativity is trivially zero) and show that the topological term $\gamma_N^{(4)}$ indeed exhibits distinct behaviors across the transition. We adopt the Kitaev-Preskill prescription to extract γ_N [146]. More specifically, we consider the subsystems A, B, C depicted below, and γ_N is given by

$$-\gamma_N := \mathcal{E}_A + \mathcal{E}_B + \mathcal{E}_C + \mathcal{E}_{ABC} \\ - \mathcal{E}_{AB} - \mathcal{E}_{BC} - \mathcal{E}_{AC} . \tag{7.31}$$

Our choice of the subsystems further simplifies the above expression to $-\gamma_N = 2\mathcal{E}_A - 2\mathcal{E}_{AC} + \mathcal{E}_{ABC}$ [2].

---

[1]We thank Tarun Grover for pointing it out to us.

[2]Obtaining the negativity from the Monte-Carlo simulation is not an easy task. Here, one directly

The result is presented in Fig. 7.5, where $\gamma_N^{(4)}$ approaches $\log 2$ and 0 for small and large p_z, respectively. The curves become steeper as the system size increases, which is consistent with the predicted step function in the thermodynamic limit. One can also observe a dip of $\gamma_N^{(4)}$ below zero. This phenomenon has also appeared in the numerical study of the topological entanglement entropy across transitions [255]. We believe that this dip is due to the finite-size effect, which might be more severe for information quantities with a large Rényi index n [131].

So far, we only considered a simply connected sub-region. If A is not simply connected, that is, ∂A contains k disconnected curves (for example the boundary of an annular region that contains two disconnected curves), then the constraints only require the Ising spins to align with other spins on the same boundary curve. In this case the topological entanglement negativity is $k \log 2$. This is the same dependence on the number of disconnected components as in the topological entanglement entropy of ground states [160].

$n \to 1$ limit, duality and connection to optimal decoding

In this subsection, we determine p_c in the limit $n \to 1$ via a duality between the statistical mechanical model established in Sec. 7.3 and the 2D random bond Ising model (RBIM) along the Nishimori line. The RBIM is also known to govern the error threshold of the optimal decoding algorithm for the 2D Toric code with incoherent errors [74]. The duality shows that the decoding threshold indeed saturates the upper bound given by the threshold in our information theoretical diagnostics. This duality was derived before via a binary Fourier transformation [196, 204]. Here, it follows naturally from two distinct expansions of the error-corrupted state.

The statistical mechanical model in Sec. 7.3 is based on the loop picture (7.15). Here, we work in an alternative error configuration picture, writing the error corrupted state as

$$
\rho = \sum_{\mathcal{C}_x, \mathcal{C}_z} P(\mathcal{C}_x) P(\mathcal{C}_z)
$$

$$
Z^{\mathcal{C}_z} X^{\mathcal{C}_x} \rho_0 X^{\mathcal{C}_x} Z^{\mathcal{C}_z} , \tag{7.32}
$$

where $\mathcal{C}_z$ ($\mathcal{C}_x$) denotes the error strings on the original (dual) lattice. The corresponding error syndromes are e and m anyons on the boundary $\partial \mathcal{C}_z$ and $\partial \mathcal{C}_x$, respectively. Let $|\mathcal{C}_a|$ denote the total length of the error string, the probability for each string configuration is

$$
P(\mathcal{C}_a) = p_a^{|\mathcal{C}_a|} (1 - p_a)^{N - |\mathcal{C}_a|} , \tag{7.33}
$$

where N is the total number of qubits.

---

computes $e^{(2-n)\mathcal{E}_A^{(n)}}$, which is exponentially small due to the area-law scaling of $\mathcal{E}_A^{(n)}$ and thus requires exponentially many samples to accurately determine its value. This limits the largest accessible subsystem size.

The expansion in error configurations allows writing the n-th moment as

$$
\operatorname{tr} \rho^n = \sum_{\{\mathcal{C}_x^{(s)}, \mathcal{C}_z^{(s)}\}} \prod_{s=1}^n P\big(\mathcal{C}_x^{(s)}\big) P\big(\mathcal{C}_z^{(s)}\big)
$$
$$
\operatorname{tr}\Big(\prod_{s=1}^n Z^{\mathcal{C}_z^{(s)}} X^{\mathcal{C}_x^{(s)}} \rho_0 X^{\mathcal{C}_x^{(s)}} Z^{\mathcal{C}_z^{(s)}}\Big).
$$
(7.34)

We choose $\rho_0 = |\Psi_0\rangle\langle\Psi_0|$ to be an eigenstate of the logical operators. Then, we can rewrite the trace as

$$
\prod_{s=1}^{n-1} \langle\Psi_0| X^{\mathcal{C}_x^{(s)}} Z^{\mathcal{C}_z^{(s)}} Z^{\mathcal{C}_z^{(s+1)}} X^{\mathcal{C}_x^{(s+1)}} |\Psi_0\rangle \,,
$$

and see that the trace is non-vanishing only if error strings of different copies differ only by homologically trivial loops. Namely, the error strings in the $2, \ldots, n$-th copies are related to that in the first copy via

$$
\mathcal{C}_{z(x)}^{(s+1)} = \mathcal{C}_{z(x)}^{(1)} + \partial v_{z(x)}^{(s)},
$$
$$
s = 1, 2, \ldots, n-1 \,,
$$
(7.35)

where $v_{z(x)}^{(s)}$ is a set of plaquettes on the original (dual) lattice, and its boundary $\partial v_{z(x)}^{(s)}$ only consists of homologically trivial loops. Noticing the decoupling between Z and X, we have

$$
\operatorname{tr}\rho^n = \mathcal{Z}_{n,z}' \mathcal{Z}_{n,x}' \,,
$$
$$
\mathcal{Z}_{n,a}' = \sum_{\mathcal{C}_a^{(1)}} P\big(\mathcal{C}_a^{(1)}\big) \sum_{\{v_a^{(s)}\}} \prod_{s=1}^{n-1} P\big(\mathcal{C}_a^{(1)} + \partial v_a^{(s)}\big) \,.
$$
(7.36)

By comparing the above expression with Eq. (7.19), we must have the following duality

$$
\mathcal{Z}_{n,x} = 2^{\frac{(n-1)N}{2}} \mathcal{Z}_{n,z}' \,, \quad \mathcal{Z}_{n,z} = 2^{\frac{(n-1)N}{2}} \mathcal{Z}_{n,x}' \,.
$$
(7.37)

In the following, we will focus on $\mathcal{Z}_{n,z}'$ and suppress the subscripts for the sake of clarity. The analysis of $\mathcal{Z}_{n,x}'$ is similar.

We now interpret $\mathcal{Z}_{n,z}'$ as a partition function of Ising spins that is related to the replicated RBIM. Let us replace $v^{(s)}, s = 1, \ldots, n-1$ by $n-1$ flavors of Ising spins that live on the plaquettes such that each $v^{(s)}$ is in one-to-one correspondence to a configuration of Ising spins, as is drawn below
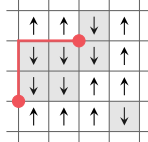
Namely, the boundary $\partial v^{(s)}$ is mapped to the domain walls of the s-th Ising spin. There are nearest neighbor antiferromagneticinteractions between spins of the same flavor on links that cross the path $\mathcal{C}^{(1)}$ and ferromagnetic interaction across other links. More explicitly, one can verify

$$\mathcal{Z}'_n = ((1-p)p)^{N/2} \sum_{\{J_{ij}\}} P(\{\eta_{ij}\})$$
$$\sum_{\{\tau^{(s)}\}} \exp\left(J \sum_{s=1}^{n-1} \sum_{\langle ij|ij\rangle} \eta_{ij} \tau_i^{(s)} \tau_j^{(s)} \right) \tag{7.38}$$

where $e^{-2J} = p/(1-p)$ and $\eta_{ij} \in \{-1,1\}$ is a binary random variable on links determined by $\mathcal{C}^{(1)}$. Hence, we recognize $\mathcal{Z}'_n = \overline{\mathcal{Z}_{\text{RBIM}}^{n-1}}$ as the disorder-averaged partition function of $n-1$ copies of RBIM along the Nishimori line [194].

The replicated RBIM in the error configuration picture and the spin model in the loop picture are both derived from the n-th moment of the error corrupted state. Therefore, they must be dual to each other and share the same critical error rate for all replica indices. Note that the replicated RBIM exhibits two phases, a ferromagnetic and a paramagnetic phase at small and large error rates, respectively. This is exactly opposite to the phase diagrams of the spin model in the loop picture, which is a common feature in Kramers-Wannier dualities.

In the replica limit $n \to 1$, the replicated RBIM reduces to the RBIM derived for the optimal quantum error correction algorithm [74] and undergoes an ordering transition at $p_c = 0.109$ [118]. This implies that all three diagnostics should also undergo the transition at the same p_c in the replica limit and confirms that the optimal decoding threshold saturates the upper bound in Eq. (7.6).

7.4 Discussion

In this work, we introduced information theoretic diagnostics of error-corrupted mixed states $\rho = \prod_i \mathcal{N}_i[\rho_0]$, which probe their intrinsic topological order and capacity for protecting quantum information. We focused on a concrete example, where $\rho_0 = |\psi_{\text{TC}}\rangle\langle\psi_{\text{TC}}|$ is in the ground state subspace of the Toric code and $\mathcal{N}_i$ the bit-flip and phase errors. We noted that the n-th moment $\text{tr}\,\rho^n$ can be written as the partition function of a 2D classical spin model, that is dual to the (replicated) random-bond Ising model along the Nishimori line, which is used to establish the following results. We consider three complementary diagnostics, quantum relative entropy, coherent information, and topological entanglement negativity, which are mapped to different observables in the spin model and shown to undergo a transition at the same critical error rate. Generally speaking, this critical error rate is an upper bound for the error threshold that can be achieved by any decoding algorithm. The aforementioned duality implies that the critical error rate identified here is exactly saturated by the famous error threshold of the optimal decoding algorithm for the Toric code proposed by Dennis et al [74]. This result unveils a connection between the breakdown of topological quantum

memory and a transition in the mixed-state topological order, and also provides physical interpretation for the decoding transition.

We have focused on Toric code with incoherent errors. It will be interesting to generalize the discussion to coherent errors that create anyons with coherence, e.g., amplitude damping or unitary rotations [72, 71, 42, 254]. In these cases, one has to concatenate coherent errors and dephasing channels that mimic the syndrome measurement in order to make better contact to quantum error correction based on that syndrome measurement. It is also interesting to further consider non-Abelian quantum codes [44, 273, 227].

It might be surprising that the intrinsic properties of the 2D error corrupted quantum states are captured by 2D *classical* statistical mechanical models. In Appendix F.2, we give a brief discussion on $\mathbb{Z}_N$ Toric code with specific incoherent errors and show that this is also the case. A more general perspective is the so-called *errorfield double formalism*, which is proposed by the same authors. It follows from this general formalism that the intrinsic properties of the 2D error corrupted states can always be captured by a 1+1D quantum model. Details are reported in Chap. 6.

For the 2D random-bond Ising model along the Nishimori line, physical quantities, such as the specific heat, change smoothly despite crossing the phase transition [194]. For quantum memories under local errors, we have argued in Sec. 7.2 that any physical observables must also behave smoothly across the error-induced transition. This similarity between the two sides may be the deeper underlying reason why the corrupted quantum memories are mapped to the Nishimori line. It will be interesting to leverage this to identify more exotic Nishimori physics and also help develop a better understanding of quantum memory.

As we have commented in Sec. 7.2, the error-induced transition acquires a different nature from the thermal transition in finite-temperature topological order. This distinction suggests a hierarchy of topological transitions in general mixed states. For example, it suffices to use physical observables (linear in the density matrix) to detect the thermal transition, while it requires at least second Rényi quantities (quadratic in the density matrix) to detect the error-induced transition. It is interesting to explore more exotic topological transitions in mixed states that are detectable only by non-linear functions of the density matrix of even higher orders, such as the entanglement Hamiltonian.

The above task is intimately related to the goal of classifying mixed-state topological order. A suitable definition of mixed state topological order should be both operationally meaningful and also identify computable topological invariants. Our discussion which focuses on the error-corrupted mixed states represents one particular aspect of this more general question. Here, the coherent information provides the operational definition, namely, a locally corrupted state is in a different phase if QEC is impossible, while the topological entanglement negativity is believed to provide a computable topological invariant that diagnoses the present transition. However, note that both the local error channel and QEC process are generally non-unitary, for which the Lieb-Robinson bound does not apply. Therefore, understanding the role of locality is key to obtaining a general notion of equivalence classes of mixed states. Similarly, a more general justification of topological negativity and its universality, in the sense of establishing its invariance under the application of local quantum channels at a

certain place, is left for future work. The main difficulty comes from understanding how local perturbations affect the spectrum of a partially transposed density matrix, which is an interesting problem in its own right and is left to future work.

Bibliography

[1]   Scott Aaronson and Daniel Gottesman. "Improved simulation of stabilizer circuits". In: *Physical Review A* 70.5 (2004), p. 052328.

[2]   Dmitry A Abanin et al. "Colloquium: Many-body localization, thermalization, and entanglement". In: *Reviews of Modern Physics* 91.2 (2019), p. 021001.

[3]   Anura Abeyesinghe et al. "The mother of all protocols: Restructuring quantum information's family tree". In: *Proceedings of the Royal Society A: Mathematical, Physical and Engineering Sciences* 465.2108 (2009), pp. 2537–2563.

[4]   Dorit Aharonov. "Quantum to classical phase transition in noisy quantum computers". In: *Physical Review A* 62.6 (2000), p. 062311.

[5]   Google Quantum AI. "Suppressing quantum errors by scaling a surface code logical qubit". In: *Nature* 614.7949 (2023), pp. 676–681.

[6]   Google Quantum AI and Collaborators. "Non-Abelian braiding of graph vertices in a superconducting processor". In: *Nature* 618 (2023), pp. 264–269.

[7]   Tameem Albash and Daniel A Lidar. "Adiabatic quantum computation". In: *Reviews of Modern Physics* 90.1 (2018), p. 015002.

[8]   Ori Alberton, Michael Buchhold, and Sebastian Diehl. "Entanglement transition in a monitored free-fermion chain: From extended criticality to area law". In: *Physical Review Letters* 126.17 (2021), p. 170602.

[9]   R Alicki and Mark Fannes. "Defining quantum dynamical entropy". In: *letters in mathematical physics* 32.1 (1994), pp. 75–82.

[10]   Ehud Altman et al. "Quantum simulators: Architectures and opportunities". In: *PRX Quantum* 2.1 (2021), p. 017003.

[11]   Trond I Andersen et al. "Observation of non-Abelian exchange statistics on a superconducting processor". In: *arXiv preprint arXiv:2210.10255* (2022).

[12]   Philip W Anderson. "More is different". In: *Science* 177.4047 (1972), pp. 393–396.

[13]   PW Anderson and G Yuval. "Some numerical results on the Kondo problem and the inverse square one-dimensional Ising model". In: *Journal of Physics C: Solid State Physics* 4.5 (1971), p. 607.

[14] Huzihiro Araki. "Relative entropy of states of von Neumann algebras". In: *Publications of the Research Institute for Mathematical Sciences* 11.3 (1976), pp. 809–833.

[15] Frank Arute et al. "Quantum supremacy using a programmable superconducting processor". In: *Nature* 574.7779 (2019), pp. 505–510.

[16] Yimu Bao, Maxwell Block, and Ehud Altman. "Finite time teleportation phase transition in random quantum circuits". In: *arXiv preprint arXiv:2110.06963* (2021).

[17] Yimu Bao, Soonwon Choi, and Ehud Altman. "Symmetry enriched phases of quantum circuits". In: *Annals of Physics* 435 (2021), p. 168618.

[18] Yimu Bao, Soonwon Choi, and Ehud Altman. "Theory of the phase transition in random unitary circuits with measurements". In: *Physical Review B* 101.10 (2020), p. 104301.

[19] Yimu Bao et al. "Mixed-state topological order and the errorfield double formulation of decoherence-induced transitions". In: *arXiv preprint arXiv:2301.05687* (2023).

[20] Maissam Barkeshli, Chao-Ming Jian, and Xiao-Liang Qi. "Theory of defects in Abelian topological states". In: *Physical Review B* 88.23 (2013), p. 235103.

[21] Hugo Bartolomei et al. "Fractional statistics in anyon collisions". In: *Science* 368.6487 (2020), pp. 173–177.

[22] Rodney J Baxter. "Potts model at the critical temperature". In: *Journal of Physics C: Solid State Physics* 6.23 (1973), p. L445.

[23] Rodney James Baxter, HNV Temperley, and Susan E Ashley. "Triangular Potts model at its transition temperature, and related models". In: *Proceedings of the Royal Society of London. A. Mathematical and Physical Sciences* 358.1695 (1978), pp. 535–559.

[24] Jan Behrends, Florian Venn, and Benjamin Béri. "Surface codes, quantum circuits, and entanglement phases". In: *arXiv preprint arXiv:2212.08084* (2022).

[25] Salman Beigi, Peter W Shor, and Daniel Whalen. "The quantum double model with boundary: condensations and symmetries". In: *Communications in mathematical physics* 306 (2011), pp. 663–694.

[26] Charles H Bennett et al. "Mixed-state entanglement and quantum error correction". In: *Physical Review A* 54.5 (1996), p. 3824.

[27] Charles H Bennett et al. "Teleporting an unknown quantum state via dual classical and Einstein-Podolsky-Rosen channels". In: *Physical review letters* 70.13 (1993), p. 1895.

[28] Erez Berg et al. "Rise and fall of hidden string order of lattice bosons". In: *Physical Review B* 77.24 (2008), p. 245119.

[29] Hannes Bernien et al. "Probing many-body dynamics on a 51-atom quantum simulator". In: *Nature* 551.7682 (2017), p. 579.

[30] J Bhattacharjee et al. "Some properties of a one-dimensional Ising chain with an inverse-square interaction". In: *Physical Review B* 24.7 (1981), p. 3862.

[31] Jayanta K Bhattacharjee, John L Cardy, and DJ Scalapino. "O (n) Heisenberg model with long-range interactions". In: *Physical Review B* 25.3 (1982), p. 1681.

[32] Kurt Binder and DP Landau. "Finite-size scaling at first-order phase transitions". In: *Physical Review B* 30.3 (1984), p. 1477.

[33] Maxwell Block et al. "Measurement-induced transition in long-range interacting quantum circuits". In: *Physical Review Letters* 128.1 (2022), p. 010604.

[34] Dolev Bluvstein et al. "A quantum processor based on coherent transport of entangled atom arrays". In: *Nature* 604.7906 (2022), pp. 451–456.

[35] Sergio Boixo et al. "Characterizing quantum supremacy in near-term devices". In: *Nature Physics* 14.6 (2018), p. 595.

[36] Héctor Bombin et al. "Strong resilience of topological codes to depolarization". In: *Physical Review X* 2.2 (2012), p. 021004.

[37] Danilo Boschi et al. "Experimental realization of teleporting an unknown pure quantum state via dual classical and Einstein-Podolsky-Rosen channels". In: *Physical Review Letters* 80.6 (1998), p. 1121.

[38] Adam Bouland et al. "On the complexity and verification of quantum random circuit sampling". In: *Nature Physics* 15.2 (2019), pp. 159–163.

[39] Dik Bouwmeester et al. "Experimental quantum teleportation". In: *Nature* 390.6660 (1997), pp. 575–579.

[40] Fernando GSL Brandao, Aram W Harrow, and Michał Horodecki. "Local random quantum circuits are approximate polynomial-designs". In: *Communications in Mathematical Physics* 346 (2016), pp. 397–434.

[41] Sergey Bravyi and Barbara Terhal. "A no-go theorem for a two-dimensional self-correcting quantum memory based on stabilizer codes". In: *New Journal of Physics* 11.4 (2009), p. 043029.

[42] Sergey Bravyi et al. "Correcting coherent errors with surface codes". In: *npj Quantum Information* 4.1 (2018), p. 55.

[43] Sergey B Bravyi and A Yu Kitaev. "Quantum codes on a lattice with boundary". In: *arXiv preprint quant-ph/9811052* (1998).

[44] Courtney G Brell et al. "Thermalization, error correction, and memory lifetime for ising anyon systems". In: *Physical Review X* 4.3 (2014), p. 031058.

[45] Nikolas P Breuckmann and Jens Niklas Eberhardt. "Quantum low-density parity-check codes". In: *PRX Quantum* 2.4 (2021), p. 040101.

[46] H-J Briegel et al. "Quantum repeaters: the role of imperfect local operations in quantum communication". In: *Physical Review Letters* 81.26 (1998), p. 5932.

[47] Hans J Briegel and Robert Raussendorf. "Persistent entanglement in arrays of interacting particles". In: *Physical Review Letters* 86.5 (2001), p. 910.

[48] Antoine Browaeys and Thierry Lahaye. "Many-body physics with individually controlled Rydberg atoms". In: *Nature Physics* 16.2 (2020), pp. 132–142.

[49] Adam R Brown et al. "Quantum gravity in the lab. i. teleportation by size and traversable wormholes". In: *PRX quantum* 4.1 (2023), p. 010320.

[50] Benjamin J Brown et al. "Quantum memories at finite temperature". In: *Reviews of Modern Physics* 88.4 (2016), p. 045005.

[51] Tiff Brydges et al. "Probing Rényi entanglement entropy via randomized measurements". In: *Science* 364.6437 (2019), pp. 260–263.

[52] Fiona J Burnell. "Anyon condensation and its applications". In: *Annual Review of Condensed Matter Physics* 9 (2018), pp. 307–327.

[53] A Robert Calderbank and Peter W Shor. "Good quantum error-correcting codes exist". In: *Physical Review A* 54.2 (1996), p. 1098.

[54] A Robert Calderbank et al. "Quantum error correction and orthogonal geometry". In: *Physical Review Letters* 78.3 (1997), p. 405.

[55] Xiangyu Cao, Antoine Tilloy, and Andrea De Luca. "Entanglement in a fermion chain under continuous monitoring". In: *SciPost Physics* 7.2 (2019), p. 024.

[56] John L Cardy. "Critical percolation in finite geometries". In: *Journal of Physics A: Mathematical and General* 25.4 (1992), p. L201.

[57] John L Cardy. "One-dimensional models with 1/r2 interactions". In: *Journal of Physics A: Mathematical and General* 14.6 (1981), p. 1407.

[58] Claudio Castelnovo and Claudio Chamon. "Quantum topological phase transition at the microscopic level". In: *Physical Review B* 77.5 (2008), p. 054433.

[59] Amos Chan et al. "Unitary-projective entanglement dynamics". In: *Physical Review B* 99.22 (2019), p. 224307.

[60] Wei Chen, Kazuo Hida, and BC Sanctuary. "Ground-state phase diagram of S= 1 XXZ chains with uniaxial single-ion-type anisotropy". In: *Physical Review B* 67.10 (2003), p. 104401.

[61] Xiao Chen et al. "Emergent conformal symmetry in nonunitary random dynamics of free fermions". In: *Physical Review Research* 2.3 (2020), p. 033017.

[62] Xie Chen, Zheng-Cheng Gu, and Xiao-Gang Wen. "Classification of gapped symmetric phases in one-dimensional spin systems". In: *Physical review b* 83.3 (2011), p. 035107.

[63] Xie Chen, Yuan-Ming Lu, and Ashvin Vishwanath. "Symmetry-protected topological phases from decorated domain walls". In: *Nature communications* 5.1 (2014), pp. 1–11.

[64] Joonhee Choi et al. "Preparing random states and benchmarking with many-body quantum chaos". In: *Nature* 613.7944 (2023), pp. 468–473.

[65] Soonwon Choi et al. "Quantum error correction in scrambling dynamics and measurement-induced phase transition". In: *Physical Review Letters* 125.3 (2020), p. 030505.

[66] Christopher T Chubb and Steven T Flammia. "Statistical mechanical models for quantum codes with correlated noise". In: *Annales de l'Institut Henri Poincaré D* 8.2 (2021), pp. 269–321.

[67] Benoît Collins. "Moments and cumulants of polynomial random variables on unitary groups, the Itzykson-Zuber integral, and free probability". In: *International Mathematics Research Notices* 2003.17 (2003), pp. 953–982.

[68] Benoît Collins and Piotr Śniady. "Integration with respect to the Haar measure on unitary, orthogonal and symplectic group". In: *Communications in Mathematical Physics* 264.3 (2006), pp. 773–795.

[69] Jordan Cotler et al. "Superdensity operators for spacetime quantum mechanics". In: *Journal of High Energy Physics* 2018.9 (2018), p. 93.

[70] Jordan S Cotler et al. "Emergent quantum state designs from individual many-body wave functions". In: *PRX Quantum* 4.1 (2023), p. 010311.

[71] Andrew S Darmawan and David Poulin. "Linear-time general decoding algorithm for the surface code". In: *Physical Review E* 97.5 (2018), p. 051302.

[72] Andrew S Darmawan and David Poulin. "Tensor-network simulations of the surface code under realistic noise". In: *Physical review letters* 119.4 (2017), p. 040502.

[73] Morris H DeGroot and Mark J Schervish. *Probability and statistics*. Pearson Education, 2012.

[74] Eric Dennis et al. "Topological quantum memory". In: *Journal of Mathematical Physics* 43.9 (2002), pp. 4452–4505.

[75] Josh M Deutsch. "Quantum statistical mechanics in a closed system". In: *Physical review a* 43.4 (1991), p. 2046.

[76] Igor Devetak. "The private classical capacity and quantum capacity of a quantum channel". In: *IEEE Transactions on Information Theory* 51.1 (2005), pp. 44–55.

[77] Igor Devetak and Peter W Shor. "The capacity of a quantum channel for simultaneous transmission of classical and quantum information". In: *Communications in Mathematical Physics* 256.2 (2005), pp. 287–303.

[78] David P DiVincenzo, Debbie W Leung, and Barbara M Terhal. "Quantum data hiding". In: *IEEE Transactions on Information Theory* 48.3 (2002), pp. 580–598.

[79] Freeman J Dyson. "Existence of a phase-transition in a one-dimensional Ising ferromagnet". In: *Communications in Mathematical Physics* 12.2 (1969), pp. 91–107.

[80] Sepehr Ebadi et al. "Quantum phases of matter on a 256-atom programmable quantum simulator". In: *Nature* 595.7866 (2021), pp. 227–232.

[81] Samuel Frederick Edwards and Phil W Anderson. "Theory of spin glasses". In: *Journal of Physics F: Metal Physics* 5.5 (1975), p. 965.

[82] TP Eggarter. "Triangular antiferromagnetic Ising model". In: *Physical Review B* 12.5 (1975), p. 1933.

[83] Shmuel Elitzur et al. "Remarks on the canonical quantization of the Chern-Simons-Witten theory". In: *Nuclear Physics B* 326.1 (1989), pp. 108–134.

[84] Ruihua Fan et al. "Diagnostics of mixed-state topological order and breakdown of quantum memory". In: *arXiv preprint arXiv:2301.05689* (2023).

[85] Ruihua Fan et al. "Self-organized error correction in random unitary circuits with measurement". In: *Physical Review B* 103.17 (2021), p. 174309.

[86] Paul Fendley, Matthew PA Fisher, and Chetan Nayak. "Topological entanglement entropy from the holographic partition function". In: *Journal of Statistical Physics* 126 (2007), pp. 1111–1144.

[87] Lukasz Fidkowski, Jeongwan Haah, and Matthew B Hastings. "How dynamical quantum memories forget". In: *Quantum* 5 (2021), p. 382.

[88] Eduardo Fradkin. *Field theories of condensed matter physics*. Cambridge University Press, 2013.

[89] Klaus Fredenhagen and Mihail Marcu. "Charged States in Z2 Gauge Theories". In: *Commun. Math. Phys.* 92 (1983), p. 81.

[90] Klaus Fredenhagen and Mihail Marcu. "Confinement criterion for QCD with dynamical quarks". In: *Physical review letters* 56.3 (1986), p. 223.

[91] Klaus Fredenhagen and Mihail Marcu. "Dual interpretation of order parameters for lattice gauge theories with matter fields". In: *Nuclear Physics B-Proceedings Supplements* 4 (1988), pp. 352–357.

[92] J Fröhlich and A Zee. "Large scale physics of the quantum Hall fluid". In: *Nuclear Physics B* 364.3 (1991), pp. 517–540.

[93] Liang Fu and Charles L Kane. "Topology, delocalization via average symmetry and the symplectic anderson transition". In: *Physical review letters* 109.24 (2012), p. 246605.

[94] Keisuke Fujii. *Quantum Computation with Topological Codes: from qubit to topological fault-tolerance*. Vol. 8. Springer, 2015.

[95] Samuel J Garratt, Zack Weinstein, and Ehud Altman. "Measurements conspire non-locally to restructure critical quantum states". In: *Physical Review X* 13.2 (2023), p. 021026.

[96] Iulia M Georgescu, Sahel Ashhab, and Franco Nori. "Quantum simulation". In: *Reviews of Modern Physics* 86.1 (2014), p. 153.

[97] Thierry Giamarchi. *Quantum physics in one dimension*. Vol. 121. Clarendon press, 2003.

[98] Daniel Gottesman. "An introduction to quantum error correction and fault-tolerant quantum computation". In: *Quantum information science and its contributions to mathematics, Proceedings of Symposia in Applied Mathematics.* Vol. 68. 2010, pp. 13–58.

[99] Daniel Gottesman. "Class of quantum error-correcting codes saturating the quantum Hamming bound". In: *Physical Review A* 54.3 (1996), p. 1862.

[100] Daniel Gottesman. "The Heisenberg representation of quantum computers". In: *arXiv preprint quant-ph/9807006* (1998).

[101] K Gregor et al. "Diagnosing deconfinement and topological order". In: *New Journal of Physics* 13.2 (2011), p. 025009.

[102] Geoffrey Grimmett. "What is percolation?" In: *Percolation.* Springer, 1999, pp. 1–31.

[103] Tarun Grover, Ari M Turner, and Ashvin Vishwanath. "Entanglement entropy of gapped phases and topological order in three dimensions". In: *Physical Review B* 84.19 (2011), p. 195120.

[104] Michael J Gullans and David A Huse. "Dynamical purification phase transition induced by quantum measurements". In: *Physical Review X* 10.4 (2020), p. 041020.

[105] Michael J Gullans and David A Huse. "Scalable probes of measurement-induced criticality". In: *Physical review letters* 125.7 (2020), p. 070606.

[106] Rudolf Haag. *Local quantum physics: Fields, particles, algebras.* Springer Science & Business Media, 2012.

[107] Jeongwan Haah. "Local stabilizer codes in three dimensions without string logical operators". In: *Physical Review A* 83.4 (2011), p. 042330.

[108] Alioscia Hamma, Radu Ionicioiu, and Paolo Zanardi. "Bipartite entanglement and entropic boundary law in lattice spin systems". In: *Physical Review A* 71.2 (2005), p. 022315.

[109] Alioscia Hamma, Radu Ionicioiu, and Paolo Zanardi. "Ground state entanglement and geometric entropy in the Kitaev model". In: *Physics Letters A* 337.1-2 (2005), pp. 22–28.

[110] R Harris et al. "Phase transitions in a programmable quantum spin glass simulator". In: *Science* 361.6398 (2018), pp. 162–165.

[111] Aram W Harrow and Ashley Montanaro. "Quantum computational supremacy". In: *Nature* 549.7671 (2017), pp. 203–209.

[112] Matthew B Hastings. "Topological order at nonzero temperature". In: *Physical review letters* 107.21 (2011), p. 210501.

[113] Masahito Hayashi. "Asymptotics of quantum relative entropy from a representation theoretical viewpoint". In: *Journal of Physics A: Mathematical and General* 34.16 (2001), p. 3413.

[114] Patrick Hayden and John Preskill. "Black holes as mirrors: quantum information in random subsystems". In: *Journal of High Energy Physics* 2007.09 (2007), p. 120.

[115] Patrick Hayden et al. "Holographic duality from random tensor networks". In: *Journal of High Energy Physics* 2016.11 (2016), p. 9.

[116] Fumio Hiai and Dénes Petz. "The proper formula for relative entropy and its asymptotics in quantum probability". In: *Communications in mathematical physics* 143.1 (1991), pp. 99–114.

[117] Jesse C Hoke et al. "Quantum information phases in space-time: measurement-induced entanglement and teleportation on a noisy quantum processor". In: *arXiv preprint arXiv:2303.04792* (2023).

[118] Andreas Honecker, Marco Picco, and Pierre Pujol. "Universality class of the Nishimori point in the 2D±J random-bond Ising model". In: *Physical review letters* 87.4 (2001), p. 047201.

[119] Michał Horodecki, Paweł Horodecki, and Ryszard Horodecki. "Separability of mixed states: necessary and sufficient conditions". In: *Physics Letters A* 223.1 (1996), pp. 1–8.

[120] Michał Horodecki, Jonathan Oppenheim, and Andreas Winter. "Quantum state merging and negative information". In: *Communications in Mathematical Physics* 269.1 (2007), pp. 107–136.

[121] Pavan Hosur et al. "Chaos in quantum channels". In: *Journal of High Energy Physics* 2016.2 (2016), p. 4.

[122] Jérôme Houdayer and Alexander K Hartmann. "Low-temperature behavior of two-dimensional Gaussian Ising spin glasses". In: *Physical Review B* 70.1 (2004), p. 014418.

[123] Eric Huang, Andrew C Doherty, and Steven Flammia. "Performance of quantum error correction with coherent errors". In: *Physical Review A* 99.2 (2019), p. 022313.

[124] Nicholas Hunter-Jones. "Unitary designs from statistical mechanics in random quantum circuits". In: *arXiv preprint arXiv:1905.12053* (2019).

[125] Shumpei Iino et al. "Detecting signals of weakly first-order phase transitions in two-dimensional Potts models". In: *Journal of the Physical Society of Japan* 88.3 (2019), p. 034006.

[126] John Z Imbrie and Charles M Newman. "An intermediate phase with slow decay of correlations in one dimensional 1/— x- y— 2 percolation, Ising and Potts models". In: *Communications in mathematical physics* 118.2 (1988), pp. 303–336.

[127] Matteo Ippoliti et al. "Entanglement phase transitions in measurement-only dynamics". In: *Physical Review X* 11.1 (2021), p. 011030.

[128] Joseph K Iverson and John Preskill. "Coherence in logical quantum channels". In: *New Journal of Physics* 22.7 (2020), p. 073066.

[129] Chao-Ming Jian et al. "Criticality and entanglement in nonunitary quantum circuits and tensor networks of noninteracting fermions". In: *Physical Review B* 106.13 (2022), p. 134206.

[130] Chao-Ming Jian et al. "Measurement-induced criticality in random quantum circuits". In: *Physical Review B* 101.10 (2020), p. 104302.

[131] Hong-Chen Jiang, Rajiv RP Singh, and Leon Balents. "Accuracy of topological entanglement entropy on finite cylinders". In: *Physical review letters* 111.10 (2013), p. 107205.

[132] Cheryne Jonay, David A Huse, and Adam Nahum. "Coarse-grained dynamics of operator and state entanglement". In: *arXiv preprint arXiv:1803.00089* (2018).

[133] Anton Kapustin and Natalia Saulina. "Topological boundary conditions in abelian Chern–Simons theory". In: *Nuclear Physics B* 845.3 (2011), pp. 393–435.

[134] PW Kasteleyn and CM Fortuin. "Phase transitions in lattice systems with random local properties". In: *Journal of the Physical Society of Japan Supplement* 26 (1969), p. 11.

[135] Helmut G Katzgraber, Héctor Bombín, and Martin A Martin-Delgado. "Error threshold for color codes and random three-body Ising models". In: *Physical review letters* 103.9 (2009), p. 090501.

[136] Adam M Kaufman et al. "Quantum thermalization through entanglement in an isolated many-body system". In: *Science* 353.6301 (2016), pp. 794–800.

[137] Naoki Kawashima and Nobuyasu Ito. "Critical behavior of the three-dimensional±j model in a magnetic field". In: *Journal of the Physical Society of Japan* 62.2 (1993), pp. 435–438.

[138] Harry Kesten. *Percolation theory for mathematicians.* Vol. 2. Springer, 1982.

[139] Harry Kesten. "Scaling relations for 2D-percolation". In: *Communications in Mathematical Physics* 109.1 (1987), pp. 109–156.

[140] Curt W von Keyserlingk et al. "Operator hydrodynamics, OTOCs, and entanglement growth in systems without conservation laws". In: *Physical Review X* 8.2 (2018), p. 021013.

[141] Vedika Khemani, Ashvin Vishwanath, and David A Huse. "Operator spreading and the emergence of dissipative hydrodynamics under unitary evolution with conservation laws". In: *Physical Review X* 8.3 (2018), p. 031057.

[142] Taro Kihara, Yukio Midzuno, and Toshio Shizume. "Statistics of two-dimensional lattices with many components". In: *Journal of the Physical Society of Japan* 9.5 (1954), pp. 681–687.

[143] Hyungwon Kim and David A Huse. "Ballistic spreading of entanglement in a diffusive nonintegrable system". In: *Physical review letters* 111.12 (2013), p. 127205.

[144] A Yu Kitaev. "Fault-tolerant quantum computation by anyons". In: *Annals of physics* 303.1 (2003), pp. 2–30.

[145] A Yu Kitaev. "Fault-tolerant quantum computation by anyons". In: *Annals of physics* 303.1 (2003), pp. 2–30.

[146] Alexei Kitaev and John Preskill. "Topological entanglement entropy". In: *Physical review letters* 96.11 (2006), p. 110404.

[147] Alexei Yu Kitaev et al. *Classical and quantum computation.* 47. American Mathematical Soc., 2002.

[148] Jin Ming Koh et al. "Experimental realization of a measurement-induced entanglement phase transition on a superconducting quantum processor". In: *arXiv preprint arXiv:2203.04338* (2022).

[149] Mahito Kohmoto, Marcel den Nijs, and Leo P Kadanoff. "Hamiltonian studies of the d= 2 Ashkin-Teller model". In: *Physical Review B* 24.9 (1981), p. 5229.

[150] JM Kosterlitz. "Phase transitions in long-range ferromagnetic chains". In: *Physical Review Letters* 37.23 (1976), p. 1577.

[151] Aleksander Kubica et al. "Three-dimensional color code thresholds via statistical-mechanical mapping". In: *Physical review letters* 120.18 (2018), p. 180501.

[152] Olivier Landon-Cardinal and David Poulin. "Local topological order inhibits thermal stability in 2D". In: *Physical review letters* 110.9 (2013), p. 090502.

[153] Kevin A Landsman et al. "Verified quantum information scrambling". In: *Nature* 567.7746 (2019), pp. 61–65.

[154] Nicolai Lang and Hans Peter Büchler. "Entanglement transition in the projective transverse field Ising model". In: *Physical Review B* 102.9 (2020), p. 094204.

[155] Robert B Laughlin. "Anomalous quantum Hall effect: an incompressible quantum fluid with fractionally charged excitations". In: *Physical Review Letters* 50.18 (1983), p. 1395.

[156] Ali Lavasani, Yahya Alavirad, and Maissam Barkeshli. "Measurement-induced topological entanglement transitions in symmetric random quantum circuits". In: *Nature Physics* (2021), pp. 1–6.

[157] Jong Yeon Lee, Yi-Zhuang You, and Cenke Xu. "Symmetry protected topological phases under decoherence". In: *arXiv preprint arXiv:2210.16323* (2022).

[158] Michael Levin. "Protected edge modes without symmetry". In: *Physical Review X* 3.2 (2013), p. 021009.

[159] Michael Levin and Zheng-Cheng Gu. "Braiding statistics approach to symmetry-protected topological phases". In: *Physical Review B* 86.11 (2012), p. 115109.

[160] Michael Levin and Xiao-Gang Wen. "Detecting topological order in a ground state wave function". In: *Physical review letters* 96.11 (2006), p. 110405.

[161] Tongyang Li and Xiaodi Wu. "Quantum query complexity of entropy estimation". In: *IEEE Transactions on Information Theory* 65.5 (2018), pp. 2899–2921.

[162] Yaodong Li, Xiao Chen, and Matthew PA Fisher. "Measurement-driven entanglement transition in hybrid quantum circuits". In: *Physical Review B* 100.13 (2019), p. 134306.

[163] Yaodong Li, Xiao Chen, and Matthew PA Fisher. "Quantum Zeno effect and the many-body entanglement transition". In: *Physical Review B* 98.20 (2018), p. 205136.

[164] Yaodong Li et al. "Conformal invariance and quantum nonlocality in critical hybrid circuits". In: *Physical Review B* 104.10 (2021), p. 104305.

[165] Yaodong Li et al. "Statistical mechanics model for clifford random tensor networks and monitored quantum circuits". In: *arXiv preprint arXiv:2110.02988* (2021).

[166] Tsuf Lichtman et al. "Bulk anyons as edge symmetries: Boundary phase diagrams of topologically ordered states". In: *Physical Review B* 104.7 (2021), p. 075141.

[167] Elliott H Lieb and Derek W Robinson. "The finite group velocity of quantum spin systems". In: *Statistical mechanics*. Springer, 1972, pp. 425–431.

[168] Elliott H Lieb and Mary Beth Ruskai. "Proof of the strong subadditivity of quantum-mechanical entropy". In: *Les rencontres physiciens-mathématiciens de Strasbourg-RCP25* 19 (1973), pp. 36–55.

[169] Göran Lindblad. "Completely positive maps and entropy inequalities". In: *Communications in Mathematical Physics* 40.2 (1975), pp. 147–151.

[170] Chunxiao Liu, Pengfei Zhang, and Xiao Chen. "Non-unitary dynamics of Sachdev-Ye-Kitaev chain". In: *SciPost Physics* 10.2 (2021), p. 048.

[171] Tsung-Cheng Lu, Timothy H Hsieh, and Tarun Grover. "Detecting topological order at finite temperature using entanglement negativity". In: *Physical Review Letters* 125.11 (2020), p. 116801.

[172] Tsung-Cheng Lu and Sagar Vijay. "Characterizing long-range entanglement in a mixed state through an emergent order on the entangling surface". In: *Physical Review Research* 5.3 (2023), p. 033031.

[173] Erik Luijten and Holger Meßingfeld. "Criticality in one dimension with inverse square-law potentials". In: *Physical review letters* 86.23 (2001), p. 5305.

[174] Alexander Lukin et al. "Probing entanglement in a many-body–localized system". In: *Science* 364.6437 (2019), pp. 256–260.

[175] Austin P Lund, Michael J Bremner, and Timothy C Ralph. "Quantum sampling problems, BosonSampling and quantum supremacy". In: *npj Quantum Information* 3.1 (2017), p. 15.

[176] Ruochen Ma and Chong Wang. "Average symmetry-protected topological phases". In: *arXiv preprint arXiv:2209.02723* (2022).

[177] Nishad Maskara et al. "Complexity phase diagram for interacting and long-range bosonic Hamiltonians". In: *Physical Review Letters* 129.15 (2022), p. 150604.

[178] Sho Matsumoto. "Weingarten calculus for matrix ensembles associated with compact symmetric spaces". In: *arXiv preprint arXiv:1301.5401* (2013).

[179] Max A Metlitski, Carlos A Fuertes, and Subir Sachdev. "Entanglement entropy in the O (N) model". In: *Physical Review B* 80.11 (2009), p. 115122.

[180] A Morvan et al. "Phase transition in random circuit sampling". In: *arXiv preprint arXiv:2304.11119* (2023).

[181] Hiroshi Nagaoka. "On Fisher information of quantum statistical models". In: *Asymptotic Theory Of Quantum Statistical Inference: Selected Papers*. 2005, pp. 113–124.

[182] Adam Nahum and Brian Skinner. "Entanglement and dynamics of diffusion-annihilation processes with Majorana defects". In: *Physical Review Research* 2.2 (2020), p. 023288.

[183] Adam Nahum, Sagar Vijay, and Jeongwan Haah. "Operator spreading in random unitary circuits". In: *Physical Review X* 8.2 (2018), p. 021014.

[184] Adam Nahum et al. "Loop models with crossings". In: *Physical Review B* 87.18 (2013), p. 184204.

[185] Adam Nahum et al. "Measurement and entanglement phase transitions in all-to-all quantum circuits, on quantum trees, and in Landau-Ginsburg theory". In: *PRX Quantum* 2.1 (2021), p. 010352.

[186] Adam Nahum et al. "Quantum entanglement growth under random unitary dynamics". In: *Physical Review X* 7.3 (2017), p. 031016.

[187] James Nakamura et al. "Direct observation of anyonic braiding statistics". In: *Nature Physics* 16.9 (2020), pp. 931–936.

[188] Rahul Nandkishore and David A Huse. "Many-body localization and thermalization in quantum statistical mechanics". In: *Annu. Rev. Condens. Matter Phys.* 6.1 (2015), pp. 15–38.

[189] John C Napp et al. "Efficient classical simulation of random shallow 2D quantum circuits". In: *Physical Review X* 12.2 (2022), p. 021021.

[190] Chetan Nayak et al. "Non-Abelian anyons and topological quantum computation". In: *Reviews of Modern Physics* 80.3 (2008), p. 1083.

[191] Charles Neill et al. "A blueprint for demonstrating quantum supremacy with superconducting qubits". In: *Science* 360.6385 (2018), pp. 195–199.

[192] Michael A Nielsen and Isaac L Chuang. *Quantum Computation and Quantum Information*. Cambridge University Press, 2000.

[193] Daniel Nigg et al. "Quantum computations on a topologically encoded qubit". In: *Science* 345.6194 (2014), pp. 302–305.

[194] Hidetoshi Nishimori. "Internal energy, specific heat and correlation function of the bond-random Ising model". In: *Progress of Theoretical Physics* 66.4 (1981), pp. 1169–1181.

[195] Hidetoshi Nishimori. *Statistical physics of spin glasses and information processing: an introduction.* 111. Clarendon Press, 2001.

[196] Hidetoshi Nishimori and Koji Nemoto. "Duality and multicritical point of two-dimensional spin glasses". In: *journal of the physical society of japan* 71.4 (2002), pp. 1198–1199.

[197] Crystal Noel et al. "Measurement-induced quantum phases realized in a trapped-ion quantum computer". In: *Nature Physics* 18.7 (2022), pp. 760–764.

[198] Marcel Novaes. "Elementary derivation of Weingarten functions of classical Lie groups". In: *arXiv preprint arXiv:1406.2182* (2014).

[199] Jonathan I Novak. "Jucys-Murphy elements and the unitary Weingarten function". In: *Banach Center Publications* 89 (2010), pp. 231–235.

[200] Zohar Nussinov and Gerardo Ortiz. "Autocorrelations and thermal fragility of anyonic loops in topologically quantum ordered systems". In: *Physical Review B* 77.6 (2008), p. 064302.

[201] Zohar Nussinov and Gerardo Ortiz. "Sufficient symmetry conditions for topological quantum order". In: *Proceedings of the National Academy of Sciences* 106.40 (2009), pp. 16944–16949.

[202] Ryan O'Donnell and John Wright. "Quantum spectrum testing". In: *Proceedings of the forty-seventh annual ACM symposium on Theory of computing.* ACM. 2015, pp. 529–538.

[203] Tomohiro Ogawa and Hiroshi Nagaoka. "Strong converse to the quantum channel coding theorem". In: *IEEE Transactions on Information Theory* 45.7 (1999), pp. 2486–2489.

[204] Masayuki Ohzeki. "Spin Glass a Bridge Between Quantum Computation and Statistical Mechanics". In: *Lectures on Quantum Computing, Thermodynamics and Statistical Physics.* World Scientific, 2013, pp. 63–124.

[205] Tobias J Osborne. "Efficient approximation of the dynamics of one-dimensional quantum spin systems". In: *Physical review letters* 97.15 (2006), p. 157202.

[206] Asher Peres. "Separability criterion for density matrices". In: *Physical Review Letters* 77.8 (1996), p. 1413.

[207] Martin B Plenio. "Logarithmic negativity: a full entanglement monotone that is not convex". In: *Physical review letters* 95.9 (2005), p. 090503.

[208] Frank Pollmann et al. "Entanglement spectrum of a topological phase in one dimension". In: *Physical review b* 81.6 (2010), p. 064439.

[209] Markus Popp et al. "Localizable entanglement". In: *Physical Review A* 71.4 (2005), p. 042306.

[210] Diego Porras and J Ignacio Cirac. "Effective quantum spin systems with trapped ions". In: *Physical review letters* 92.20 (2004), p. 207901.

[211] Renfrey Burnard Potts. "Some generalized order-disorder transformations". In: *Mathematical proceedings of the cambridge philosophical society*. Vol. 48. 1. Cambridge University Press. 1952, pp. 106–109.

[212] John Preskill. "Lecture notes for physics 219: Quantum computation". 2018.

[213] John Preskill. "Quantum computing in the NISQ era and beyond". In: *Quantum* 2 (2018), p. 79.

[214] Xiao-Liang Qi, Zhao Yang, and Yi-Zhuang You. "Holographic coherent states from random tensor networks". In: *Journal of High Energy Physics* 2017.8 (2017), p. 60.

[215] Tibor Rakovszky, Frank Pollmann, and CW von Keyserlingk. "Diffusive hydrodynamics of out-of-time-ordered correlators with charge conservation". In: *Physical Review X* 8.3 (2018), p. 031058.

[216] Robert Raussendorf, Sergey Bravyi, and Jim Harrington. "Long-range quantum entanglement in noisy cluster states". In: *Physical Review A* 71.6 (2005), p. 062313.

[217] Robert Raussendorf and Hans J Briegel. "A one-way quantum computer". In: *Physical Review Letters* 86.22 (2001), p. 5188.

[218] N Read. "Excitation structure of the hierarchy scheme in the fractional quantum Hall effect". In: *Physical review letters* 65.12 (1990), p. 1502.

[219] Marcos Rigol, Vanja Dunjko, and Maxim Olshanii. "Thermalization and its mechanism for generic isolated quantum systems". In: *Nature* 452.7189 (2008), p. 854.

[220] Daniel A Roberts and Beni Yoshida. "Chaos and complexity by design". In: *Journal of High Energy Physics* 2017.4 (2017), p. 121.

[221] David Ruelle. "Statistical mechanics of a one-dimensional lattice gas". In: *Communications in Mathematical Physics* 9.4 (1968), pp. 267–278.

[222] Shinsei Ryu et al. "$\mathbb{Z}_2$ topological term, the global anomaly, and the two-dimensional symplectic symmetry class of Anderson localization". In: *Physical review letters* 99.11 (2007), p. 116601.

[223] Subir Sachdev. *Quantum phase transitions*. Cambridge university press, 2011.

[224] Shengqi Sang and Timothy H Hsieh. "Measurement-protected quantum phases". In: *Physical Review Research* 3.2 (2021), p. 023200.

[225] Shengqi Sang et al. "Entanglement negativity at measurement-induced criticality". In: *PRX Quantum* 2.3 (2021), p. 030313.

[226] KJ Satzinger et al. "Realizing topologically ordered states on a quantum processor". In: *Science* 374.6572 (2021), pp. 1237–1241.

[227] Alexis Schotte et al. "Quantum error correction thresholds for the universal Fibonacci Turaev-Viro code". In: *Physical Review X* 12.2 (2022), p. 021012.

[228] Norbert Schuch et al. "Entropy scaling and simulability by matrix product states". In: *Physical review letters* 100.3 (2008), p. 030504.

[229] HJ Schulz. "Phase diagrams and correlation exponents for quantum spin chains of arbitrary spin quantum number". In: *Physical Review B* 34.9 (1986), p. 6372.

[230] Benjamin Schumacher and Michael A Nielsen. "Quantum data processing and error correction". In: *Physical Review A* 54.4 (1996), p. 2629.

[231] Benjamin Schumacher and Michael D Westmoreland. "Approximate quantum error correction". In: *Quantum Information Processing* 1.1-2 (2002), pp. 5–12.

[232] Thomas Schuster et al. "Many-body quantum teleportation via operator spreading in the traversable wormhole protocol". In: *Physical Review X* 12.3 (2022), p. 031013.

[233] Yasuhiro Sekino and Leonard Susskind. "Fast scramblers". In: *Journal of High Energy Physics* 2008.10 (2008), p. 065.

[234] Giulia Semeghini et al. "Probing topological spin liquids on a programmable quantum simulator". In: *Science* 374.6572 (2021), pp. 1242–1247.

[235] R Shankar and Ashvin Vishwanath. "Equality of bulk wave functions and edge correlations in some topological superconductors: A spacetime derivation". In: *Physical review letters* 107.10 (2011), p. 106803.

[236] Hassan Shapourian, Ken Shiozaki, and Shinsei Ryu. "Partial time-reversal transformation and entanglement negativity in fermionic systems". In: *Physical Review B* 95.16 (2017), p. 165101.

[237] Stephen H Shenker and Douglas Stanford. "Black holes and the butterfly effect". In: *Journal of High Energy Physics* 2014.3 (2014), p. 67.

[238] Peter W Shor. "Algorithms for quantum computation: discrete logarithms and factoring". In: *Proceedings 35th annual symposium on foundations of computer science*. Ieee. 1994, pp. 124–134.

[239] Brian Skinner, Jonathan Ruhman, and Adam Nahum. "Measurement-induced phase transitions in the dynamics of entanglement". In: *Physical Review X* 9.3 (2019), p. 031009.

[240] Nicolas Sourlas. "Spin-glass models as error-correcting codes". In: *Nature* 339.6227 (1989), pp. 693–695.

[241] Mark Srednicki. "Chaos and quantum thermalization". In: *Physical review e* 50.2 (1994), p. 888.

[242] Andrew M Steane. "Error correcting codes in quantum theory". In: *Physical Review Letters* 77.5 (1996), p. 793.

[243] Tilo Strutz. *Data fitting and uncertainty: A practical introduction to weighted least squares and beyond.* Vieweg and Teubner, 2010.

[244] Bill Sutherland. *Beautiful models: 70 years of exactly solved quantum many-body problems.* World Scientific Publishing Company, 2004.

[245] Marcin Szyniszewski, Alessandro Romito, and Henning Schomerus. "Entanglement transition from variable-strength weak measurements". In: *Physical Review B* 100.6 (2019), p. 064204.

[246] Yoshiaki Tanaka and Norikiyo Uryû. "Triangular Ising Lattice with Anisotropic Interactions". In: *Journal of the Physical Society of Japan* 44.4 (1978), pp. 1091–1096.

[247] Barbara M Terhal. "Quantum error correction for quantum memories". In: *Reviews of Modern Physics* 87.2 (2015), p. 307.

[248] Barbara M Terhal and David P DiVincenzo. "Classical simulation of noninteracting-fermion quantum circuits". In: *Physical Review A* 65.3 (2002), p. 032325.

[249] DJ Thouless. "Long-range order in one-dimensional Ising systems". In: *Physical Review* 187.2 (1969), p. 732.

[250] Daniel C Tsui, Horst L Stormer, and Arthur C Gossard. "Two-dimensional magneto-transport in the extreme quantum limit". In: *Physical Review Letters* 48.22 (1982), p. 1559.

[251] Armin Uhlmann. "Relative entropy and the Wigner-Yanase-Dyson-Lieb concavity in an interpolation theory". In: *Communications in Mathematical Physics* 54.1 (1977), pp. 21–32.

[252] Aad W Van der Vaart. *Asymptotic statistics.* Vol. 3. Cambridge university press, 2000.

[253] Romain Vasseur et al. "Entanglement transitions from holographic random tensor networks". In: *Physical Review B* 100.13 (2019), p. 134203.

[254] Florian Venn, Jan Behrends, and Benjamin Béri. "Coherent error threshold for surface codes from Majorana delocalization". In: *arXiv preprint arXiv:2211.00655* (2022).

[255] Ruben Verresen, Mikhail D Lukin, and Ashvin Vishwanath. "Prediction of toric code topological order from Rydberg blockade". In: *Physical Review X* 11.3 (2021), p. 031005.

[256] Frank Verstraete and J Ignacio Cirac. "Matrix product states represent ground states faithfully". In: *Physical Review B* 73.9 (2006), p. 094423.

[257] Frank Verstraete, Markus Popp, and J Ignacio Cirac. "Entanglement versus correlations in spin systems". In: *Physical review letters* 92.2 (2004), p. 027901.

[258] Guifré Vidal. "Efficient classical simulation of slightly entangled quantum computations". In: *Physical review letters* 91.14 (2003), p. 147902.

[259] Guifré Vidal. "Efficient simulation of one-dimensional quantum many-body systems". In: *Physical review letters* 93.4 (2004), p. 040502.

[260] Guifré Vidal and Reinhard F Werner. "Computable measure of entanglement". In: *Physical Review A* 65.3 (2002), p. 032314.

[261] Sagar Vijay, Jeongwan Haah, and Liang Fu. "Fracton topological order, generalized lattice gauge theory, and duality". In: *Physical Review B* 94.23 (2016), p. 235157.

[262] Chenyang Wang, Jim Harrington, and John Preskill. "Confinement-Higgs transition in a disordered gauge theory and the accuracy threshold for quantum memory". In: *Annals of Physics* 303.1 (2003), pp. 31–58.

[263] Juven C Wang and Xiao-Gang Wen. "Boundary degeneracy of topological order". In: *Physical Review B* 91.12 (2015), p. 125124.

[264] Zak Webb. "The Clifford group forms a unitary 3-design". In: *arXiv preprint arXiv:1510.02769* (2015).

[265] Xiao-Gang Wen. "Colloquium: Zoo of quantum-topological phases of matter". In: *Reviews of Modern Physics* 89.4 (2017), p. 041004.

[266] Xiao-Gang Wen. *Quantum field theory of many-body systems: from the origin of sound to an origin of light and electrons*. OUP Oxford, 2004.

[267] Xiao-Gang Wen. "Topological orders and edge excitations in fractional quantum Hall states". In: *Advances in Physics* 44.5 (1995), pp. 405–473.

[268] Xiao-Gang Wen and Anthony Zee. "Classification of Abelian quantum Hall states and matrix formulation of topological fluids". In: *Physical Review B* 46.4 (1992), p. 2290.

[269] Xueda Wen, Po-Yao Chang, and Shinsei Ryu. "Topological entanglement negativity in Chern-Simons theories". In: *Journal of High Energy Physics* 2016.9 (2016), pp. 1–30.

[270] Xueda Wen, Shunji Matsuura, and Shinsei Ryu. "Edge theory approach to topological entanglement entropy, mutual information, and entanglement negativity in Chern-Simons theories". In: *Physical Review B* 93.24 (2016), p. 245140.

[271] Mark M Wilde. *Quantum information theory*. Cambridge University Press, 2013.

[272] Edward Witten. "Topological quantum field theory". In: *Communications in Mathematical Physics* 117.3 (1988), pp. 353–386.

[273] James R Wootton et al. "Error correction for non-abelian topological quantum computation". In: *Physical review X* 4.1 (2014), p. 011051.

[274] FY Wu. "Percolation and the Potts model". In: *Journal of Statistical Physics* 18.2 (1978), pp. 115–123.

[275] Yulin Wu et al. "Strong quantum computational advantage using a superconducting quantum processor". In: *Physical review letters* 127.18 (2021), p. 180501.

[276] Chen Ning Yang and SC Zhang. "SO(4) symmetry in a Hubbard model". In: *Modern Physics Letters B* 4.11 (1990), pp. 759–766.

[277] G Yuval and PW Anderson. "Exact results for the Kondo problem: One-body theory and extension to finite temperature". In: *Physical Review B* 1.4 (1970), p. 1522.

[278] Aidan Zabalo et al. "Critical properties of the measurement-induced transition in random quantum circuits". In: *Physical Review B* 101.6 (2020), p. 060301.

[279] Bei Zeng et al. *Quantum information meets quantum matter*. Springer, 2019.

[280] Jian-Hao Zhang, Yang Qi, and Zhen Bi. "Strange Correlation Function for Average Symmetry-Protected Topological Phases". In: *arXiv preprint arXiv:2210.17485* (2022).

[281] Jiehang Zhang et al. "Observation of a many-body dynamical phase transition with a 53-qubit quantum simulator". In: *Nature* 551.7682 (2017), p. 601.

[282] Han-Sen Zhong et al. "Quantum computational advantage using photons". In: *Science* 370.6523 (2020), pp. 1460–1463.

[283] Tianci Zhou and Adam Nahum. "Emergent statistical mechanics of entanglement in random unitary circuits". In: *Physical Review B* 99.17 (2019), p. 174205.

[284] Qingling Zhu et al. "Quantum computational advantage via 60-qubit 24-cycle random circuit sampling". In: *Science bulletin* 67.3 (2022), pp. 240–245.

[285] Paul Zinn-Justin. "Jucys–Murphy elements and Weingarten matrices". In: *Letters in Mathematical Physics* 91.2 (2010), pp. 119–127.

Appendix A

Supplementary material for Chapter 2

A.1 Random Clifford circuits as unitary 2-design

One of the main results of our work relies on the decoupling inequality, which requires that the set of random unitaries to be averaged over forms a unitary 2-design. While it is well-known that the n-qubit Clifford group forms a unitary 2-design [78], it is yet to be verified that an ensemble of random quantum circuits of depth d made out of 2-qubit Clifford gates also approximates a unitary 2-design for n qubits. In this section, we numerically compute the frame potential for such unitary circuits, which quantifies the extent to which it approximates unitary designs. Our results confirm that the ensemble of depth d circuits of local 2-qubit Clifford gates indeed approximates a unitary 2-design when d is large. In what follows, we first review the frame potential, introduce our algorithm to compute it, and then present numerical results.

Frame potential

The k-th frame potential of a unitary ensemble ν is defined by

$$F_\nu^{(k)} = \frac{1}{|\nu|^2} \sum_{U,V \in \nu} \left| \mathrm{tr}\left(U^\dagger V \right) \right|^{2k}, \tag{A.1}$$

where $|\nu|$ denotes the order of the ensemble. One of the nice properties of the k-th frame potential $F_\nu^{(k)}$ is that this quantity is minimized when the unitary ensemble is drawn from the Haar measure (in which the summation in Eq. (A.1) is replaced by integration):

$$F_\nu^{(k)} \geq F_{\mu_{haar}}^{(k)} = k!. \tag{A.2}$$

Furthermore, it is well known that the k-th frame potential saturates this lower bound if and only if the unitary ensemble ν forms a unitary k-design [220]. Therefore, by explicitly computing the second frame potential $F_\nu^{(2)}$, we can verify if the ensemble of Clifford circuits forms an approximate 2-design.
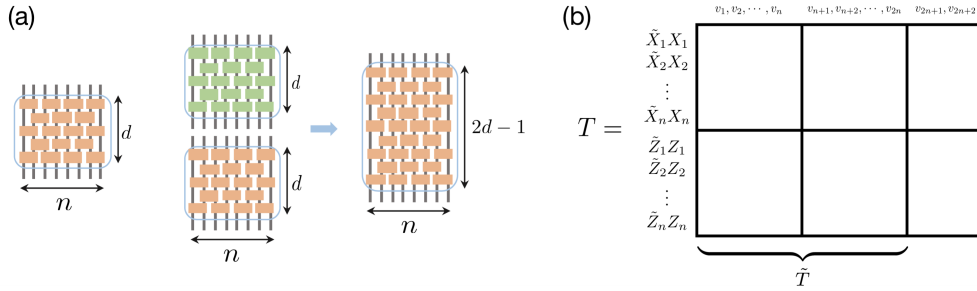
Figure A.1: (a) Left: the layout of the random Clifford circuit U considered in this work. For a pair of circuits U and V drawn from an ensemble ν_d of depth d circuits, $U^\dagger V$ is, equivalently, a unitary drawn from ν_{2d-1} of depth $2d-1$. (b) An illustration of matrix T. The first and the second n rows of T represent operators $\tilde{X}_1 X_1, \cdots, \tilde{X}_n X_n$ and $\tilde{Z}_1 Z_1, \cdots, \tilde{Z}_n Z_n$, respectively. Each operator is specified by using a length $2n+2$ binary vector, based on the Eq. (A.5).

Numerical algorithm

While it is well known that the unitary evolution of a quantum state under Clifford gates can be efficiently simulated using classical computers [26, 54, 99, 100], this does not imply that one can explicitly evaluate the matrix that implements the unitary time evolution. Computing the exact frame potential for an ensemble of Clifford circuits is a formidable task mainly due to two reasons. First, in a naïve approach, taking the trace of a Clifford unitary requires simulating the evolution of exponentially many different initial states owing to the large Hilbert space. Second, the summation over every element, U, V, from the ensemble of random Clifford circuit is computationally expensive due to the large size of the ensemble. While the second difficulty can be resolved by performing Monte Carlo sampling of the group elements, the first challenge is non-trivial.

In this section, we provide an efficient algorithm to compute the trace of a Clifford circuit. In comparison to the naïve approach of simulating the evolution of exponentially many different initial states, our approach takes only a polynomial time as a function of system size n.

Recall that the k-th frame potential for an ensemble of Clifford circuits of depth d is of the form

$$F_{\nu_d}^{(k)} = \frac{1}{|\nu_d|^2} \sum_{U,V \in \nu_d} \left| \mathrm{tr}\left(U^\dagger V\right) \right|^{2k}. \tag{A.3}$$

Here, we focus on the layout of the circuit shown in Fig. A.1(a), while our technique introduced here is more broadly applicable. Since both U and V consist of d layers of random Clifford gates, we note that $U^\dagger V$ can be also regarded as a circuit of depth $2d-1$ without loss of

generality. Therefore, we can rewrite the frame potential as

$$F_{\nu_d}^{(k)} = \frac{1}{|\nu_{2d-1}|} \sum_{U \in \nu_{2d-1}} |\mathrm{tr}\, U|^{2k} = \frac{1}{|\nu_{2d-1}|} \sum_{U \in \nu_{2d-1}} |\mathrm{tr}\, U\, \mathrm{tr}\, U^\dagger|^k = \frac{1}{|\nu_{2d-1}|} \sum_{U \in \nu_{2d-1}} |Q_U|^k, \quad \text{(A.4)}$$

where $Q_U \equiv \mathrm{tr}\, U \,\mathrm{tr}\, U^\dagger$. Thus, our problem reduces to computing Q_U exactly for a given unitary U, and then performing a Monte-Carlo sampling of U over different realizations of the depth $2d - 1$ random Clifford circuits. Below, we focus on the computation of Q_U assuming U is given as a Clifford circuit.

Our key idea is to further simplify the expression Q_U using Pauli operators. In particular, we are interested in evaluating Q_U without having to explicitly construct the unitary matrix U. This is in fact possible, because, by the definition of the Clifford group, the unitary U can be fully characterized by specifying how generators of n-qubit Pauli group $\mathcal{P}$ transform under the conjugation by U [1]. To this end, it is important to introduce an efficient notation to denote a Pauli element. Here and below, we adapt and extend the notation for Pauli operators in the existing literature [1] and denote an element in the n-qubit Pauli group by a binary string $v = v_1 v_2 \cdots v_{2n+2}$ of length $2n + 2$:

$$P_v = (-1)^{v_{2n+1}} i^{v_{2n+2}} \prod_{j=1}^{n} K_j(v_j, v_{j+n}), \quad \text{(A.5)}$$

where $K_j(1, 0) = X_j$, $K_j(0, 1) = Z_j$, or $K_j(1, 1) = Y_j$ represents one of the Pauli operators for a qubit at site j, following the convention in [1]. In other words, the first $2n$ bits in a string v specify the n-qubit Pauli string, and the last two digits control the overall coefficient. We will find that the global prefactor $(-1)^{v_{2n+1}} i^{v_{2n+2}}$ is often not very important other than that it gives rise to exactly four elements in $\mathcal{P}$ per a single Pauli string (with different prefactors). Hence, for notational brevity, we denote the first $2n$ bits of v as $\bar{v} = v_1 v_2 \ldots v_{2n}$. In this way, the product of two Pauli strings can be concisely represented as a simple XOR operation on corresponding binary strings: if $P_v \equiv P_u P_w$, then $\bar{v} = \bar{u} + \bar{w}$, where the "+" operator should be interpreted as element-wise XOR operations. This establishes the one-to-one correspondence between a binary string of length $2n$ and every group element in $\mathcal{P}$ up to a prefactor. In particular, the group multiplication in $\mathcal{P}$ corresponds to a linear operation in the binary string. Furthermore, the set of binary strings forms a vector space with respect to XOR operations. We note that the prefactor of v can be also computed from u and w.

In order to compute Q_U, we first re-express it using the fact that the Pauli group $\mathcal{P}$ forms a unitary 1-design. More specifically, for any n-qubit operator O, we have, $\mathrm{tr}(O) \cdot \mathbb{1} = \frac{1}{4D} \sum_{P \in \mathcal{P}} P O P^\dagger$. Then, it follows:

$$Q_U = \mathrm{tr}\, U^\dagger \,\mathrm{tr}\, U = \mathrm{tr}\big(U^\dagger \mathbb{1} \cdot \mathrm{tr}(U)\big) = \frac{1}{D} \sum_{P \in \mathcal{P}^+} \mathrm{tr}\big(U^\dagger P U P^\dagger\big) = \frac{1}{D} \sum_{P \in \mathcal{P}^+} \mathrm{tr}\Big(\tilde{P} P^\dagger\Big), \quad \text{(A.6)}$$

where $D = 2^n$ is the Hilbert space dimension, $\tilde{P} \equiv U^\dagger P U$, and the summation is over the operators in the set $\mathcal{P}^+ = \{\mathbb{1}, X, Y, Z\}^{\otimes n}$, ignoring the irrelevant complex prefactor

(which cancels the factor $1/4$). We note that $\tilde{P}P^\dagger$ is also a Pauli operator and its trace is non-vanishing if and only if $\tilde{P}P^\dagger \propto \mathbb{1}$. Therefore, in order to evaluate Q_U, we only need to count how many $P \in \mathcal{P}^+$ gives rise to a non-vanishing contribution. We denote the set of such Pauli operators as $\mathcal{K}_U$.

Our key observation is that $\mathcal{K}_U$ is closed under multiplications to form a subgroup of $\mathcal{P}$, and its binary representation form a linear vector space over binary field. Therefore, counting the number of element in $\mathcal{K}_U$ can be efficiently achieved by computing the dimension of the vector space $\mathcal{K}_U$. Here and below, we use the same notation $\mathcal{K}_U$ to refer to both the vector space and the subgroup of Pauli group whenever there is no ambiguity. Below, we will discuss some important properties of $\mathcal{K}_U$. In particular, we will demonstrate that the computation of Q_U always falls into one of three cases:

- $\mathcal{K}_U$ contains only the identity operator. Namely, the Pauli operator P satisfies $\tilde{P}P^\dagger \propto \mathbb{1}$ only when $P = \mathbb{1}$. $Q_U = 1$;

- $\mathcal{K}_U$ of dimension N is generated by N Pauli operators P with $\tilde{P}P^\dagger = \mathbb{1}$. $\mathcal{K}_U$ contains 2^N Pauli operators, $Q_U = 2^N$;

- There exists at least one generator P of $\mathcal{K}_U$ satisfying $\tilde{P}P^\dagger = -\mathbb{1}$. Then, there are equal numbers of Pauli operators P with $\tilde{P}P^\dagger = \mathbb{1}$ and P with $\tilde{P}P^\dagger = -\mathbb{1}$, i.e., the operators satisfying $\tilde{P}P^\dagger = \mathbb{1}$ and $-\mathbb{1}$ come in pairs. $Q_U = 0$.

To see this, we notice that, for any $P_v \in \mathcal{P}$, $\mathrm{tr}\left(\tilde{P}_v P_v^\dagger\right)$ is always real since

$$\mathrm{tr}\left(\tilde{P}_v P_v^\dagger\right)^* = \mathrm{tr}\left(U^\dagger P_v U P_v^\dagger\right)^* = \mathrm{tr}\left(P_v U^\dagger P_v^\dagger U\right) = (-1)^{2v_{2n+2}}\,\mathrm{tr}\left(P_v^\dagger U^\dagger P_v U\right) = \mathrm{tr}\left(\tilde{P}_v P_v^\dagger\right). \tag{A.7}$$

This implies $\mathrm{tr}\left(\tilde{P}_v P_v^\dagger\right) \neq 0$ if and only if $\tilde{P}_v P_v^\dagger = \pm\mathbb{1}$. We use $\mathcal{K}_U^\pm$ to denote the set of operators P_v satisfying $\tilde{P}_v P_v^\dagger = \pm\mathbb{1}$, respectively. $\mathcal{K}_U^+$ forms a normal subgroup of K_U. If $\mathcal{K}_U^-$ is trivial, i.e., contains no element, $\mathcal{K}_U^+$ is exactly $\mathcal{K}_U$. When $\mathcal{K}_U^-$ is non-trivial, we require at least one generator P of $\mathcal{K}_U$ satisfies $\tilde{P}P^\dagger = -\mathbb{1}$. In this case, $\mathcal{K}_U^+$ becomes the maximal normal subgroup of $\mathcal{K}_U$, and the quotient group $\mathcal{K}_U/\mathcal{K}_U^+ = \mathbb{Z}/2\mathbb{Z}$. Therefore, $\mathcal{K}_U^\pm$ contain the same number of elements, and, as a result, $Q_U = 0$.

Due to this correspondence between P satisfying the property $\tilde{P}P^\dagger \propto \mathbb{1}$, and the linear space $\mathcal{K}_U$, counting the number of such operators can be efficiently accomplished by finding out a set of mutually commuting generators of the group, or, equivalently, the basis of the linear space $\mathcal{K}_U$ in the binary representation. Namely, the number of elements in $\mathcal{K}_U$ is given by $2^{m_\mathcal{K}}$, where $m_\mathcal{K}$ is the dimension of $\mathcal{K}_U$. In the second case where all operators P in $\mathcal{K}_U$ satisfy $\tilde{P}P^\dagger = \mathbb{1}$, $Q_U = 2^{m_\mathcal{K}}$.

Now, the calculation of Q_U reduces to figuring out $m_\mathcal{K}$ and the existence or the absence of any generator P satisfying $\tilde{P}P^\dagger = -\mathbb{1}$. In order to find out $m_\mathcal{K}$, we introduce a matrix T of size $2n$ by $2n + 2$. The first and the second n rows of T represent the Pauli operators $\tilde{X}_i X_i$ and $\tilde{Z}_i Z_i$, respectively [see Fig. A.1(b)]. We denote the first $2n$ columns of T by $\bar{T}$. Since the
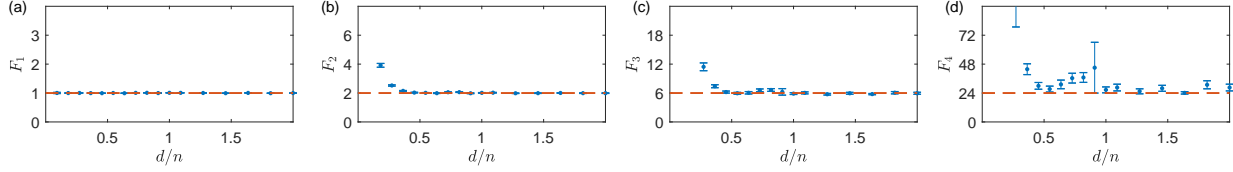
Figure A.2: Numerical computation of the first, second, third, and fourth frame potentials (from (a) to (d)) as a function of circuit depth $2 \leq d \leq 44$ for system size $n = 22$ qubits. The frame potentials are estimated from 50000 randomly generated Clifford circuits. The depths of circuit d is taken from 2 to 44 (blue markers). Orange dashed lines represent the corresponding values for the Haar random unitary ensemble.

identity operator $\mathbb{1} \in \mathcal{P}$ corresponds to the zero in the binary representation, one can easily check that the linear space $\mathcal{K}_U$ can be determined from the kernel of $\bar{T}$ (over the binary field). Furthermore, one can determine the sign of $\tilde{P}_\alpha P_\alpha$ for every basis vector in $\mathcal{K}_U$ by explicitly performing the effective "Gaussian elimination" (or row operations) that properly accounts for the changes in the prefactors of Pauli operators. Motivated from Ref. [1], we define a modified *rowsum()* function. The *rowsum()* function takes two rows of T (corresponding to operators $\tilde{P}_u P_u^\dagger$ and $\tilde{P}_v P_v^\dagger$) as input and returns a binary representation for the operator $\tilde{P}_v \tilde{P}_u P_u^\dagger P_v^\dagger$:

$$\text{rowsum}(\tilde{P}_u P_u^\dagger, \tilde{P}_v P_v^\dagger) = \tilde{P}_v \tilde{P}_u P_u^\dagger P_v^\dagger = (-1)^{-\bar{t}\Lambda_n \bar{v}} \tilde{P}_v P_v P_t, \tag{A.8}$$

where $P_t = \tilde{P}_u P_u^\dagger$, and $\Lambda_n = [0, \mathbb{1}_n; -\mathbb{1}_n, 0]$ is the symplectic form. By checking the value in the $(2n+1)$-th column, we can determine the sign for generators $\tilde{P}_v P_v$ of the kernel $\mathcal{K}_U$. In this way, we can compute Q_U for each realization of the circuit and further obtain the frame potential.

Numerical results

The results of our numerical calculations are summarized in Fig. A.2, which shows that, the first, second, and third frame potentials for the random Clifford circuit ensemble approach to corresponding values for a unitary $1, 2$ and 3-design when the depth of circuit d is sufficiently large, $\sim O(n)$, as predicted in [40]. In contrast, the fourth frame potential significantly deviates from the value for a unitary 4-design, which is expected since it has been proved that even the n-qubit Clifford group does not form a unitary 4-design [264].

In the model proposed in the main text, each cluster consists of $m = 11$ qubits, hence a nearest neighboring cluster pair have total $n = 2m = 22$ qubits. Our numerical results in Fig. A.2(b) indicate that random Clifford circuits of depth $d = 44$ are sufficient to approximate a unitary 2-design in such a case.
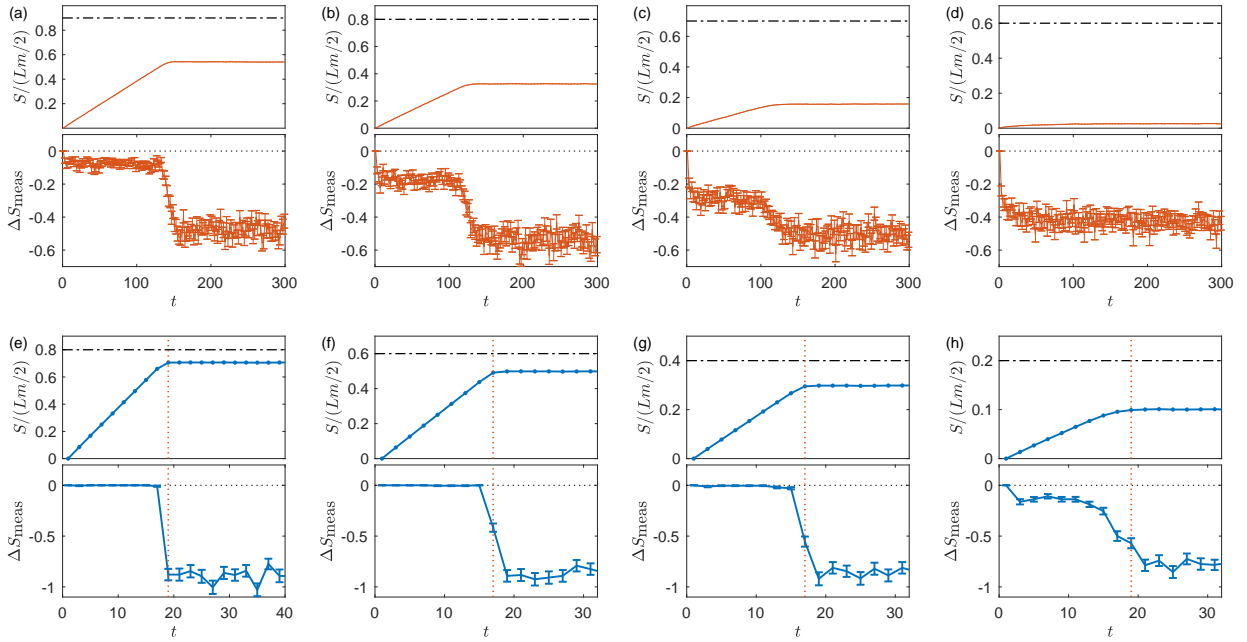
Figure A.3: Half-chain entanglement dynamics in various parameter regimes. Simulations are performed for systems with $L = 32$, $m = 11$. Upper panels in (a-h): the growth of entanglement entropy per qubit as a function of time t. Black dash-dotted lines indicate $1-p$, which correspond to the maximum possible entanglement entropy per qubit after projective measurements. Lower panels in (a-h): the change of entanglement entropy before and after random projective measurements in each time step. The errorbars represent the standard deviation of entanglement reduction by measurements. (a-d): The depth of the local Clifford circuit $d = 3$, and the measurement fraction is $p = 0.1, 0.2, 0.3, 0.4$, respectively (from left to right). (e-h): The depth of the local Clifford circuit $d = 44$, and $p = 0.2, 0.4, 0.6, 0.8$, respectively (from left to right). In this regime, the local circuit approximates a unitary 2-design. The red dotted vertical lines in (e) and (f) indicate when the entanglement entropy per qubit, $S/(Lm/2)$, reaches its steady-state value. All the results in this figure are averaged over 240 different realizations of the random unitary circuit.

A.2 Detailed numerical simulation results for the entanglement growth

Figure A.3 provides detailed information on the entanglement growth and saturation in vaious parameter regimes. We focus on two different values of the local circuit depth, $d = 3$ or 44, and simulate the quantum dynamics for various values of the measurement fraction

p [1]. When $d = 3$, each local circuit fails to approximate a unitary 2-design, and quantum information cannot be fully scrambled even within the local Hilbert space of a m-qubit box. In this regime, the growth of entanglement entropy can be significantly affected by random projective measurement. Indeed, we find that the projective measurements reduce the half-chain entanglement starting from the early time evolution at $t = 0$.

In contrast, when $d = 44$, each Clifford unitary U approximates a unitary 2-design for $2m = 22$ qubits as demonstrated in the previous section. One can apply the decoupling inequality as discussed in the main text (see Section A.5 for its derivation). In this regime, the entanglement entropy should not be significantly decreased by projective measurements during early time evolution as long as $\gamma < 1 - p$, or more precisely $2^{-(1-\gamma-p)m} \ll 1$, where γ is the entanglement entropy per qubit. This regime is indicated by using a vertical line with the identification $\gamma = S/(Lm/2)$. Strictly speaking, this identification is not exact, since the relevant γ for decoupling theorem should have been obtained from the entanglement entropy between a neighboring qubit blocks and the rest of the system, rather than from the half-chain entanglement S. Still, we expect the qualitatively similar behavior. Our expectation is explicitly verified in Figs. A.3(e-g), where $\Delta S_{meas} \approx 0$ within errorbars. For the largest measurement probability $p = 0.8$ in Fig. A.3(h), ΔS_{meas} is nonnegligible as the required condition, $2^{-(1-\gamma-p)m} \ll 1$, for our improve decoupling inequality in Section A.5 is no longer satisfied.

A.3 Detailed numerical simulation results for the phase transition

In this section, we present detailed numerical simulation results for the entanglement phase transition. We first study the phase transition when the size of qubit block $m = 11$ is large. We extract critical measurement probabilities p_c and critical exponents ν using the finite-size scaling analysis of half-chain entanglement entropy and tripartite mutual information in Sec. A.3 and A.3, respectively. Furthermore, we investigate the phase transition for various m with a fixed $d/m = 3$ in Sec. A.3. We extract p_c, ν as well as the prefactor of logarithmic scaling of entanglement entropy at the critical point for various m and compare the results to the existing theoretical predictions.

Half-chain entanglement entropy

Following the entanglement scaling hypothesis proposed in a recent work [162], we perform a finite-size scaling analysis with the scaling ansatz:

$$S(p, L) = \alpha \ln L + \mathcal{F}\left((p - p_c)L^{1/\nu}\right), \tag{A.9}$$

---

[1]We measure pm number of qubits within each block after applying a layer of unitary gates to pairs of qubit blocks. For a noninteger pm, the number of measured qubits is determined from a binomial distribution between $\lfloor pm \rfloor$ and $\lceil pm \rceil$ with the mean value being pm.
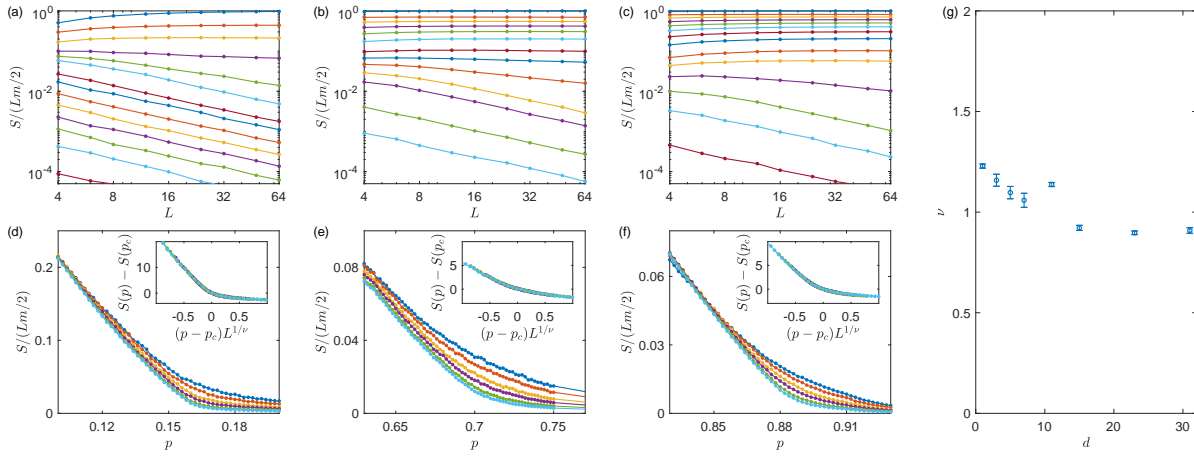
Figure A.4: Finite size scaling analysis and critical exponents. (a-c) The entanglement density $S/(Lm/2)$ as a function of system size L for different depths of local circuits, $d = 1, 7, 31$, respectively (from left to right). Different curves correspond to our numerical results with different measurement fractions. System size L ranges from 4 to 64. (d-f) The entanglement density as a function of measurement fraction for $d = 1, 7, 31$, respectively (from left to right). Different curves correspond to results from different system sizes $L = 12, 16, 24, 32, 48, 64$. Data collapses are presented in the insets using the scaling hypothesis Eq. A.9. (g) Numerically extracted critical exponents ν for different values of d. The error bars are estimated using the bootstrapping method.

where α is a constant, characterizing the logarithmic entropy at the critical point, p_c is the critical measurement fraction, ν is the correlation length critical exponent, and $\mathcal{F}(x)$ is a universal function. We expect that the universal function $\mathcal{F}(x)$ takes the following qualitative behaviors:

$$\mathcal{F}(x) \approx \begin{cases} |x|^{\nu} & (x \to -\infty) \\ \text{const.} & (x = 0) \\ -\alpha\nu \ln x & (x \to \infty). \end{cases} \tag{A.10}$$

Thus, in the thermodynamic limit $L \to \infty$, when $p > p_c$, $S(p, L)$ converges to a constant with no dependence on L, indicating the area-law phase. In the case $p < p_c$, $S(p, L)$ scales linearly in L with a log correction. In practice, we substract the entropy at the critical point, $\alpha \ln L$, (with numerically optimized p_c) from both sides of Eq. (A.9), converting it into a conventional finite size scaling form [239], i.e.,

$$S(p, L) - S(p_c, L) = \mathcal{F}\left((p - p_c)L^{1/\nu}\right). \tag{A.11}$$

More specifically, we numerically optimize the parameter p_c and ν by minimizing the cost function

$$Q = \frac{1}{\mathcal{N}} \sum_{i,j} \frac{(y_{ij} - Y_{ij})^2}{dy_{ij}^2 + dY_{ij}^2}, \tag{A.12}$$

where Y_{ij}, dY_{ij} are the values given by the scaled function and its standard error at x_{ij}, and y_{ij}, dy_{ij} are the data points at x_{ij}. The index j labels different system sizes and i labels different measurement fractions. The detailed algorithm can be found in [122, 137].

In Figs. A.4(a-f), we present our numerical results for the phase transition with various local circuit depths d and fixed qubit block size $m = 11$. The half-chain entanglement entropy normalized by the number of qubits $S/(Lm/2)$ approaches a constant in the volume-law phase, while it decays as $1/L$ in the area-law phase [see Figs. A.4(a-c)]. $S/(Lm/2)$ as a function of measurement probability p shows that the transition becomes sharper when increasing the system size [see Figs. A.4(d-f)]. We obtain data collapses in the insets of Figs. A.4(d-f) using the scaling formula in Eq. (A.11) [239]. Critical measurement probabilities p_c and critical exponents ν are extracted by optimizing the cost function Q in two steps: (1) choose a p_c in the critical regime and find the minimum of the cost function $Q_{\min}(p_c)$ for the given p_c by optimizing over ν; (2) find the global minimum of $Q_{\min}(p_c)$ to extract the optimal p_c and ν. The extracted p_c and ν for various d with fixed $m = 11$ are presented in Fig. 2(e) in the main text and Fig. A.4(g), respectively. We estimate the error bars for ν in Fig. A.4(g) using the bootstrapping method. More specifically, out of 100 measurement probabilities in the critical regime for each d, we randomly choose 80 data points and perform the scaling analysis described above to extract ν and p_c. We repeat the analysis for 100 times and use the standard deviation of ν as an estimation of the error bars. We note that the estimated error bars only reflect the goodness of data collapse using the aforementioned method (statistical errors), and do not reflect the accuracy of this method, i.e. any potential systematic errors may not be accounted for. Using this method, we numerically extract critical exponents $\nu \approx 1$, which is in rough agreement with the results in Refs. [162]. However, the extracted ν fluctuates as a function of d. This is due to the presence of a logarithmic correction to entanglement entropy in the volume-law phase. The resulting scaling formula in Eq. (A.11) requires an additional optimization over p_c, which limits the accuracy (p_c, ν) of finite size scaling. For these reasons, we find that extracting ν from tripartite mutual information is more reliable as we discuss in the next section.

Tripartite mutual information

In order to improve the accuracy of the extracted critical measurement strength p_c and critical exponent ν, Ref. [104] proposed to use the tripartite mutual information I_3 as an alternative probe of the phase transition. More specifically, we consider an one-dimensional chain of qubits with the periodic boundary condition that contains four contiguous subsystems A, B, C and D of size $L/4$. The tripartite mutual information I_3 characterizes the nonlocal
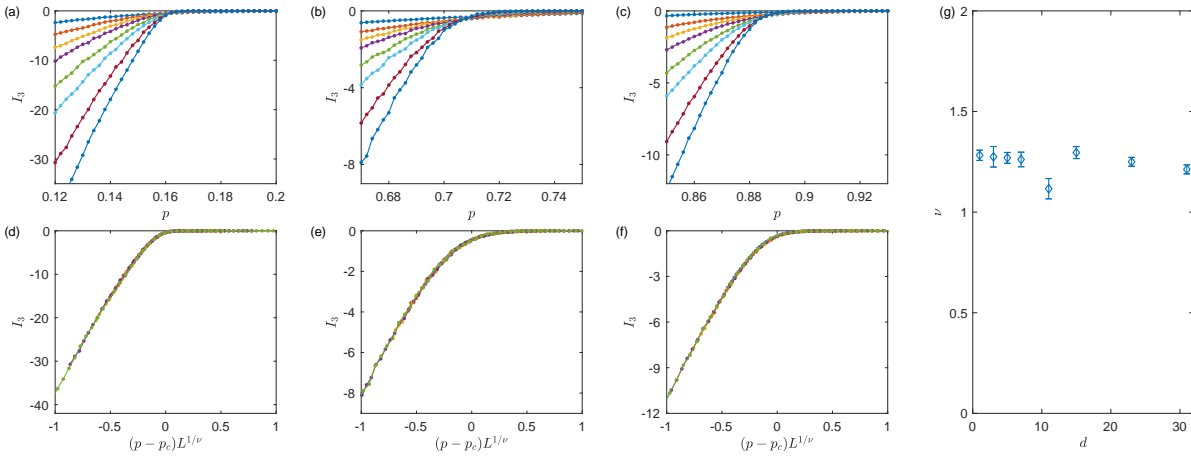
Figure A.5: Finite size scaling analysis and critical exponents. (a-c) The tripartite mutual information I_3 as a function of measurement probability p for different depths of local circuits, $d = 1, 7, 31$, respectively (from left to right). Different curves correspond to our numerical results for various system sizes ranging from 4 to 64. (d-f) Data collapses for $d = 1, 7, 31$ (from left to right) obtained using the scaling hypothesis Eq. (A.14). (g) Extracted critical exponents ν for various local circuit depth d. The numerical values of p_c and ν are also summarized in Table A.1.

entanglement among four partitions and is defined as

$$I_3(A : B : C) \equiv S_A + S_B + S_C - S_{AB} - S_{BC} - S_{AC} + S_{ABC}, \tag{A.13}$$

where S represents the entropy for the corresponding reduced density matrix. This quantity scales with the size of the system L in the volume-law phase, while exhibits an area-law scaling in the area-law phase. More importantly, the logarithmic corrections to the entropy in the volume-law phase cancel in the expression for $I_3(A : B : C)$, and I_3 takes an $O(1)$ value at the critical point.

Near the critical point, I_3 follows the scaling ansatz [104]:

$$I_3(p, L) = \mathcal{G}\left((p - p_c)L^{1/\nu}\right), \tag{A.14}$$

where $\mathcal{G}(\cdot)$ is a universal function. Our finite-size scaling and numerically extracted p_c and ν are summarized in Fig. A.5 and Table A.1. The extracted critical exponent $\nu \approx 1.25$ shows no (or very weak) dependence on the depth d, suggesting its universal behavior. The exponent ν in our model is consistent with the value from the brick-layer random Clifford circuit model studied in Refs. [162], which (approximately) corresponds to the special case $d = 1$ in our model.

d	1	3	5	7
ν	1.28 ± 0.03	1.28 ± 0.05	1.27 ± 0.03	1.26 ± 0.04
p_c	0.162	0.412	0.589	0.707
d	11	15	23	31
ν	1.12 ± 0.05	1.30 ± 0.03	1.25 ± 0.02	1.21 ± 0.02
p_c	0.826	0.862	0.883	0.886

Table A.1: Critical exponents ν and phase transition points p_c for our toy model in the main text with different depths d for local random Clifford circuits. The results are extracted from the finite-size scaling analysis of tripartite mutual information I_3 according to the scaling ansatz given in Eq. (A.14). The number of qubits in a cluster $m = 11$. The error bars of the critical exponent ν are estimated using the bootstrapping method.

Phase transition for various sizes of qubit block

In this section, we focus on deep local Clifford circuits, i.e., $d/(2m) \gtrsim 1$, in which the local circuit approximates a unitary 2-design (see Sec. A.1). The entire local unitary circuit of depth d can be considered as a single Clifford gate acting on nearest neighbor qudits with a local Hilbert space dimension $q = 2^m$. Therefore, changing the size of qubit blocks in this regime is equivalent to tuning local Hilbert space dimension q, and it allows us to study the phase transition for various q. The behavior of the limiting case $q \to \infty$ (or $m \to \infty$) has been previously discussed for a brick-layer circuits in Ref. [18, 130].

In our model, the critical measurement probability p_c approaches unity in the limit of $m \to \infty$, as we can show by using the newly developed decoupling inequality in Sec. A.5. We note that this limit in our model is different from the $q \to \infty$ limit in the brick layer random unitary circuit model studied in Refs. [18, 130]. The projective measurements in our model measures a deterministic fraction of qubits within each qubit block, while the measurements in the brick-layer random circuit projects qudits of dimension q (or, equivalently, the entire qubits in a block) with a certain probability. This distinction may lead to a different universality of the phase transition, which remains largely unexplored. We also note that Refs. [18, 130] has shown that brick-layer random circuit models with measurements can be mapped to a 2D bond percolation problem on square lattice in the $q \to \infty$ limit. However, the mapping to the percolation problem is not applicable to our present model in the same limit.

Here, we investigate the phase transition as a function of q in our qubit-block model by fixing $d/m = 3$. We extract critical measurement probabilities p_c and critical exponents ν for various m, as presented in Figs. A.6(a,b). The critical measurement probability p_c grows monotonically with m [Fig. A.6(a)]. This is consistent with the prediction that $p_c \to 1$ when $m \to \infty$. The critical exponent ν shows no obvious dependence on m and takes a universal value $\nu \approx 1.25$ [Fig. A.6(b)], which suggests the universality of the phase transition remains the same for different m's. In addition, the entanglement entropy at the critical point scales
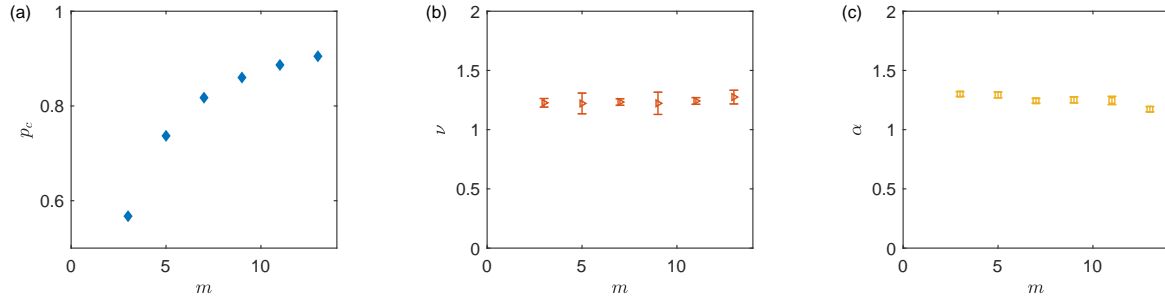
Figure A.6: Numerically extracted phase transition points and critical exponents for various sizes of qubit clusters m with a fixed relative depth $d/m = 3$, based on the finite size scaling ansatz of I_3 in Eq. (A.14) for system sizes up to $L = 64$. (a) Critical measurement strength p_c for various $m = 3, 5, 7, 9, 11, 13$. (b) Critical exponent ν for various m. The error bars are estimated by using the bootstrapping method. (c) Coefficient α for the logarithmic entanglement entropy scaling at the critical point p_c for various m.

logarithmically with the system size:

$$S(p_c, L) = \alpha \log L, \tag{A.15}$$

where α is expected to be universal [239, 130] and determined by the underlying theory of the critical point. Here, we evaluate the entropy $S(p_c, L)$ at the critical point for various system sizes up to $L = 64$. We observe a logarithmic scaling of the entanglement entropy and extract α as a function of m [Fig. A.6(c)], which does not show any substantial change for different values of m.

A.4 Quantum channel capacity and entanglement phase transition

In this section, we establish a connection between the quantum channel capacity and the entanglement phase transition. More specifically, we consider a generic unitary evolution interspersed by projective measurements as a quantum channel jointly acting on the system and measurement devices, and show that the quantum channel capacity $\mathcal{Q}$ of such a channel can be related to the entropy of the system $\langle S \rangle$ conditioned on measurement outcomes when the system is initialized in a certain optimized state [see Fig. A.7(a)]. We note that the former, $\mathcal{Q}$, characterizes the maximum amount of quantum information that can be transmitted through a quantum channel, while the latter, $\langle S \rangle$ is proposed as an alternative signature to identify the entanglement phase transition in Ref. [104]. In what follows, we first introduce our setup and notations that would allow us to quantitatively study the quantum channel capacity. Then, we derive the relation between $\mathcal{Q}$ and $\langle S \rangle$.
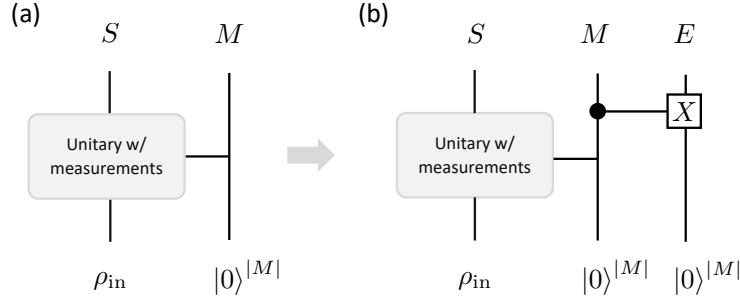
Figure A.7: (a) We consider an maximally mixed input state ρ_{in} evolved under unitary dynamics interspersed with measurements. The output of the system and the classical measurement outcomes are denoted as S and M. (b) The scenario illustrated (a) can be understood as a unitary evolution by considering the measurements as unitary coupling between the system and measurement device, followed by the dephasing of the measurement device. The measurement device M is dephased through the coupling with an auxiliary environment E. The coupling is realized by the controlled-X operation that couples every single ancilla qudit in M to a qudit in E. Here, we consider a specific environment E that contains $|M|$ qudits prepared in $|0\rangle$.

The quantum channel capacity is given by the coherent information about the input state that remains in the output state, optimized over all possible input encoding state ρ_{in}. In our case, we are interested in the coherent information stored in the resultant quantum state of the system *as well as* in the set of projective measurement outcomes. In order to quantify the coherent information that remains in both the system and measurement outcomes, we adapt the weak measurement framework for projective measurements.

In this framework, for each weak measurement, we introduce an ancilla qudit, representing a part of a measurement device M, prepared in a predetermined state, e.g. $|0\rangle$. The ancilla is then correlated with system degrees of freedom by a generic unitary operation. Finally, the ancilla qudit is dephased by additional degrees of freedom, E, that represents environment [Fig. A.7(b)]. The dephasing by the environment ensures that only the classical information remains in the measurement devices. By varying the unitary operation that correlates the ancilla and system degrees of freedom, this formulation allows to characterize measurements in arbitrary positive operator-valued measure (POVM). The dephasing of M can be realized by coupling to E with generalized controlled-X gates,

$$\text{CX}_{ab} = |0\rangle_a \langle 0|_a \otimes \mathbb{1}_b + \sum_{i=1}^{d-1} |i\rangle_a \langle i|_a \otimes \exp\left[-i\frac{\pi}{2}\left(|i\rangle_b \langle 0|_b + |0\rangle_b \langle i|_b\right)\right], \qquad (A.16)$$

acting on $a \in M$ (control) and $b \in E$ (target). Here, $|i\rangle$ with $i \in \{0, 1, \ldots d-1\}$ forms the computational basis for a qudit in M or E. Tracing out every qudit in E after applying the

set of CX_{ab} gates indeed realizes a dephasing channel $\mathcal{D}_{\phi,M}$ applied to M. Therefore, an arbitrary quantum channel $\mathcal{M}$ that consists of generic unitary evolutions interspersed by measurements in any POVM can be formulated as

$$\mathcal{M}[\rho] = \mathcal{D}_{\phi,M} \left[U \left(\rho \otimes (|0\rangle \langle 0|)^{|M|} \right) U^\dagger \right], \tag{A.17}$$

with some unitary U. Here, $|M|$ denotes the number of qudits in M. Fig. A.7 illustrates our framework, in which each of M and E consists of $|M|$ number of qudits.

In this setting, we investigate the quantum channel capacity of $\mathcal{M}$. We note that the output of the quantum channel $\mathcal{M}$ can be explicitly divided into two parts: (i) the density matrix of the system quantum state and (ii) classical information (diagonal density matrix) associated with the dephased measurement device M. The quantum channel capacity $\mathcal{Q}$ for a channel $\mathcal{M}$ is defined by the maximum coherent information per single channel usage when n copies of the channel are simultaneously utilized [212, 271]:

$$\mathcal{Q} = \lim_{n\to\infty} \frac{1}{n} \max_{\rho^{(n)}} \mathcal{I}_c \left(\mathcal{M}^{\otimes n}, \rho^{(n)} \right), \tag{A.18}$$

where $\rho^{(n)} \in \mathcal{H}^{\otimes n}$ is an input quantum state in the n-replicated Hilbert space to be optimized, $\mathcal{I}_c$ is the coherent quantum information defined below. For a special class of quantum channel, so-called *degradable quantum channels* [77, 212, 271], Eq. (A.18) dramatically simplifies to

$$\mathcal{Q} = \max_{\rho} \mathcal{I}_c \left(\mathcal{M}, \rho \right). \tag{A.19}$$

This is because, for degradable quantum channels, the quantum channel capacity is additive [77, 212, 271].

A degradable quantum channel is defined by the following property. For a quantum channel $\mathcal{N}$ that transmits a quantum state from a sender A to receiver A', let $\mathcal{N}_c$ be the complementary channel of $\mathcal{N} : \mathcal{H}_A \to \mathcal{H}_{A'}$. That is, we consider an isometric embedding $U_\mathcal{N} : \mathcal{H}_A \to \mathcal{H}_{A'} \otimes \mathcal{H}_B$ of $\mathcal{N}$ in an extended Hilbert space, i.e. for any $\rho_A \in \mathcal{H}_A$,

$$\mathcal{N}[\rho_A] = \mathrm{tr}_B \left(U_\mathcal{N} \rho_A U_\mathcal{N}^\dagger \right). \tag{A.20}$$

Then, the complementary channel $\mathcal{N}_c$ is defined by

$$\mathcal{N}_c[\rho_A] \equiv \mathrm{tr}_{A'} \left(U_\mathcal{N} \rho_A U_\mathcal{N}^\dagger \right). \tag{A.21}$$

The channel $\mathcal{N}$ is degradable if there exists another quantum channel $\mathcal{T}$ such that $\mathcal{N}_c = \mathcal{T} \circ \mathcal{N}$. For any quantum channel of the form in Eq. (A.17), its isometric embedding can be written as a unitary. This is illustrated in Fig. A.7(a,b). Therefore, by identifying $A = S$, $A' = SM$ and $B = E$, we find that

$$\mathcal{M}[\rho] \equiv \mathrm{tr}_E \left(U \rho U^\dagger \right), \tag{A.22}$$

$$\mathcal{M}_c[\rho] \equiv \mathrm{tr}_{SM} \left(U \rho U^\dagger \right). \tag{A.23}$$

Crucially, by tracing out system degrees of freedom, $\mathcal{M}$ can be degraded into $\mathcal{M}_c$, i.e. $\mathcal{M}_c[\rho] \simeq \text{tr}_S \mathcal{M}[\rho]$. This can be easily shown by considering the reduced density matrix of M and E after applying the set of generalized controlled-X gates, which must be of the form $\rho_{ME} = \sum_{ij} \rho_{ij} |i\rangle_M \langle j|_M \otimes |i\rangle_E \langle j|_E$. In turn, the reduced density matrices for M and E are given by $\rho_{M(E)} = \sum_i \rho_{ii} |i\rangle \langle i|$ in their corresponding Hilbert spaces. Below, we focus on establishing a relation between Eq. (A.19) and $\langle S \rangle$.

For an input state ρ and a quantum channel $\mathcal{N} : \mathcal{H}_A \to \mathcal{H}_{A'}$, the coherent information $\mathcal{I}_c(\mathcal{N}, \rho)$ is defined as

$$\mathcal{I}_c(\mathcal{N}, \rho) \equiv S_{A'} - S_B, \tag{A.24}$$

where $S_{A'(B)}$ is the von Neumann entropy of the output reduced density matrix for subsystem $A'(B)$, and B is an auxiliary system introduced for an isometric embedding of $\mathcal{N}$. In our case, the identification $A = S$, $A' = SM$, and $B = E$ leads to

$$\mathcal{I}_c(\mathcal{M}, \rho_{\text{in}}) = S_{SM} - S_E = S_{SM} - S_M = \langle S \rangle, \tag{A.25}$$

where the second equality arises from the fact that $\rho_B \simeq \rho_E$ discussed above. For the third equality, we used the definition of the entropy of the system averaged over different measurement outcomes

$$\langle S \rangle = \sum_i p_i S(\rho_S[i]), \tag{A.26}$$

where the index i runs over all possible projective measurement outcomes, p_i is the probability for a particular outcome i, and $\rho_S[i]$ is reduced density matrix of the system conditioned on the measurement outcome i. Then, the third equality in Eq. (A.25) holds because of the block diagonal form of the reduced density matrix for S and M [18]:

$$\rho_{SM} = \sum_i p_i \rho_S[i] \otimes |i\rangle_M \langle i|_M. \tag{A.27}$$

Finally, combining Eq. (A.19) and (A.25), we obtain the key result presented in the main text, which we produce here:

$$\mathcal{Q} = \max_{\rho_{\text{in}}} \langle S \rangle. \tag{A.28}$$

In general, the optimization over ρ_{in} for a given channel $\mathcal{M}$ is difficult because it may depends on the detailed information of the unitary evolution as well as set of POVMs. In the case $\mathcal{M}$ is random, as random circuit models, we can define a closely related quantity to characterize the maximal amount of information that can be transmitted through $\mathcal{M}$ *without a priori specifying the instance $\mathcal{M}$*:

$$\bar{\mathcal{Q}} \equiv \max_{\rho_{\text{in}}} \mathbb{E}\left[\langle S \rangle\right], \tag{A.29}$$

where $\mathbb{E}$ denotes averaging over random unitary gates and measurement positions. We note that $\bar{\mathcal{Q}}$ is distinct from average quantum channel capacity $\mathbb{E}[\mathcal{Q}]$ since the optimization over ρ_{in} is performed after averaging over different realization of quantum circuits. Nevertheless, $\bar{\mathcal{Q}}$ has an operational meaning; it quantifies the maximum amount of coherent information that a randomly chosen random unitary circuit with randomly positioned projective measurements can achieve. In other words, $\bar{\mathcal{Q}}$ is the capacity for random quantum channel $\mathcal{M}$ in which the random realizations of unitary gates and measurement positions are a priori not known to an encoder.

In Ref. [104], for a maximally mixed input state $\rho_{\text{in}} = \rho^{\text{max}}$, $\mathbb{E}[\langle S \rangle]$ has been identified as an alternative signature of the entanglement phase transition based on numerical simulations of random Clifford circuits with projective measurements. In more recent work [18], it has been proven that the transition in the scaling behavior in $\mathbb{E}[\langle S \rangle]$ indeed coincides with the entanglement phase transition for Haar random unitary circuits with measurements. Based on the mapping of such quantum circuits to a class of statistical mechanics models and the replica technique introduced in Ref. [18], one can show $\mathbb{E}[\langle S \rangle]$ is maximized when ρ_{in} is maximally mixed. Therefore, $\bar{\mathcal{Q}}$ exactly corresponds to the numerical results of $\mathbb{E}[\langle S \rangle]$ studied in Ref. [104] and is indeed a signature of the entanglement phase transition.

An alternative way to understand the meaning of $\bar{\mathcal{Q}}$ is to introduce a new channel $\tilde{\mathcal{M}}$ that incorporates the randomness of $\mathcal{M}$ as parts of the definition. To be more specific, one can consider that unitary gates applied to the system are determined by quantum states of additionally introduced ancilla qudits M_U. If the qudits are initialized in equal superposition of their computational basis states, the projective measurements on M_U in the basis realize a certain instance of random unitary gates. A similar argument can be made for different positioning of measurements on system qudits (with additional ancilla M_P). In this way, the classical information associated with the randomness (in unitary gates and measurement positions) corresponds to the diagonal elements of the density matrix of ancilla $M_{U,P}$. Following the same analysis described above for $\mathcal{M}$, it follows that $\bar{\mathcal{Q}}$ is the quantum channel capacity of $\tilde{\mathcal{M}}$:

$$\tilde{\mathcal{Q}} = \max_{\rho_{\text{in}}} \mathbb{E}\left[\langle S \rangle\right] = \bar{\mathcal{Q}}. \tag{A.30}$$

This channel capacity is achieved with the maximally mixed input state ρ_{in} since it must be invariant under any local unitary rotations. We note that the new channel $\tilde{\mathcal{M}}$ defined by the dynamics of the system and entire collection of ancilla is again a degradable quantum channel following the same reasoning as in the case of $\mathcal{M}$. This completes the relation between the quantum channel capacity and the averaged entropy of the system conditioned on measurement outcomes.
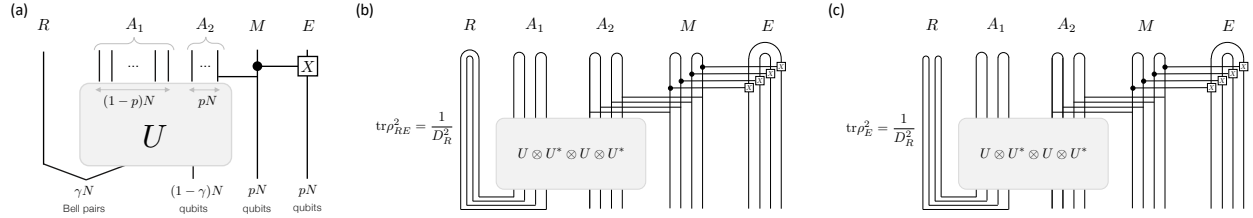
Figure A.8: (a) An illustration of the toy model. (b, c) Tensor network representations of $\operatorname{tr} \rho_{RE}^2$ and $\operatorname{tr} \rho_E^2$, respectively.

A.5 An improved bound on the entanglement reduction by measurements

In the previous section, we define a quantum channel $\mathcal{M}$ that describes a generic unitary evolution interspersed by measurements. The channel $\mathcal{M}$ acts on both the system and ancilla (representing measurement devices) qubits. The coherent information $\mathcal{I}_c(\mathcal{M}, \rho_{\text{in}})$ associated with the quantum channel $\mathcal{M}$ describes the transmission of quantum information encoded both in the output state of the system qubits and in the classical measurement outcomes. Furthermore, we have shown that the coherent information exactly equals the entanglement entropy of the output quantum state averaged over different classical measurement outcomes [see Eq. (A.25)].

Motivated by these new understandings, we revisit the analysis of the toy model in Fig. 1 of the main text and present an improved, tight version of the decoupling inequality, analogous to Eq. (1). The newly derived decoupling inequality is strictly stronger than the previous one. In particular, our new inequality predicts that the phase transition point asymptotically approaches to $p_c = 1$ as $m \to \infty$ for the qubit-block model introduced in the main text in the strongly scrambling regime $d/(2m) \gtrsim 1$. The key idea behind our approach is to explicitly separate out the accessible classical information and inaccessible (lost) information in projective measurement processes.

We consider an N-qubit system A initially sharing γN bell pairs with the reference R. The rest $(1 - \gamma)N$ qubits in the system are prepared in an unentangled product state. We apply a random unitary $U \in \mathrm{U}(2^N)$ drawn from a unitary 2-design to the system qubits and perform projective measurements on randomly chosen pN qubits. We use A_1 and A_2 to denote the unmeasured and measured qubits, respectively. Our goal is to show that, under certain conditions, the extensive number of measurements on A_2 do not reduce the initial entanglement, $S_R = \gamma N$, between A and R. We show this in two steps: (i) we evaluate the coherent information $\mathcal{I}_c$ of this quantum channel and prove $\mathcal{I}_c \approx S_R = \gamma N$ up to exponentially small corrections in N, and (ii) we use Eq. (A.25) to show that $\langle S \rangle = \mathcal{I}_c = \gamma N$. This implies that the average entanglement $\langle S \rangle$ after projective measurements equals its initial value γN, hence no entanglement is reduced by measurements. Here, we focus on proving (i).

Our first step is to formulate the projective measurements on A_2 as weak measurements explained in Sec. A.4. This formalism is useful to keep track of classical information encoded in measurement outcomes. Instead of projective measurements, we introduce a set of ancilla qubits M (representing measurement devices), apply entangling unitaries between A and M (to represent the measurement processes), and then dephase M with a dephasing bath E by applying control-X gates between M and E. The last dephasing procedure is crucial and necessary because a measurement device can hold only classical information (i.e., diagonal elements of its reduced density matrix in computational basis). Using this formalism does not lead to any loss of generality. An illustration of the setup is presented in Fig. A.8(a). We are interested in how much of the initial entanglement (γN Bell pairs) remains (can be recovered) in the quantum state of A *and* classical measurement outcomes in M. This can be quantified by the coherent quantum information [77]:

$$\mathcal{I}_c(\mathcal{M}, \rho_{\mathrm{in}}) \equiv S_R - I(R:E), \tag{A.31}$$

which implies that the reduction in $\mathcal{I}_c$ is determined by the mutual information $I(R:E)$ between the reference and environment. Therefore, it suffices to show $I(R:E) = 0$. Instead of directly evaluating the vanishing mutual information, we show an equivalent statement that the reference R and the dephasing bath E are decoupled,

$$\rho_{RE} \approx \rho_R \otimes \rho_E \tag{A.32}$$

up to exponentially small corrections, provided that inequality $p < 1 - \gamma$ is satisfied. More specifically, we provide an upper bound to the L_1-distance between both sides of Eq. (A.32). According to the Cauchy-Schwarz inequality, we have

$$\|\rho_{RE} - \rho_R \otimes \rho_E\|_1^2 \leq D_R D_E \operatorname{tr}\left[(\rho_{RE} - \rho_R \otimes \rho_E)^2\right] \tag{A.33}$$

$$= 2^{\gamma N} 2^{pN} \left[\operatorname{tr} \rho_{RE}^2 - \frac{1}{2^{\gamma N}} \operatorname{tr} \rho_E^2\right], \tag{A.34}$$

where $D_R = 2^{\gamma N}$ and $D_E = 2^{pN}$ are the Hilbert space dimension of the reference R and dephasing bath E, respectively, and the reduced density matrix for the reference is maximally mixed, i.e., $\rho_R = 2^{-\gamma N} \mathbb{1}_R$. Two terms, $\operatorname{tr} \rho_{RE}^2$ and $\operatorname{tr} \rho_E^2$ on the right-hand side, can be written as the expectation value of a swap operator in a duplicated Hilbert space [212]:

$$\operatorname{tr} \rho_X^2 = \operatorname{tr}\left[\mathrm{SWAP}\left(\rho_X \otimes \rho_X\right)\right] \quad \text{with} \quad X \in \{\mathrm{RE}, \mathrm{E}\}, \tag{A.35}$$

where SWAP is an operator that swaps wavefunctions in two different copies. Equation (A.35) can be pictorially represented by using tensor network diagrams in Figs. A.8(b,c), where taking the trace or the expectation values of SWAP correspond to different contractions at the top of diagrams.

Evaluating the right hand side of Eq. (A.34) for an arbitrary U is computationally intractable. However, we can exactly evaluate it once it is averaged over all possible unitaries

in $U(2^N)$ in Haar measure (or any unitary 2-design). On the right-hand side, evaluating the average $\operatorname{tr} \rho_{RE}^2$ and $\operatorname{tr} \rho_E^2$ involves computing the second moment $\mathbb{E}_U[U \otimes U^* \otimes U \otimes U^*]$ of random unitary U:

$$\mathbb{E}_U\left[U \otimes U^* \otimes U \otimes U^*\right] = \sum_{\sigma,\tau=\pm 1} w_g^{(2)}(\sigma,\tau)\hat{\tau}_{\mathbf{ab}}\hat{\sigma}_{\mathbf{cd}}, \tag{A.36}$$

where the coefficient

$$w_g^{(2)}(\sigma,\tau) = \frac{\delta_{\sigma,\tau}}{d^2 - 1} - \frac{1 - \delta_{\sigma,\tau}}{d(d^2 - 1)}, \tag{A.37}$$

which is the so-called Weingarten function [67], and $\hat{\sigma}$ and $\hat{\tau}$ are tensors associated with the binary variables $\sigma, \tau \in \{\pm 1\}$ defined as

$$\hat{\xi}_{\mathbf{ab}} = \begin{cases} \delta_{a_1 b_1}\delta_{a_2 b_2} & \text{if } \xi = +1 \\ \delta_{a_1 b_2}\delta_{a_2 b_1} & \text{if } \xi = -1 \end{cases}. \tag{A.38}$$

Using this property, we can explicitly evaluate $\mathbb{E}_U\left[\operatorname{tr}\rho_{RE}^2\right]$ and $\mathbb{E}_U\left[\operatorname{tr}\rho_E^2\right]$:

$$\mathbb{E}_U\left[\operatorname{tr}\rho_{RE}^2\right] = \frac{1}{D_R^2}\left[\frac{D_R D_{A_1}^2}{D_A^2 - 1} - \frac{D_R^2 D_{A_1}^2}{D_A(D_A^2 - 1)} - \frac{D_R D_{A_1}}{D_A(D_A^2 - 1)} + \frac{D_R^2 D_{A_1}}{D_A^2 - 1}\right]D_{A_2}$$
$$\simeq 2^{-(\gamma+p)N} - 2^{-(1+p)N} - 2^{-(2+\gamma)N} + 2^{-N}, \tag{A.39}$$

$$\frac{1}{2^{\gamma N}}\mathbb{E}_U\left[\operatorname{tr}\rho_E^2\right] = \frac{1}{2^{\gamma N}}\frac{1}{D_R^2}\left[\frac{D_R^2 D_{A_1}^2}{D_A^2 - 1} - \frac{D_R D_{A_1}^2}{D_A(D_A^2 - 1)} - \frac{D_R^2 D_{A_1}}{D_A(D_A^2 - 1)} + \frac{D_R D_{A_1}}{D_A^2 - 1}\right]D_{A_2}$$
$$\simeq 2^{-(\gamma+p)N} - 2^{-(1+2\gamma+p)N} - 2^{-(2+\gamma)N} + 2^{-(1+2\gamma)N}, \tag{A.40}$$

where $D_{A_1} = 2^{(1-p)N}$, $D_{A_2} = 2^{pN}$ and $D_A = 2^N$ are the Hilbert space dimension of subsystem A_1, A_2 and system A, respectively, and we considered the limit $N \gg 1$ in the second line of both equations. In the first equalities of Eqs. (A.39) and (A.40), we used the results of tensor contractions presented in Fig. A.9. Plugging above two results into Eq. (A.34), we obtain a new decopuling inequality. In particular, in the limit $N \gg 1$, the decoupling inequality becomes

$$\mathbb{E}_U\left[\|\rho_{RE} - \rho_R \otimes \rho_E\|_1\right] \leq \sqrt{\mathbb{E}_U\left[\|\rho_{RE} - \rho_R \otimes \rho_E\|_1^2\right]} \lesssim 2^{-(1-\gamma-p)N/2}. \tag{A.41}$$

We find that when $p < 1 - \gamma$ with $N \to \infty$, ρ_{RE} factorizes as desired. We emphasize that this condition is strictly stronger than the näive sufficient condition $p < (1-\gamma)/2$ presented in the main text, which demands the decoupling between R and A_2. At the technical level, the distinction between two results arises from the fact that we include dephased measurement devices M as part of accessible information in the present approach.

Using this newly derived inequality, we can obtain a quantitative prediction on the critical measurement probability in the 1D qubit-block model. When $d/(2m) \gtrsim 1$, we can
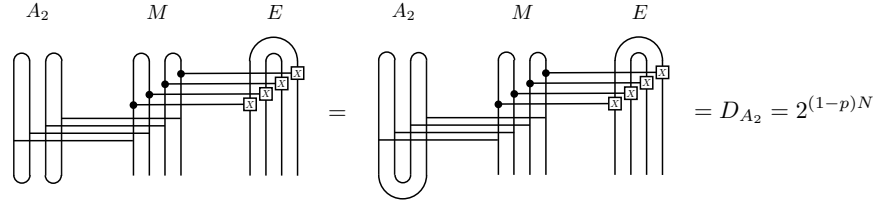
Figure A.9: Tensor network diagrams associated with the measured qubits A_2, measurement device M and the dephasing bath E in Eqs. (A.39) and (A.40).

approximate the local Clifford circuit by a random unitary gate drawn from a unitary 2-design acting on $2m$ qubits. Further considering the limit $m \gg 1$, we can directly apply our analysis here to estimate the amount of entanglement reduction due to measurements. The decoupling inequality above suggests no (or exponentially small in m) entanglement reduction as long as the entanglement entropy per qubit cluster $\gamma < 1 - p$. Since the phase transition occurs when the entanglement density vanishes $\gamma = 0$, we expect $p_c = 1$, provided $d/(2m) \gtrsim 1$ and $m \to \infty$. This prediction suggests $p_c(m)$ in Fig. A.6(a) should asymptotically approach unity in the strongly scrambling regime $d/(2m) \gtrsim 1$ as $m \to \infty$, consistent with our numerical simulation results.

Appendix B

Supplementary material for Chapter 3

B.1 Details of the mapping to classical spin models

Derivation of $w_d^{(n)}$

As discussed in the main text, contracting a pair of diagonally neighboring $\hat{\sigma}$ and $\hat{\tau}$ tensors leads to a weight $w_d^{(n)}(\sigma, \tau)$ that depends on q and α. Using the TN representation given in Fig. B.1, a simple expression of $w_d^{(n)}$ can be written as

$$w_d^{(n)}(\sigma, \tau) = \sum_{\mathbf{aba'b'}} \hat{\sigma}_{\mathbf{ab}} \hat{\tau}_{\mathbf{a'b'}} \mathcal{M}_{\mathbf{ab,a'b'}}^{(n)}, \tag{B.1}$$

where $\hat{\sigma}_{\mathbf{ab}}$ and $\hat{\tau}_{\mathbf{a'b'}}$ denotes the rank-$2n$ tensor in Eq. (3.49) for a single qudit and $\mathcal{M}_{\mathbf{ab,a'b'}}^{(n)}$ denotes the tensor associated with the contraction of ancilla degrees of freedom. We note that $\mathcal{M}_{\mathbf{ab,a'b'}}^{(n)}$ vanishes unless $\mathbf{a} = \mathbf{a'}$ and $\mathbf{b} = \mathbf{b'}$ due to our choice $\hat{R}_\alpha$, which does not have any off-diagonal element for system qudits in the computational basis [Fig. B.1(b)]. Hence, we simplify our notation by using $\mathcal{M}_{\mathbf{ab}}^{(n)}$. For given indices $\mathbf{ab}$, $\mathcal{M}_{\mathbf{ab}}^{(n)}$ takes the form

$$\mathcal{M}_{\mathbf{ab}}^{(n)} = \mathrm{tr} \left[\prod_{k=1}^{n} \left(\mathcal{N}_\phi \left[\rho_{a_k b_k}^{(k)} \right] \right) \right], \tag{B.2}$$

where $\rho_{a_k b_k}^{(k)}$ is the k-th copy of the density matrix of ancilla qudits defined as

$$\rho_{a_k b_k}^{(k)} \equiv e^{-i\hat{X}_{a_k}\alpha} |0\rangle \langle 0| e^{i\hat{X}_{b_k}\alpha}. \tag{B.3}$$

We note that the subscript $a_k, b_k \in \{1, \ldots q\}$ (c.f. not including 0) are indices for system qudits and do not refer a matrix element, i.e., $\rho_{a_k,b_k}^{(k)}$ is a density matrix for an ancilla by itself. The dephasing channel removes the off-diagonal elements of $\rho_{a_k b_k}^{(k)}$: $\mathcal{N}_\phi[\rho_{a_k b_k}^{(k)}] = \cos^2 \alpha |0\rangle \langle 0| + \sin^2 \alpha \, \delta_{a_k b_k} |a_k\rangle \langle a_k|$, leading to a simple expression

$$\mathcal{M}_{\mathbf{ab}}^{(n)} = \cos^{2n} \alpha + \sin^{2n} \alpha \prod_{k=1}^{n} \delta_{b_k a_{k+1}} \delta_{a_k b_k}, \tag{B.4}$$
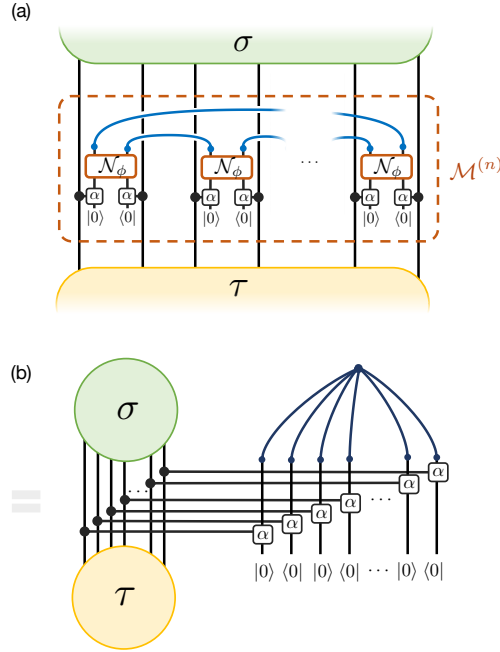
Figure B.1: Tensor network representation of the diagonal weight $w_d^{(n)}$. (a) Every qudit is coupled to an ancilla qudit for a weak measurement. The ancilla qudits undergo the dephasing channel, $\mathcal{N}_\phi$, before contracted across different copies. (b) Rearrangement of the tensor network representation. Note that the diagrammatic representations of dephasing gates are simple in the computational basis of ancilla qudits.

where $a_{n+1} \equiv a_1$, and the product of delta function is nonvanishing unless all $2n$ indices take the same value. Using this expression for $\mathcal{M}_{\mathbf{ab}}^{(n)}$, we obtain

$$
\begin{aligned}
w_d^{(n)}(\sigma, \tau) \\
= \sum_{\mathbf{ab}} \hat{\sigma}_{\mathbf{ab}} \hat{\tau}_{\mathbf{ab}} \left(\cos^{2n} \alpha + \sin^{2n} \alpha \prod_{k=1}^{n} \delta_{a_k b_{k+1}} \delta_{a_k b_k} \right) \\
= q^{\#\mathrm{cycle}(\sigma\tau^{-1})} \cos^{2n} \alpha + q \sin^{2n} \alpha.
\end{aligned}
\tag{B.5}
$$

In the second equality, the tensor contraction of $\hat{\sigma}_{\mathbf{ab}}$ and $\hat{\tau}_{\mathbf{ab}}$ can be represented by a disconnected TN that consists of $\#\mathrm{cycle}(\sigma\tau^{-1})$ loops. Each loop contributes a factor of q to the summation and leads to $\sum_{\mathbf{ab}} \hat{\sigma}_{\mathbf{ab}} \hat{\tau}_{\mathbf{ab}} = q^{\#\mathrm{cycle}(\sigma\tau^{-1})}$. Hence, we derive $w_d^{(n)}$ in Eq. (3.52). Equation (3.34) can be obtained as a special case of $n = 2$. In the limit $\alpha = 0$, $w_d^{(n)} = q^{\#\mathrm{cycle}(\sigma\tau^{-1})}$ reduces to the result in Ref. [183].

Derivation of $\bar{w}^{(2)}$

In the case of $n = 2$, we have seen that the purity of a subsystem maps to the partition function of the classical Ising model on triangular lattice. Here, we derive and explicitly present the three-body weight $\bar{w}^{(2)}(\sigma_1, \sigma_2, \sigma_3)$ in Eq. (3.39) associated with three spin variables living on the vertices of a lower facing triangle, where σ_1, σ_2, and σ_3 refer to the spin variables located at the top left, top right, and bottom center of a triangle. The three-body weight $\bar{w}^{(2)}(\sigma_1, \sigma_2, \sigma_3)$ is given by

$$\bar{w}^{(2)}(\sigma_1, \sigma_2, \sigma_3) = \sum_{\tau = \pm 1} w_d^{(2)}(\sigma_1, \tau) w_d^{(2)}(\sigma_2, \tau) w_g^{(2)}(\sigma_3, \tau). \tag{B.6}$$

Using $w_d^{(2)}$ in Eq. (3.34) and $w_g^{(2)}$ in Eq. (3.32), we can derive the full expression for $\bar{w}^{(2)}$. Considering that $\bar{w}^{(2)}$ is symmetric with respect to the exchange of σ_1 and σ_2, i.e., $\bar{w}^{(2)}(\sigma_1, \sigma_2, \sigma_3) = \bar{w}^{(2)}(\sigma_2, \sigma_1, \sigma_3)$, and that it has Ising symmetry, we only need to specify

$$\bar{w}^{(2)}(\sigma, \sigma, \sigma) = \frac{(q^2 \cos^4 \alpha + q \sin^4 \alpha)^2 - (\cos^4 \alpha + \sin^4 \alpha)^2}{q^4 - 1}, \tag{B.7}$$

$$\bar{w}^{(2)}(\sigma, \sigma, \bar{\sigma}) = \frac{(q \cos^4 \alpha + q \sin^4 \alpha)^2 - (q \cos^4 \alpha + \sin^4 \alpha)^2}{q^4 - 1}, \tag{B.8}$$

$$\bar{w}^{(2)}(\sigma, \bar{\sigma}, \sigma) = \frac{(q \cos^4 \alpha + \sin^4 \alpha)(\cos^4 \alpha + \sin^4 \alpha)}{q^2 + 1}, \tag{B.9}$$

where $\bar{\sigma} = -\sigma$ represents the negation of σ.

We notice that, unlike in the absence of measurements studied in Ref. [183], $\bar{w}^{(2)}(\sigma, \sigma, \bar{\sigma}) \neq 0$ for $\alpha > 0$. We provide an explanation and discuss the implication of unitarity in Appendix B.3.

Derivation of Ising couplings J_h and J_d

The three-body weight factorizes into pairwise contributions in the presence of Ising symmetry. Here, we derive the two-body Ising coupling J_h and J_d in Eq. (3.59). In terms of J_h and J_d, $\bar{w}^{(2)}$ can be written as

$$\bar{w}^{(2)}(\sigma, \sigma, \sigma) = C e^{-2J_d - J_h}, \tag{B.10}$$

$$\bar{w}^{(2)}(\sigma, \bar{\sigma}, \sigma) = C e^{J_h}, \tag{B.11}$$

$$\bar{w}^{(2)}(\sigma, \sigma, \bar{\sigma}) = C e^{-2J_d + J_h}, \tag{B.12}$$

where C is a constant prefactor. Using the expressions for $\bar{w}^{(2)}$, we have

$$J_d = \frac{1}{4} \log \left(\frac{-u_2^2/q^2 + u_1^2}{u_2^2 - u_1^2/q^2} \right), \tag{B.13}$$

$$J_h = \frac{1}{4} \log \left(\frac{(u_1 u_2 (1 - 1/q^2))^2}{(u_2^2 - u_1^2/q^2)(u_1^2 - u_2^2/q^2)} \right), \tag{B.14}$$

where

$$u_2 = q^2 \cos^4 \alpha + q \sin^4 \alpha, \tag{B.15}$$

$$u_1 = q \cos^4 \alpha + q \sin^4 \alpha. \tag{B.16}$$

Since $u_2 \geq u_1$, we can explicitly show that $J_d \leq 0$ is ferromagnetic, $J_h \geq 0$ is anti-ferromagnetic, and $J_d + J_h \leq 0$.

Using the explicit expressions for the Ising couplings, we can analyze the phase transition in the spin model. In the large q limit, J_d dominates over J_h for any given α (i.e., $|J_d| \gg |J_h|$). The phase transition happens when $J_d \sim O(1)$. For this reason, α_c is close to $\pi/2$, and it's reasonable to consider the physically interesting limit $q \gg 1$ and $\pi/2 - \alpha \ll 1$.

A sufficient condition for nonnegative weights for $n \geq 3$

In general, the negative weights in the expression of the n-th moment cannot be eliminated for arbitrary q and α by simply integrating out τ variables. Here, we derive a sufficient condition [Eq. (3.54)] for the weights being nonnegative, which allows the interpretation of the n-th moment as the partition function of a classical spin model.

After integrating out τ variables, the three-body weight in our classical spin model takes the form

$$\bar{w}^{(n)}(\sigma_1, \sigma_2, \sigma_3)$$
$$= \sum_{\tau \in \mathcal{S}_n} w_d^{(n)}(\sigma_1, \tau) w_d^{(n)}(\sigma_2, \tau) w_g^{(n)}(\sigma_3 \tau^{-1}; q^2). \tag{B.17}$$

Here, we simplify the notation by using $w_g^{(n)}(\sigma_3 \tau^{-1}; q^2)$ for Weingarten function instead of $w_g^{(n)}(\sigma_3, \tau; q^2)$ in the main text as it only depends on $\sigma_3 \tau^{-1}$. Also, we will often omit the dependence on q^2. An exact formula for $w_g^{(n)}$ is known [67, 68, 285, 199, 178, 198],

$$w_g^{(n)}(\sigma; d) = \frac{1}{n!} \sum_{\substack{\lambda \vdash n \\ \ell(\lambda) \leq d}} \frac{d_\lambda}{\mathcal{J}_\lambda^{(1)}(1^d)} \chi_\lambda(\sigma), \tag{B.18}$$

where λ denotes a partition of n elements and labels the irreducible representation (irrep) of the permutation group $\mathcal{S}_n$, $\ell(\lambda)$ is the length of the partition λ, χ_λ is the character of the irrep λ, d_λ is the dimension of the irrep λ, and $\mathcal{J}_\lambda^{(1)}$ is the Jack Polynomial given by

$$\mathcal{J}_\lambda^{(1)}(1^d) = \prod_{j=1}^{\ell(\lambda)} \frac{\Gamma(\lambda_j + d - j + 1)}{\Gamma(d - j + 1)}. \tag{B.19}$$

In Chapter 3, we are generally interested in the large q behavior in the model and consider the case $d = q^2 > n$. We can therefore ignore the criterion $\ell(\lambda) \leq d$ in the summation.

The three-body weight $\bar{w}^{(n)}$ can be negative owing to the existence of negative characters that appear in $w_g^{(n)}$. Here, we provide a lower bound of $\bar{w}^{(n)}$ and show that the lower bound becomes positive in a certain limit of q and α. The key idea is to realize that the leading order term in Eq. (B.17) is positive and parametrically larger than the rest of the terms for a sufficiently large q and fixed κ. More specifically, the summation in $\bar{w}^{(n)}$ contains $n!$ terms, among which the term involving $w_g^{(n)}(\mathbb{1}; q^2) > 0$ provides the leading order contribution in the limit of a large q and fixed κ. To start with, we have a lower bound of the three-body weight:

$$\bar{w}^{(n)} > \left(u_1^{(n)}\right)^2 w_g^{(n)}(\mathbb{1})$$
$$- (n! - 1)\left(u_n^{(n)}\right)^2 \max_{\sigma \neq \mathbb{1}}\left(\left|w_g^{(n)}(\sigma)\right|\right), \tag{B.20}$$

where $u_m^{(n)} \equiv q^m \cos^{2n}\alpha + q\sin^{2n}\alpha$. We note that $u_m^{(n)} \geq u_1^{(n)} > 0$.

Now, we provide a lower bound of $w_g^{(n)}(\mathbb{1})$ and an upper bound of $|w_g^{(n)}(\sigma)|$ for $\sigma \neq \mathbb{1}$. The lower bound

$$w_g^{(n)}(\mathbb{1}) > \frac{1}{n!}\sum_\lambda \frac{d_\lambda^2}{(q^2 + n)^n} = \frac{1}{(q^2 + n)^n} \tag{B.21}$$

is obtained by considering the upper bound of the Jack Polynomial. In order to obtain the upper bound of $|w_g^{(n)}(\sigma)|$ with $\sigma \neq \mathbb{1}$, we first introduce $\mathcal{K}_\lambda = 1/\mathcal{J}_\lambda^{(1)}(1^d)$ and utilize the orthogonality relation between characters $\sum_{\lambda \vdash n}\chi_\lambda(\mathbb{1})\chi_\lambda(\sigma) = 0$. We note that $\chi_\lambda(\mathbb{1}) = d_\lambda$. Multiplying both sides of this equation by $\mathcal{K}_{1^n}/n!$ and subtracting it from an expression for $w_g^{(n)}(\sigma)$, we obtain

$$|w_g^{(n)}(\sigma)| = \frac{1}{n!}\left|\sum_{\lambda \vdash n}(\mathcal{K}_\lambda - \mathcal{K}_{1^n})d_\lambda\chi_\lambda(\sigma)\right|$$
$$\leq \frac{1}{n!}\sqrt{\sum_\lambda (\mathcal{K}_\lambda - \mathcal{K}_{1^n})^2 d_\lambda^2 \sum_\lambda \chi_\lambda(\sigma)^2}$$
$$\leq \frac{1}{n!}\max|\mathcal{K}_\lambda - \mathcal{K}_{1^n}|\sqrt{\sum_\lambda d_\lambda^2 \sum_\lambda \chi_\lambda(\sigma)^2}$$
$$< \max|\mathcal{K}_\lambda - \mathcal{K}_{1^n}|. \tag{B.22}$$

In the second line, we used the Cauchy-Schwarz inequality, and in the the fourth line, we used the properties of irreps of a finite group $\sum_\lambda \chi_\lambda(\sigma)^2 < \sum_\lambda d_\lambda^2 = n!$. $\max|\mathcal{K}_\lambda - \mathcal{K}_{1^n}|$ has an upper bound

$$\max|\mathcal{K}_\lambda - \mathcal{K}_{1^n}| < \frac{1}{(q^2 - n)^n} - \frac{1}{(q^2 + n)^n}, \tag{B.23}$$

when $q^2 > n$. Combining these bounds in Eqs. (B.21), (B.22), and (B.23) together and plugging them into Eq. (B.20), we obtain a lower bound

$$\bar{w}^{(n)} > \frac{u_1^2}{(q^2 + n)^n} - n! \left(\frac{u_n^2}{(q^2 - n)^n} - \frac{u_n^2}{(q^2 + n)^n} \right). \tag{B.24}$$

Finally, a sufficient condition of nonnegative $\bar{w}^{(n)}(\sigma_1, \sigma_2, \sigma_3)$ for an arbitrary $(\sigma_1, \sigma_2, \sigma_3)$ can be written as

$$\frac{1}{n!} \frac{1}{(1 + \kappa)^2} > \left(\frac{q^2 + n}{q^2 - n} \right)^n - 1. \tag{B.25}$$

When $\kappa = q^{n-1} \cot^{2n} \alpha$ is fixed and $q \gg 1$, the leading order on the right-hand side is $2n^2/q^2$, and the inequality can be satisfied for a sufficiently large but finite q. This completes the proof that there exists a finite region of (q, α) in which $\bar{w}^{(n)}$ is nonnegative and the n-th moment can be interpreted as the partition function of a classical spin model.

B.2 Spin model for quantum relative entropy

We provide detailed derivations of the spin model for quantum relative entropy in Sec. 3.6.

Derivation of two-body weight

Here, we derive the two-body weight $v_d^{(n)}$ in the spin model description of the quantum relative entropy. Compared to the derivation of $w_d^{(n)}$ in Appendix B.1, the only modification is the absence of the dephasing channel $\mathcal{N}_\phi$ applying to ancilla qudits. The two-body weight is written as

$$v_d^{(n)}(\sigma, \tau) = \sum_{\mathbf{ab}} \hat{\sigma}_{\mathbf{ab}} \hat{\tau}_{\mathbf{ab}} \mathcal{M}_{\mathcal{Q}, \mathbf{ab}}^{(n)}, \tag{B.26}$$

where $\mathcal{M}_{\mathcal{Q}, \mathbf{ab}}^{(n)}$ is the tensor associate with the tensor contraction of ancilla density matrices in the case without dephasing:

$$\mathcal{M}_{\mathcal{Q}, \mathbf{ab}}^{(n)} = \mathrm{tr} \left(\prod_{k=1}^{n} \rho_{a_k b_k}^{(k)} \right) = \prod_{k=1}^{n} \left(\cos^2 \alpha + \delta_{b_k a_{k+1}} \sin^2 \alpha \right). \tag{B.27}$$

An explicit expression for $v_d^{(n)}$ can be obtained using Eq. (3.49) and the expression for $\mathcal{M}_{\mathcal{Q}, \mathbf{ab}}^{(n)}$ above. We should notice the two-body weight $v_d^{(n)}$ does not respect the permutation symmetry for any integer $n \geq 2$. This is manifested in both the mathematical expression and diagrammatic representation of $\mathcal{M}_{\mathcal{Q}, \mathbf{ab}}^{(n)}$. Diagrammatically, without dephasing, n copies of ancilla density matrices are contracted by $\mathcal{C}^{(n)}$ at the top illustrated in Fig. 3.5(a), which explicitly breaks the symmetry $\mathcal{S}_n$ associated with the permutation of n replicated Hilbert

spaces. Mathematically, the permutation symmetry transformation maps $\sigma, \tau \mapsto \xi_1 \circ \sigma \circ \xi_2, \xi_1 \circ \tau \circ \xi_2$ for any pair $(\xi_1, \xi_2) \in \mathcal{S}_n \times \mathcal{S}_n$, and the invariance of $v_d^{(n)}$ requires $\mathcal{M}_{Q,\mathbf{ab}}^{(n)} = \mathcal{M}_{Q,\xi_1(\mathbf{a})\xi_2^{-1}(\mathbf{b})}^{(n)}$, which is generally not satisfied. Despite the absence of the symmetry, $v_d^{(n)}$ has interesting properties. Particularly, $v_d^{(n)}$ has the maximally value q^n when $\sigma = \tau = \mathcal{C}^{(n)}$. Furthermore, when either σ or τ represents the cyclic permutation $\mathcal{C}^{(n)}$, $v_d^{(n)}$ becomes independent of α and reduces to $q^{\#\text{cycle}(\sigma\tau^{-1})}$, which is the result for the spin model description of a RUC without measurements [183, 283].

Specifically, in the case of $n = 2$, $v_d^{(2)}$ takes the form

$$v_d^{(2)}(+, +) = q^2 \cos^2 \alpha + q \sin^2 \alpha, \tag{B.28}$$

$$v_d^{(2)}(+, -) = v_d^{(2)}(-, +) = q, \tag{B.29}$$

$$v_d^{(2)}(-, -) = q^2. \tag{B.30}$$

Derivation of three-body weight

The negative weights in the second moment due to negative Weingarten functions can be eliminated by integrating out τ variables. Hence, we obtain a Ising spin model on a triangular lattice with three-body interaction. The three-body weights $\bar{v}^{(2)}(\sigma_1, \sigma_2, \sigma_3)$ associated with three spins living on the vertices of lower-facing triangle can be explicitly written down. Considering the symmetry of exchange σ_1 and σ_2, i.e., $\bar{v}^{(2)}(\sigma_1, \sigma_2, \sigma_3) = \bar{v}^{(2)}(\sigma_2, \sigma_1, \sigma_3)$, all the independent $\bar{v}^{(2)}$ are written as

$$\bar{v}^{(2)}(+, +, +) = \frac{(q^2 \cos^2 \alpha + q \sin^2 \alpha)^2 - 1}{q^4 - 1}, \tag{B.31}$$

$$\bar{v}^{(2)}(+, +, -) = \frac{q^2 - (q \cos^2 \alpha + \sin^2 \alpha)^2}{q^4 - 1}, \tag{B.32}$$

$$\bar{v}^{(2)}(+, -, +) = \frac{q^3 \cos^2 \alpha + q^2 \sin^2 \alpha - q}{q^4 - 1}, \tag{B.33}$$

$$\bar{v}^{(2)}(+, -, -) = \frac{q^3 - q \cos^2 \alpha - \sin^2 \alpha}{q^4 - 1}, \tag{B.34}$$

$$\bar{v}^{(2)}(-, -, +) = 0, \tag{B.35}$$

$$\bar{v}^{(2)}(-, -, -) = 1. \tag{B.36}$$

The three-body weight $\bar{v}^{(2)}$ is nonnegative, which allows the interpretation of the second moment as the partition function of classical Ising model on a triangular lattice. Monte Carlo simulation in Fig. 3.10 is based on the Ising spin model derived here. In this Ising spin model, we note that the spin variable with $\sigma = -1$ is preferred. More specifically, the average density of spins with $\sigma = -1$ is strictly increasing towards the bottom boundary (as t decreases). In the thermodynamic limit $T \to \infty$, the spin at the bottom layer will polarize to $\sigma = -1$, which implies $\langle m_1^- \rangle = 1$.

B.3 Implication of unitarity in classical spin models

The presence of weak measurements leads to a significant difference between weights from our mapping to spin models and those in Ref. [183]. In what follows, we show that, in the absence of measurements, the three-body weight satisfies a special property that $\bar{w}^{(n)}(\sigma, \sigma, \sigma') = \delta_{\sigma\sigma'}$ when $q^2 \geq n$. We note that this property is explicitly shown in Ref. [183] for a special case $n = 2$ without measurements. This property is a consequence of the unitarity of the RUC and generally not satisfied in the presence of measurements.

The three-body weight $\bar{w}^{(n)}(\sigma, \sigma, \sigma')$ for three spins living on the vertices of lower-facing triangle can be written as

$$\bar{w}^{(n)}(\sigma, \sigma, \sigma') = \sum_{\tau \in \mathcal{S}_n} w_d^{(n)}(\sigma, \tau; q)^2 w_g^{(n)}(\tau, \sigma'; q^2), \tag{B.37}$$

where we put the explicit q dependence in $w_d^{(n)}$ and $w_g^{(n)}$. In the case without measurements, $w_d^{(n)}(\sigma, \tau; q) = q^{\#\mathrm{cycle}(\sigma\tau^{-1})}$, the three-body weight reduces to

$$\bar{w}^{(n)}(\sigma, \sigma, \sigma') = \sum_{\tau \in \mathcal{S}_n} \left(q^2\right)^{\#\mathrm{cycle}(\sigma\tau^{-1})} w_g^{(n)}(\tau, \sigma'; q^2). \tag{B.38}$$

We notice that the Weingarten function $w_g^{(n)}(\sigma, \tau; d)$ can be interpreted as a matrix with two indices σ and τ running over $n!$ elements of $\mathcal{S}_n$ when $d \geq n$. A simple expression is written as [220]

$$w_g^{(n)}(\sigma, \tau; d) = \left(M^{-1}(d)\right)_{\sigma\tau}, \quad (d \geq n) \tag{B.39}$$

where the matrix $(M(d))_{\sigma\tau} \equiv d^{\#\mathrm{cycle}(\sigma\tau^{-1})}$. Hence, the unitarity leads to the property of $\bar{w}^{(n)}$:

$$\bar{w}^{(n)}(\sigma, \sigma, \sigma') = \sum_{\tau \in \mathcal{S}_n} \left(q^2\right)^{\#\mathrm{cycle}(\sigma\tau^{-1})} \left(M^{-1}(q^2)\right)_{\tau\sigma'},$$
$$= \delta_{\sigma\sigma'}. \tag{B.40}$$

In our model, weak measurements explicitly break the unitarity, and this property does not hold.

B.4 Duality in standard Potts models

The phase transition point of the 2D standard Potts model on square lattice given by Eq. (3.64) is known to be exactly solvable using the Kramers-Wannier duality [211, 142]. Here, we briefly review the duality and derive the phase transition point.

In the low-temperature limit, $J < 0$ and $|J| \gg 1$, we can perform the low temperature expansion of the partition function $\mathcal{Z} = \exp(-\beta H_{\mathrm{Potts}})$:

$$\mathcal{Z} = Q e^{-2N_{\mathrm{sq}}J}\big[1 + e^{4J}N_{\mathrm{sq}}(Q-1) + 2e^{6J}N_{\mathrm{sq}}(Q-1)$$
$$+ 2e^{7J}N_{\mathrm{sq}}(Q-1)(Q-2) + \mathrm{O}(e^{8J})\big], \tag{B.41}$$

where N_{sq} is the total number of sites on the square lattice, the Potts model contains $Q = n!$ local degrees of freedom.

In the high-temperature limit, $|J| \ll 1$, we can perform the high temperature expansion of the partition function:

$$\begin{aligned}
\mathcal{Z} &= \sum_{\{\sigma_i\}} \prod_{\langle i,j \rangle} \left(1 + \kappa \delta_{\sigma_i,\sigma_j}\right) = \sum_{\{\sigma_i\}} \prod_{\langle i,j \rangle} \left(\frac{1 + rQs(\sigma_i,\sigma_j)}{1 - r}\right) \\
&= \frac{Q^{N_{\text{sq}}}}{(1-r)^{2N_{\text{sq}}}} \Big[1 + r^4 N_{\text{sq}}(Q-1) + 2r^6 N_{\text{sq}}(Q-1) \\
&\quad + 2r^7 N_{\text{sq}}(Q-1)(Q-2) + \mathrm{O}(r^8) \Big],
\end{aligned} \tag{B.42}$$

where we recall that $\kappa = e^{-J} - 1$, the small parameter $r \equiv \kappa/(Q+\kappa)$ and $s(\sigma_i, \sigma_j) \equiv \delta_{\sigma_i \sigma_j} - 1/Q$.

A duality is observed in the low- and high-temperature expansion. This connects the partition function at high and low temperature through the relation $e^J = r$:

$$\frac{1}{\tilde{\kappa} + 1} = \frac{\kappa}{Q + \kappa}, \tag{B.43}$$

where κ and $\tilde{\kappa}$ parametrize the high- and low-temperature expansion. The phase transition point, where the free energy exhibits a singular behavior, satisfies the self-dual relation $\tilde{\kappa} = \kappa$. Hence, the transition point κ_c is given by

$$\kappa_c = \sqrt{Q}. \tag{B.44}$$

At $Q = 2$, the result reduces to the well-known Kramers-Wannier duality in 2D classical Ising model on a square lattice.

B.5   Monte-Carlo simulation of the transition in $\mathcal{F}^{(2)}$

We present the numeric simulation of the phase transition using the Monte Carlo algorithm. Here, we focus on the case of $n = 2$, where the second divergence and Fisher information have an Ising spin model description. In the spin model description, the second Fisher information $\mathcal{F}^{(2)}$ is given by the density of $\sigma = -1$ spins at the bottom through the relation $\mathcal{F}^{(2)} = 2\langle m_1^- \rangle$.

In Fig. B.2, we show $\langle m_1^- \rangle$ as a function of time for various measurement strengths α computed from Monte-Carlo simulations. $\langle m_1^- \rangle$ generally grows at early time, indicating that the measurement device gains more information about the initial state. As T is further increased, $\langle m_1^- \rangle$ eventually saturates to a value determined by α and q. When $\alpha > \alpha_c^{(2)}$, $\langle m_1^- \rangle$ saturates to $1/2$, which implies the equal numbers of $\sigma = \pm 1$ spins at the bottom, corresponding to the paramagnetic phase. In contrast, when $\alpha < \alpha_c^{(2)}$, the saturation value of $\langle m_1^- \rangle$ is less than $1/2$, implying long range correlations between spin variables at top and bottom boundaries. This phase corresponds to the ferromagnetic phase.
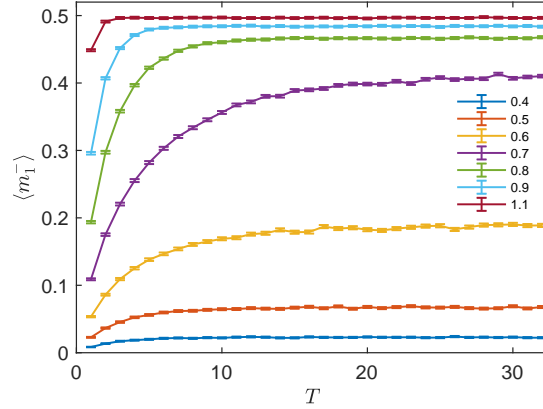
Figure B.2: Density of spins with $\sigma = -1$ in the bottom layer $\langle m_1^- \rangle$ as a function of time T. Different curves represent different measurement strength α given on the right. The Monte-Carlo simulation is done with $q = 2$, $N = 32$. The data are averaged over 72000 Monte Carlo samples.
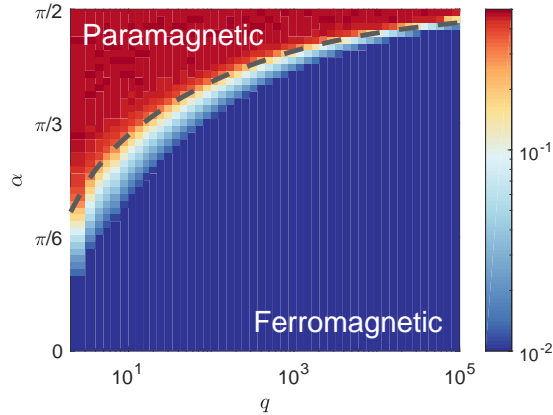
Figure B.3: Phase diagram of the transition in the second Fisher information $\mathcal{F}^{(2)}$, a proxy of the ability of the measurements to distinguish between two different initial states. Horizontal and vertical axes represent q and α, respectively. The gray line represents the exact solution of critical point in the classical Ising model in Eq. (3.61). The color-coded background displays the density of spins with $\sigma = -1$ in the bottom layer $\langle m_1^- \rangle$. The simulation is done in a system of $N = 20, T = 40$.

Figure B.3 shows the phase diagram of the transition in the second Fisher information $\mathcal{F}^{(2)}$ as a function of α and q. Two distinct phases are seen in the color-coded background representing $\langle m_1^- \rangle$. Large α and small q correspond to the high-temperature limit in the

classical Ising model and lead to the paramagnetic phase. On the contrary, small α and large q correspond to the low-temperature limit and lead to the ferromagnetic phase. We find that the phase boundary between two phases matches with the exact solution of critical point in classical Ising model in Eq. (3.61) as expected.

B.6 Exact Numeric simulation for the entanglement phase transition

Algorithm

Here, we provide the details of the numerical simulations presented in Sec. 3.5. In order to efficiently store exact many-body wave functions for as large as $N = 30$ qubits, we leverage the fact that a fraction of qudits are disentangled in every time step. More specifically, we define a single discrete time step at even (odd) time t as the applications of nearest neighboring two-qubit unitary gates at site i and $i + 1$ for every even (odd) i and the projective measurement of each qubit in the computational basis with probability p. The measurement outcomes are probabilistically determined according to the Born rules, and the wave function is normalized after each measurement. At any given time t, on average pN qubits are projected and remain disentangled from the rest of the system. In our numerical algorithm, we only store the wave function for the entangled spins and separately keep track of the configuration of the disentangled ones. In order to simulate the time evolution, we update the many-body wave function at every time step in the following way: (1) generate $N/2$ (or $N/2 - 1$) random two-qubit gates to apply and determine which qubits to measure projectively, and (2) sequentially update the wave function by applying a unitary gate at site i and $i + 1$ followed by the projection of the qubit(s) at i, $i + 1$, or both, if necessary. Crucially, our sequential update of the wave function and the sampling of the projective measurement outcomes are equilvalent to applying the entire unitary gates first and then performing projective measurements, since different unitary gates within a single time step have disjoint supports. The order of the sequential updates within a single time step can be further optimized in order to minimize the number of entangled spins during the time evolution. Our simulation involves only even N with open boundary conditions. Half chain entanglement entropies are computed after time step $t = 3N$ (or $t = 3N - 1$) when $N/2$ is even (odd), in order to minimize the even/odd effect associated with the layout of our unitary circuits.

Finite-size scaling

Here, we present the details of finite size scaling in Sec. 3.5. We use the scaling ansatz proposed in Ref. [239]:

$$S(p, L) - S(p_c, L) = g\left((p - p_c)N^{1/\nu}\right). \tag{B.45}$$

The critical measurement probability p_c and critical exponent ν are extracted by numerically optimizing the quality function of data collapse introduced in Refs. [137, 122]:

$$K(p_c, \nu) = \frac{1}{\mathcal{N}} \sum_{i,j} \frac{(y_{ij} - Y_{ij})^2}{dy_{ij}^2 + dY_{ij}^2}, \tag{B.46}$$

where i and j run over the set of measurement probabilities and system sizes in the simulation, respectively. y_{ij} and dy_{ij} are the data points $S(p_i, L_j) - S(p_c, L_j)$ and its error, Y_{ij} and dY_{ij} are the estimated value of the master curve and its corresponding error. The master curve is obtained by linear fit with weighted least squares using the data points nearby, and its error is obtained from the fit as described in Refs. [122, 243]. Specifically, the optimization is done in the following way: (1) choose a $p_c \in [0.2, 0.35]$ and compute $S(p_c, L)$ by polynomial fitting of $S(p, N)$ using the seventh-th order polynomials; (2) find ν that optimize to the quality function for the given p_c, which gives the corresponding minimum $K_{\min}(p_c)$; (3) find the global minimum of $K_{\min}(p_c)$ for $p_c \in [0.2, 0.35]$ in order to extract the optimal p_c and ν. The error bars of p_c and ν are estimated using the bootstrapping method. More specifically, out of 15 measurement probabilities for $p \in [0.2, 0.35]$ in our simulation, we randomly choose 10 data points and perform the aforementioned finite size scaling analysis to obtain p_c and ν. We repeat the analysis for 100 times with independently randomly chosen data points and use the standard deviation of p_c and ν as the estimated error bars.

B.7 The Fisher information for nonlocal measurements

Here, we review the connection between the KMB Fisher information and measurements in an optimal nonlocal basis. The most general form of projective measurement can be characterized by the positive-operator valued measure (POVM) Π [192], which consists of a complete set of observables $\{\Pi_i\}$ that need not be mutually orthogonal. For a given Π, the measurement outcome i is drawn from a probability distribution $p_i^\Pi \equiv \mathrm{tr}\{\rho\Pi_i\}$. Hence, analogous to local projective measurements, we can compute the KL divergence

$$D_\Pi(\theta) \equiv \sum_i p_{0,i}^\Pi \left(\log p_{0,i}^\Pi - \log p_{\theta,i}^\Pi \right), \tag{B.47}$$

where $p_{\theta,i}^\Pi = \mathrm{tr}[\rho_\theta \Pi_i]$ is the measurement probability distribution when the system is initialized in $|\Psi_\theta\rangle$. We note that our original simple local measurements in the main text correspond to a special choice of Π that consists of a set of $(q')^{NT}$ projectors in the computational basis of ancilla qudits. The amount of information carried in the measurement outcomes is quantified by the Fisher information

$$\mathcal{F}_\Pi = \partial_\theta^2 D_\Pi(\theta)\Big|_{\theta=0}. \tag{B.48}$$

Most importantly, the KMB Fisher information $\mathcal{F}_{\mathrm{KMB}}$ provides an attainable upper bound to $\mathcal{F}_{\Pi}$ [251, 116, 203, 113, 181]:

$$\mathcal{F}_{\mathrm{KMB}} = \max_{\Pi} \mathcal{F}_{\Pi}, \tag{B.49}$$

where Π is optimized over all possible POVM. In our work, we compute $\mathcal{F}_{\mathrm{KMB}}$ averaged over unitary gates $\mathcal{U}$, and the optimal Π for each $\mathcal{U}$ may not be the same.

Appendix C

Supplementary material for Chapter 4

C.1   Local symmetries

Qubit circuit

Here we show that, for the circuits considered in Section 4.2 and 4.3, the average hybrid dynamics in $\mathcal{H}^{(n)}$ exhibits local symmetries generated by $\mathcal{X}_j = \prod_{a=1}^{n}(X_a X_{\bar{a}})_j$, $\mathcal{Y}_j = \prod_{a=1}^{n}(Y_a Y_{\bar{a}})_j$, and $\mathcal{Z}_j = \prod_{a=1}^{n}(Z_a Z_{\bar{a}})_j$. Our proof relies on the facts: (i) unitary gates $U = e^{-i\theta O_P}$ are generated by Pauli string operators O_P, e.g. $O_P = \tau_i^\alpha \tau_j^\beta$; (ii) the random couplings θ are drawn from a symmetric distribution to zero; (iii) measurement operators are Pauli strings. We note that, as a special case discussed in Section 4.2, the average hybrid dynamics in $\mathcal{H}^{(2)}$ generated by uniformly random single-qubit phase rotations $e^{-i\theta_i Z_i}$ exhibits these local symmetries. In the following, we demonstrate the symmetries for the average dynamics in $\mathcal{H}^{(n)}$ generated by unitary gates and projective measurements separately.

Without lose of generality, we consider a unitary gate $U_i = e^{-i\theta_i^{\alpha\beta}\tau_i^\alpha\tau_{i+1}^\beta}$. U_i acts on $\mathcal{H}^{(n)}$ after averaging over the random coupling as

$$\mathcal{U}_i^{(n)} = \overline{e^{-i\theta_i^{\alpha\beta}H_i^{(n)}}} = \sum_{k=0}^{\infty}\frac{(-1)^k}{(2k)!}\overline{\left(\theta_i^{\alpha\beta}\right)^{2k}}\left(H_i^{(n)}\right)^{2k}, \tag{C.1}$$

where $H_i^{(n)} = \sum_{a=1}^{n}\tau_{i,a}^\alpha\tau_{i+1,a}^\beta - \tau_{i,\bar{a}}^\alpha\tau_{i+1,\bar{a}}^\beta$. Here, we use the fact that $\theta_i^{\alpha\beta}$ is drawn from a symmetric distribution to zero, and odd powers of $H_i^{(n)}$ in the expansion of $\mathcal{U}_i^{(n)}$ vanish. A special case of $\mathcal{U}_i^{(n)}$ with $n = 2$ and Gaussian random $\theta_i^{\alpha\beta}$ is given in Eq. (4.33). To demonstrate the local symmetries in the averaged dynamics $\mathcal{U}_i^{(n)}$, it suffices to show

$$\left[\left(H_i^{(n)}\right)^2, \mathcal{R}_j\right] = 0 \tag{C.2}$$

for any i, j and $\mathcal{R}_j \in \{\mathcal{X}_j, \mathcal{Y}_j, \mathcal{Z}_j\}$. Each nontrivial term in $(H_i^{(n)})^2$ contains a product of Pauli matrices $\tau_{i,a}^\alpha\tau_{i,a'}^\alpha$ on site i and $\tau_{i+1,a}^\beta\tau_{i+1,a'}^\beta$ on site $i+1$, which commutes with $\mathcal{R}_j$. Hence,

$(H_i^{(n)})^2$ commutes with $\mathcal{R}_j$, and $\mathcal{R}_j$ are local symmetries of $\mathcal{U}_i^{(n)}$. The generalization to other unitary gates generated by Pauli string operators is straightforward.

The probabilistic application of a projective measurement averaged over measurement results acts on $\mathcal{H}^{(n)}$ as

$$\mathcal{M}_\nu^{(n)} = (1 - \Gamma_\nu \delta t) \mathbb{1}^{\otimes 2n} + \Gamma_\nu \delta t \sum_{m_\nu = \pm} P_{m_\nu}^{\otimes 2n}. \tag{C.3}$$

A special case of $\mathcal{M}_\nu^{(2)}$ is given in Eq. (4.32). Here, $P_{m_\nu} = (1 \pm M_\nu)/2$ are the projection operators associated with the measurements on the Pauli string M_ν. We note that measurement results for any Pauli string can only be $m_\nu = \pm 1$. To demonstrate the local symmetries of $\mathcal{M}_\nu^{(n)}$, it suffices to show

$$[P_+^{\otimes 2n} + P_-^{\otimes 2n}, \mathcal{R}_j] = 0 \tag{C.4}$$

for any j and $\mathcal{R}_j \in \{\mathcal{X}_j, \mathcal{Y}_j, \mathcal{Z}_j\}$. To verify that Eq. (C.4) is satisfied, we expand $P_+^{\otimes 2n} + P_-^{\otimes 2n}$ according to the power of operator M_ν. Each nonvanishing term contains a product of even number of operator M_ν (acting on different branches) and therefore commute with $\mathcal{X}_j, \mathcal{Y}_j$, and $\mathcal{Z}_j$.

Fermionic circuit

For the Gaussian fermionic circuits considered in Section 4.4, the averaged dynamics preserves local symmetries generated by $\mathcal{R}_\ell = \prod_{\alpha=1}^n i\gamma_{\ell,\alpha\uparrow}\gamma_{\ell,\alpha\downarrow}$ at every Majorana site ℓ. The local symmetry $\mathcal{R}_\ell$ commutes with any Majorana bilinear defined on the same site, i.e. $[\mathcal{R}_\ell, \gamma_{\ell',\alpha\sigma}\gamma_{\ell',\beta\sigma'}] = 0$. Using this property, we can verify, for any replica index n, both the averaged unitary gates $\mathcal{U}_{s/b,j}^{(n)}$ and the averaged measurements $\mathcal{M}_{s/b,j}^{(n)}$ commute with $\mathcal{R}_\ell$.

C.2 Effective quantum Hamiltonian for $\mathbb{Z}_2$ symmetric quantum circuits

To demonstrate our method, we present an explicit formula of H_{eff} for a simple paradigmatic 1D circuit model with $\mathbb{Z}_2$ symmetry that conserves the total parity of Pauli-Z operator. Our model follows the structure depicted in Fig. 4.1. The inter-layer hybrid dynamics involves the following unitary gate and measurements: (i) random $\theta_{ij}^{xx} X_i X_j$ interactions with Gaussian random θ_{ij}^{xx} of zero mean, (ii) random $\theta_{ij}^{zz} Z_i Z_j$ interactions with Gaussian random θ_{ij}^{xx} of zero mean, (iii) measurements of Z_j with probability $\Gamma_j^z \delta t$, and (iv) measurements of $X_i X_j$ with probability $\Gamma_{ij}^{xx} \delta t$. All unitary couplings and measurement projections in this model respect the $\mathbb{Z}_2$-parity symmetry generated by $\hat{\pi} = \prod_j Z_j$. As explained in Appendix C.1, $\mathcal{X}_j$ are local conserved quantities, and s_j variables denote local integrals of motion.

Using the framework developed in Section 4.2, we can show the effective Hamiltonian $H_{\text{eff},+}$ for the dynamics of two copies of density matrices in the even sector of local parities is of the form

$$H_{\text{eff},+} = H_{JXX} + H_{JZZ} + H_{PZ} + H_{PXX}, \tag{C.5}$$

where H_{JXX} and H_{JZZ} arise from unitary gates with random couplings θ_{ij}^{xx} and θ_{ij}^{zz}, and H_{PZ} and H_{PXX} arise from Z_j and $X_i X_j$ measurements. The Hamiltonian terms can be written in terms of spin-1 operators

$$H_{JZZ} = \sum_{i<j} J_{ij}^{zz} \left(M_{i,+} M_{j,-} + M_{i,-} M_{j,+} \right), \tag{C.6}$$

$$H_{JXX} = \sum_{i<j} - J_{ij}^{xx} \left(S_i^x S_j^x + S_i^y e^{\mathrm{i}\pi S_i^x} e^{\mathrm{i}\pi S_j^x} S_j^y - L_i L_j \right), \tag{C.7}$$

$$H_{PXX} = \sum_{i<j} - \frac{\Gamma_{ij}^{xx}}{4} \left(S_i^x S_j^x + S_i^y e^{\mathrm{i}\pi S_i^x} e^{\mathrm{i}\pi S_j^x} S_j^y + L_i L_j \right), \tag{C.8}$$

$$H_{PZ} = \sum_{j} \Gamma_j^z \left(S_j^z \right)^2, \tag{C.9}$$

where the coupling $J_{ij}^{zz} \delta t = 8 \overline{(\theta_{ij}^{zz})^2}$, $J_{ij}^{xx} \delta t = 2 \overline{(\theta_{ij}^{xx})^2}$, the operator $L_i = [(S_i^+)^2 + (S_i^-)^2]/2$ with $S_i^\pm$ being the spin ladder operators, and $M_{j,\pm} = |m = \pm 1\rangle\!\rangle \langle\!\langle m = \pm 1|_j$ are projectors to the state $|m = \pm 1\rangle\!\rangle$ at site j.

The effective Hamiltonian exhibits a $D_4 \times \mathbb{Z}_2^{\mathbb{H}}$ symmetry, where $D_4 = (\mathbb{Z}_2^{\Pi_L} \times \mathbb{Z}_2^{\Pi_1}) \rtimes \mathcal{S}_2$. In the spin-1 Hilbert space, the symmetry generators are given by $\hat{\Pi}_L = \prod_j \mathrm{diag}(-1, 1, -1)_j$, $\hat{\Pi}_1 = \prod_j \mathrm{diag}(1, 1, -1)_j$, and $\mathcal{C}_\ell = \prod_j - \exp\left(\mathrm{i}\pi \sum_j S_j^x\right)$. The Hermitian conjugate $\mathbb{H}$ manifests as the complex conjugation $\mathcal{K}$. This $D_4 \times \mathbb{Z}_2^{\mathbb{H}}$ symmetry agrees with the analysis in Section 4.3.

C.3 Exchange symmetry and hermiticity symmetry in the $n = 2$ qubit model

In this section, we derive the exchange operation $\mathcal{C}_\ell \mathcal{C}_r$ and Hermitian conjugation $\mathbb{H}$ in the representation of $\mathcal{G}_{\text{eff}}^{(2)}$ on the even parity sector of the $n = 2$ qubit model. In particular, we show the exchange operation acts trivially as an identity matrix in the even parity sector and therefore cannot be broken. This proof only relies on the presence of local conserved quantities $\mathcal{X}_j$, $\mathcal{Y}_j$, and $\mathcal{Z}_j = 1$ in the qubit model and does not require the physical circuit symmetry.

To start with, the exchange operation $\mathcal{C}_\ell \mathcal{C}_r$ is given by a product of single-site exchange operations $\mathcal{C}_{\ell,i} \mathcal{C}_{r,i}$. The single-site left and right permutation can be written in terms of Pauli

operators as

$$\mathcal{C}_{\ell,i} = (IIII + XIXI + YIYI + ZIZI)_i/2, \tag{C.10}$$

$$\mathcal{C}_{r,i} = (IIII + IXIX + IYIY + IZIZ)_i/2. \tag{C.11}$$

In the even parity sector, one can show the product $\mathcal{C}_{\ell,i}\mathcal{C}_{r,i}$ acts as an identity matrix regardless of the physical symmetry, and so is $\mathcal{C}_{\ell}\mathcal{C}_r$. Hence, $\mathcal{S}_2^X$ is in the kernel of the representation and cannot be broken.

The hermiticity symmetry can be written as a combination of transpose $\mathcal{T}$ and complex conjugation $\mathcal{K}$. The transpose operation $\mathcal{T} = \mathcal{T}_1\mathcal{T}_2$ is a product of transpose for the first and second copy. $\mathcal{T}_1$ and $\mathcal{T}_2$ can be further written respectively as a product of single-site transpose operations $\mathcal{T}_{1,i}$ and $\mathcal{T}_{2,i}$ which take the form

$$\mathcal{T}_{1,i} = (IIII + XXII + YYII + ZZII)_i/2, \tag{C.12}$$

$$\mathcal{T}_{2,i} = (IIII + IIXX + IIYY + IIZZ)_i/2. \tag{C.13}$$

We can verify the product $\mathcal{T}_{1,i}\mathcal{T}_{2,i}$ is identity in the even parity sector, and so is $\mathcal{T} = \prod_i \mathcal{T}_{1,i}\mathcal{T}_{2,i}$. Hence, the Hermitian conjugate $\mathbb{H} = \mathcal{K}$ in the even parity sector.

C.4 Higher replicas ($n \geq 3$)

Having shown the existence of a broad array of symmetry enriched phases in the case of two replica copies $n = 2$, we here discuss the correspondence of each phase in the higher replica models ($n \geq 3$). We verify that two area-law and three volume-law phases found in the two-chain model in Section 4.3 have natural generalizations in the higher replica models with identical physical signatures. This provides evidence that these phases can be extrapolated to the replica limit $n \to 1$, predicting distinct phases of quantum circuits.

Among the rest five (two area-law and three volume-law) phases which haven't been realized in a concrete model, we show that only the composite volume-law phase has a higher replica generalization. The coexistence of EA order and parity variance is generically not allowed in the higher replica models; four coexistence phases (two area-law and two volume-law phases) do not have natural higher replica generalizations. However, we note this does not exclude the possibility of the realizing these phases in the replica limit. Whether there is fundamental physical obstruction to realizing these phases in a concrete quantum circuit remains an open question.

According to the analysis in Section 4.2, the dynamics of n replicas exhibits an enlarged symmetry $\mathcal{G}^{(n)} = (B_n \times B_n) \rtimes \mathbb{Z}_2^{\mathbb{H}}$, where the hyperoctahedral group $B_n = \mathbb{Z}_2 \wr \mathcal{S}_n = \mathbb{Z}_2^{\otimes n} \rtimes \mathcal{S}_n$ is the symmetry group of an n-dimensional hypercube. The dynamics also conserves local parities $\mathcal{X}_j$, $\mathcal{Y}_j$, and $\mathcal{Z}_j$ (see Appendix C.1).

Similar to the case of two replicas $n = 2$, the effective symmetry that determines the ground state phases is reduced due to the conservation of local parities. We are interested in the ground state in the same sector of local parities as the reference state, i.e. $\mathcal{X}_j = \mathcal{Z}_j = +1$ and

$\mathcal{Y}_j = (-1)^n$. In this sector, the nonvanishing expectation values of local parities necessitate the breaking of single-branch symmetries. Hence, we are left with an effective global symmetry $\mathcal{G}_{\text{eff}}^{(n)}$ generated by the elements of the left and right permutation in $\mathcal{S}_n$, $\mathbb{H}$ together with $\hat{\Pi}_1 \equiv \prod_j (Z_1 Z_{\bar{1}})_j$ and $\hat{\Pi}_{12} \equiv \prod_j (Z_1 Z_2)_j$. Distinct phases of quantum circuits are characterized by the residual symmetry which is a subgroup of $\mathcal{G}_{\text{eff}}^{(n)}$.

We note that, in contrast to the case of two replicas ($n = 2$), the generators of the $\mathcal{S}_n^X$ exchange symmetry, i.e. $\mathcal{C}_{\ell,\xi} \mathcal{C}_{r,\xi}$ for $\xi \in \mathcal{S}_n$, act nontrivially in the even parity sector; $\mathcal{S}_n^X$ can in principle be broken for $n \geq 3$.

Area-law phases.— The area-law phase is again characterized by the unbroken $\mathcal{S}_n$ symmetry or the composite symmetry of the cyclic permutation $\mathcal{C}_\ell$ and $g_{\mathcal{I}}$ present in the reference state $|\mathcal{I}\rangle\rangle$. The presence of the hermiticity symmetry necessitates the dynamical symmetry $(\mathcal{S}_n \times \mathcal{S}_n) \rtimes \mathbb{Z}_2^{\mathbb{H}}$.

Starting from the fully symmetric area-law phase with residual symmetry $\mathcal{G}_{\text{eff}}^{(n)}$, we can condense the charge $\mathcal{Q}_1 \equiv X_1 X_{\bar{1}}$ together with all operators related to it by the $(\mathcal{S}_n \times \mathcal{S}_n) \rtimes \mathbb{Z}_2^{\mathbb{H}}$ symmetry. This leads to a broken symmetry area-law phase with the residual symmetry $(\mathcal{S}_n \times \mathcal{S}_n) \rtimes \mathbb{Z}_2^{\mathbb{H}}$. It is easily verified that both the symmetric and the broken symmetry state have exactly the same physical signatures as their corresponding state in the $n = 2$ model.

The coexistence of EA order and parity variance is generically not allowed in the model of higher replicas. To obtain a nonvanishing EA order, one needs to condense $\mathcal{Q}_{ab} \equiv X_a X_b$ for $a, b = 1, 2, \cdots, n$. Such a condensate breaks not only $\hat{\Pi}_a \equiv \prod_j (Z_a Z_{\bar{a}})_j$ but also $\hat{\Pi}_{ab} \equiv \prod_j (Z_a Z_b)_j$, indicating an exponentially decaying parity variance. One can also verify that condensing $X_a Z_b Y_c$ and its related charges by $(\mathcal{S}_n \times \mathcal{S}_n) \rtimes \mathbb{Z}_2^{\mathbb{H}}$ in the composite area-law phase breaks both $\hat{\Pi}_a$ and $\hat{\Pi}_{ab}$, giving a vanishing parity variance. Hence, two area-law phases with coexisting orders do not have a higher replica generlation.

The symmetric SPT phase, generalized to $n \geq 3$, is found starting from the broken symmetry area-law phase. We can restore the full symmetry by condensing domain walls of $\hat{\Pi}_{12}$ and $\hat{\Pi}_1$ as well as all domain walls related to them by the symmetry $(\mathcal{S}_n \times \mathcal{S}_n) \rtimes \mathbb{Z}_2^{\mathbb{H}}$. The symmetric SPT phase is obtained by condensing $\hat{\Pi}_{ab}$ and $\hat{\Pi}_a$ domain walls bound to charges of the $\mathcal{S}_n$ symmetries. The dual picture of the same phase is a condensate of the $\mathcal{S}_n$ domain walls bound to the charge $\mathcal{Q}_1$ and symmetry related operators.

Volume-law phases.— We now turn to the volume-law regime. One correspondence of the symmetric volume-law phase in the higher replicas is the phase with fully broken left and right $\mathcal{S}_n$, while retaining the symmetry $\hat{\Pi}_a \equiv \prod_j (Z_a Z_{\bar{a}})_j$, $\hat{\Pi}_{ab} \equiv \prod_j (Z_a Z_b)_j$, and $\mathbb{Z}_2^{\mathbb{H}}$.[1] One can check that the physical quantities in this phase behave the same as in its $n = 2$ correspondence.

Starting from the symmetric volume-law phase, we can condense $\mathcal{Q}_a = X_a X_{\bar{a}}$, leading to a featureless phase preserving symmetry $\hat{\Pi}_a$, while breaking $\hat{\Pi}_{ab} = Z_a Z_b$. We can further condense $\mathcal{Q}_{ab}$ in the featureless phase to break the symmetry $\hat{\Pi}_a$, leading the broken

---

[1]We note that the volume-law phase in the replica limit is believed to be a condensate of elementary domain walls [130], which breaks the full $\mathcal{S}_n$ symmetry. Hence, in higher replica models, we only consider the volume-law phase with fully broken $\mathcal{S}_n$.

symmetry volume-law phase with $\mathbb{Z}_2^{\mathbb{H}}$ symmetry. Two coexistence volume-law phases do not have natural generalizations in the higher replicas as condensing either $\mathcal{Q}_{ab}$ or $\mathcal{Q}_{a\bar{b}} \equiv X_a X_{\bar{b}}$ for all $a, b = 1, 2, \dots, n$ breaks $\hat{\Pi}_{a'b'}$ leading to vanishing parity variance.

A correspondence of the composite volume-law phase can be shown to exist in the model of even number of replicas (n being even). This phase features a residual symmetry group $(\mathbb{Z}_n \times \mathbb{Z}_n) \rtimes \mathbb{Z}_2^{\mathbb{H}}$. Two $\mathbb{Z}_n$ subgroups are generated respectively by the composite symmetry $\mathcal{C}_\ell \hat{\Pi}_L$ and $\mathcal{C}_\ell \mathcal{C}_r$, where $\hat{\Pi}_L \equiv \prod_j (\prod_{a=1}^n Z_a)_j$. Starting from the symmetric area-law phase, we can obtain this phase by condensing $(X_1 Y_{\bar{1}} Z_2)_j$ symmetrized under the residual symmetry. We note that the symmetrized operator is nonvanishing for the even replicas.

C.5 Fermionic states and operators in the duplicated Hilbert space

Here we detail the correspondence between second quantized fermionic operators f_j, acting in the Hilbert space of a single copy of quantum circuit, and the $f_{j,\alpha,\sigma}$ acting in the duplicated Hilbert space of the effective Hamiltonian.

We start from the Fock states $|\vec{n}\rangle = \prod_j (f_j^\dagger)^{n_j} |0\rangle$ in the Hilbert space of quantum circuit. The space of double density matrices is accordingly spanned by the states: $|\vec{n}_1\rangle \langle \vec{m}_1| \otimes |\vec{n}_2\rangle \langle \vec{m}_2|$. To define a proper fermionic Fock space for the duplicated system, we make the correspondence:

$$|\vec{n}_1\rangle \langle \vec{m}_1| \otimes |\vec{n}_2\rangle \langle \vec{m}_2| \leftrightarrow \tag{C.14}$$

$$\prod_i (f_{i,1,\uparrow}^\dagger)^{n_{1i}} \prod_j (f_{j,1,\downarrow}^\dagger)^{m_{1j}} \prod_k (f_{k,2,\uparrow}^\dagger)^{n_{2k}} \prod_l (f_{l,2,\downarrow}^\dagger)^{m_{2l}} |\mathrm{vac}\rangle\!\rangle_f$$

$$\equiv |\vec{n}_1, \vec{m}_1, \vec{n}_2, \vec{m}_2\rangle\!\rangle.$$

Here, the second quantized operators $f_{i,\alpha,\sigma}^\dagger$ create a fermion in the σ branch (ket or bra) of copy α.

The above correspondence between states gives a simple representation of the boundary state $\langle\!\langle \mathcal{I}|$, which implements the doubled trace operation:

$$\langle\!\langle \mathcal{I}| = \sum_{\vec{n}_1, \vec{n}_2} \langle\!\langle \vec{n}_1, \vec{n}_1, \vec{n}_2, \vec{n}_2|. \tag{C.15}$$

Indeed we can check that $\langle\!\langle \mathcal{I}|\rho^{(2)}\rangle\!\rangle = \mathrm{tr}\, \rho^{(2)}$.

The above correspondence between states implies a correspondence between operators

$$f_j^\dagger \otimes \mathbb{1} \otimes \mathbb{1} \otimes \mathbb{1} \leftrightarrow f_{j,1,\uparrow}^\dagger, \tag{C.16a}$$

$$\mathbb{1} \otimes f_j \otimes \mathbb{1} \otimes \mathbb{1} \leftrightarrow f_{j,1,\downarrow}^\dagger (-1)^{N_{1\uparrow}}, \tag{C.16b}$$

$$\mathbb{1} \otimes \mathbb{1} \otimes f_j^\dagger \otimes \mathbb{1} \leftrightarrow f_{j,2,\uparrow}^\dagger (-1)^{N_{1\uparrow} + N_{1\downarrow}}, \tag{C.16c}$$

$$\mathbb{1} \otimes \mathbb{1} \otimes \mathbb{1} \otimes f_j \leftrightarrow f_{j,2,\downarrow}^\dagger (-1)^{N_{1\uparrow} + N_{1\downarrow} + N_{2\uparrow}}. \tag{C.16d}$$

The sign factors on the right are needed to ensure that operators on the two sides of the correspondence have identical action on the respective states. $N_{\alpha\sigma}$ denote the total number in copy α and "branch" σ (ket $\uparrow$ or bra $\downarrow$). We make the following remarks. First, with this correspondence, all the fermion parity conserving local operators, acting on a single circuit state (in any copy or branch) remain local and the sign factors cancel out of them. The extension to any number of copies is obvious. Second, due to the additional sign factors, the hermiticity symmetry transformation appears to be nonlocal in the duplicated Hilbert space, namely $\mathbb{H} f_{j,\alpha,\uparrow}^{\dagger} \mathbb{H}^{-1} = (-1)^{N_{\alpha,\uparrow}} f_{j,\alpha,\downarrow}^{\dagger}$. However, $\mathbb{H}$ is local for any bosonic operator made of fermionic bilinears and therefore becomes a local symmetry in the effective Hilbert space.

Having defined the operators in the duplicated Hilbert space $\mathcal{H}^{(2)}$, we can write the effective Hamiltonian in a Fock basis using any ordering convention of the fermions. In particular, the form of the effective spin-1 Hamiltonian in Section 4.4 implicitly assumes that it operates between Fock states with a site-local ordering convention:

$$\bigotimes_{j} |n_{j,1,\uparrow}, n_{j,1,\downarrow}, n_{j,2,\uparrow}, n_{j,2,\downarrow}\rangle\!\rangle \equiv \tag{C.17}$$

$$\prod_{j} \left[(f_{j,1,\uparrow}^{\dagger})^{n_{j,1,\uparrow}} (f_{j,1,\downarrow}^{\dagger})^{n_{j,1,\downarrow}} (f_{j,2,\uparrow}^{\dagger})^{n_{j,2,\uparrow}} (f_{j,2,\downarrow}^{\dagger})^{n_{j,2,\downarrow}} \right] |\text{vac}\rangle\!\rangle_{f}.$$

The same Hamiltonian will take a different form if written in terms of Fock states with copy-local ordering $|\vec{n}_{1\uparrow}, \vec{n}_{1\downarrow}, \vec{n}_{2\uparrow}, \vec{n}_{2\downarrow}\rangle\!\rangle$. In particular, the $U(1)$ symmetries will become nonlocal and not be explicitly apparent because they are generated by conservation of the $c_{\ell,\sigma}^{\dagger}$, which are not local to one copy.

The price we pay for working with the site-local Fock states $|\mathbf{n}\rangle\!\rangle$ in which the effective spin Hamiltonian is simple and the $U(1)$ symmetry apparent is that we also need to rewrite the boundary state $\langle\!\langle \mathcal{I} |$ with the same Fock states. This in order to compute its overlap with the state generated by the effective imaginary time evolution (together with any boundary operators we want to measure). We have seen that $\langle\!\langle \mathcal{I} |$ has a simple representation in terms of the copy-local Fock states in Eq. (C.15). The Fock states in the two ordering conventions are related to each other by a sign factor which is a function of the occupation numbers in the state. These factors take a simple form for the basis states included in the boundary state, giving:

$$\langle\!\langle \mathcal{I} | = \sum_{\vec{n}_1, \vec{n}_2} g(N_1, N_2) \bigotimes_{j} \langle\!\langle n_{j,1}, n_{j,1}, n_{j,2}, n_{j,2} |, \tag{C.18}$$

where the factor $g(N_1, N_2) = (-1)^{\frac{1}{2} N_1 (N_1 - 1) + \frac{1}{2} N_2 (N_2 - 1)}$.

C.6 $U(1)$ symmetry breaking in $|\mathcal{I}\rangle\!\rangle$

In this section, we show the boundary state $|\mathcal{I}\rangle\!\rangle$ breaks both $U(1)$ symmetries corresponding to the conservation of Σ^z and η^z. We demonstrate the long-range order in $|\mathcal{I}\rangle\!\rangle$ manifested by

nondecaying correlation functions of order parameters $\langle\!\langle \mathcal{I}|\eta_i^y\eta_j^y|\mathcal{I}\rangle\!\rangle/4^L = \langle\!\langle \mathcal{I}|\Sigma_i^y\Sigma_j^y|\mathcal{I}\rangle\!\rangle/4^L = 1/2$.

To evaluate the correlation of order parameters in $|\mathcal{I}\rangle\!\rangle$, we write the boundary state $|\mathcal{I}\rangle\!\rangle$ [Eq. (C.15)] in terms of second quantized fermionic operators $f_{j,\alpha,\sigma}$ acting on the Hilbert space of branch σ of copy α

$$|\mathcal{I}\rangle\!\rangle = \prod_{i=1}^{N}\left[1 + f_{i,1,\uparrow}^{\dagger}f_{i,1,\downarrow}^{\dagger}e^{\mathrm{i}\pi\sum_{i'=i+1}^{N}n_{1i'}}\right]$$
$$\left[1 + f_{i,2,\uparrow}^{\dagger}f_{i,2,\downarrow}^{\dagger}e^{\mathrm{i}\pi\sum_{i'=i+1}^{N}n_{2i'}}\right]|\text{vac}\rangle\!\rangle_f. \tag{C.19}$$

Here, the state $|\mathcal{I}\rangle\!\rangle$ has a definite f-fermion parity on every site in the Hilbert space of forward and backward branch of each copy, i.e. $\langle\!\langle \mathcal{I}|\hat{\Pi}_{j,\alpha,\uparrow}\hat{\Pi}_{j,\alpha,\downarrow}|\mathcal{I}\rangle\!\rangle = 1$, where $\hat{\Pi}_{j,\alpha,\sigma} = 1 - 2f_{j,\alpha,\sigma}^{\dagger}f_{j,\alpha,\sigma}$ is the f-fermion parity.

In terms of f-fermion operators, the order parameters $\Sigma_j^{\pm}$ and $\eta_j^{\pm}$ take the form

$$\Sigma_j^{+} = -\mathrm{i}\mathcal{O}_{j,1\uparrow,1\downarrow} - \mathcal{O}_{j,1\uparrow,2\downarrow} - \mathcal{O}_{j,2\uparrow,1\downarrow} + \mathrm{i}\mathcal{O}_{j,2\uparrow,2\downarrow}, \tag{C.20}$$
$$\Sigma_j^{-} = \mathrm{i}\mathcal{O}_{j,1\uparrow,1\downarrow} - \mathcal{O}_{j,1\uparrow,2\downarrow} - \mathcal{O}_{j,2\uparrow,1\downarrow} - \mathrm{i}\mathcal{O}_{j,2\uparrow,2\downarrow}, \tag{C.21}$$
$$\eta_j^{+} = \mathrm{i}\mathcal{O}_{j,1\uparrow,1\downarrow} - \mathcal{O}_{j,1\uparrow,2\downarrow} + \mathcal{O}_{j,2\uparrow,1\downarrow} + \mathrm{i}\mathcal{O}_{j,2\uparrow,2\downarrow}, \tag{C.22}$$
$$\eta_j^{-} = -\mathrm{i}\mathcal{O}_{j,1\uparrow,1\downarrow} - \mathcal{O}_{j,1\uparrow,2\downarrow} + \mathcal{O}_{j,2\uparrow,1\downarrow} - \mathrm{i}\mathcal{O}_{j,2\uparrow,2\downarrow}, \tag{C.23}$$

where $\mathcal{O}_{j,\alpha\sigma,\beta\sigma'}$ is the fermion bilinear defined as

$$\mathcal{O}_{j,\alpha\sigma,\beta\sigma'} = \frac{\mathrm{i}}{2}\left(f_{j,\alpha,\sigma}^{\dagger}f_{j,\beta,\sigma'}^{\dagger} - f_{j,\beta,\sigma'}f_{j,\alpha,\sigma}\right). \tag{C.24}$$

Operator $\mathcal{O}_{j,\alpha\sigma,\beta\sigma'}$ flips the local f-fermion parity in Hilbert space of copy α and β on site j. Therefore, the correlation function of $\mathcal{O}_{j,\alpha\sigma,\beta\sigma'}$ in the boundary state $|\mathcal{I}\rangle\!\rangle$ is non-vanishing only when $\alpha = \beta$. We can further show the only nonvanishing two-point correlations are given by

$$\frac{1}{4^L}\langle\!\langle \mathcal{I}|\mathcal{O}_{i,\alpha\uparrow,\alpha\downarrow}\mathcal{O}_{j,\alpha\uparrow,\alpha\downarrow}|\mathcal{I}\rangle\!\rangle = \frac{1}{4}, \tag{C.25}$$

where $1/4^L$ is the normalization of $|\mathcal{I}\rangle\!\rangle$, i.e. $\langle\!\langle \mathcal{I}|\mathcal{I}\rangle\!\rangle = 4^L$. Using Eq. (C.25), we can show the order parameter correlation functions in the boundary state $|\mathcal{I}\rangle\!\rangle$ is nondecaying

$$\frac{1}{4^L}\langle\!\langle \mathcal{I}|\Sigma_i^y\Sigma_j^y|\mathcal{I}\rangle\!\rangle = \frac{1}{4^L}\langle\!\langle \mathcal{I}|\eta_i^y\eta_j^y|\mathcal{I}\rangle\!\rangle = \frac{1}{2}. \tag{C.26}$$

Hence, the boundary state exhibits long-range orders and breaks both the $U(1)$ symmetries generated by η^z and Σ^z. Furthermore, we note that the expectation value of order parameters in $|\mathcal{I}\rangle\!\rangle$ is vanishing, i.e. $\langle\!\langle \mathcal{I}|\Sigma_j^{\pm}|\mathcal{I}\rangle\!\rangle = \langle\!\langle \mathcal{I}|\eta_j^{\pm}|\mathcal{I}\rangle\!\rangle = 0$. For this reason, the boundary state $|\mathcal{I}\rangle\!\rangle$ can be understood as a superposition of $U(1)$ symmetry breaking states with the ordering of $U(1)$ phase in different directions.

C.7 Swap operator in fermionic duplicated Hilbert space

The swap operator $\mathcal{C}_{\ell,A}$ is in general nonlocal in the fermionic duplicated Hilbert space $\mathcal{H}^{(2)}$. In this section, we show that $\mathcal{C}_{\ell,A}$ bears a simple local description when acting on the boundary state $|\mathcal{I}\rangle\!\rangle$. This allows a long wavelength description for the swap boundary state $|\mathcal{C}_{\ell,A}\rangle\!\rangle \equiv \mathcal{C}_{\ell,A}|\mathcal{I}\rangle\!\rangle$ in Section 4.4.

To start with, we consider the swap operator in the Hilbert space of two copies of quantum circuits

$$\mathcal{C}_A = \sum_{\vec{n}_1,\vec{n}_2} |\vec{n}_{2A}\vec{n}_{1B}\rangle \langle\vec{n}_{1A}\vec{n}_{1B}| \otimes |\vec{n}_{1A}\vec{n}_{2B}\rangle \langle\vec{n}_{2A}\vec{n}_{2B}|, \tag{C.27}$$

where $\vec{n}_\alpha = (\vec{n}_{\alpha,A}, \vec{n}_{\alpha,B})$ is the occupation of fermionic modes in the subsystem A and its complement B. The purity of subsystem can be obtained by applying the permutation operator to the double density matrix either from left and then taking the trace, i.e. $\operatorname{tr}\rho_A^2 = \operatorname{tr}(\mathcal{C}_A\,\rho\otimes\rho)$.

Using the correspondence established in Appendix C.5, we can formulate the purity as an overlap between the swap boundary state $\langle\!\langle\mathcal{C}_{\ell,A}|$ and $|\rho\rangle\!\rangle$, where $|\mathcal{C}_{\ell,A}\rangle\!\rangle$ takes the form

$$|\mathcal{C}_{\ell,A}\rangle\!\rangle = \sum_{\vec{n}_1,\vec{n}_2} |\vec{n}_{2A}\vec{n}_{1B}, \vec{n}_{1A}\vec{n}_{1B}, \vec{n}_{1A}\vec{n}_{2B}, \vec{n}_{2A}\vec{n}_{2B}\rangle\!\rangle. \tag{C.28}$$

Alternatively, we can write $|\mathcal{C}_{\ell,A}\rangle\!\rangle$ in the site-local ordering convention as

$$|\mathcal{C}_{\ell,A}\rangle\!\rangle = \sum_{\vec{n}_1,\vec{n}_2} g(N_1, N_2) \tag{C.29}$$

$$\bigotimes_{j\in A} |n_{j,2}, n_{j,1}, n_{j,1}, n_{j,2}\rangle\!\rangle \bigotimes_{j\in B} |n_{j,1}, n_{j,1}, n_{j,2}, n_{j,2}\rangle\!\rangle.$$

We note that the boundary state $|\mathcal{C}_{\ell,A}\rangle\!\rangle$ [Eq. (C.29)] and $|\mathcal{I}\rangle\!\rangle$ [Eq. (C.18)] in the site-local convention only differ by a local exchange of the occupation in the forward branches of copy 1 and 2 in subsystem A. This allows one to define an effective swap operator $\widetilde{\mathcal{C}}_{\ell,A} = \prod_{j\in A}\widetilde{\mathcal{C}}_{\ell,j}$ such that $\widetilde{\mathcal{C}}_{\ell,A}|\mathcal{I}\rangle\!\rangle = |\mathcal{C}_{\ell,A}\rangle\!\rangle$, where $\widetilde{\mathcal{C}}_{\ell,j}$ is the single-site swap operator satisfying

$$\widetilde{\mathcal{C}}_{\ell,j}|n_{j,1}, n_{j,1}, n_{j,2}, n_{j,2}\rangle\!\rangle = |n_{j,2}, n_{j,1}, n_{j,1}, n_{j,2}\rangle\!\rangle. \tag{C.30}$$

The single-site swap operator $\widetilde{\mathcal{C}}_{\ell,j}$ can be written in terms of f-fermionic operators and further in terms of $U(1)$ symmetry generators

$$\begin{aligned}\widetilde{\mathcal{C}}_{\ell,j} &= f_{j,1,\uparrow}^\dagger f_{j,2,\uparrow} + f_{j,1,\uparrow}f_{j,2,\uparrow}^\dagger + \frac{1}{2}\left(1 + \hat{\Pi}_{j,1,\uparrow}\hat{\Pi}_{j,2,\uparrow}\right) \\ &= e^{-\mathrm{i}\frac{\pi}{2}\left(\Sigma_j^z + \eta_j^z\right)}, \end{aligned} \tag{C.31}$$
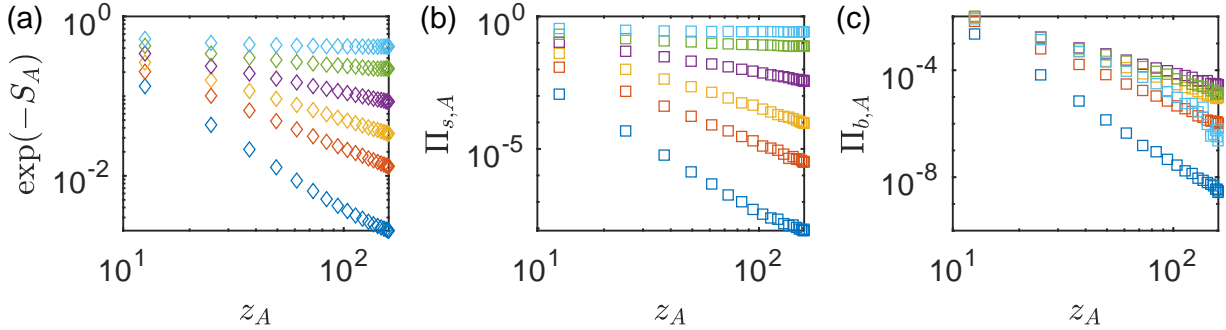
Figure C.1: Phase transition in Gaussian fermionic circuits along Cut 1 in Fig. 4.6. Entanglement entropy $\exp(-S_A)$ [panel (a)], parity variances $\Pi_{s,A}$ [panel (b)] and $\Pi_{b,A}$ [panel (c)] as function of the conformal coordinate z_A for various measurement probabilities p_s. Data points for the same p_s are marked in the same color in different panels. p_s ranges from 0.02 to 0.25 and increases from the bottom to the top in panel (a). The numerical results are obtained with system size $L = 160$, averaged over 400 realizations, and plotted in a log-log scale.

where $\hat{\Pi}_{j,\alpha,\uparrow} = 1 - 2f_{j,\alpha,\uparrow}^\dagger f_{j,\alpha,\uparrow}$ is the fermion parity in the forward branch of copy α at site j. Therefore, the swap operator $\mathcal{C}_{\ell,A}$, when acting on the boundary state $|\mathcal{I}\rangle\rangle$, is equivalent to $\widetilde{\mathcal{C}}_{\ell,A}$, which rotates both $U(1)$ order parameters (η_j^+ and Σ_j^+) counterclockwise by an angle $\pi/2$ in region A. In the long-wavelength description developed in Section 4.4, $\widetilde{\mathcal{C}}_{\ell,A}$ inserts a pair of half vortices at the edges of region A on the boundary of (1+1)d XY model. Here, we note again that $\widetilde{\mathcal{C}}_{\ell,A}$ is not the swap operator when acting on a general state and $\widetilde{\mathcal{C}}_{\ell,A}^2 \neq \mathbb{1}$. We also note that the swap operator breaks the time-reversal symmetry for the spin-1/2 fermions as it only operates on the forward branches ($\sigma = \uparrow$).

C.8   Details of the numerical simulation in Gaussian fermionic circuits

Power-law decay exponents of correlations in the critical phase

In this section, we present the numerical results of e^{-S_A}, $\Pi_{s,A}$ and $\Pi_{b,A}$ in Gaussian fermionic circuits along cut 1. We use the numerical results to extract power-law exponents presented in Fig. 4.7(a-c).

Figure C.1 presents e^{-S_A} [panel(a)], $\Pi_{s,A}$ [panel(b)] and $\Pi_{b,A}$ [panel(c)] as a function of the conformal coordinate z_A for various measurement probabilities p_s. We show that these quantities exhibit power-law decay in the critical phase (when $p_s < p_{s,c}$ on cut 1). The scaling deviates from power laws when increasing the measurement probability p_s. Numerical

results show an area-law S_A, a constant $\Pi_{s,A}$, and an exponentially decaying $\Pi_{b,A}$ in the trivial area-law phase (when $p_s > p_{s,c}$ on cut 1), which verifies our theoretical predictions. Our theoretical understanding also explains the non-monotonic behavior in the bond parity variance $\Pi_{b,A}$ as a function of p_s. In the critical phase, $\Pi_{b,A}$ increases with p_s owing to the decreasing Luttinger parameter K towards the critical point. On the other hand, in the trivial area-law phase, $\Pi_{b,A}$ decreases with p_s due to the decreasing correlation length. We note that the values of $\Pi_{b,A}$ are small along cut 1 owing to the vanishing bond measurement probability, i.e. $p_b = 0$.

Correlation length in the area-law phase of Gaussian fermionic circuit

We present the details on numerically extracting correlation length in the area-law phase of the Gaussian fermionic circuit. Specifically, we show the entanglement entropy data used to extract the correlation length and provide the procedure to determine the logarithmic coefficient $\alpha_S(p_s)$ and constant $b(p_s)$ in Eq. (4.65).

To start with, we show in Fig. C.2 the entanglement entropy along cut 1 exhibits distinct behaviors across the phase transition. When measurement rate p_s is small, the entanglement exhibits a critical scaling as a function of the subsystem size L_A (linear in $\log z_A$). Increasing p_s along cut 1, the circuit enters an area-law phase, which is characterized by the saturation of entanglement entropy as a function of L_A.
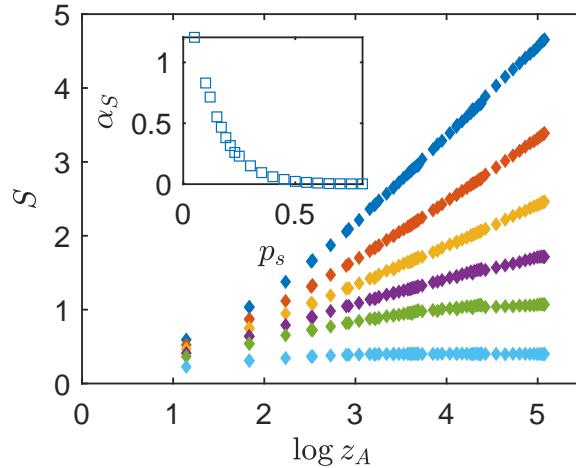
Figure C.2: Subsystem entanglement entropy as a function of conformal coordinate $z_A = L\cos(\pi L_A/L)$ for various different measurement probabilities p_s along cut 1. p_s ranges from 0.05 to 0.35 and increases in the data points from the top to the bottom. (Inset) Logarithmic coefficient $\alpha(p_s)$ of the entanglement entropy as a function of p_s.

Here, we focus on the area-law phase and use the entanglement data to extract the finite correlation length ξ. The entanglement exhibits distinct scaling for different subsystem sizes L_A. When $L_A \ll \xi$, the entanglement exhibits critical scaling as Eq. (4.65). Increasing the subsystem size L_A, the entanglement scaling changes to Eq. (4.66). We extract ξ in two steps: (1) extract $\alpha(p_s)$ and $b(p_s)$ using the entanglement data for small subsystem sizes, i.e. $L_A \ll \xi$; (2) extract ξ using the entanglement data for larger subsystem sizes by fitting to Eq. (4.66).

To extract $\alpha(p_s)$ and $b(p_s)$, we use the data for various L_A and L in the following way: (1) For a given p_s, we plot $S(z_A, p_s, L)$ as a function of $\log z_A$ for various L; (2) We choose at least seven consecutive data points of z_A and perform the linear regression according to Eq. (4.65). We optimize the r^2 of the linear regression over all possible choices to obtain the best $\alpha(p_s)$ and $b(p_s)$. The optimized $\alpha(p_s)$ is shown in the inset of Fig. C.2.

Using the optimized $\alpha(p_s)$ and $b(p_s)$, we perform the least square fitting for $S(z_A, p_s, L)$ as a function of z_A according to Eq. (4.66) for every p_s and L to extract $\xi(p_s, L)$. The result is presented in Fig. 4.8.

Appendix D

Supplementary material for Chapter 5

D.1 Teleportation in the finite-time circuit

In the finite-time circuit [shown in Fig. 1(a) of the main text], we are interested in the teleportation from the reference qubit A to the output qubit B. The teleportation is equivalent to transmitting quantum information through a quantum channel from the leftmost qubit in the initial state to the output of the circuit. The maximum number of teleported qubits (or in our case the fidelity of teleporting a single qubit A) is characterized by the channel capacity. It is worth noting that we here consider the information retained in both the quantum state of qubit B and the classical measurement results in M. Thus, the output of the channel is the entire system including B and M.

In Ref. [65], the authors showed that the channel capacity of such a monitored circuit is given by the entropy of the output B conditioned on measured qubits M, which is also the averaged entropy of B over measurement outcomes in M, i.e. $\sum_m p_m S_{B,m}$. We use this quantity throughout Chapter 5 to detect the potential transition in teleportation fidelity.

D.2 Effective quantum Hamiltonian

In this section, we show that the finite-time random unitary circuit evolution maps to the thermal state of an effective ferromagnetic Ising Hamiltonian at a finite temperature. As emphasized in the main text, the finite-temperature ferromagnetic transition in the effective Hamiltonian manifests as the finite-time transition in the maximum teleportation fidelity, i.e. the conditional entropy, $S_{B|M}$. In particular, we derive the boundary conditions associated with $S_{B|M}$ and show it maps to the order parameter correlation function that detects the transition.

We consider random unitary circuits in Fig. 1(a) of the main text and compute the entropy of the output qubit B conditioned on measurement results on the rest of the output qubits M. The conditional entropy $S_{B|M}$ provides an upper bound on the teleportation fidelity. We seek its average value over the ensemble of trajectories defined by random circuit realizations

and measurement results on M,

$$S_{B|M} = \overline{\sum_m p_m S_{B,m}}, \tag{D.1}$$

where $\overline{\cdot}$ represents the average over unitary gates, and m labels the measurement results. Using the framework developed in Ref. [17, 33], we can express $S_{B|M}$ using the replica method as the $n \to 1$ limit of the replicated quantities

$$S_{B|M}^{(n)} = \frac{1}{1-n} \log \left(\frac{\overline{\sum_m \operatorname{tr} \tilde{\rho}_{B,m}^n}}{\overline{\sum_m \operatorname{tr} \tilde{\rho}_m^n}} \right), \tag{D.2}$$

where $\tilde{\rho}_m := P_m \rho P_m$ is the unnormalized density matrix after measurements. These replicated quantities are analytically tractable and capture the qualitative behaviors of $S_{B|M}$ despite exhibiting a different universality at the critical point [18, 130]. To study the transition in $S_{B|M}$, one needs to consider $S_{B|M}^{(n)}$ for all n and then take the replica limit $n \to 1$.

To gain qualitative insights, we focus on $S_{B|M}^{(2)}$, which can be studied analytically via a mapping to the effective Hamiltonian. The essence of the mapping is to identify the average second moments $\overline{\operatorname{tr} \tilde{\rho}_{B,m}^2}$ and $\overline{\operatorname{tr} \tilde{\rho}_m^2}$ in Eq. (D.2) with the partition function of a classical spin model with certain boundary conditions. To establish the mapping, we formulate the dynamics of the average purity, which involves two copies of density matrix, as the evolution of state vector $|\rho\rangle\!\rangle \simeq \rho \otimes \rho$ in the duplicated Hilbert space $\mathcal{H}^{(2)} = (\mathcal{H} \otimes \mathcal{H}^*)^{\otimes 2}$. Computing the subsystem purity is given by the overlap between $|\rho\rangle\!\rangle$ and a reference state, which will manifest as boundary conditions in the classical spin model at final times [17, 33].

To start with, the dynamics of $|\rho\rangle\!\rangle$ in the random unitary circuits [illustrated in Fig. 1(a) of the main text] is generated by an unitary operator $\mathcal{U} = (U \otimes U^*)^{\otimes 2}$ in $\mathcal{H}^{(2)}$. Two copies of U and U^* in $\mathcal{U}$ act on ket and bra vector spaces, respectively. The output state can be expressed as $|\rho(t)\rangle\!\rangle = \prod_{\tau=1}^{N_t} \mathcal{U}_{2,\tau} \mathcal{U}_{1,\tau} |\rho_0\rangle\!\rangle$, where $\mathcal{U}_{1,\tau}$ and $\mathcal{U}_{2,\tau}$ are the single-qubit and two-qubit Haar random gates in the τ-th time step, respectively, and N_t is the total number of time step, i.e. $t = N_t \delta t$.

Averaging over the single-qubit unitary gates yields a projector onto a two-dimensional reduced local Hilbert space

$$\overline{(U_{j,\tau} \otimes U_{j,\tau}^*)^{\otimes 2}} = \frac{1}{3} |\mathcal{I}_j\rangle\!\rangle \langle\!\langle \mathcal{I}_j| + \frac{1}{3} |\mathcal{C}_j\rangle\!\rangle \langle\!\langle \mathcal{C}_j| - \frac{1}{6} |\mathcal{I}_j\rangle\!\rangle \langle\!\langle \mathcal{C}_j| - \frac{1}{6} |\mathcal{C}_j\rangle\!\rangle \langle\!\langle \mathcal{I}_j|, \tag{D.3}$$

where $|\mathcal{I}_j\rangle\!\rangle \equiv \sum_{ab} |aabb\rangle\!\rangle$ and $|\mathcal{C}_j\rangle\!\rangle \equiv \sum_{ab} |abba\rangle\!\rangle$ with a, b run over the local Hilbert space of qubit j. The coefficients on the right-hand side are given by the Weingarten function for a single-qubit random unitary [67, 183]. We note that $|\mathcal{I}\rangle\!\rangle$ and $|\mathcal{C}\rangle\!\rangle$ are not orthogonal and choose an orthonormal basis labeled by a spin-1/2 variable $s_{j,\tau} = \uparrow, \downarrow$ such that

$$\overline{(U_{j,\tau} \otimes U_{j,\tau}^*)^{\otimes 2}} = \sum_{s_{j,\tau} = \uparrow, \downarrow} |s_{j,\tau}\rangle\!\rangle \langle\!\langle s_{j,\tau}|. \tag{D.4}$$

We choose to define Pauli matrices such that the eigenstates of σ_j^x are given by

$$|+\rangle\!\rangle = \frac{1}{\sqrt{2}} \left(| \uparrow \rangle\!\rangle + | \downarrow \rangle\!\rangle\right) \equiv \frac{1}{2\sqrt{3}}(|\mathcal{I}_j\rangle\!\rangle + |\mathcal{C}_j\rangle\!\rangle), \tag{D.5}$$

$$|-\rangle\!\rangle = \frac{1}{\sqrt{2}} \left(| \uparrow \rangle\!\rangle - | \downarrow \rangle\!\rangle\right) \equiv \frac{1}{2}(|\mathcal{I}_j\rangle\!\rangle - |\mathcal{C}_j\rangle\!\rangle). \tag{D.6}$$

Analogously, the average two-qubit unitary operation $\overline{\mathcal{U}_{ij,\tau}}$ on site i and j leads to a projector onto reduced Hilbert space of two spins

$$\begin{aligned}
\overline{\mathcal{U}_{ij,\tau}} &= \overline{(U_{ij,\tau} \otimes U_{ij,\tau}^*)^{\otimes 2}} \\
&= \frac{1}{15}|\mathcal{I}_i\mathcal{I}_j\rangle\!\rangle\langle\!\langle\mathcal{I}_i\mathcal{I}_j| + \frac{1}{15}|\mathcal{C}_i\mathcal{C}_j\rangle\!\rangle\langle\!\langle\mathcal{C}_i\mathcal{C}_j| - \frac{1}{60}|\mathcal{I}_i\mathcal{I}_j\rangle\!\rangle\langle\!\langle\mathcal{C}_i\mathcal{C}_j| - \frac{1}{60}|\mathcal{C}_i\mathcal{C}_j\rangle\!\rangle\langle\!\langle\mathcal{I}_i\mathcal{I}_j|,
\end{aligned} \tag{D.7}$$

where the coefficients on the right-hand side are given by the Weingarten functions for a random unitary on two qubits [67, 183].

In each time step δt, the layer of two-qubit gates $\mathcal{U}_{2,\tau}$ consists of $N\delta t$ gates $\mathcal{U}_{ij,\tau}$. Each gate acts on a pair of qubits at site i and j drawn randomly from distribution $P(i, j)$. The projection of $\overline{\mathcal{U}_{2,\tau}}$ onto the reduced Hilbert space of each site defines a transfer matrix $\mathcal{T} \equiv \langle\!\langle\{s_{j,\tau+1}\}|\overline{\mathcal{U}_{2,\tau}}|\{s_{j,\tau}\}\rangle\!\rangle$ that describes the transition amplitude between the effective Hilbert space at two consecutive time steps. In the limit $\delta t \to 0$, the transfer matrix can be written as the imaginary time evolution $\mathcal{T} = e^{-\delta t H_{\mathrm{eff}}}$ generated by the effective quantum Hamiltonian of the form [Eq. (1) in the main text]

$$H_{\mathrm{eff}} = \sum_{i,j} J_{ij} \left[-\frac{2}{5}\sigma_i^z\sigma_j^z - \frac{1}{10}\sigma_i^y\sigma_j^y - \frac{1}{5}(\sigma_i^x + \sigma_j^x) \right]. \tag{D.8}$$

We note that the effective Hamiltonian H_{eff} exhibits an Ising symmetry generated by $\prod_i \sigma_i^x$, which originates from the invariance of $\mathcal{U}$ under swapping two copies of U.

Having established the mapping for the dynamics of double density matrix, we now discuss the boundary conditions associated with $\mathrm{tr}\,\tilde{\rho}_{B,m}^2$. In the output state, we first perform measurements on M, which enforce a projection on the replicated density matrix by $\mathcal{P}_m = P_m^{\otimes 4}$. Then, we compute the purity of subsystem B which is given by the overlap

$$\mathrm{tr}\,\tilde{\rho}_{B,m}^2 = \langle\!\langle\mathcal{I}|\mathcal{C}_B\mathcal{P}_m|\rho(t)\rangle\!\rangle, \tag{D.9}$$

where $\mathcal{C}_B$ is the swap operator of two copies of ket vectors in region B, and $\mathcal{C}_B|\mathcal{I}\rangle\!\rangle = |\mathcal{C}_B\rangle\!\rangle$.

Measurements enforce symmetric boundary conditions on M at final times since the reference state $\langle\!\langle\mathcal{I}|\mathcal{P}_m = \langle\!\langle mmmm|$ is symmetric under swapping of two ket vectors. Similarly, the initial product state also enforces open boundary conditions as $|\rho_0\rangle\!\rangle = |0000\rangle\!\rangle$. At the position of the input qubit A and output qubit B, Eq. (D.9) imposes symmetry breaking boundary conditions: $\langle\!\langle\mathcal{I}_A|$ at site i_A and $\langle\!\langle\mathcal{C}_B|$ at site i_B. The overlap contributes a Boltzmann

weight e^{-hs}

$$\langle\!\langle \mathcal{I}_A | s_A \rangle\!\rangle = \frac{\sqrt{3}}{2} + \frac{s_A}{2}, \tag{D.10}$$

$$\langle\!\langle \mathcal{C}_B | s_B \rangle\!\rangle = \frac{\sqrt{3}}{2} - \frac{s_B}{2}, \tag{D.11}$$

which corresponds to a magnetic field $h = \log\left(\sqrt{3/2} - \sqrt{1/2}\right) = -0.66$ for $\mathcal{I}$ boundary conditions and $-h$ for $\mathcal{C}$ boundary conditions. We use s_A and s_B to label the basis states of the Hilbert space at spacetime locations $(i_A, 1)$ and (i_B, N_t), respectively. For the denominator $\operatorname{tr} \tilde{\rho}_m^2$ in Eq. (D.2), $\mathcal{I}$ boundary conditions are imposed at both A and B.

Hence, $S_{B|M}^{(2)}$ is given by

$$S_{B|M}^{(2)} = -\log\left(\frac{\langle\!\langle \mathcal{I} | \mathcal{P}_m e^{h\sigma_B^z} e^{-tH_{\text{eff}}} e^{-h\sigma_A^z} |\rho_0\rangle\!\rangle}{\langle\!\langle \mathcal{I} | \mathcal{P}_m e^{-h\sigma_B^z} e^{-tH_{\text{eff}}} e^{-h\sigma_A^z} |\rho_0\rangle\!\rangle}\right). \tag{D.12}$$

where $\sigma_{A/B}^z$ is the Pauli-Z operator at site A/B. In the case that magnetization is small, e.g. close to the critical point, one can treat the magnetic field perturbatively. We expand $S_{B|M}^{(2)}$ to second order in h and obtain

$$S_{B|M}^{(2)} = 2h^2 \frac{\langle\!\langle \mathcal{I} | \mathcal{P}_m \sigma_B^z e^{-tH_{\text{eff}}} \sigma_A^z |\rho_0\rangle\!\rangle}{\langle\!\langle \mathcal{I} | \mathcal{P}_m e^{-tH_{\text{eff}}} |\rho_0\rangle\!\rangle} := 2h^2 \langle \sigma_B^z(t)\sigma_A^z(0)\rangle. \tag{D.13}$$

Hence, $S_{B|M}^{(2)}$ is proportional to the imaginary time order parameter correlation function $\langle \sigma_B^z(t)\sigma_A^z(0)\rangle$ near the critical point and reflects the universal properties of the phase transition in the effective spin model.

D.3 Mean-field theory for finite-temperature transition in all-to-all coupled quantum Ising model

In this section, we perform the exact mean-field calculation for the phase transition in the effective Hamiltonian for all-to-all coupled random unitary circuits. We first perform the quantum-to-classical mapping. Then, we use mean-field theory, which is exact in the thermodynamic limit, to determine the critical time and critical exponents.

The effective quantum Hamiltonian of the all-to-all coupled RUC is given by

$$H_{\text{eff}} = \sum_{(i,j)} h_{ij} = \sum_{(i,j)} \frac{2}{N-1}\left[-\frac{2}{5}\sigma_i^z\sigma_j^z - \frac{1}{10}\sigma_i^y\sigma_j^y - \frac{1}{5}(\sigma_i^x + \sigma_j^x)\right], \tag{D.14}$$
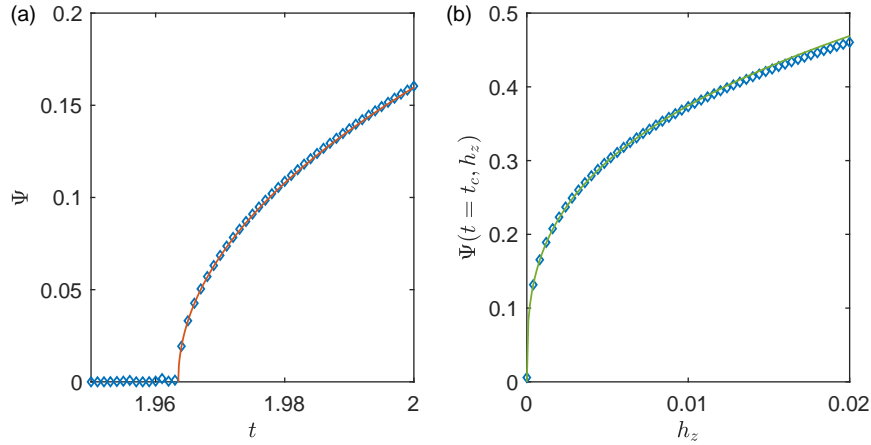
Figure D.1: Mean-field theory of the ordering phase transition in the effective classical spin model of the all-to-all coupled quantum circuit. (a) Average magnetization Ψ as a function of time t. We obtain critical time $t_c = 1.96$ and critical exponent $\beta = 0.49 \pm 0.04$. The red solid line represents $\Psi = c_1(t - t_c)^\beta$ for $t > t_c$. (b) Critical scaling of magnetization Ψ as a function symmetry breaking field h_z. We obtain $h_z \sim \Psi^\delta$ with $\delta = 3.1 \pm 0.1$ at the critical point. The green solid line represents $\Psi(t_c, h_z) = c_2 h_z^{1/\delta}$.

where (i, j) represents a pair of qubits on sites i and j. We note that $J_{ij} = 2/(N - 1)$ such that $\sum_{(i,j)} J_{ij} = N$. The partition function of the effective spin model for the circuit of finite time t is

$$Z = \int Ds \, e^{-\int_0^t d\tau H_{\text{eff}}}. \tag{D.15}$$

The only difference between this partition function and that of the quantum Hamiltonian at finite temperature are the boundary conditions in the temporal direction. The spin model we derived takes open boundary conditions at $\tau = 0$ and t. If one assumes periodic temporal boundary conditions, the finite temperature transition can be analyzed by standard mean-field theory, which gives rise to critical exponents $\beta = 1/2$ and $\nu = 2$.

To incorporate the effects of open temporal boundary conditions, we perform the quantum-to-classical mapping. First, we divide the time interval $[0, t]$ into N_t steps, i.e. $t = N_t \delta t$, and index these time steps by τ. Within each time step τ, we Trotterize the imaginary time evolution into the product of $N(N - 1)/2$ terms as $e^{-\delta t H_{\text{eff}}} = \prod_{(i,j)} e^{-\delta t h_{ij}}$. Then, we insert resolutions of the identity using the eigenstates of σ_i^z, labeled by a classical spin $s_i = \pm 1$, before and after each Trotterized time step ζ. The classical spins at two consecutive

Trotterized time steps ζ and $\zeta + 1$ are coupled by the transfer matrix

$$
\begin{aligned}
\mathcal{T}_{ij,\tau} &\equiv \langle s_{i,\tau,\zeta+1} s_{j,\tau,\zeta+1} | e^{-\delta t h_{ij}} | s_{i,\tau,\zeta} s_{j,\tau,\zeta} \rangle \\
&= -\log(1 - 2h)\frac{1 + s_{i,\tau,\zeta+1} s_{i,\tau,\zeta}}{2} \frac{1 + s_{j,\tau,\zeta+1} s_{j,\tau,\zeta}}{2} - \log(h)\frac{1 - s_{i,\tau,\zeta+1} s_{i,\tau,\zeta} s_{j,\tau,\zeta+1} s_{j,\tau,\zeta}}{2}
\end{aligned}
$$

$$
- \left(\log(J_{yy}) + i\pi \frac{1 + s_{i,\tau,\zeta} s_{j,\tau,\zeta}}{2} \right) \frac{1 - s_{i,\tau,\zeta+1} s_{i,\tau,\zeta}}{2} \frac{1 - s_{j,\tau,\zeta+1} s_{j,\tau,\zeta}}{2} - J_{zz} s_{i,\tau,\zeta} s_{j,\tau,\zeta},
\tag{D.16}
$$

where $h = 2\delta t/5(N-1)$, $J_{yy} = \delta t/5(N-1)$, and $J_{zz} = 4\delta t/5(N-1)$.

In terms of the classical spins $s_{i,\tau,\zeta}$, the partition function is

$$
Z = \sum_{\{s_{i,\tau,\zeta}\}} \prod_{\tau=1}^{N_t} \prod_{(i,j)} \mathcal{T}_{ij,\tau}.
\tag{D.17}
$$

In the following, we analyze the phase transition as a function of t.

We use mean-field theory, which is exact in the thermodynamic limit $N \to \infty$. To this end, we introduce the mean fields $\Psi_{\tau,\zeta} = \sum_i \langle s_{i,\tau,\zeta} \rangle / N$ and $\Phi_{\tau,\zeta} = \sum_i \langle s_{i,\tau,\zeta} s_{i,\tau,\zeta+1} \rangle / N$. This allows one to factor the transfer matrix as $\mathcal{T}_{ij,\tau} = \mathcal{T}_{i,\tau}^{(MF)} \mathcal{T}_{j,\tau}^{(MF)}$, yielding

$$
Z = \prod_i Z_{1d,i} = \prod_i \left[\sum_{\{s_{i,\tau,\zeta}\}} \prod_{\tau=1}^{N_t} \left(\mathcal{T}_{i,\tau}^{(MF)} \right)^{N-1} \right],
\tag{D.18}
$$

where the partition function Z decouples into N 1d classical Ising models in the temporal direction for spins living on every spatial site, $Z_{1d,i} = \sum_{\{s_{\tau,\zeta}\}} e^{-H_{1d}}$. We note that, after the Trotterization, $N-1$ transfer matrices $\mathcal{T}_{ij,\tau}$ act on site i.

Before we derive the mean-field solution, we can first simplify the classical model. Each Trotterized time step $e^{\delta t h_{ij}}$ can only change the order parameter by at-most $O(\delta t/N)$, where the factor $1/N$ from the coupling $J_{ij} \sim 1/N$. Hence, $\Phi_{\tau,\zeta}$ which measures the correlation in two consecutive Trotterized steps is given by $\Phi_{\tau,\zeta} = 1 + O(\delta t/N)$. We can therefore, to the leading order, replace $\Phi_{\tau,\zeta}$ by unity. Moreover, we drop ζ dependence in $\Psi_{\tau,\zeta}$ because $\Psi_{\tau,\zeta}$ is slowly varying within each time step, i.e. we approximate $\Psi_{\tau,\zeta} \approx \Psi_\tau$ in δt, where Ψ_τ is the average $\Psi_{\tau,\zeta}$ over Trotterized steps ζ.

After the simplification, the 1d classical Hamiltonian takes the form

$$
H_{1d} = \sum_{\tau=1}^{N_t} \sum_{\kappa=1}^{N-1} -\tilde{J}_\tau s_{\tau,\kappa} s_{\tau,\kappa+1} - \tilde{h}_\tau s_{\tau,\kappa},
\tag{D.19}
$$

where $s_{\tau,\kappa}$ are spins inserted before and after $N-1$ transfer matrices $\mathcal{T}_{i,\tau}^{(MF)}$ labeled by κ, and $s_{\tau,N} \equiv s_{\tau+1,1}$. The couplings in the 1d Ising model to the leading order in $1/N$ are given

by

$$\tilde{J}_\tau = -\frac{\log h}{2}, \tag{D.20}$$

$$\tilde{h}_\tau = J_{zz}\Psi_\tau. \tag{D.21}$$

We determine the critical point and critical exponents by numerically solving the self-consistency equations

$$\Psi_\tau = \frac{1}{Z_{1d}} \sum_{\{s_\tau\}} s_\tau e^{-H_{1d}}. \tag{D.22}$$

The global magnetization Ψ as a function of time is plotted in Fig. D.1(a). We obtain a critical time $t_c = 1.96$. Near the critical time, $\Psi \sim (t - t_c)^\beta$ with the order parameter critical exponent $\beta = 0.49 \pm 0.04$. We determine the other critical exponent by considering the scaling of the order parameter as a function of external magnetic field h_z at the critical time, i.e. $h_z \sim \Psi^\delta$. The external magnetic field introduces an additional term to the 1d Hamiltonian [Eq. (D.19)]

$$H_m(h_z) = \sum_{\tau=1}^{N_t} \sum_{\kappa=1}^{N-1} -\frac{h_z \delta t}{N-1} s_{\tau,\kappa}. \tag{D.23}$$

Now solving the self-consistency equations in the presence of h_z yields $\delta = 3.1 \pm 0.1$ as shown in Fig. D.1(b). Using the scaling relations in 1d, we have $\nu = \beta(\delta + 1) = 2.0 \pm 0.2$. The numerically extracted critical exponents agree with the standard mean-field exponents $\beta = 1/2$, $\delta = 3$, and $\nu = 2$.

D.4 Details of finite-time transition in 1d long-range circuits

The effective quantum Hamiltonian predicts ordering phase transitions for $\alpha < 2$ [221, 79, 249, 13], a Kosterlitz-Thouless (KT) like phase transition at $\alpha = 2$ [150, 57, 30, 31, 126, 173], and the absence of a phase transition for $\alpha > 2$. In this section, we present details concerning our numerical evidence for these qualitative predictions, as well as on our estimation of the critical exponents shown in Fig. 2(c) of the main text.

Phase transitions for $\alpha < 2$

Based on the mapping of the conditional entropy to the order parameter correlation function in the effective spin model, we can derive a finite-size scaling formula. Assuming the second-order phase transition, the order parameter $\langle \sigma^z \rangle$ would vanish as $\langle \sigma^z \rangle \sim (t - t_c)^\beta$ close to the critical
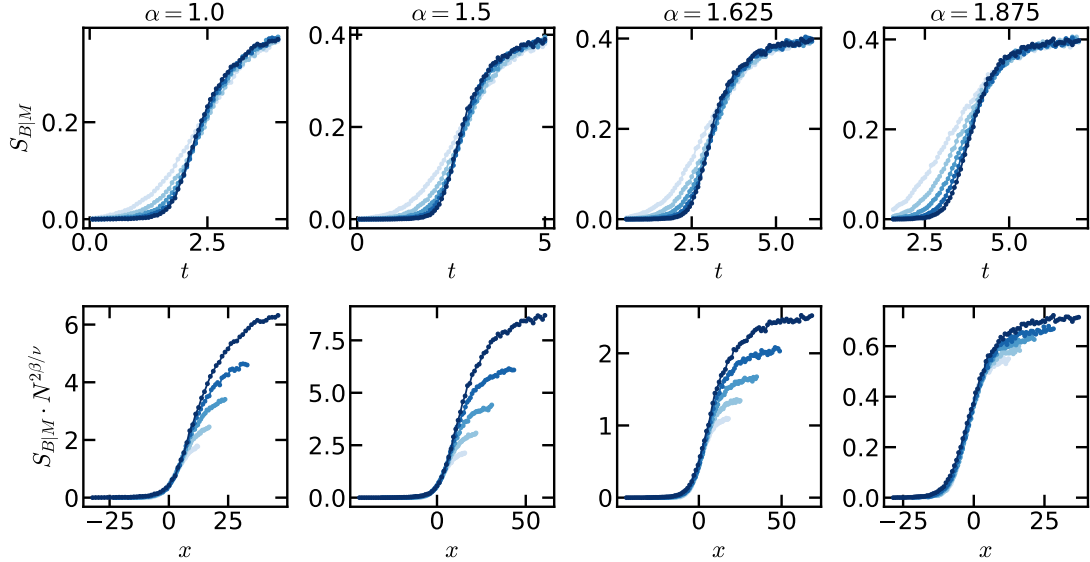
Figure D.2: (Top row) Finite time teleportation transition in 1d long-range circuits with $\alpha = 1.0, 1.5, 1.625, 1.875$ (from left to right) for various system sizes N from 32 to 512 indicated by increasing opacity. (Bottom row) Finite-size scaling collapse using Eq. (3) in the main text. The numerically extracted critical exponents are presented in Fig. 2(c) in the main text. The x-axis represents $(t - t_c)N^{1/\nu}$. The results were averaged over $1.5 \cdot 10^4$ circuit realizations (as for $\alpha = 0.0, 1.75$ in the main text).

point in the ordered phase ($t > t_c$). Here, we use β to denote the order parameter critical exponent. Accordingly, the conditional entropy decays as $S_{B|M} \sim \langle \sigma_B^z(t)\sigma_A^z(0)\rangle \sim (t - t_c)^{2\beta}$. In numerical simulation, the singularity at $t = t_c$ is smeared out due to the finite size effect. Specifically, we have $S_{B|M} = (t - t_c)^{2\beta} f(N/\xi)$, where $f(N/\xi)$ is a universal function that only depends on the ratio between the system size N and the correlation length ξ. Knowing that the correlation length diverges as $\xi \sim (t - t_c)^{-\nu}$, we can obtain the scaling formula in Eq. (3) of the main text, which we recast here

$$S_{B|M} = N^{-2\beta/\nu}\mathcal{F}((t - t_c)N^{1/\nu}). \tag{D.24}$$

Figure D.2 shows the numerical results for $S_{B|M}(t, N)$ (top row) and associated finite-size scaling (FSS) collapse (bottom row) for $\alpha = 1.0, 1.5, 1.625, 1.875$ (analogous plots for $\alpha = 0.0, 1.75$ are in the main text). The analysis yields the critical exponents ν and β, and the critical time t_c. Specifically, we optimize the least-squared error (LSE) of the fit of $S_{B|M}(t, N)$ as a function of β, ν, and t_c. We weight errors in the collapse according to a Gaussian distribution centered near the critical time with standard deviation 40 for the parameter $(t - t_c)L^{1/\nu}$. The critical exponents are close to their mean-field values below

$\alpha = 1.5$ and vary continuously when $1.5 < \alpha < 2$, which is consistent with the prediction from the effective Hamiltonian. We note that the effective Hamiltonian also predicts the divergence of ν as $\nu = 1/(2 - \alpha)$ [150]. To confidently examine this behavior requires a more accurate scheme to extract ν, which is left for future work.

To obtain estimates and errors for our FSS analysis, we employ a standard bootstrap scheme: (1) 15000 circuit realizations are simulated for $N \in \{32, 64, 128, 256, 512\}$, from which we obtain samples of $S_{B|M}(t, N)$; (2) we select 7500 random sub-samples which we average to estimate $S_{B|M}(t, N)$; (3) we perform 3-parameter curve-fitting to extract samples ν, β and t_c; (4) steps (2-3) are repeated 1000 times to obtain distributions for ν, β and t_c. We report the mean of the distribution as our estimate and all error bars reflect one standard deviation from the mean. This procedure is used for all FSS analysis *except* $\alpha = 2.0$, which requires special attention due to the expected failure of scaling form Eq. (3) (see discussion below).

We note that the saturation value of $S_{B|M}$ at a long time to 0.4 is universal for the Clifford simulation. After projective measurements on M, the unmeasured qubit A and B are in the *projective ensemble* defined by measurement results and circuits realizations [70, 64]. In the projective ensemble of deep Clifford circuits, A and B are entangled by a two-qubit random Clifford gate with an average entropy 0.4, which can be shown analytically.

Kosterlitz-Thouless like transition at $\alpha = 2$

The effective quantum Hamiltonian for the 1d long-range random circuit at $\alpha = 2$ is given by

$$H_{\text{eff}} = \sum_{i,j} \frac{J}{|i - j|^2} \left[-\frac{2}{5}\sigma_i^z \sigma_j^z - \frac{1}{10}\sigma_i^y \sigma_j^y - \frac{1}{5}(\sigma_i^x + \sigma_j^x) \right]. \tag{D.25}$$

At finite temperature, the model is in the same universality as the 1d classical Ising model with inverse square interaction, which exhibits a finite-temperature Kosterlitz-Thouless phase transition [150, 57, 30, 31, 126, 173].

According to the mapping discussed above, the conditional entropy is related to the order parameter correlation function, i.e. $S_{B|M} \simeq \langle \sigma_B^z(t)\sigma_A^z(0) \rangle$. Near the critical point, the correlation function $\langle \sigma_B^z(t)\sigma_A^z(0) \rangle$ is of the same asymptotic form as the correlation $G(r) := \langle s(r)s(0) \rangle$ in the 1d classical Ising model, where r is the distance between qubits A and B. Using the renormalization group method developed in Ref. [277], the scaling form of $G(r)$ has been derived [30]. In the ordered phase close to the critical point, $G(r)$ exhibits a subleading power-law decay

$$G(r) = \bar{s}^2 \left(1 + \frac{4\sqrt{|(T - T_c)/T_c|}}{r^{4\sqrt{|(T-T_c)/T_c|}}} \right), \quad (T < T_c). \tag{D.26}$$

At the critical point, the scaling changes to

$$G(r) = \bar{s}^2 e^{1/\ln r}, \quad (T = T_c). \tag{D.27}$$
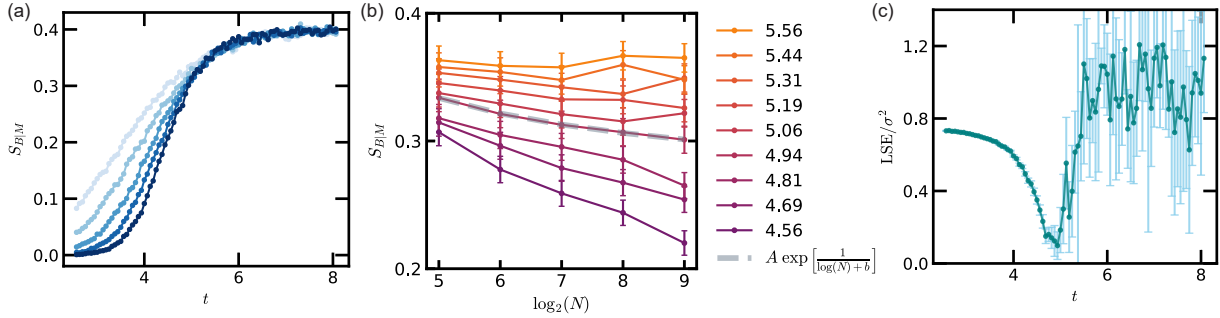
Figure D.3: Finite-time teleportation transition in 1d long-range circuits with $\alpha = 2$. (a) Conditional entropy $S_{B|M}$ as a function of time t for various system sizes N from 32 to 512 indicated by increasing opacity. The results are averaged over 15000 random circuit realizations. (b) $S_{B|M}$ as a function of N for various time t given in the legend. Dash-dotted line indicates the best fit of critical scaling form $S_{B|M}(t_c, N) = A \exp[1/(\log N + b)]$ for a KT-like transition. (c) LSE (obtained fitting $S_{B|M}$ to the critical scaling form $A \exp[1/(\log N + b)]$) divided by the variance σ^2. Error bars on this figure of merit (FOM) are obtained from 1000 "synthetic" simulations where noise is added to $S_{B|M}(t, N)$ according to the observed noise in the true simulation. The critical time $t_c = 4.95 \pm 0.12$ is determined by the minimum of the FOM (error obtained from the same synthetic simulations).

In the numerical simulation, we obtain $S_{B|M}$ as a function of t for various system sizes N. We fix the distance between A and B to be $N/2$. Hence, at the critical point, $S_{B|M}$ exhibits the finite-size scaling

$$S_{B|M}(t_c, N) = A \exp\left[\frac{1}{\ln N + b}\right]. \tag{D.28}$$

To determine the critical point, we fit $S_{B|M}(t, N)$ as a function of N for each t to the critical scaling form. The LSE divided by the total variance is plotted in Fig. D.3(c) as a function of time. We determine the critical time $t_c = 4.95 \pm 0.12$ according to the minimum of the LSE/variance curve – this is the time at which the most variance in the raw data is explained by the critical scaling function. The excellent agreement between the critical scaling function and the numerical data is shown in Fig. D.3(b), where the dashed-dotted line denotes the expected critical behavior.

Absence of phase transition for $\alpha > 2$

The effective Hamiltonian does not exhibit finite temperature phase transition for $\alpha > 2$. As an example, in the circuit with $\alpha = 3$, we compute the conditional entropy as a function of t for various system sizes (see Fig. D.4). Notably, the $S_{B|M}$ curves do not exhibit a crossing
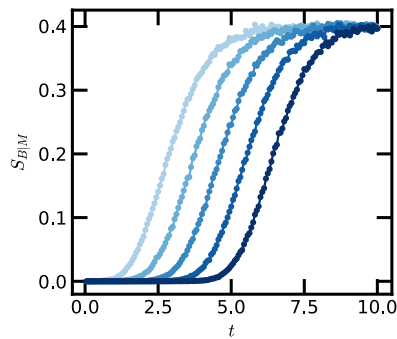
Figure D.4: Absence of finite-time teleportation transition in 1d long-range circuits with $\alpha = 3.0$. $S_{B|M}$ is plotted as a function of t for various system sizes N from 32 to 512. The numerical results are averaged over $3.0 \cdot 10^4$ random circuit realizations.

with varying system sizes, indicating the lack of a finite-time singularity in the thermodynamic limit.

Appendix E

Supplementary material for Chapter 6

E.1   Phase transition in Toric code subject to incoherent errors

In this section, we provide details of the phase transition in the Toric code subject to bit-flip errors. In Sec. E.1, we show that the anyon condensation transition in the EFD is exactly solvable. It occurs at $p_c^{(2)} = 0.178$ and is of the 2D classical Ising universality. In Sec. E.1, we compute the topological entanglement entropy in the EFD state and show it sharply changes from $2 \log 2$ to $\log 2$ at the condensation transition.

Critical point

As mentioned in the main text, the bit-flip errors in the Toric code can induce a condensation of $m\bar{m}$-anyon in the EFD at a finite error threshold. The transition is exactly solvable and of 2D classical Ising universality. Here, we provide details on exactly solving the transition.

To start, we consider the EFD state describing the Toric code subject to bit-flip (Pauli-X) errors

$$|\rho\rangle\rangle = \prod_l \left((1-p) + pX_l \otimes X_l\right) |\Psi_0\rangle \otimes |\Psi_0^*\rangle \propto e^{\mu \sum_i X_l \otimes X_l} |\Psi_0\rangle \otimes |\Psi_0^*\rangle, \qquad \text{(E.1)}$$

where p is the bit-flip error rate, $\mu = \tanh^{-1}[p/(1-p)]$, l labels the edges in the square lattice, and $|\Psi_0\rangle$ is one of the Toric code ground states specified below.

We work in a loop picture of the Toric code ground state

$$|\Psi_0\rangle \propto \prod_p \frac{1 + B_p}{2} |+\rangle \propto \sum_{\{g\}} |g\rangle, \qquad \text{(E.2)}$$

where p in the subscript labels the plaquette, $|+\rangle := \prod_i |+\rangle_i$ is a product state with each qubit initialized in the $+1$ eigenstate of Pauli-X operator, i.e. $X_i |+\rangle = |+\rangle$. A product of B_p gives g_z, which is a product of the Pauli-Z operators along a closed loop. When acting

on $|+\rangle$, g_z flips qubits into -1 eigenstates of X_i along a loop g and leads to a product state $|g\rangle := g_z |+\rangle$. This allows writing the ground state in terms of closed loops g, represented by binary variables.

The EFD can be written in the loop picture accordingly. Before applying the error channel, the double ground state is expressed as

$$|\rho_0\rangle\rangle = |\Psi_0\rangle \otimes |\Psi_0^*\rangle = \frac{1}{\sqrt{\mathcal{Z}(0)}} \sum_{g,\bar{g}} |g, \bar{g}\rangle\rangle, \tag{E.3}$$

where $|g, \bar{g}\rangle\rangle := (g_z \otimes \bar{g}_z) |+\rangle \otimes |+\rangle$, g and $\bar{g}$ label two independent loop configurations in the ket and bra copy, respectively. The error channel assigns a weight in the summation of loops and leads to

$$|\rho\rangle\rangle = \frac{1}{\sqrt{\mathcal{Z}(\mu)}} \sum_{g,\bar{g}} e^{-2\mu|g+\bar{g}|} |g, \bar{g}\rangle\rangle, \tag{E.4}$$

where $g + \bar{g}$ is a binary sum and represents the relative loop configuration, $\mathcal{Z}(\mu)$ is the normalization factor, and μ can be interpreted as the loop tension. We note that only the relative loop $h := g + \bar{g}$ acquires a loop tension. Hence, it is more convenient to rewrite the EFD as
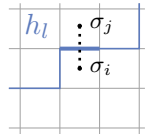
$$|\rho\rangle\rangle = \frac{1}{\sqrt{\mathcal{Z}(\mu)}} \sum_{g,h} e^{-2\mu|h|} |g, h\rangle\rangle. \tag{E.5}$$

The anyon condensation transition is detected by the open string operator

$$\langle\langle W_{m\bar{m}}(\mathcal{P})\rangle\rangle = \frac{\langle\langle \rho | w_m(\mathcal{P}) \otimes w_{\bar{m}}(\mathcal{P}) | \rho \rangle\rangle}{\langle\langle \rho | \rho \rangle\rangle} = \frac{1}{\mathcal{Z}(\mu)} \sum_{g,h} (-1)^{\#\text{crossing}(\mathcal{P},h)} e^{-4\mu|h|}, \tag{E.6}$$

where $\#\text{crossing}(\mathcal{P}, h)$ counts the number of crossings between the open string $\mathcal{P}$ and loop h. In this expression, the open string $\langle\langle W_{m\bar{m}}(\mathcal{P})\rangle\rangle$ can be interpreted as an observable in a statistical mechanical model of loops. The normalization factor $\mathcal{Z}(\mu)$ is the partition function $\mathcal{Z}(\mu) = \Omega(0)\Omega(\mu)$, where the partition function $\Omega(0)$ of g loops is a constant independent of μ, and the partition function of h loop, $\Omega(\mu) = \sum_h e^{-H(\mu)}$, has an effective Hamiltonian $H(\mu) = 4\mu|h|$.

We can identify the loop configuration h with domain walls in a spin model with Ising degrees of freedom living on the plaquettes, i.e.

$$h_l = \frac{1 - \sigma_i \sigma_j}{2}. \tag{E.7}$$

Then, the loop model reduces to the square lattice Ising model up to a constant

$$H = \sum_{\langle i,j \rangle} -2\mu \sigma_i \sigma_j. \tag{E.8}$$

Thus, the condensation transition in the EFD is of the 2D classical Ising universality class. The critical point is exactly solvable and determined by the Kramers-Wannier duality, $\mu_c = (1/4)\log\left(1 + \sqrt{2}\right)$, i.e. $p_c^{(2)} = 0.178$. We remark that this critical point is associated with the partition function $\mathcal{Z}(\mu) = \operatorname{tr}\rho^2$ and indicates the singularity in the second moment of ρ.

Topological entanglement entropy

Another diagnostic of the anyon condensation is the topological entanglement entropy (TEE) of the EFD state. In the case of the Toric code subject to incoherent errors, the EFD state can be written as the ground state of a gapped local Hamiltonian. One can therefore use TEE to detect the transition. In this subsection, we first construct the parent Hamiltonian of the EFD. We then compute the Rényi-n entropy of the EFD and show that the subleading topological term undergoes a transition from $2\log 2$ to $\log 2$ upon the condensation of $m\bar{m}$ regardless of the Rényi order n. This indicates a singularity also in the topological term of von Neumann entropy ($n \to 1$). We remark that, in a related problem of the Toric code undergoing imaginary time evolution, the TEE changes sharply from $\log 2$ to zero across the phase transition as shown in Ref. [58].

The EFD describing the Toric code subject to bit-flip errors is the ground state of a local parent Hamiltonian [1]

$$\tilde{H} = V^{-1}H_0 V V H_0 V^{-1}, \tag{E.9}$$

where $V = e^{\mu\sum_i X_i \otimes X_i}$, and H_0 is a projector Hamiltonian given by

$$H_0 = \sum_s \frac{1 - A_s \otimes \mathbb{I}}{2} + \frac{1 - \mathbb{I} \otimes A_s}{2} + \sum_p \frac{1 - B_p \otimes \mathbb{I}}{2} + \frac{1 - \mathbb{I} \otimes B_p}{2}. \tag{E.10}$$

Here, the eigenvalue of $\tilde{H}$ is non-negative. One can show $|\rho\rangle\rangle$ is a zero eigenstate of $\tilde{H}$ and therefore is the ground state. It is then legitimate to use the TEE to characterize the topological order in the EFD. The TEE sharply changes when the gap of $\tilde{H}$ closes.

We now compute the TEE in the EFD and show it undergoes a transition when tuning the error rate. First, we show the TEE takes distinct values in two limits, the error rate $p = 0$ and $p = 1/2$. To gain an understanding away from these two limits, we then consider the Rényi-n entropy and map it to the free energy cost of spin pinning in a classical spin model. We show its subleading term undergoes a transition at the critical point and take the analytic limit $n \to 1$ to extract the behavior of the TEE. We remark that, as far as the entanglement entropy of a finite disk is concerned, the boundary condition of the total system is not important and will not be specified explicitly throughout the entire calculation.

In the limits $p = 0, 1/2$, the EFD state is a stabilizer state, and the TEE can be easily determined. In the absence of errors, the EFD contains two copies of decoupled Toric code

---

[1]We thank Meng Cheng for pointing this out to us.

states and exhibits a TEE $\gamma = 2\log 2$. In the case of $p = 1/2$, the tension $\mu \to \infty$ imposes the stabilizers $X_i \otimes X_i$ in the EFD. The resulting EFD is the mutual eigenstate of stabilizers

$$\{A_s \otimes \mathbb{I}, \quad \mathbb{I} \otimes A_s, \quad X_i \otimes X_i, \quad B_p \otimes B_p\}.$$

For a simply connected region A, its entanglement entropy is given by

$$S_A / \log 2 = 2|A| - \#\text{stabilizer}(\text{supp}(s) \in A) \tag{E.11}$$

where $2|A|$ counts the total number of degrees of freedom in region A, and $\#\text{stabilizer}(\text{supp}(s) \in A)$ is the number of stabilizers whose support is completely in A. One can show $S_A = (|\partial A| - 1)\log 2$, and the TEE $\gamma = \log 2$. The distinct values of TEE in two limits indicate its potential singularity as a function of error rate.

To understand the TEE away from two limits, we consider the Rényi-n entropies of a simply connected region A and develop a classical spin model description. The first step is to write down the reduced density matrix. Here, we separate the loop configuration g (h) into two parts g_A and $g_{\bar{A}}$ $(h_A$ and $h_{\bar{A}})$, which support on region A and its complement $\bar{A}$, respectively. To form a closed loop configuration, two parts must agree on the boundary of A, i.e., $\partial g_A = \partial g_{\bar{A}} = b$, and $\partial h_A = \partial h_{\bar{A}} = c$.
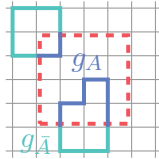
The reduced density matrix can be written as

$$
\begin{aligned}
\varrho_A(\mu) &= \text{Tr}_{\bar{A}} |\rho(\mu)\rangle\!\rangle \langle\!\langle \rho(\mu)| \\
&= \frac{1}{\mathcal{Z}(\mu)} \sum_{b,c} \sum_{\substack{g_A, \tilde{g}_A, \\ \partial g_A = \partial \tilde{g}_A = b}} \sum_{\substack{h_A, \tilde{h}_A, \\ \partial h_A = \partial \tilde{h}_A = c}} \Omega_{\bar{A}}(0;b)\Omega_{\bar{A}}(\mu;c)e^{-2\mu|h_A|-2\mu|\tilde{h}_A|} |g_A, h_A\rangle\!\rangle \langle\!\langle \tilde{g}_A, \tilde{h}_A|,
\end{aligned}
\tag{E.12}
$$

where $\Omega_{\bar{A}}(0;b)$ and $\Omega_{\bar{A}}(\mu;c)$ are the partition function of g and h loops in region $\bar{A}$ with a given boundary condition b and c, respectively,

$$\Omega_{\bar{A}}(\mu;c) = \sum_{h_{\bar{A}}, \partial h_{\bar{A}} = c} e^{-4\mu|h_{\bar{A}}|}. \tag{E.13}$$

The normalization factor $\mathcal{Z}(\mu) = \Omega(0)\Omega(\mu)$ can be written accordingly as

$$\Omega(\mu) = \sum_c \Omega_A(\mu;c)\Omega_{\bar{A}}(\mu;c). \tag{E.14}$$

Next, we write down the n-th moment of the reduced density matrix

$$\mathrm{Tr}\,\varrho_A^n(\mu) = \Gamma_A(0)\Gamma_A(\mu), \tag{E.15}$$

where $\Gamma_A(0)$ and $\Gamma_A(\mu)$ are associated with g and h loops, respectively, and

$$\Gamma_A(\mu) = \frac{1}{\Omega^n(\mu)} \sum_c \Omega_A^n(\mu;c)\Omega_{\bar{A}}^n(\mu;c). \tag{E.16}$$

Equation (E.16) can be viewed as a ratio between two partition functions. The denominator represents the partition function of n copies of loop models, while the loop model in the numerator is further subject to the constraint that loops in different copies have the same boundary condition c.

The Rényi entropy therefore can also be interpreted as the excess free energy related to the above constraint

$$S_A^{(n)} = \frac{1}{1-n}\log\mathrm{Tr}\,\varrho_A^n(\mu) = \frac{1}{n-1}\left(F_A^{(n)}(0) - nF_0(0)\right) + \frac{1}{n-1}\left(F_A^{(n)}(\mu) - nF_0(\mu)\right) \tag{E.17}$$

where $F_0(\mu) = -\log\Omega(\mu)$ is the free energy of the loop model with tension μ, $F_A^{(n)}(\mu) = -\log\sum_c \Omega_A^n(\mu;c)\Omega_{\bar{A}}^n(\mu;c)$ is the free energy of n copies of the loop model subject to the constraint.

The scaling of the excess free energy is easier to analyze when formulating the loop model in terms of Ising spins. We again identify the loop configuration with Ising domain walls

$$g_l^{(s)} = \frac{1 - \sigma_i^{(s)}\sigma_j^{(s)}}{2}, \quad h_l^{(s)} = \frac{1 - \sigma_i'^{(s)}\sigma_j'^{(s)}}{2}, \quad s = 1, 2, \cdots, n \tag{E.18}$$

Furthermore, we redefine the Ising variables

$$\sigma_i^{(s)} := \sigma_i^{(1)}\tau_i^{(s-1)}, \quad \sigma_i'^{(s)} := \sigma_i'^{(1)}\tau_i'^{(s-1)}, \quad s = 2, 3, \cdots, n. \tag{E.19}$$

The constraints on the loop configurations require n copies of the Ising spins, $\sigma^{(s)}$ and $\sigma'^{(s)}$, on the boundary of the region A having the same domain wall configurations. Thus, they require the relative Ising spin $\tau_i^{(s)}$ and $\tau_i'^{(s)}$ having no domain wall on the boundary of A, i.e. pointing in the same direction. There are $(n-1)$ such constraints in $F_A^{(n)}(\mu)$, therefore $F_A^{(n)}(\mu) = nF_0(\mu) + (n-1)\Delta F(\mu)$, where ΔF is the excess free energy for aligning one copy of the τ spins on the boundary of A. Correspondingly, the Rényi entropy $S_A^{(n)} = \Delta F(0) + \Delta F(\mu)$.

The excess free energy has two contributions. The energetic part is always proportional to $|\partial A|$. The entropic part counts the loss of degrees of freedom due to spin aligning. In the ferromagnetic phase, the spins can fluctuate below the scale of correlation length ξ. Thus, $\Delta F \propto |\partial A|/\xi$ exhibits a strict area-law scaling. In the paramagnetic phase, the spins can both fluctuate freely above the scale of correlation length ξ. At the leading order, the free energy cost is proportional to $|\partial A|$. However, the aligned spin can fluctuate globally giving

rise to a subleading correction, i.e. $\Delta F = a|\partial A| - \log 2$. Thus, the subleading term sharply changes at the ferromagnetic transition.

The above analysis indicates the Rényi entropy exhibits an area-law scaling $S_A^{(n)} = a|\partial A| - \gamma^{(n)}$, and the topological term $\gamma^{(n)}$ distinguishes two phases of the effective spin model. When $\mu < \mu_c$, both spin models for σ and σ' are in the paramagnetic phase, giving rise to $\gamma^{(n)} = 2\log 2$. When $\mu > \mu_c$, the spin model for σ' (i.e. the loop model for h) is in the ferrmagnetic phase, reducing $\gamma^{(n)}$ to $\log 2$. The result holds for an arbitrary Rényi order n and also in the replica limit $n \to 1$. Hence, the TEE of the EFD state sharply changes from $2\log 2$ to $\log 2$ when $m\bar{m}$ condenses at $p_c^{(2)}$.

We make an important remark that the effective model for the Rényi-n entropy of the EFD is merely n decoupled loop models. The partition function $\mathcal{Z}^n(\mu) = (\text{tr}\,\rho^2)^n$. Therefore, the transition occurs at the same critical threshold $p_c^{(2)}$ regardless of n. This is fundamentally different from the transition in the n-th moment $\text{tr}\,\rho^n$ of the corrupted density matrix, which occurs at a different critical threshold $p_c^{(n)}$.

The Toric code state subject to Pauli-Y and Z errors can be similarly analyzed. These errors can induce a condensation of $f\bar{f}$ and $e\bar{e}$ in the EFD at the same critical threshold $p_c^{(2)}$. We also note that, anyon bound states $\alpha\bar{\alpha}$ and $\beta\bar{\beta}$ are mutual bosons and therefore can condense independently. When two types of anyons are condensed, e.g. $e\bar{e}$ and $m\bar{m}$, the rest one $f\bar{f}$ is also condensed as $e \times m = f$. The resulting EFD no longer contains condensed loop objects and will exhibit a vanishing TEE.

E.2 Mapping decoherence-induced phases to boundary anyon condensates

In this section, we map the decoherence-induced phases in the EFD to the boundary phases of a topologically ordered system. In Sec. E.2, we start with the path integral formulation of the EFD state. In Sec. E.2, we map the decoherence-induced phases to the boundary phases of topologically ordered systems. In particular, we establish the classification scheme for the possible phases in abelian topological order subject to incoherent errors. In Sec. E.2, we carry out the classification in three examples, the Toric code, double semion, and $\nu = 1/3$ Laughlin state with incoherent errors. The results are summarized in Table I of the main text. Section E.2 generalizes the field theory description for the second moment to the n-th moment $\text{tr}\,\rho^n$. We remark that, for abelian topological order with incoherent errors, the number of possible phases is independent of n. The possible phases in the EFD have one-to-one correspondence to that in the replica limit $n \to 1$.

Path integral formulation of the EFD

Here, we develop a path integral formulation of the EFD $|\rho\rangle\!\rangle$. The double ground state $|\Psi_0\rangle \otimes |\Psi_0^*\rangle$ in the EFD can be prepared using an infinite imaginary time evolution from an

arbitrary state, which is equivalently a Euclidean path integral in spacetime region $\tau < 0$. The wavefunction component at $\tau = 0$ can be formally written as

$$\mathcal{Z}_{\tau<0}[\varphi, \bar{\varphi}] := \big(\langle\varphi| \otimes \langle\bar{\varphi}| \big)\big(|\Psi_0\rangle \otimes |\Psi_0^*\rangle \big) = \int\limits_{(\varphi', \bar{\varphi}')|_{\tau=0^-}=(\varphi, \bar{\varphi})} \mathcal{D}(\varphi', \bar{\varphi}')e^{-\mathcal{S}(\varphi')-\mathcal{S}^*(\bar{\varphi}')} , \quad \text{(E.20)}$$

where φ and $\bar{\varphi}$ are the dynamical variables in the ket and bra Hilbert space, the path integral is defined in the past spacetime region $\tau < 0$, $\mathcal{S}(\varphi')$ and $\mathcal{S}^*(\bar{\varphi}')$ are a pair of conjugate Euclidean actions that yield the ground states $|\Psi_0\rangle$ and $|\Psi_0^*\rangle$, respectively. The EFD $|\rho\rangle\!\rangle$ is then obtained by turning on the error channel which couples the field φ and $\bar{\varphi}$ at $\tau = 0$ time slice locally [illustrated in Fig. 1(b) of the main text].

The norm $\langle\!\langle\rho|\rho\rangle\!\rangle$ is accordingly written as a Euclidean path integral in the entire spacetime, i.e. two path integrals in the future ($\tau > 0$) and past ($\tau < 0$) glued at $\tau = 0$:

$$\langle\!\langle\rho|\rho\rangle\!\rangle = \int \mathcal{D}(\varphi_p, \bar{\varphi}_p, \varphi_f, \bar{\varphi}_f) \, \mathcal{Z}_{\tau>0}[\varphi_f, \bar{\varphi}_f]\mathcal{Z}_{\tau<0}[\varphi_p, \bar{\varphi}_p]e^{-\mathcal{S}_{int}(\varphi_f, \bar{\varphi}_f, \varphi_p, \bar{\varphi}_p)}, \quad \text{(E.21)}$$

where $\varphi_{f(p)}$ and $\bar{\varphi}_{f(p)}$ denote the future (past) field variables at the time slice $\tau = 0^+$ ($\tau = 0^-$). The future and past fields are coupled by the error channel, and the coupling is formally written as

$$e^{-\mathcal{S}_{int}(\varphi_f, \bar{\varphi}_f, \varphi_p, \bar{\varphi}_p)} = \langle\!\langle\varphi_f, \bar{\varphi}_f|\mathcal{N}^\dagger\mathcal{N}|\varphi_p, \bar{\varphi}_p\rangle\!\rangle .$$

In the absence of errors, $\mathcal{N} = \mathbb{I}$ and $e^{-\mathcal{S}_{int}} = \delta_{\varphi_p, \varphi_f}\delta_{\bar{\varphi}_p, \bar{\varphi}_f}$ becomes a constraint. We further remark that individual Kraus operators and $\mathcal{N}$ are generally non-Hermitian. However, $\mathcal{S}_{int}$ only contains terms determined by the Hermitian combination $\mathcal{N}^\dagger\mathcal{N}$, which guarantees $\langle\!\langle\rho|\rho\rangle\!\rangle$ being a real number.

Mapping to (1+1)D boundary phases

In this subsection, we take advantage of the path-integral formulation and work with the topological quantum field theory (TQFT) describing the long-distance physics of topological orders. The invariance of TQFT under the $\pi/2$ spacetime rotation allows mapping decoherence-induced phases in the EFD to $(1+1)$D quantum phases on the edge of topologically ordered systems. Here, we consider specifically the abelian topological order described by the Chern-Simons (CS) theory. In the case of incoherent errors, we carry out a classification of the possible decoherence-induced phases using the effective theory on the edge. We demonstrate our general ideas with two concrete examples, the Toric code and double semion, and find five phases in each model. The possible phases in the case of coherent errors are also commented.

We consider the EFD for the Abelian topologically ordered ground state subject to incoherent errors. The ground state $|\Psi_0\rangle$ is described by a $U(1)^M$ Chern-Simons theory with the following Lagrangian

$$\mathcal{L}_{CS}[a] = \frac{1}{4\pi} \sum_{I,J=1}^{M} K_{IJ} \, a^I \wedge \mathrm{d}a^J + \cdots , \quad \text{(E.22)}$$

where K is a symmetric $M \times M$ integer matrix and $a^{I=1,2,...,M}$ are the $U(1)$ gauge fields, the ellipsis denotes parts that involve matter fields [218, 268, 92, 267]. Matter fields are gapped and do not enter the dynamics at long distances, yet, they are necessary in giving rise to the anyonic excitations. Accordingly, $|\Psi_0^*\rangle$ carries the conjugate topological order and is described by the same Lagrangian except that the K-matrix has an additional minus sign. To better distinguish them, we use $\bar{a}^{I=1,2,...,M}$ to denote the gauge fields for $|\Psi_0^*\rangle$. We can combine these two parts and write the path integral $\mathcal{Z}_{\tau<0}$ or $\mathcal{Z}_{\tau>0}$ in terms of the following Lagrangian

$$\mathcal{L}_{CS}[\mathbf{a}] = \frac{1}{4\pi} \sum_{I,J=1}^{2M} \mathbb{K}_{IJ} \, \mathbf{a}^I \wedge d\mathbf{a}^J + \cdots , \tag{E.23}$$

where $\mathbb{K} = K \oplus (-K)$, and $\mathbf{a} = [a, \bar{a}]^T$ is a $2M$ component vector of the gauge fields in the Hilbert space $\mathcal{H} \otimes \mathcal{H}$.

Studying the decoherence-induced phases and the potential phase transitions in the EFD in the current form is not convenient. On one hand, in general, anyonic excitations created by local errors explicitly involve matter fields and are complicated to analyze. On the other hand, the transition, which happens at the temporal interface, is different from a ground state problem and largely unexplored.

These technical difficulties necessitate our following trick. We perform a spacetime rotation to exchange the imaginary time τ and the spatial coordinate x [Fig. 1(c) of the main text], i.e.,

$$\tau \to -x , \quad x \to \tau , \quad y \to y , \tag{E.24}$$

where x, y denote the spatial coordinates. The rotation turns the temporal interface at $\tau = 0$ into a spatial one at $x = 0$. The original path integral (E.21) can be formally rewritten as

$$\langle\!\langle \rho | \rho \rangle\!\rangle = \int \mathcal{D}(\varphi_L, \bar{\varphi}_L, \varphi_R, \bar{\varphi}_R) \, \mathcal{Z}_{x>0}[\varphi_R, \bar{\varphi}_R] \mathcal{Z}_{x<0}[\varphi_L, \bar{\varphi}_L] e^{-\tilde{S}_{int}(\varphi_R, \bar{\varphi}_R, \varphi_L, \bar{\varphi}_L)} ,$$

where $\mathcal{Z}_{x<0}$, obtained by rotating $\mathcal{Z}_{\tau<0}$, is the path integral on the left side of the spatial interface $x = 0^-$, and $(\varphi_L, \bar{\varphi}_L)$ specify the value of the fields at the spatial interface. The meaning of $\mathcal{Z}_{x>0}$ and $(\varphi_R, \bar{\varphi}_R)$ is similar. $\tilde{S}_{int}$ describes the coupling between the two half systems at the spatial interface and generally takes a different form from the original one $\mathcal{S}_{int}$.

After the rotation, the path integral is translationally invariant in the new time direction and describes the norm of a $(2+1)$D ground state [Fig. 1(c) of the main text]. In the rotated picture, the decoherence-induced phases correspond to the $(1+1)$D phases on the 1D defect at $x = 0$.

The Lagrangian that describes the 1D defect has three contributions

$$\mathcal{L} = \mathcal{L}_0 + \mathcal{L}_1 + \mathcal{L}_{\mathcal{N}}, \tag{E.25}$$

where $\mathcal{L}_0$ describes the low energy edge excitations for the $(2+1)D$ theory in the region $x > 0$ and $x < 0$. The interaction on the defect is derived from $\tilde{S}_{int}$ and contains two parts.

The first part originates from the definition of path integral and couples degrees of freedom on the left and the right given by $\mathcal{L}_1$, which is present even in the absence of a quantum channel. The second part $\mathcal{L}_\mathcal{N}$ is introduced by the quantum channel. In what follows, we explicitly write down the three terms in the Lagrangian and analyze the possible phases.

We start with the low energy edge theory $\mathcal{L}_0$ for the CS theory in the bulk. We consider how the path integral for the past $\mathcal{Z}_{\tau<0}$ changes under the rotation:

- Originally, $\mathcal{Z}_{\tau<0}[\varphi_p, \bar{\varphi}_p]$ describes the path integral that prepares the ground state of a system on a whole plane, where $\varphi_p, \bar{\varphi}_p$ specifies the component of the wavefunction. Note that φ_p and $\bar{\varphi}_p$ includes both the CS gauge fields and the matter fields, and thus they are complicated to deal with.

- The spacetime rotation transforms it into $\mathcal{Z}_{x>0}[\varphi_R, \bar{\varphi}_R]$, a path integral defined on the half-space but the entire time domain, and $\varphi_R, \bar{\varphi}_R$ specifies the boundary value of the fields. The bulk part of the path integral contains the same CS action as that before the rotation and the part involving matter fields. The boundary has a simple description in terms of compact bosons, which is the main reason why the rotation trick can be useful.

- From now on, we will replace φ_R and $\bar{\varphi}_R$ by the compact boson fields $\phi_R, \bar{\phi}_R$, which correspond to the bulk gauge fields $a, \bar{a}$. Then, the low-energy dynamics of the boundary of the CS theory is governed by the following effective Lagrangian

$$\mathcal{L}_R[\Phi_R] = \frac{1}{4\pi} \sum_{I,J=1}^{2M} -\mathbb{K}_{IJ}\mathrm{i}\partial_\tau \Phi_R^I \partial_y \Phi_R^J - \mathbb{V}_{IJ}\partial_y \Phi_R^I \partial_y \Phi_R^J, \tag{E.26}$$

where $\Phi_R := [\phi_R, \bar{\phi}_R]$, $\mathbb{K}$ is the same K-matrix as the one for the bulk CS action, and $\mathbb{V}$ is a positive semi-definition matrix that determines the velocity of the boson fields. The path integral with fixed boundary values of the boson fields is then determined by $\mathcal{L}_R[\Phi_R]$ classically:

$$\mathcal{Z}_{x<0}[\Phi_R] = \exp\left(-\int \mathrm{d}\tau\mathrm{d}y \mathcal{L}_R[\Phi_R]\right). \tag{E.27}$$

The transformation of the path integral for the future $\mathcal{Z}_{\tau>0}$ can be analyzed similarly. The result is related to what we have obtained above by a spatial reflection

$$\mathcal{L}_L[\Phi_L] = \frac{1}{4\pi} \sum_{I,J=1}^{2M} \mathbb{K}_{IJ}\mathrm{i}\partial_\tau \Phi_L^I \partial_y \Phi_L^J - \mathbb{V}_{IJ}\partial_y \Phi_L^I \partial_y \Phi_L^J,$$

where $\Phi_L := [\phi_L, \bar{\phi}_L]$, and the minus sign in front of the K-matrix comes from the spatial reflection. The path integral $\mathcal{Z}_{x>0}[\Phi_L]$ can also be determined classically

$$\mathcal{Z}_{x>0}[\Phi_L] = \exp\left(-\int \mathrm{d}\tau\mathrm{d}y \mathcal{L}_L[\Phi_L]\right). \tag{E.28}$$

We combine the low-energy excitations from the left and the right and obtain the Lagrangian describing the edge of the quadruple topological order

$$\mathcal{L}_0[\phi] = \frac{1}{4\pi} \sum_{I,J} \mathbb{K}^{(2)}_{IJ} \mathrm{i}\partial_\tau \phi^I \partial_y \phi^J - \mathbb{V}^{(2)}_{IJ} \partial_y \phi^I \partial_y \phi^J \,, \tag{E.29}$$

where the $4M \times 4M$ K-matrix $\mathbb{K}^{(2)} = \mathbb{K} \oplus \mathbb{K}$, velocity matrix $\mathbb{V}^{(2)} = \mathbb{V} \oplus \mathbb{V}$, and $\phi := [\bar{\phi}_R, \phi_R, \phi_L, \bar{\phi}_L]$.

Next, we discuss the interaction in the effective theory. The first part $\mathcal{L}_1$ is associated with the definition of path integral and couples ϕ_L to ϕ_R and $\bar{\phi}_L$ to $\bar{\phi}_R$. It leads to a gapped phase of the defect in the absence of errors. The second part $\mathcal{L}_{\mathcal{N}}$ is introduced by the error channel. It couples the bosonic fields from the same copy of the density matrix (or equivalently EFD), namely ϕ_s to $\bar{\phi}_s$ for $s = L, R$.

To explicitly write down the interaction in terms of the compact bosons, we first list the excitations in the effective theory $\mathcal{L}_0$. The excitations are labeled by integer vectors $\boldsymbol{l}_\alpha$ and are created by $e^{\mathrm{i}\boldsymbol{l}_\alpha^T \cdot \phi}$. They have anyonic statistics, and the braiding of two anyons $\boldsymbol{l}_\alpha$ and $\boldsymbol{l}_\beta$ yields a phase

$$\theta_{\alpha\beta} = 2\pi \boldsymbol{l}_\alpha^T (\mathbb{K}^{(2)})^{-1} \boldsymbol{l}_\beta. \tag{E.30}$$

We remark that, in general, a single anyon cannot be created using a local operator. Instead, a pair of anyon α and its antiparticle α' can be created using a local operator, which is described by $\Psi_\Lambda := e^{\mathrm{i}(\mathbb{K}^{(2)}\Lambda)^T \cdot \phi}$ with Λ being an integer vector. Such excitation has trivial braiding with other excitations, i.e. $\theta_{\alpha, \mathbb{K}^{(2)}\Lambda} = 0 \mod 2\pi, \forall \alpha$.

Furthermore, the form of the interaction is limited by the global $\mathcal{G}^{(2)} = \mathbb{Z}_2 \times \mathbb{Z}_2^{\mathbb{H}}$ symmetry of 1D defect. The first $\mathbb{Z}_2$ is an anti-unitary symmetry generated by the hermitian conjugation in the double Hilbert space. The path integral represents the norm of the EFD, which is a real number. Thus, the effective theory is invariant under the transformation

$$\phi_L^I \leftrightarrow \phi_R^I, \quad \bar{\phi}_L^I \leftrightarrow \bar{\phi}_R^I. \tag{E.31}$$

In addition, the EFD represents the density matrix, which is hermitian in the original Hilbert space. Thus, edge theory exhibits another anti-unitary $\mathbb{Z}_2^{\mathbb{H}}$ symmetry due to the hermiticity of the density matrix, which acts as

$$\phi_s^I \leftrightarrow \bar{\phi}_s^I, \quad s = L, R. \tag{E.32}$$

We remark that the K-matrix $\mathbb{K}^{(2)}$ flips the sign under the anti-unitary symmetry, however, the Lagrangian $\mathcal{L}_0$ is invariant as the minus sign cancels that from the imaginary identity.

We are now ready to explicitly write down the interaction in terms of edge excitations. The first part $\mathcal{L}_1$ from the definition of path integral can be written in terms of the back-scattering between the left and the right fields. It is generally given by a hopping term between the left and the right

$$\sum_\Lambda \frac{B_\Lambda(y) e^{\mathrm{i}\theta(y)}}{2} \left(\Psi_{L,\Lambda}^\dagger \Psi_{R,\Lambda} + \bar{\Psi}_{R,\Lambda}^\dagger \bar{\Psi}_{L,\Lambda} \right) + h.c., \tag{E.33}$$

where $\Psi_{L,\Lambda} := e^{i(K\Lambda)^T \phi_L}$, $\Psi_{R,\Lambda} := e^{-i(K\Lambda)^T \phi_R}$, $\bar{\Psi}_{L,\Lambda} := e^{i(-K\Lambda)^T \bar{\phi}_L}$, and $\bar{\Psi}_{R,\Lambda} := e^{i(K\Lambda)^T \bar{\phi}_R}$ are local operators on the edge, Λ is a M-component integer vector, the real coefficient B_Λ and phase factor θ have spatial dependence in general. In terms of the compact boson fields, the back-scattering takes the form

$$\mathcal{L}_1 = \sum_\Lambda B_\Lambda \left[\cos \left(\sum_{I=1}^M (K\Lambda)_I (\phi_L^I + \phi_R^I) + \theta \right) + \cos \left(\sum_{I=1}^M (K\Lambda)_I (\bar{\phi}_L^I + \bar{\phi}_R^I) + \theta \right) \right]. \quad \text{(E.34)}$$

We remark that the coefficients for two cosine terms are forced to the same real number due to the global symmetry $\mathcal{G}^{(2)}$. With large coefficients, such cosine terms tend to pin the bosonic fields $\phi + \bar{\phi}$ and lead to a gapped phase of the defect without any error channel. These interaction terms only create anyon bound states on the left and the right in the form $\alpha_L \alpha_R' = e^{i\mathbf{l}^T \cdot (\phi_L + \phi_R)}$ and $\bar{\alpha}_L \bar{\alpha}_R' = e^{-i\mathbf{l}^T \cdot (\bar{\phi}_L + \bar{\phi}_R)}$.

The second part $\mathcal{L}_\mathcal{N}$ of the interaction is introduced by the quantum channel and couples the fields from the same copy of the density matrix. For incoherent error channels, before the rotation, only anyon bound states $\alpha\bar{\alpha}$ are created in the EFD. In the rotated picture, the quantum channel creates excitations $\alpha_s \bar{\alpha}_s = e^{i\mathbf{l}^T \cdot (\phi_s - \bar{\phi}_s)}$. At the 1D defect, it corresponds to the cosine term

$$\mathcal{L}_\mathcal{N} = \sum_\Lambda C_\Lambda \sum_{s=L,R} \cos \left(\sum_{I=1}^M (K\Lambda)_I (\phi_s^I - \bar{\phi}_s^I) \right), \quad \text{(E.35)}$$

where C_Λ is a real coefficient with spatial dependence. We remark that the coefficient of the different cosine terms for $s = L, R$ are the same due to the $\mathbb{Z}_2$ symmetry.

The possible phases of the defect are classified by the inequivalent ways of gapping out $\mathcal{L}_0$ in Eq. (E.29) by condensing bosonic excitations. For abelian topological order, the bosonic objects form a group, dubbed the Lagrangian subgroup $\mathcal{M}$ [158, 20]. Thus, the phases of abelian topological order subject to incoherent errors are classfied by the subgroup $\mathcal{M}$ that satisfying the following criteria:

1. $e^{i\theta_{mm'}} = 1, \forall \mathbf{m}, \mathbf{m'} \in \mathcal{M}$;

2. $\forall \mathbf{l} \notin \mathcal{M}, \exists \mathbf{m}$ s.t. $e^{i\theta_{ml}} \neq 1$;

3. $\forall \mathbf{m} \in \mathcal{M}, g\mathbf{m}g^{-1} \in \mathcal{M}, \forall g \in \mathcal{G}^{(2)}$;

4. (Incoherent error) $[\mathbf{1}, \mathbf{1}, -\mathbf{1}, -\mathbf{1}]^T \cdot \mathbf{m} = 0 \mod \mathbb{K}^{(2)}\Lambda, \forall \mathbf{m} \in \mathcal{M}$,

where Λ is a $4M$-component integer vector, $\mathbf{1}$ is an M-component vector with each element being unity. Here, the third criterion originates from the symmetry constraints, i.e. the excitations related by symmetry transformations must condense simultaneously. The last criterion is due to incoherent errors. The interaction on the edge only creates anyon bound states $\alpha_L \bar{\alpha}_L$, $\alpha_R \bar{\alpha}_R$, $\alpha_L \alpha_R'$, $\bar{\alpha}_L \bar{\alpha}_R'$ and their fusion results. Therefore, the condensed objects satisfy the last criterion.

In the case of coherent errors, the phases are still classified by the Lagrangian subgroup. However, since the Kraus operators can, for example, create anyon excitation α and $\bar{\alpha}$ in a single copy, the condensed objects need not to satisfy the last criterion. Correspondingly, in the Lagrangian, the coherent errors can introduce the cosine terms, $\cos\big((K\Lambda)^T \cdot \phi_s\big)$ and $\cos\big((K\Lambda)^T \cdot \bar{\phi}_s\big)$, which solely depends on the compact boson in an individual copy of the topological order. This can possibly lead to additional decoherence-induced phases.

Each edge condensate corresponds to a distinct phase of the EFD, and its condensed objects also determine the capability of encoding information in the error-corrupted state. In the main text, we mention that the logical operator $W_{\alpha\bar{\alpha}}(\ell)$ can no longer encode quantum information in the condensate of anyon bound state $\alpha\bar{\alpha}$ in the EFD, which is equivalent to condensing $\alpha_s\bar{\alpha}_s$ with $s = L, R$ in the (1+1)D theory of the defect. Hence, examining whether $\alpha_s\bar{\alpha}_s$ is condensed on the edge can determine the encoding properties in the error-corrupted state.

Examples

Here, we classify the possible phases by enumerating the Lagrangian subgroups in three examples, 2D Toric code, double semion model, and $\nu = 1/3$ Laughlin state, subject to incoherent errors. We comment on the information encoding in each phase. The results are summarized in Table I of the main text.

Example 1: Toric code.— The first example we consider is the 2D Toric code subject to incoherent errors. We find five distinct gapped phases [see Table I [2]].

To start with, the low energy excitations in 2D Toric code are described by the CS theory with K-matrix

$$K_{TC} = \begin{pmatrix} 0 & 2 \\ 2 & 0 \end{pmatrix}. \tag{E.36}$$

The Toric code has four superselection sectors: $1, e, m, f$. Here, e and m are self-boson and exhibit mutual semionic statistics. The fermion f is a composite object of e and m. These anyonic quasiparticles are labeled by integer vectors

$$\boldsymbol{l}_e = \begin{pmatrix} 1 \\ 0 \end{pmatrix}, \quad \boldsymbol{l}_m = \begin{pmatrix} 0 \\ 1 \end{pmatrix}, \quad \boldsymbol{l}_f = \begin{pmatrix} 1 \\ 1 \end{pmatrix}. \tag{E.37}$$

The first gapped phase is achieved when no error is present. In this case, the definition of path integral introduces the cosine terms in Eq. (E.34)

$$\mathcal{L}_1 = \sum_{I=1,2} B_I \bigg[\cos \big(2(\phi_L^I + \phi_R^I) + \theta \big) + (\phi_s \leftrightarrow \bar{\phi}_s) \bigg] + \cdots . \tag{E.38}$$

Here, the ellipses represent the less relevant terms. With sufficiently large coefficients B_I, these cosine terms can induce an edge condensate of $e_L e_R, \bar{e}_L \bar{e}_R, m_L m_R$, and $\bar{m}_L \bar{m}_R$ (Phase I

---
[2]Here and in the following, Table I refers to the table in the main text.

in Table I). The corrupted density matrix in this phase can encode quantum information because $\alpha_s \bar{\alpha}_s$ is not condensed.

The incoherent error channel can induce distinct edge phases. Here, we have three cosine terms in the form of Eq. (E.35)

$$
\begin{aligned}
\mathcal{L}_{\mathcal{N},e} &= C_e \sum_{s=L,R} \cos\left(2(\boldsymbol{l}_e^T \cdot \phi_s - \boldsymbol{l}_e^T \cdot \bar{\phi}_s)\right), \\
\mathcal{L}_{\mathcal{N},m} &= C_m \sum_{s=L,R} \cos\left(2(\boldsymbol{l}_m^T \cdot \phi_s - \boldsymbol{l}_m^T \cdot \bar{\phi}_s)\right), \\
\mathcal{L}_{\mathcal{N},f} &= C_f \sum_{s=L,R} \cos\left(2(\boldsymbol{l}_f^T \cdot \phi_s - \boldsymbol{l}_f^T \cdot \bar{\phi}_s)\right),
\end{aligned}
\tag{E.39}
$$

which are generated by the incoherent channels that create e, m, and f, respectively. With a sufficiently large coefficient, any one of three cosine terms can develop a classical value leading to a condensate of $\alpha_s \bar{\alpha}_s$ with $\alpha = e, m, f$, which corresponds to Phase II-IV in Table I, respectively. In these phases, the remaining logical operators mutually commute, and the corrupted state is a classical memory.

Finally, when two cosine terms develop a classical value, the remaining one also achieves a classical value (Phase V in Table I). Here, the corrupted state is a trivial state, and one cannot encode any information.

Allowing coherent errors may lead to additional gapped phases beyond the above five possibilities. For example, the amplitude-damping channel

$$
\mathcal{K}_{1,i} = \frac{1+\sqrt{1-\kappa}}{2}\mathbb{I} + \frac{1-\sqrt{1-\kappa}}{2}Z_i, \quad \mathcal{K}_{2,i} = \frac{\sqrt{\kappa}}{2}(X_i + \mathrm{i}Y_i),
\tag{E.40}
$$

which can generate $e_s, \bar{e}_s, m_s, \bar{m}_s, e_s\bar{m}_s, m_s\bar{e}_s$ for $s = L, R$ in the effective theory. These anyons cannot be created by incoherent errors; condensing a subset of them can lead to distinct phases. This possibly leads to additional phases of the 1D defect labeled by the Lagrangian subgroups with following generators:

- $e_s, \bar{e}_s$ for $s = L, R$;

- $m_s, \bar{m}_s$ for $s = L, R$;

- $e_s\bar{m}_s, m_s\bar{e}_s$ for $s = L, R$.

However, as the coherent channel creates all these anyons together with the anyon bound state $\alpha_s\bar{\alpha}_s$, these possible phases will compete. It requires numerical simulation to determine which anyon condenses at low energy. It remains open whether a specific coherent error channel can realize any of these phases.

We make a few remarks. First, the phase with e or m anyon condensed in individual copies can be obtained by an imaginary time evolution of the Toric code ground state. For example, $|\Psi_0\rangle \rightarrow e^{\mu \sum_i Z_i} |\Psi_0\rangle$ can realize the edge condensate of e_s and $\bar{e}_s$. Second, the above

three phases are studied in the context of 1D defect phases in double Toric code and are referred to as the "cut-open" and "SPT" boundary [166].

Example 2: Double semion.— The second example we consider is the double semion model subject to incoherent errors [159]. Again, we enumerate the possible Lagrangian subgroups that characterize the distinct phases. We find five phases summarized in Table I.

The low-energy theory for double semion topological order is the abelian CS theory with K-matrix

$$K_{DS} = \begin{pmatrix} 2 & 0 \\ 0 & -2 \end{pmatrix}. \tag{E.41}$$

The double semion model has four superselection sectors: $1, m_a, m_b, b$, where m_a is a semion, m_b is an anti-semion, and the boson b is a composite object of m_a and m_b. The semion m_a and anti-semion m_b are mutual boson. These anyons are characterized by the integer vectors

$$\boldsymbol{l}_{m_a} = \begin{pmatrix} 1 \\ 0 \end{pmatrix}, \quad \boldsymbol{l}_{m_b} = \begin{pmatrix} 0 \\ 1 \end{pmatrix}, \quad \boldsymbol{l}_b = \begin{pmatrix} 1 \\ 1 \end{pmatrix}. \tag{E.42}$$

The double semion model on the torus has a four-fold degenerate ground state that can encode two logical qubits. The logical operators are the loop operators $w_\alpha(\ell)$ transporting $\alpha = m_a, m_b$ along two inequivalent large loops $\ell = \ell_1, \ell_2$. Distinct from the case of Toric code, the operators along different loops, $w_\alpha(\ell_1)$ and $w_\alpha(\ell_2)$ for $\alpha = m_a, m_b$, anti-commute due to the anyon self-statistics and therefore serve as Pauli-X and Z operators for a logical qubit.

The first gapped phase (Phase I in Table I) of the defect is realized when no error is present. The backscattering term $\mathcal{L}_1$ condenses the anyon bound states $\alpha_L \alpha'_R$ and $\bar{\alpha}_L \bar{\alpha}'_R$ for $\alpha = m_a, m_b, b$. This phase can encode two qubits of quantum information.

The incoherent channel in the double semion model can introduce the following cosine terms:

$$\mathcal{L}_{\mathcal{N},m_a} = C_{m_a} \sum_{s=L,R} \cos\left(2(\boldsymbol{l}_{m_a}^T \cdot \phi_s - \boldsymbol{l}_{m_a}^T \cdot \bar{\phi}_s)\right),$$

$$\mathcal{L}_{\mathcal{N},m_b} = C_{m_b} \sum_{s=L,R} \cos\left(2(\boldsymbol{l}_{m_b}^T \cdot \phi_s - \boldsymbol{l}_{m_a}^T \cdot \bar{\phi}_s)\right), \tag{E.43}$$

$$\mathcal{L}_{\mathcal{N},b} = C_b \sum_{s=L,R} \cos\left(2(\boldsymbol{l}_b^T \cdot \phi_s - \boldsymbol{l}_b^T \cdot \bar{\phi}_s)\right),$$

which creates anyon bound states $\alpha_s \bar{\alpha}_s$ for $\alpha = m_a, m_b, b$, respectively. Condensing each one of these terms induces Phase II-IV in Table I, respectively. In Phase II [III], one can encode information in $w_{m_a}(\ell)$ [$w_{m_b}(\ell)$] for $\ell = \ell_1, \ell_2$. These logical operators do not mutually commute and therefore can encode one qubit of quantum information. In Phase IV, the corrupted state can still encode one qubit of quantum information, despite that w_{m_a} and w_{m_b} are identified due to the condensation of $b_s \bar{b}_s$. Condensing two terms in Eq. (E.43) indicates the third is condensed and leads to Phase V, which cannot encode information.

Introducing coherent errors can potentially realize an additional phase by condensing the boson in individual copies, b_s and $\bar{b}_s$. Again, designing a specific coherent error channel to possibly realize this phase is left for future study.
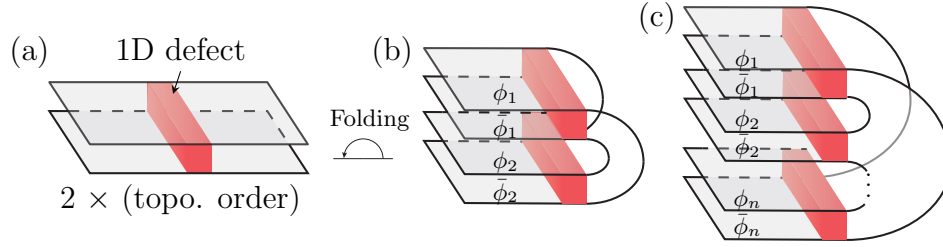
Figure E.1: (a) The path integral represents the norm of the ground state of double 2D topological order with 1D defect (red region). (b) Folding the double topological order around the 1D defect results in quadruple topological order with a 1D boundary. The red regions represent the coupling $\mathcal{L}_\mathcal{N}$ induced by the quantum channel. The couplings between ϕ_1 and $\bar\phi_2$ (also $\bar\phi_1$ and ϕ_2) are denoted by $\mathcal{L}_1$ inherited from the definition of path integral. (c) The edge theory associated with the n-th moment $\operatorname{tr}\rho^n$ of the density matrix. The generalized swap interaction $\mathcal{L}_1^{(n)}$ couples the compact bosons in the neighboring copies, i.e. $\bar\phi_s$ and ϕ_{s+1} for $s = 1, 2, \cdots, n$.

Example 3: $\nu = 1/3$ Laughlin state.— The third example is $\nu = 1/3$ Laughlin state [155] with incoherent errors. In this case, we find two phases summarized in Table I.

The low-energy excitations in the Laughlin state is described by the abelian CS theory with K-matrix $K_{1/3} = (3)$. It contains three superselection sectors $\{1, \eta, \eta^2\}$. η and η^2 are the quasiparticle and quasihole, and they are labeled by the charge vector $\boldsymbol{l}_\eta = (1)$ and $\boldsymbol{l}_{\eta^2} = (2)$ and carry charge $e/3$ and $-e/3$, respectively.

There is only one type of incoherent channel; its Kraus operators create a pair of quasiparticle and quasihole. When the error is below the threshold, the corrupted state is a quantum memory characterized by the Lagrangian subgroup generated by $\eta_L \eta_R^2$ and $\bar\eta_L \bar\eta_R^2$ (Phase I in Table I). When error proliferates, we obtain a trivial phase with a subgroup generated by $\eta_L \bar\eta_L$ and $\eta_R \bar\eta_R$ (Phase II in Table I).

Generalization to the n-th moment

So far, the analysis focuses on the distinct phases in the EFD, which pertains to analyzing the second moment of the density matrix, i.e. the norm of the EFD $\langle\!\langle \rho | \rho \rangle\!\rangle = \operatorname{tr}\rho^2$. In this subsection, we generalize the problem to the n-th moment $\operatorname{tr}\rho^n$ and map the decoherence-induced phases to $(1+1)$D boundary phases.

Before discussing the n-th moment, we develop an equivalent formulation of the second moment $\operatorname{tr}\rho^2$. The phases of the $(1+1)$D defect can be converted to the $(1+1)$D edge phases by folding around the defect as shown in Fig. E.1(b) [25, 133]. In the folded picture, we have four copies of the topological order. On the edge, we relabel the bosonic fields as

$$\phi := [\bar\phi_R, \phi_R, \phi_L, \bar\phi_L] = [\phi_1, \bar\phi_1, \phi_2, \bar\phi_2], \tag{E.44}$$

where $\phi_{1(2)}$ and $\bar{\phi}_{1(2)}$ denote the fields associated with the copy-1(2) of the density matrix.

The path integral describing the ground state of quadruple topological order with an edge corresponds to an overlap in the quadruple Hilbert space $\mathcal{H}^{\otimes 4}$ before the rotation

$$\operatorname{tr}\rho^2 = \langle\!\langle \mathbb{C}^{(2)}|\, (|\rho\rangle\!\rangle \otimes |\rho\rangle\!\rangle) := \int \mathcal{D}(\varphi_1, \varphi_2)\,(\langle\varphi_1| \otimes \langle\varphi_2|) \otimes |\rho\rangle\!\rangle\,(\langle\varphi_2| \otimes \langle\varphi_1|) \otimes |\rho\rangle\!\rangle, \quad \text{(E.45)}$$

where $\langle\!\langle \mathbb{C}^{(2)}|$ is a "swap" reference state that couples the fields in the ket and bra Hilbert space of the different copies of the EFD.

The overlap is readily generalized to describe the n-th moment $\operatorname{tr}\rho^n$. Here, in $2n$ copies of the Hilbert space $\mathcal{H}^{\otimes 2n}$, we consider

$$\operatorname{tr}\rho^n = \langle\!\langle \mathbb{C}^{(n)}|\, (|\rho\rangle\!\rangle^{\otimes n}) := \int \mathcal{D}(\varphi_1, \varphi_2, \cdots, \varphi_n) \prod_{s=1}^{n} (\langle\varphi_s| \otimes \langle\varphi_{s+1}|) \otimes |\rho\rangle\!\rangle, \quad \text{(E.46)}$$

where $\varphi_{n+1} := \varphi_1$, and $\langle\!\langle \mathbb{C}^{(n)}|$ is a generalized swap reference state.

We can similarly develop a path integral formulation of the overlap. In the rotated picture, it corresponds to the ground state of $2n$ copies of the topological order with an $(1+1)$D edge. The effective edge theory also contains three parts

$$\mathcal{L}^{(n)} = \mathcal{L}_0^{(n)} + \mathcal{L}_1^{(n)} + \mathcal{L}_{\mathcal{N}}^{(n)}. \quad \text{(E.47)}$$

The first part $\mathcal{L}_0^{(n)}$ describes the low-energy excitations in $2n$ copies of the topological order

$$\mathcal{L}_0^{(n)}[\phi] = \frac{1}{4\pi} \sum_{I,J} \mathbb{K}_{IJ}^{(n)} i\partial_\tau \phi^I \partial_y \phi^J - \mathbb{V}_{IJ}^{(n)} \partial_y \phi^I \partial_y \phi^J \quad \text{(E.48)}$$

where the compact bosonic field $\phi := [\phi_1, \bar{\phi}_1, \phi_2, \bar{\phi}_2, \cdots, \phi_n, \bar{\phi}_n]$ is a $2nM$-component vector, $\mathbb{K}^{(n)} = [K \oplus (-K)]^{\oplus n}$, and $\mathbb{V}^{(n)} = V^{\oplus 2n}$. The second part $\mathcal{L}_1^{(n)}$ is the interaction introduced by the reference state, which takes a general form

$$\mathcal{L}_1^{(n)} = \sum_{\Lambda} B_\Lambda \sum_{s=1}^{n} \cos\left(\sum_I (K\Lambda)_I(\phi_s^I + \bar{\phi}_{s+1}^I) + \theta\right). \quad \text{(E.49)}$$

where $\bar{\phi}_{n+1} := \bar{\phi}_1$. The last part $\mathcal{L}_{\mathcal{N}}^{(n)}$ describes the error channel. For incoherent errors, we have

$$\mathcal{L}_{\mathcal{N}}^{(n)} = \sum_{\Lambda} C_\Lambda \sum_{s=1}^{n} \cos\left(\sum_I (K\Lambda)_I(\phi_s^I - \bar{\phi}_s^I)\right). \quad \text{(E.50)}$$

The edge theory exhibits a global symmetry $\mathcal{G}^{(n)} = \mathbb{Z}_n \times \mathbb{Z}_2^{\mathbb{H}}$. We note that the $\mathbb{Z}_n$ symmetry is a unitary symmetry generated by the cyclic permutation over n copies of the density matrix

$$\phi_s \leftrightarrow \phi_{s+1}, \quad \bar{\phi}_s \leftrightarrow \bar{\phi}_{s+1}. \quad \text{(E.51)}$$

In the case of $n = 2$, $\mathcal{G}^{(n)}$ reduces to $\mathcal{G}^{(2)}$ in Sec. E.2 as the permutation over two copies of the density matrix is a combination of the Hermitian conjugation of the EFD and that of the density matrix.

We remark that the incoherent errors can induce condensation of $\alpha_s \bar{\alpha}_s$ for $s = 1, 2, \cdots n$ on the edge. Since the different anyon bound states $\alpha_s \bar{\alpha}_s$ and $\beta_{s'} \bar{\beta}_{s'}$ are mutual bosons, different incoherent channels do not compete with each other. Thus, the number of possible condensates is independent of the replica index n, and so is the classification for abelian topological with incoherent errors. Hence, we expect each phase of $\operatorname{tr} \rho^2$ in Table I has a correspondence in the replica limit $n \to 1$.

Appendix F

Supplementary material for Chapter 7

F.1 Details of the mapping

In this section, we detail the mapping between the three diagnostics and observables in the statistical mechanical models.

Quantum relative entropy

We here explicitly show that the Rényi quantum relative entropy is related to the correlation function in the classical spin model. Specifically, we consider the relative entropy between the error corrupted ground state and an excited state $|\Psi_m\rangle := w_m(\mathcal{C})\,|\Psi_0\rangle$ with a pair of m-particles created at the end of path $\mathcal{C}$.

First, we write down the error corrupted state ρ_m in the loop representation

$$\rho_m = \frac{1}{2^N} \sum_g \text{sgn}\left(g_z, X^{\mathcal{C}}\right) g_z g_x e^{-\mu_x|g_x|-\mu_z|g_z|}. \tag{F.1}$$

where the commutation relation between the loop operator and the string operator is accounted by $\text{sgn}(g_z, X^{\mathcal{C}})$; the sign function equals $+1$ when g_z and $X^{\mathcal{C}}$ commute and -1 otherwise. The above expression allows one to write $\text{tr}\,\rho\rho_m^{n-1}$ as

$$\text{tr}\,\rho\rho_m^{n-1} = \frac{\mathcal{Z}_{n,x}}{2^{(n-1)N}} \sum_{\{g_z^{(s)}\}} \mathcal{O}_D^{(n)} e^{-H_{n,z}}, \tag{F.2}$$

where $\mathcal{O}_D^{(n)}$ denotes the product of sign functions in $n-1$ copies of ρ_m

$$\mathcal{O}_D^{(n)} = \text{sgn}\left(g_z^{(1)}, X^{\mathcal{C}}\right). \tag{F.3}$$

Here, we have used the constraint $g_z^{(1)} = \prod_{s=2}^n g_z^{(s)}$ for nonvanishing trace in the loop representation. Using this expression, the n-th Rényi relative entropy takes the form

$$D^{(n)}(\rho||\rho_m) = \frac{1}{1-n} \log\langle \mathcal{O}_D^{(n)}\rangle. \tag{F.4}$$
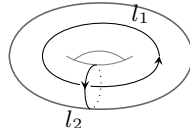
Our next step is to express the observable $\langle \mathcal{O}_D^{(n)} \rangle$ in terms of the Ising spins. In the spin model, the closed loop $g_z^{(1)}$ is identified with the domain wall of $\sigma_i^{(1)}$, and the Ising spins on two sides of $g_z^{(1)}$ anti-align. Thus, $\sigma_{i_l}^{(1)}$ and $\sigma_{i_r}^{(1)}$ on the two ends of the open string $\mathcal{C}$ is aligned if $g_z^{(1)}$ crosses $\mathcal{C}$ for even number of times and is anti-aligned otherwise. The parity of the crossing is exactly measured by the sign function $\text{sgn}(g_z^{(1)}, X^{\mathcal{C}})$. Hence, the observable $\langle \mathcal{O}_D^{(n)} \rangle$ maps to the correlation function

$$\langle \mathcal{O}_D^{(n)} \rangle = \langle \sigma_{i_l}^{(1)} \sigma_{i_r}^{(1)} \rangle . \tag{F.5}$$

Coherent information

We now develop a spin model description for the Rényi coherent information $I_c^{(n)}$ in Eq. (7.7). In the definition of coherent information, the system density matrix ρ_Q is the error corrupted state ρ in Sec. 7.3, and its n-th moment is mapped to the partition function of the $(n-1)$-flavor Ising model on the torus. Here, we show that the n-th moment of ρ_{RQ} maps to the partition function of the same model with defects (domain walls) inserted along large loops on the torus.

First, we write down the initial state of the system Q and the reference R. We consider two reference qubits and two logical qubits in the ground state subspace, and maximally entangle them in a Bell state. Let $s_l^{a=x,z}$ be the Pauli operator of two reference qubits, and $\bar{g}_{al}$ be the four logical operators

$$\bar{g}_{zl} := \prod_{\ell \in l} Z_\ell , \qquad \bar{g}_{xl} := \prod_{\ell \in l^*} X_\ell , \tag{F.6}$$

where $l = l_{1,2}$ and $l^* = l_{1,2}^*$ are on the original and dual lattice. We consider the Bell state prepared as the $+1$ eigenstate of stabilizers $\bar{g}_{zl} s_l^z$ and $\bar{g}_{xl} s_l^x$, and write the initial density matrix for the system and reference as

$$\rho_{0,RQ} = \prod_{l=l_1,l_2} \prod_{a=x,z} \frac{1 + \bar{g}_{al} s_l^a}{2} \prod_s \frac{1 + A_s}{2} \prod_p \frac{1 + B_p}{2} . \tag{F.7}$$

Here, we again work in the loop picture of $\rho_{0,RQ}$, and further factorize the density matrix into a product

$$\rho_{0,RQ} = \frac{1}{2^{N+2}} \Gamma_{0,RQ}^x \Gamma_{0,RQ}^z , \tag{F.8}$$

where $\Gamma_{0,RQ}^a$ is a summation of $a = x, z$ loops and takes the form

$$\Gamma_{0,RQ}^a = \sum_{g_a} g_a \prod_{l=l_1,l_2} \left(1 + \bar{g}_{a,l} s_l^a \right) . \tag{F.9}$$

In the error corrupted state ρ_{RQ}, the X and Z error channels act on $\Gamma^z_{0,RQ}$ and $\Gamma^x_{0,RQ}$, respectively, giving rise to $\rho_{RQ} = \Gamma^x_{RQ}\Gamma^z_{RQ}/2^{N+2}$ with

$$\Gamma^a_{RQ} = \sum_{g_a} \sum_{d_{al}=0,1} e^{-\mu_a \left| \Pi_{l=l_1,l_2} (\bar{g}_{al})^{d_{al}} g_a \right|}$$
$$g_a \prod_{l=l_1,l_2} (\bar{g}_{al} s^a_l)^{d_{al}}, \tag{F.10}$$

where d_{al} is a binary variable indicating whether the loop operator in the summation acts on the non-contractible loop l of the torus.

Our next step is to write down the n-th moment of ρ_{RQ} in the loop picture

$$\text{tr}\,\rho^n_{RQ} = \frac{1}{2^{n(N+2)}} \text{tr}\left((\Gamma^x_{RQ})^n (\Gamma^z_{RQ})^n\right), \tag{F.11}$$

where each $\Gamma^{x(z)}_{RQ}$ is a sum over all possible $X(Z)$ loop operators with positive weights. The product of loop operators from n copies has a non-vanishing trace only if the product is identity. This imposes the constraint on loop configurations and allows expressing the n-th moment as a sum of partition functions

$$\text{tr}\,\rho^n_{RQ} = \frac{1}{2^{(n-1)(N+2)}} \prod_{a=x,z} \sum_{\mathbf{d}_{a1}\mathbf{d}_{a2}} \mathcal{Z}^{(\mathbf{d}_{a1},\mathbf{d}_{a2})}_{n,a}, \tag{F.12}$$

where $\mathbf{d}_{al}$ with $l = 1,2$ is a $(n-1)$-component binary vector, the sum runs over all possible $\mathbf{d}_{al}$, and $\mathcal{Z}^{(\mathbf{d}_{a1},\mathbf{d}_{a2})}_{n,a} = \sum_{\{g^{(s)}_a\}} e^{-H^{(\mathbf{d}_{a1},\mathbf{d}_{a2})}_{n,a}}$ is the partition function with an effective Hamiltonian

$$H^{(\mathbf{d}_{1a},\mathbf{d}_{2a})}_{n,a} = \mu_a \sum_{s=1}^{n-1} \left| (\bar{g}^{(s)}_{a1})^{d_{a1,s}} (\bar{g}^{(s)}_{a2})^{d_{a2,s}} g^{(s)}_a \right|$$
$$+ \mu_a \left| \prod_{s=1}^{n-1} (\bar{g}^{(s)}_{a1})^{d_{a1,s}} (\bar{g}^{(s)}_{a2})^{d_{a2,s}} g^{(s)}_a \right|. \tag{F.13}$$

Here, $d_{al,s}$ denotes the s-th component of vector $\mathbf{d}_{al}$.

The loop model in Eq. (F.13) can be identified with a classical spin model similar to Eq. (7.21). However, there is an important difference due to the presence of the homologically nontrivial loop $\bar{g}^{(s)}_{al}$. Here, we interpret the homologically trivial loop $g^{(s)}_a$ as the Ising domain wall and $\bar{g}^{(s)}_{al}$ as a defect along the non-contractible loop. The defect corresponds to flipping the sign of Ising coupling along a large loop. Specifically, for Z (X) loops on the original lattice, we introduce Ising spin on the plaquettes (vertices) such that

$$\left| (\bar{g}_{a1})^{d_{a1,s}}_\ell (\bar{g}_{a2})^{d_{a2,s}}_\ell g^{(s)}_{a,\ell} \right| = \frac{1 - (-1)^{\lambda^{(s)}_\ell} \sigma^{(s)}_i \sigma^{(s)}_j}{2}, \tag{F.14}$$

where i, j are connected by the link ℓ, and $\lambda_\ell^{(s)} = |(\bar{g}_{a1})_\ell^{d_{a1,s}} (\bar{g}_{a2})_\ell^{d_{a2,s}}|$ is binary variable that denotes whether the defect goes through the link ℓ. This results in an effective Hamiltonian

$$
\begin{aligned}
H_{n,a}^{(\mathbf{d}_{1a}, \mathbf{d}_{2a})} = & - J_a \sum_{\langle i,j \rangle} \sum_{s=1}^{n-1} (-1)^{\lambda_\ell^{(s)}} \sigma_i^{(s)} \sigma_j^{(s)} \\
& + \prod_{s=1}^{n-1} (-1)^{\lambda_\ell^{(s)}} \sigma_i^{(s)} \sigma_j^{(s)}.
\end{aligned}
\tag{F.15}
$$

Hence, $\mathcal{Z}_{n,a}^{(\mathbf{d}_{a1}, \mathbf{d}_{a2})}$ becomes the partition function of the classical spin model with defects inserting along the non-contractible loops labeled by binary vectors $\mathbf{d}_{al}$.

The mapping developed above allows a spin model description for the n-th Rényi coherent information $I_c^{(n)}$. The n-th moment of ρ_Q is identified with the partition function with no defect, i.e. $\mathrm{tr}\,\rho_Q^n = \mathcal{Z}_{n,x}^{(\mathbf{0,0})} \mathcal{Z}_{n,z}^{(\mathbf{0,0})} / 2^{(n-1)N}$. Therefore, we have

$$
I_c^{(n)} = \frac{1}{n-1} \sum_{a=x,z} \log \frac{\sum_{\mathbf{d}_{a1} \mathbf{d}_{a2}} \mathcal{Z}_{n,a}^{(\mathbf{d}_{a1}, \mathbf{d}_{a2})}}{2^{n-1} \mathcal{Z}_{n,a}^{(\mathbf{0,0})}}.
\tag{F.16}
$$

Thus, the Rényi coherent information is associated with the excess free energy of inserting defects along non-contractible loops

$$
\Delta F_{n,a}^{(\mathbf{d}_{a1}, \mathbf{d}_{a2})} := -\log \left(\mathcal{Z}_{n,a}^{(\mathbf{d}_{a1}, \mathbf{d}_{a2})} / \mathcal{Z}_{n,a}^{(\mathbf{0,0})} \right).
\tag{F.17}
$$

Entanglement negativity

Here, we show that the Rényi negativity in the error-corrupted state maps to the excess free energy for aligning spins in the statistical mechanical model. Specifically, we consider the case when only one type of error, e.g. bit-flip errors, is present.

The first step is to write down the partially transposed density matrix ρ^{T_A}. We again work in the loop representation, where the error corrupted state is expressed as a sum of Pauli strings $g = g_x g_z$ in Eq. (7.16). The Pauli string g is invariant under the partial transpose up to a sign factor $y_A(g) = (-1)^{N_Y}$ depending on the number N_Y of Pauli-Y operators inside the subsystem A. Hence,

$$
\rho^{T_A} = \frac{1}{2^N} \sum_g y_A(g) e^{-\mu_x |g_x| - \mu_z |g_z|} g.
\tag{F.18}
$$

Using the above expression, one can write down the n-th moment of ρ^{T_A}

$$
\mathrm{tr} \left(\rho^{T_A} \right)^n = \frac{1}{2^{(n-1)N}} \sum_{\{g^{(s)}\}} \mathcal{O}_N^{(n)} e^{-H_{n,x} - H_{n,z}}.
\tag{F.19}
$$

Here, similar to $\operatorname{tr} \rho^n$, the trace imposes a constraint on the loop operators $g^{(s)}$, and the summation runs over $g^{(s)}$ only in the first $n-1$ copies. The sign factors collected from the partial transpose in each copy are combined in $\mathcal{O}_N^{(n)}$,

$$\mathcal{O}_N^{(n)} = \left[\prod_{s=1}^{n-1} y_A\left(g^{(s)}\right) \right] y_A\left(\prod_{s=1}^{n-1} g^{(s)} \right). \tag{F.20}$$

Eq. (F.19) allows expressing the $2n$-th Rényi negativity in terms of the expectation value of $\mathcal{O}_{2n}$:

$$\mathcal{E}_A^{(2n)} = \frac{1}{2-2n} \log \left\langle \mathcal{O}_N^{(2n)} \right\rangle. \tag{F.21}$$

Yet, analyzing the number of Pauli-Y operators in Eq. (F.20) is a formidable task. Moreover, the observable $\mathcal{O}_N^{(n)}$ derived from the partial transpose should be a basis-independent quantity. Indeed, one can express $O_N^{(n)}$ in terms of loop configurations

$$\begin{aligned}
\mathcal{O}_N^{(n)} &= \prod_{r=1}^{n-2} \operatorname{sgn}_A \left(\prod_{s=1}^{r} g^{(s)}, g^{(r+1)} \right) \\
&= \prod_{r=2}^{n-1} \prod_{s=1}^{r-1} \operatorname{sgn}_A \left(g^{(s)}, g^{(r)} \right).
\end{aligned} \tag{F.22}$$

Here, we use the property

$$y_A(g) y_A(h) = y_A(gh) \operatorname{sgn}_A(g, h), \tag{F.23}$$

where the sign function $\operatorname{sgn}_A(g, h) = \pm 1$ depending on the commutation relation between the support of Pauli string g and h on subsystem A:

$$\operatorname{sgn}_A(g, h) = \begin{cases} 1 & [g_A, \, h_A] = 0 \\ -1 & \{g_A, \, h_A\} = 0 \end{cases}. \tag{F.24}$$

In the second equality of Eq. (F.22), we use the property of sign function

$$\operatorname{sgn}_A(g_1 g_2, g_3) = \operatorname{sgn}_A(g_1, g_3) \operatorname{sgn}_A(g_2, g_3). \tag{F.25}$$

In the Toric code, the operator g further factorizes into $g = g_x g_z$, where g_x, g_z are closed loop operators of Pauli X and Z, respectively. The sign function between two such loop operators g and h reduces to

$$\operatorname{sgn}_A(g, h) = \operatorname{sgn}_A(g_x, h_z) \operatorname{sgn}_A(g_z, h_x). \tag{F.26}$$

We then arrive at

$$\mathcal{O}_N^{(n)} = \prod_{s,r=1, s\neq r}^{n-1} \operatorname{sgn}_A \left(g_x^{(s)}, g_z^{(r)} \right). \tag{F.27}$$

To develop an analytic understanding of the observable $\mathcal{O}_N^{(n)}$ and how it detects the ferromagnetic transition, we first consider the situation when only X or Z error is present. In this case, we show that $\log\langle\mathcal{O}_N^{(n)}\rangle$ exactly maps to the excess free energy of spin pinning and sharply distinguish the two phases. After that, we discuss the general situation when both types of error are present.

We here consider the case when only X errors are present, namely $p_z = 0$ and $\mu_x = 0$. The vanishing X-loop tension indicates that $H_{n,x}$ is in the paramagnetic phase, and the domain walls g_x of arbitrary sizes occur with the same probability. Thus, we can perform an exact summation over all possible g_x and obtain

$$\text{tr}\big(\rho^{T_A}\big)^n = \frac{1}{2^{(n-1)N}}\sum_{\{g_z^{(s)}\}}\mathcal{O}_{N,z}^{(n)}e^{-\mu_z H_{n,z}}, \tag{F.28}$$

where $\mathcal{O}_{N,z}^{(n)} = \sum_{\{g_x^{(s)}\}}\mathcal{O}_N^{(n)}$. The summation in $\mathcal{O}_{N,z}^{(n)}$ is non-vanishing only if the sign functions in Eq. (F.27) for different $g_x^{(s)}$ interfere constructively. This yields a constraint on the $g_z^{(s)}$

$$\mathcal{O}_{N,z}^{(n)} = \prod_{r=1}^{n-1}N_{g_x}\delta_{h^{(r)}(A)} \tag{F.29}$$

where $h^{(r)} = \prod_{s=1,s\neq r}^{n-1}g_z^{(s)}$, the Kronecker delta function $\delta_{h^{(r)}(A)}$ takes the value unity only if the support of $h^{(r)}$ on subsystem A is a closed loop and equals zero otherwise, and N_{g_x} is an unimportant prefactor that denotes the number of possible g_x in each copy. The $n-1$ delta function constraints are independent for odd n, whereas for even n they give rise to only $n-2$ independent constraints as $\prod_{r=1}^{n-1}h^{(r)} = I$.

The constraint requires $h^{(r)}$ not to go through the boundary of subsystem A. In the statistical mechanical model of Ising spins, this corresponds to no domain wall going through the boundary of A, namely forcing $|\partial A|$ boundary spins aligning in the same direction (see Fig. 7.4). Thus, the negativity is associated with the excess free energy for aligning spins

$$\mathcal{E}_A^{(2n)} = \frac{1}{2n-2}(F_A^{(2n)} - F_0^{(2n)}) := \frac{\Delta F_A^{(2n)}}{2n-2}, \tag{F.30}$$

where $F_0^{(2n)} := -\log\mathcal{Z}_{2n,x}\mathcal{Z}_{2n,z}$ and $F_A^{(2n)}$ are the free energy without and with constraints, respectively. Since we have in total $2n-2$ constraints, $\mathcal{E}_A^{(2n)} = \Delta F_A$ with ΔF_A being the excess free energy for aligning one species of Ising spins.

F.2 $\mathbb{Z}_N$ Toric code

So far, we only focus on the $\mathbb{Z}_2$ Toric code with incoherent errors. It is natural to inquire whether our methods are still applicable to $\mathbb{Z}_N$ Toric code and whether the results change.

We provide a brief discussion on the $\mathbb{Z}_3$ Toric code in this subsection. We will use similar symbols to denote the basic operators and stabilizers, although their meanings are different from those in the $\mathbb{Z}_2$ case.

Let us first specify the Hamiltonian and the error models. Consider an $L \times L$ square lattice with periodic boundary conditions. The physical qutrits live on the edges of the lattice. We introduce the clock and shift operators
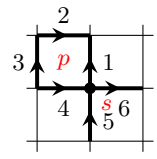
$$XZ = wZX\,, \quad w = e^{2\pi i/3}\,,$$

$$Z = \begin{pmatrix} 1 & & \\ & w & \\ & & w^2 \end{pmatrix}, \quad X = \begin{pmatrix} & 1 & \\ & & 1 \\ 1 & & \end{pmatrix}. \tag{F.31}$$

In and only in this subsection, X and Z refer to the clock and shift, respectively. The code subspace is given by the ground state subspace of the Hamiltonian

$$H_{\mathbb{Z}_3} = -\sum_s A_s - \sum_p B_p \tag{F.32}$$

where A_s and B_p are mutually commuting projectors associated with vertices and plaquettes, e.g.,

$$A_s = \frac{1}{3} \sum_{n=0}^{3} \left(X_4 X_5 X_1^{-1} X_6^{-1}\right)^n$$

$$B_p = \frac{1}{3} \sum_{n=0}^{3} \left(Z_4 Z_1 Z_2^{-1} Z_3^{-1}\right)^n \tag{F.33}$$

One can verify that $A_s^2 = A_s$, $B_p^2 = B_p$. The ground state $|\Psi\rangle$ satisfies $A_s |\Psi\rangle = B_p |\Psi\rangle = |\Psi\rangle$, and the violation of A_s and B_p will be refered to as e (and its anti-particle $\bar{e}$) and m (and its anti-particle $\bar{m}$) anyons, respectively. For simplicity, we only consider the following incoherent error

$$\mathcal{N}_{X,i}[\rho] = (1-p_1 - p_2)\rho$$
$$+ p_1 Z_i \rho Z_i^\dagger + p_2 Z_i^2 \rho Z_i^{2,\dagger}\,, \tag{F.34}$$

which creates a pair of e anyons in two different ways with probabilities p_1 and p_2. In the following, we will first assume $p_1 = p_2 = p$ and comment on what could change without this assumption.

To compute the three diagnostics, one can still work in the loop picture and map the n-th momentum of the error-corrupted state to a partition function of a classical spin model that involves n-flavor 3-state Potts spins. As the error rate increases, the spin model undergoes a paramagnet-to-ferromagnet transition. The three diagnostics are mapped to the corresponding observables in a similar fashion as what we have shown in the $\mathbb{Z}_2$ case. Therefore, they should undergo a transition simultaneously and yield a consistent characterization of the error-induced phase.

When $p_1 \neq p_2$, the spin models obtained in the loop picture contain complex phases and do not admit a statistical mechanical interpretation. Technically, it brings sign problems to the Monte Carlo simulation. It is unclear whether the three diagnostics still exhibit transition simultaneously, which may be an interesting question for future study.